



**HAL**  
open science

# A study of the kinetic energy pathways and routes to dissipation in the Gulf Stream

Marcela Contreras Contreras

► **To cite this version:**

Marcela Contreras Contreras. A study of the kinetic energy pathways and routes to dissipation in the Gulf Stream. Oceanography. Université Paul Sabatier - Toulouse III, 2023. English. NNT : 2023TOU30309 . tel-04558081

**HAL Id: tel-04558081**

**<https://theses.hal.science/tel-04558081>**

Submitted on 24 Apr 2024

**HAL** is a multi-disciplinary open access archive for the deposit and dissemination of scientific research documents, whether they are published or not. The documents may come from teaching and research institutions in France or abroad, or from public or private research centers.

L'archive ouverte pluridisciplinaire **HAL**, est destinée au dépôt et à la diffusion de documents scientifiques de niveau recherche, publiés ou non, émanant des établissements d'enseignement et de recherche français ou étrangers, des laboratoires publics ou privés.



# THÈSE

En vue de l'obtention du

## DOCTORAT DE L'UNIVERSITÉ DE TOULOUSE

Délivré par : *l'Université Toulouse 3 Paul Sabatier (UT3 Paul Sabatier)*

---

---

Présentée et soutenue le 27/11/2023 par :

**Marcela CONTRERAS CONTRERAS**

---

---

**Etude du cycle de l'énergie cinétique et des voies de dissipation dans le Gulf Stream**

---

---

### JURY

JULIEN LESOMMER	Directeur de Recherche (IGE/CNRS, Grenoble)	Rapporteur
XAVIER CAPET	Directeur de Recherche (LOCEAN/CNRS, Paris)	Rapporteur
YVES MOREL	Directeur de recherche (LEGOS/CNRS, Toulouse)	Président du jury
CLAIRE MÉNESGUEN	Chargée de recherche (IFREMER, Brest)	Examinatrice
HÉCTOR HITO SEPÚLVEDA	Associate Professor (DGEO, Chili)	Examineur
ÓSCAR PIZARRO	Full Professor (DGEO, Chili)	Examineur
LIONEL RENAULT	Directeur de recherche (LEGOS/IRD, Toulouse)	Directeur de thèse
PATRICK MARCHESIELLO	Directeur de recherche (LEGOS/IRD, Toulouse)	Co-directeur de thèse

---

#### École doctorale et spécialité :

*SDU2E : Océan, Atmosphère, Climat*

#### Unité de Recherche :

*LEGOS (UMR 5566)*

#### Directeur(s) de Thèse :

*Lionel RENAULT et Patrick MARCHESIELLO*

#### Rapporteurs :

*Julien LESOMMER et Xavier CAPET*



---

## Résumé —

La circulation méridienne de retournement de l’océan Atlantique (AMOC) joue un rôle essentiel sur le climat en convoyant la chaleur à l’échelle du globe. Le Gulf Stream (GS) est un courant de bord ouest, composante majeure de l’AMOC. Les observations et modèles océaniques ont montré sa complexité sur une large gamme d’échelles spatio-temporelles. Notre compréhension de la dynamique du GS présente encore des lacunes importantes, et les simulations numériques montrent des biais par rapport aux observations. Une amélioration significative est obtenue en résolvant l’activité de mésoéchelle (résolution  $<1/10^\circ$ ), mais dans ce cas une énergie excessive est souvent générée, suggérant des processus de dissipation manquants.

L’objectif principal de cette étude est d’évaluer le cycle de l’énergie cinétique dans le GS, en insistant sur les mécanismes de dissipation. Nous présentons tout d’abord une simulation forcée de l’océan résolvant en partie la sous-mésoéchelle ( $dx = 2$  km) pour décrire la distribution spatio-temporelle des cascades turbulentes, basée sur une méthode de coarse-graining. L’étude confirme que les mouvements équilibrés conduisent à une cascade inverse d’énergie depuis les échelles d’injection vers les grandes échelles. Inversement, l’interaction des courants équilibrés et déséquilibrés (advection agéostrophique) entraîne une cascade directe vers les plus fines échelles. Le changement de direction de ce transfert d’énergie varie dans l’espace et le temps, mais se situe en moyenne autour de 10 km dans le GS.

Pour identifier les principaux puits d’énergie, nous avons comparé la dissipation intérieure (provenant de la cascade directe) avec la dissipation numérique et dissipation frictionnelle au fond et en surface (interaction océan-atmosphère). Nos résultats indiquent que la dissipation intérieure est bien inférieure aux autres puits d’énergie. La dissipation numérique est sensible au choix des schémas d’advection et un schéma d’ordre supérieur conduit à une réduction significative, mais compensée par une augmentation de friction aux limites, plutôt que de la cascade directe.

Nous avons également évalué l’influence de la marée sur le cycle énergétique de la circulation. En comparant la simulation précédente avec une simulation similaire ne différant que par le forçage des marées, nous constatons que les marées internes modulent la cascade turbulente du GS via l’interaction vague-courant, conduisant finalement à une augmentation de la cascade directe. Cependant, malgré l’intensification, la cascade directe d’énergie cinétique reste significativement inférieur à la dissipation numérique et frictionnelle.

Afin d’obtenir une compréhension globale du bilan énergétique du GS, nous avons réalisé pour finir une simulation couplée océan-atmosphère d’une durée d’un an et résolvant de manière plus complète la gamme sous-mésoéchelle ( $dx = 700$  m). Nous représentons le cycle énergétique par un diagramme de Lorenz, couvrant à la fois l’énergie potentielle et cinétique. Les résultats montrent qu’il existe des voies distinctes pour le transfert de l’énergie cinétique et potentielle. La principale route vers la sous-mésoéchelle est permis par le transfert direct de l’énergie potentielle (par brassage tourbillonnaire et frontogénèse), qui subit une conversion

barocline pour former de l'énergie cinétique à toutes les échelles. L'énergie cinétique subit alors une atténuation par friction, ou par mélange vertical dans la couche de surface. L'énergie cinétique se déplace également par interaction nonlinéaire, d'une part de la sous-mésoéchelle équilibrée ( $> 10$  km) vers les échelles supérieures, et, d'autre part, de la sous-mésoéchelle déséquilibrée ( $< 10$  km) vers les plus fines échelles suivant une cascade directe.

**Mots clés:** *Gulf Stream, Modélisation forcée et couplée océan-atmosphère, Processus à sous-mésoéchelle, Bilan énergétique, Dissipation de l'énergie, Interactions air-mer, Marée*

---

---

**Abstract** —

The Atlantic Meridional Ocean Circulation (AMOC) plays a critical role in the climate system, conveying heat around the globe. The Gulf Stream (GS) is a major surface component of the AMOC, renowned as a strong western boundary current. Observations and ocean models have shown that the GS is complex with diverse mechanisms affecting a wide spectrum of temporal and spatial scales. Our understanding of GS dynamics still has major gaps, and numerical simulations have biases compared with observations. A significant improvement is achieved by resolving the mesoscale activity (grid scale  $<1/10^\circ$ ), but in this case the models often generate excessive kinetic energy, suggesting missing dissipation processes.

The main objective of this study is to assess the kinetic energy (KE) pathway in the GS, with a focus on the mechanisms of dissipation. We first present a submesoscale-permitting ( $dx = 2$  km) forced ocean simulation to describe the spatial and temporal distribution of turbulent cascades based on a coarse-graining method. The study confirms that balanced motions lead to an inverse KE cascade from injection scales to large scales. Conversely, the interaction of balanced and unbalanced motions (ageostrophic advection) results in a forward cascade to smaller scales. The scale at which energy transfer changes direction depends on the dominant mechanisms, which vary in space and time, but is on average around 10 km in the GS.

To identify the main kinetic energy sinks, we compared interior dissipation — assumed to ensue from the forward cascade — with numerical dissipation and frictional dissipation at the vertical boundaries (*i.e.*, bottom drag and top drag). Our results indicate that the interior dissipation is an order of magnitude lower than other energy sinks. Numerical dissipation is sensitive to the choice of horizontal momentum advection schemes and using a higher-order scheme leads to a significant reduction in numerical dissipation, as expected. However, this reduction is offset by an increase in boundary friction rather than downscale flux. Top and bottom boundary friction therefore appears to be the most important and most robust dissipation process.

In addition, we evaluate the influence of tides on the energy pathways of wind-driven circulation. Comparing the previous simulation with a similar one differing only in tidal forcing, we find that internal tides modulate the turbulent GS cascade via wave-flow interaction, ultimately leading to an increase in the forward cascade. However, despite intensification, the downscale energy flux remains significantly lower than numerical and boundary dissipation.

To gain a global understand of the GS's energy balance, we finally carried out a year-long coupled ocean-atmosphere simulation with submesoscale resolution ( $dx = 700$  m). We assessed the accuracy of the simulation using observational data and constructed a Lorenz diagram to represent the complete energy cycle at submesoscale, covering both potential and kinetic energy pathways. The results confirm that wind stress is the primary external source of energy, injecting it on a large scale. However, there are distinct pathways for the travel and sink of kinetic and potential energy. The primary pathway for potential energy is a downscale flux to submesoscales, while converting to kinetic energy through baroclinic processes.

Meanwhile, kinetic energy experience depletion at all scales through boundary dissipation, including vertical mixing in the surface boundary layer. However, kinetic energy also travels across scales as balanced submesoscales ( $> 10$  km) energize the larger scale through shear production and unbalanced submesoscales ( $< 10$  km) follow a forward cascade. The submesoscale range therefore appears to be divided into two ranges, whose dynamic regime is determined by the extent of ageostrophic advection.

**Keywords:** *Gulf Stream, Ocean-Atmosphere Coupled and Uncoupled Models, Submesoscale processes, Energy Budget, Energy Dissipation, Air-Sea interactions, Tides*

---



# Acknowledgments

First, I would like to thank my supervisors Lionel Renault and Patrick Marchesiello for their constant support and patience during these three years of work. This thesis would not have been the same without their suggestions, ideas, comments, and discussions that nurtured this work. Both Lionel and Patrick contributed to making the PhD an enriching experience.

I'd also like to thank the referees and examiners composing the jury for their comments and suggestions. In particular: Xavier Capet and Julien Lesommer, for their interest in reviewing the thesis and their comments. To Claire Menesguen for attending the PhD defence in person. To Yves Morel for his participation in the thesis commissions during the PhD. Finally, to Oscar Pizarro and Andrés Sepúlveda, who contributed to the beginning of my training in oceanography, providing me with the basic knowledge that allowed me to complete this thesis.

I'm grateful to the Doctoral School and GESSEC for their helpfulness and support in all procedures during these years.

I appreciate the sympathy of the people I met in the lab. Also to the Latin Legos community for the shared moments, which were an opportunity to improve my Spanish :).

Finally, I would like to thank my family, especially my parents. Their unconditional support and trust in me have been the foundation that has allowed me to get this far.

This thesis was funded by Becas Chile from ANID (Agencia Nacional de Investigacion y Desarrollo; CONICYT-PFCHA/Doctorado Becas Chile/2020-72210196).



# Contents

<b>Acronyms</b>	<b>xiii</b>
<b>General introduction</b>	<b>1</b>
<b>Introduction Générale</b>	<b>5</b>
<b>1 The Gulf Stream System</b>	<b>9</b>
1.1 Introduction . . . . .	10
1.2 General Description . . . . .	12
1.3 Classical models of wind-driven gyre circulation . . . . .	16
1.4 The role of topography and eddies . . . . .	21
1.5 Gulf Stream representation in numerical ocean models . . . . .	25
<b>2 Kinetic energy pathway</b>	<b>31</b>
2.1 Introduction . . . . .	32
2.2 Description of spatial and temporal kinetic energy distribution . . . . .	32
2.3 External kinetic energy sources . . . . .	36
2.4 Ocean scale interactions . . . . .	36
2.5 Kinetic energy dissipation . . . . .	43
2.6 Final comments . . . . .	47
<b>3 Methodology</b>	<b>49</b>
3.1 Numerical Models . . . . .	50
3.2 Post-processing . . . . .	56
<b>4 Understanding energy pathways in the Gulf Stream.</b>	<b>61</b>
4.1 Preamble . . . . .	62

4.2	AMS Copyright Notice . . . . .	63
4.3	Article . . . . .	63
4.4	Conclusion . . . . .	82
<b>5</b>	<b>Tidal modulation of energy dissipation routes in the Gulf Stream</b>	<b>83</b>
5.1	Preamble . . . . .	84
5.2	Article . . . . .	84
5.3	Supporting Information . . . . .	96
5.4	Conclusion . . . . .	101
<b>6</b>	<b>A full description of the Lorenz Energy Cycle over the Gulf Stream</b>	<b>103</b>
6.1	Introduction . . . . .	104
6.2	Models Configuration . . . . .	105
6.3	Energy budget equations . . . . .	111
6.4	Submesoscale energy cycle . . . . .	119
6.5	Quasi-balanced and unbalanced submesoscale ranges . . . . .	125
6.6	Seasonal Variability . . . . .	128
6.7	Conclusion and Discussion . . . . .	134
	<b>Conclusion and perspectives</b>	<b>137</b>
	<b>Conclusion et perspectives</b>	<b>145</b>
	<b>Bibliography</b>	<b>153</b>

# List of Figures

1	Schematic of the energy pathway involving mesoscales and submesoscales: The upper line depicts the forward cascade of potential energy (PE) caused by eddy stirring, while the lower line represents the kinetic energy (KE) pathway. At a fine scale of approximately 10-20 km, submesoscales enable the conversion of PE into KE through frontogenesis and the expansion of the inverse KE cascade spectral range. Conventional satellite altimeters only capture the energy pathway involving interior baroclinic instability at the mesoscale (down to 100 km). In the future, wider swath altimeters, like Surface Water and Ocean Topography, should capture the energy pathway involving finer scales (down to approximately 10-20 km). Reprinted from Klein et al. (2019). . . . .	2
1.1	Eddy kinetic energy (EKE) estimated from the AVISO geostrophic currents. Black outlines indicate the GS region. Reprinted and adapted from Renault et al. (2017). . . . .	10
1.2	Time-mean (1988-2017) global surface net heat flux obtained from J-OFURO3 V1.1. Positive values are upward heat flux. Unit in $\text{W m}^{-2}$ . Black outlines indicate the GS region. Reprinted and adapted from Tomita et al. (2021) . .	11
1.3	A schematic of the North Atlantic Ocean circulation: (top) the entire basin and (bottom) a close-up of the western boundary region. Surface currents, including the Gulf Stream, the North Atlantic Current (NAC), and Labrador Current, are shown in red, and the deep western boundary current (DWBC) is shown in blue. Reprinted from Buckley and Marshall (2016). . . . .	11
1.4	(a) Representation of the Azores High (red ellipses) and the Icelandic Low (shaded light blue) along with the westerlies and trade winds. (b) Annual (c) Winter (January, February, and March) (d) Summer (July, August, and September) means of the wind (vectors) and its magnitude (shaded). Data were obtained from SCOW (Chelton et al., 2000). . . . .	13
1.5	(a) Annual (b) Winter (January, February, and March) (c) Summer (July, August, and September) total heat flux. Thick and thin lines represent the 200 and $400 \text{ Wm}^{-2}$ contours, respectively. Data were obtained from COADS05 (da Silva et al., 1994). . . . .	13
1.6	Scheme of the currents in the North Atlantic Ocean. . . . .	14
1.7	Topography (m) of the North Atlantic. The area marked with a magenta border represents the South Atlantic Bight. Data were obtained from ETOPO2 ( <a href="https://doi.org/10.7289/V5J1012Q">https://doi.org/10.7289/V5J1012Q</a> ). . . . .	17

1.8	(a) Idealized zonal wind pattern, where westerlies winds (trade winds) blow in the north (south). (b) Representation of the transport generated by the winds of (a) estimated from Sverdrup's theory. Reprinted and adapted from <a href="#">Colling (2001)</a> . . . . .	18
1.9	Transport in the eastern Pacific calculated from Eq. 1.2 and 1.3 using observed winds (solid lines) and pressure calculated from hydrographic data from ships (dots). Reprinted from <a href="#">Stewart (2008)</a> . . . . .	19
1.10	(a) Wind Stress used by Stommel to estimate the circulation. Streamfunction solution for (b) constant Earth rotation and (c) differential Earth rotation (varying linearly with latitude). Reprinted from <a href="#">Stewart (2008)</a> . . . . .	20
1.11	Simulated SST downstream of the Charleston Bump and to the south of the Gulf Stream separation point reveals the propagation of a large frontal eddy, which is visible as a cold anomaly. The surface velocities are represented by black vectors, while the topography is depicted through black contours at levels of -200, -600, -1000, and -2000 meters. Reprinted from <a href="#">Gula et al. (2016)</a> . . .	23
1.12	Simulated SST for the Gulf Stream showing a typical GS deflection at the Charleston bump. Inserts show corresponding sketches, retraced from AVHRR SST image, taken from <a href="#">Bane Jr and Dewar (1988)</a> . Topography is shown in black contours by the 0-, 200-, 600-, 1000-, and 2000-m isobaths. Reprinted from <a href="#">Gula et al. (2015b)</a> . . . . .	23
1.13	Simulated (a) surface relative vorticity (normalized by $f$ ) and (b) sea surface temperature in March 2007. Adapted from <a href="#">Contreras et al. (2023b)</a> . . . . .	25
1.14	Snapshot of surface relative vorticity normalized by the local Coriolis parameter on 1 February at 00:00 from several model run over the Gulf Stream. Reprinted from <a href="#">Uchida et al. (2022)</a> . . . . .	29
1.15	Mean (a) and RMS (b) GS trajectory estimated by mean geostrophic currents (contour $0.6 \text{ ms}^{-1}$ ): from AVISO (red), a forced oceanic simulation without top drag parameterization (blue), and a coupled air-sea simulation (black), for the period 2000-04. Reprinted from <a href="#">Renault et al. (2016a)</a> . . . . .	30
2.1	Time and space scales of the ocean processes. Reprinted from <a href="#">Dickey (2001)</a> and adapted by <a href="#">Chelton (2011)</a> . . . . .	32
2.2	KE spectrum estimated from winter currents observed across the GS at 50 m depth. The light shading is the 95% confidence interval and the lines are the reference for the slopes $k^{-2}$ and $k^{-3}$ . Reprinted and adapted from <a href="#">Callies et al. (2015)</a> . . . . .	34

2.3 KE spectrum estimated from a current meter at 128 m depth on a mooring located over the Mid-Atlantic Ridge near 27°N. The peaks showing the inertial frequency, principal lunar semidiurnal M2, and diurnal O1, K1 tidal are represented, along with the percentage of KE concentrated around these peaks. Reprinted and adapted from [Ferrari and Wunsch \(2009\)](#). . . . . 35

2.4 (a) Frequency-wave number spectrum of KE in the Kuroshio-Extension, during January-February-March winter season. (b) schematic frequency-wave number spectrum, where is displays the multiple dynamical regimes: RW stands for Rossby waves, MBM for mesoscale balanced motions, SBM for submesoscale balanced motions, USM for unbalanced submesoscale motions, and IGW for internal gravity waves. The schematic spectrum shows the dispersion relation of the first ten baroclinic modes: mode-1 in gray dotted line, mode-2 to mode-9 green dashed lines, and mode-10 in black. The nondispersive line,  $\omega - ck = 0$ , is drawn with  $c$  corresponding to an eddy speed of 8.5 km/day (10 m/s). Reprinted and adapted from [Torres et al. \(2018\)](#). . . . . 35

2.5 Spectral KE flux estimated from altimeter data over the Antarctic Circumpolar Current: the black curve using SSH on a 32 × 32 grid, red curve using SSH on a 64 × 64 grid, blue curve using velocity on a 64 × 64 grid. Error bars represent standard error. Reprinted from [Scott and Wang \(2005\)](#). . . . . 37

2.6 Spectral KE flux estimated from surface geostrophic ocean currents in the GS, using AVISO data (cyan curves) and four versions of estimation from a realistic ocean model simulation: unfiltered (black curves), spatially filtered (red curves), temporally filtered (blue curves), and spatially and temporally filtered (green curves). The vertical dashed line indicates the Rossby deformation wavenumber. Reprinted and adapted from [Arbic et al. \(2013\)](#). . . . . 39

2.7 Surface EKE time series from the ocean simulation (OFES) over the Subtropical Countercurrent (red line) vs the AVISO SSH data (blue line) in 2001. (b) Time series of mesoscale EKE (green line) vs submesoscale EKE (red line) from the simulation. Blue line is same as that in (a). Reprinted and adapted from [Qiu et al. \(2014\)](#). . . . . 39

2.8 Schematic presentation of an intensifying surface front (frontogenesis) caused by a large-scale straining flow. The downfront flow  $v(x)$  is approximately geostrophic, and variables with primes are local perturbations presenting the ageostrophic secondary circulation across the front. Reprinted and adapted from [McWilliams \(2016\)](#). . . . . 41

2.9 Schematic representation of the current feedback effects over an anticyclonic eddy, considering a uniform southward wind. The arrows represent the wind (green), surface stress (black), and surface current (blue). The red (blue) shade indicates a positive (negative)  $F_e K_e$ . The black (green) +/- signs indicate the current-induced stress (wind) curl. Reprinted from [Renault et al. \(2016b\)](#). . . 46

3.1	Representation of the physics schemes included in WRF. Reprinted from <a href="https://www2.mmm.ucar.edu/wrf/users/wrf_users_guide/build/html/physics.html">https://www2.mmm.ucar.edu/wrf/users/wrf_users_guide/build/html/physics.html</a> . . . . .	54
3.2	(Top) Domain of the 6 km atmospheric simulation. The black line indicates the area covered by the 2 km oceanic simulation. The purple lines indicate the domains of high-resolution simulations for both the atmosphere (2 km) and the ocean (700 m). (Bottom) The domain for the 2 km atmospheric simulation is depicted, with the purple line indicating the domain for the 700 m oceanic simulation. . . . .	55
3.3	Summary of the oceanic and atmospheric simulations used throughout the thesis.	57
6.1	Mean dynamic topography (m) from (a) CROCO and (b) AVISO. . . . .	108
6.2	Sea surface temperature ( $^{\circ}C$ ) from (a) CROCO and (b) drifter data (Laurindo et al., 2017) and (c) their differences. Magenta and green contours represent the mean GS path ( $0.5 \text{ m s}^{-1}$ ). . . . .	108
6.3	Annual-mean (2005-2007) heat fluxes ( $\text{mW m}^{-2}$ ) from: (left) low-resolution atmospheric simulation (LR-W); (middle) OAFLUX; and (right) their difference. . . . .	109
6.4	Annual-mean (2005-2007) air temperature at 2 m ( $^{\circ}C$ ) from: (a) low-resolution atmospheric simulation (LR-W); (b) OAFLUX data; and (c) their difference. . . . .	110
6.5	Annual-mean (2005-2007) wind stress curl ( $\text{N m}^{-2}$ ) from: (a) low-resolution atmospheric simulation (LR-W); (b) SCOW data; and (c) their difference. . . . .	110
6.6	Annual-mean (May 2005-April 2006) heat fluxes ( $\text{mW m}^{-2}$ ) from: (left) high-resolution atmospheric simulation (HR-W); (middle) OAFLUX; and (right) their difference. . . . .	111
6.7	Annual-mean (May 2005-April 2006) air temperature at 2 m ( $^{\circ}C$ ) from: (a) high-resolution atmospheric simulation (HR-W); (b) OAFLUX; and (c) their difference. . . . .	112
6.8	Annual-mean (May 2005-April 2006) wind stress curl ( $\text{N m}^{-2}$ ) from: (a) high-resolution atmospheric simulation (HR-W); (b) SCOW data; and (c) their difference. . . . .	112
6.9	Annual-mean (May, 2005 - April, 2006) energy reservoirs: (a) <i>BKE</i> , (b) <i>BPE</i> , (c) <i>SKE</i> and (d) <i>SPE</i> integrated between 1 and 150 m. The units are $1000 \cdot \text{Jm}^{-2}$ . (e-h) Relative difference (percentage) between energy reservoirs using 16 km and 8 km cutoff filters . . . . .	118

6.10	Lorenz diagram showing sources and sinks of the background and submesoscale potential and kinetic energy reservoirs. The terms are averaged for the period May 2005 to April 2006 and over the entire domain excluding the shelf zone, and integrated between 1 and 150 m depth. The arrows indicate the direction of energy transfer. The unit is in $\text{mW m}^{-2}$ . . . . .	120
6.11	Annual-mean (May, 2005 - April, 2006) KE budget terms: (a) $PK_B$ , (b) $FK_B$ , (c) $DK_B$ (d) $PK_S$ , (e) $10 \cdot FK_S$ , (f) $DK_S$ integrated between 1 m and 150 m depth ( $\text{mW m}^{-2}$ ). . . . .	122
6.12	Annual-mean (May, 2005 - April, 2006) barotropic transfer terms of KE and APE budgets: (a) $BSK$ , (b) $SBK$ , (c) $BnK$ (d) $BSP$ , (e) $SBP$ , (f) $10 \cdot BnP$ integrated between 1 m and 150 m depth ( $\text{mW m}^{-2}$ ). . . . .	124
6.13	Annual-mean (May, 2005 - April, 2006) forcing and diffusion terms of APE budget: (a) $FP_B$ , (b) $DP_B$ , (c) $100 \cdot FP_S$ and (d) $DP_S$ , integrated between 1 m and 150 m depth ( $\text{mW m}^{-2}$ ). . . . .	126
6.14	Schematic of the energy cycle, where the cutoff scale between background and submesoscales is taken at 8 km. The terms are averaged for the period May 2005 - April 2006 and over the whole domain (excluding the shelf zone), and integrated between 1 and 150 m depth. The arrow indicates the direction of energy transfer. The unit is in $\text{mW m}^{-2}$ . . . . .	127
6.15	Snapshot of the surface relative vorticity (normalized by $f$ ) on February 16, 2006 and August 01, 2005. . . . .	129
6.16	Schematic of the energy cycle, for the background scale and submesoscale reservoirs using a 16 km cutoff for scale separation. The terms are averaged for January 2006 - March 2006 and over the whole domain (excluding the shelf zone), and integrated between 1 and 150 m depth. The arrow indicates the direction of energy transfer. The unit is in $\text{mW m}^{-2}$ . . . . .	131
6.17	(a and e) $BKE$ , (b and f) $BPE$ , (c and g) $SKE$ and (d and h) $SPE$ integrated between 1 m and 150 m, and averaged in (left) winter and (right) summer. The units are $1000 \cdot Jm^{-2}$ . . . . .	132
6.18	Schematic of the energy cycle, for the background scale and submesoscale reservoirs using a 16 km cutoff for scale separation. The terms are averaged for July - September 2005 and over the whole domain (excluding the shelf zone), and integrated between 1 and 150 m depth. The arrow indicates the direction of energy transfer. The unit is in $\text{mW m}^{-2}$ . . . . .	133

- 6.19 Schematic view of the kinetic (KE) and potential (PE) energy cycles of the wind-driven ocean circulation. The motions are decomposed into planetary scale (PS), mesoscale (MS), balanced submesoscale (BSM), and unbalanced submesoscale (USM). Dark and light green arrows represent, respectively, the cross-scale transfer of PE and KE through shear production. The length of the arrows indicates the relative magnitudes of energy exchange. The orange arrows represent the transfer between PE and KE through buoyancy production (baroclinic conversion). The dominant mechanisms involved in energy fluxes are indicated in corresponding colors. The arrows outside the gray area show the contribution of external sources and sinks. Note that the main input of energy is provided by wind work at large scale (at all scales below, wind work is a sink of energy). The scale at which the forward cascade is observed marks the transition to from quasi-balanced to unbalanced submesoscale motions. . 140

# List of Tables

2.1	Classification of oceanic dynamical regimes from temporal and spatial scales.	33
-----	---	----



# Acronyms

<b>GS</b>	<i>Gulf Stream</i>
<b>AMOC</b>	<i>Atlantic Meridional Overturning Circulation</i>
<b>WBC</b>	<i>Western Boundary Current</i>
<b>SST</b>	<i>Sea Surface Temperature</i>
<b>SSH</b>	<i>Sea Surface Height</i>
<b>KE</b>	<i>Kinetic Energy</i>
<b>PE</b>	<i>Potential Energy</i>
<b>EKE</b>	<i>Eddy Kinetic Energy</i>
<b>APE</b>	<i>Available Potential Energy</i>
<b>CFB</b>	<i>Current Feedback</i>
<b>TFB</b>	<i>Thermal Feedback</i>
<b>CROCO</b>	<i>Coastal and Regional Ocean COmmunity model</i>
<b>WRF</b>	<i>Weather Research &amp; Forecasting Model</i>



# General introduction

The Gulf Stream (GS) is a surface, strong, persistent, warm, and narrow current that is part of the Western Boundary Currents of the global ocean. The GS is a key component of the global circulation, in particular the Atlantic Meridional Ocean Circulation (AMOC). The AMOC transports warm upper waters towards the pole and draws cold deep waters back southward over the equator. The AMOC's conveyance of warm water plays a leading role in regulating oceanic and continental climates (Bryden et al., 2005).

Previous studies show that the GS is a complex system in which multiple mechanisms exert a strong influence over a wide range of temporal and spatial scales. At large scale, it is partly driven by the Sverdrup balance between wind stress curl and differential Earth rotation (Sverdrup, 1947). However, its trajectory and transport near the western border are strongly influenced by topography and eddy-mean interaction (Kang and Curchitser, 2015; Schoonover et al., 2016; Özgökmen and Chassignet, 2002; Hughes and De Cuevas, 2001).

The GS system is the subject of a great deal of oceanographic research. However, there are still important gaps in our understanding of its dynamics. Its representation by numerical ocean models shows significant dispersion in solutions and significant biases compared with in situ and satellite observations. Low-resolution simulations ( $> 100$  km) fail to correctly reproduce the GS separation from the coast, as the current continues along the western margin north of Cape Hatteras, resulting in weak eastward penetration into the basin interior (Chassignet and Xu, 2017; Bryan et al., 2007). A significant improvement is achieved by solving mesoscale activity (grid scale  $< 1/10^\circ$ ), although excessive kinetic energy is often produced by the models in this case (Chassignet and Xu, 2017; Özgökmen and Chassignet, 2002), suggesting missing dissipation processes. A realistic representation of the GS is then only possible with adequate kinetic energy sources and sinks in the kinetic energy balance.

Current theory suggests that atmospheric forcing and tides are the main external energy sources, injecting kinetic and potential energy on a large scale ( $> \mathcal{O}(100\text{km})$ ) (Ferrari and Wunsch, 2009). The large scale flow generate mesoscale eddies through baroclinic instability, which convert potential into kinetic energy. Mesoscale eddies interact with each other and, through eddy merging, transfer kinetic energy back up the scale (inverse cascade) (Charney, 1971; Scott and Wang, 2005). At the same time, however, they induce transfer of potential energy down the scale through eddy stirring and frontogenesis (Klein et al., 2019). As a result, horizontal density anomalies develop at submesoscale (below a few 10 km), forming potential energy that converts to kinetic energy through vertical fluxes of buoyancy – associated with ageostrophic secondary circulation or mixed layer instabilities (Capet et al., 2008a). Due to the weakened effects of rotation and stratification at these scales, unbalanced motions can interact with balanced motions and promote a transfer of kinetic energy to smaller scales (forward cascade) in route to dissipation (Molemaker et al., 2010; Capet et al., 2008a). However, at the same time, submesoscale fronts can also energize larger scales through interaction with mesoscale eddies, thus extending the inverse energy cascade to the submesoscale range (Klein

et al., 2008; Qiu et al., 2014; Schubert et al., 2020). Consequently, the scale at which cross-scale fluxes change sign is in the submesoscale range (around 10 km according to Klein et al. 2008), but the dissipation pathway can start at a larger scale via potential energy transfers (Figure 1).

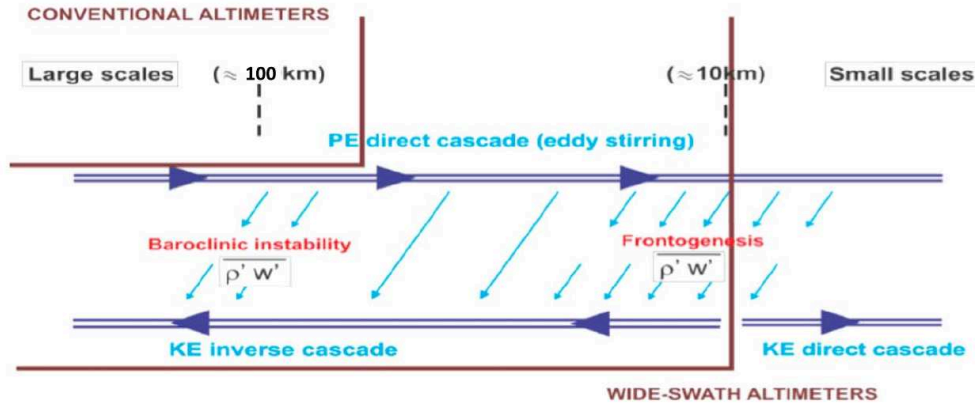


Figure 1: Schematic of the energy pathway involving mesoscales and submesoscales: The upper line depicts the forward cascade of potential energy (PE) caused by eddy stirring, while the lower line represents the kinetic energy (KE) pathway. At a fine scale of approximately 10-20 km, submesoscales enable the conversion of PE into KE through frontogenesis and the expansion of the inverse KE cascade spectral range. Conventional satellite altimeters only capture the energy pathway involving interior baroclinic instability at the mesoscale (down to 100 km). In the future, wider swath altimeters, like Surface Water and Ocean Topography, should capture the energy pathway involving finer scales (down to approximately 10-20 km). Reprinted from Klein et al. (2019).

In addition to the interior route of energy dissipation, other energy sinks have been recognized as contributing to the maintenance of energy balances. At the boundaries, there is dissipation due to bottom drag caused by the interaction between bottom topography and bottom currents (Sen et al., 2008; Trossman et al., 2017) and top drag - also known as the current feedback effect - caused by the interaction between surface currents and surface winds (Renault et al., 2016b). Vertical mixing, particularly in the oceanic planetary boundary layer, is also highlighted as a very important energy sink (Wunsch and Ferrari, 2004). Finally, numerical ocean models also generate numerical dissipation (implicitly or explicitly) to dampen dispersion errors resulting from the spatial and temporal discretization of the equations, in particular the advection terms (Soufflet et al., 2016; Marchesiello et al., 2011).

The kinetic energy pathway described above is a general theory, but it has not been fully demonstrated in the GS. Furthermore, the role of mechanisms such as tides and air-sea interactions is not fully integrated in the theory. The main objective of the present study is to describe the kinetic energy pathway over the GS and the mechanisms involved in the kinetic energy dissipation, attempting to quantify and compare the various components. These analyses are performed using numerical ocean and atmospheric models.

In Chapter 1, we describe the regional circulation of the GS and the mechanisms that

modulate its dynamics. We also describe the main difficulties of numerical ocean models in representing the GS. A summary of the theory of the kinetic energy pathway is described in Chapter 2. In Chapter 3, we present the methodology implemented in this thesis. Specifically, we describe the main features of the numerical oceanic and atmospheric models used (CROCO and WRF, respectively). In addition, we describe the coarse-grained method that allows us to estimate the cross-scale kinetic energy flux. This estimation will be key to our research.

In Chapter 4, we analyze the kinetic energy cascade over the GS estimated by the coarse-grained method, using a forced submesoscale-permitting oceanic simulation. This method allows us to describe the spatial variability of the cross-scale kinetic energy flux. We then discussed the mechanisms involved in the forward cascade, *i.e.*, mainly ageostrophic advection associated with frontogenesis. Interior dissipation (dissipation following the forward cascade) is quantitatively compared with both numerical and boundary dissipation. We find that interior dissipation is an order of magnitude smaller than the other energy sinks. Finally, we evaluate the sensitivity of energy sinks to the horizontal momentum advection scheme and show that lower numerical dissipation in a higher-order scheme leads to a compensatory increase in boundary dissipation.

Tides are one factor that can modulate the kinetic energy pathway and are not yet fully understood. Their effects on the energy cascade and energy sinks are discussed in Chapter 5. By comparing a series of submesoscale simulations with and without tides, we found that internal tides modulate the GS turbulent cascade through wave-flow interaction while external tides increase the bottom drag of the subtidal circulation in the deep ocean.

Chapter 6 described the submesoscale energy cycle, as part of a Lorenz energy cycle describing the generation, conversion and dissipation of potential and kinetic energy in the ocean, including the effects of air-sea interaction. Using a high-resolution coupled ocean-atmosphere simulation over the GS, we estimate the terms of the energy budget equations. The main results found are that kinetic energy reservoirs are fed at all scales (mesoscale and submesoscale) by potential energy transfers, and drained by boundary friction, vertical mixing and numerical dissipation. In addition, the inverse kinetic energy cascade extend to the submesoscale range, down to 8 km, and only a small amount follows a forward cascade below 8 km.

Finally, Chapter 7 presents the conclusions and perspectives of our study.



# Introduction Générale

Le Gulf Stream (GS) est un courant de surface, fort, persistant, chaud et étroit qui fait partie des courants de Bord Ouest de l’océan mondial. Le GS est un élément clé de la circulation mondiale, en particulier de la circulation méridienne de retournement de l’océan Atlantique (AMOC). L’AMOC transporte des eaux chaudes de surface vers le pôle et les eaux profondes froides vers le sud à travers l’équateur. L’acheminement des eaux chaudes par l’AMOC joue un rôle majeur dans la régulation des climats océaniques et continentaux (Bryden et al., 2005).

Des études antérieures ont démontré que le GS est un système complexe dans lequel de multiples mécanismes exercent une forte influence sur un large éventail d’échelles temporelles et spatiales. Il forme la branche occidentale du gyre subtropical de l’Atlantique Nord, qui à grande échelle, est régi par l’équilibre de Sverdrup entre le rotationnel de la tension de vent et la rotation de la Terre (Sverdrup, 1947; Munk, 1950). Cependant, sa trajectoire et son transport le long de la côte sont fortement influencés par la topographie et l’interaction tourbillon-grande-échelle (Kang and Curchitser, 2015; Schoonover et al., 2016; Özgökmen and Chassignet, 2002; Hughes and De Cuevas, 2001).

Le GS a été l’objet de nombreuses recherches océanographiques. Cependant, il existe encore d’importantes lacunes dans notre compréhension de sa dynamique. Sa représentation par les modèles numériques océaniques montre une dispersion importante des solutions et des biais significatifs par rapport aux observations in situ et satellitaires. Les simulations à basse résolution ( $> 100$  km) ne parviennent pas à reproduire correctement la séparation du GS de la côte au niveau du Cap Hatteras, et le courant continue son chemin le long de la marge occidentale au nord du Cap Hatteras, ce qui entraîne une faible pénétration vers l’est dans l’intérieur du bassin (Chassignet and Xu, 2017; Bryan et al., 2007). Une amélioration significative est obtenue en résolvant l’activité à méso-échelle (échelle de grille  $< 1/10^\circ$ ), cependant une énergie cinétique excessive est souvent produite par les modèles dans ce cas (Chassignet and Xu, 2017; Özgökmen and Chassignet, 2002). Ces biais énergétiques persistants suggèrent des processus de dissipation manquants. Une représentation réaliste du GS n’est alors possible qu’avec des sources et des puits d’énergie cinétique adéquats dans le bilan d’énergie cinétique.

La théorie actuelle suggère que le forçage atmosphérique et les marées sont les principales sources d’énergie externe, injectant à grande échelle ( $> \mathcal{O}(100\text{km})$ ) (Ferrari and Wunsch, 2009). L’apport à grande échelle génère des tourbillons de méso-échelle par le biais de l’instabilité barocline, qui convertit l’énergie potentielle en énergie cinétique. Les tourbillons de méso-échelle interagissent les uns avec les autres et, par coalescence, transfèrent l’énergie cinétique vers le haut de l’échelle (cascade inverse) (Charney, 1971; Scott and Wang, 2005). Dans le même temps, cependant, ils induisent un transfert d’énergie potentielle vers le bas de l’échelle par le brassage tourbillonnaire et la frontogénèse (Klein et al., 2019). En conséquence, des anomalies horizontales de densité se développent à petite échelle, où l’énergie potentielle

se transforme en énergie cinétique par le biais de flux verticaux de flottabilité — associés à une circulation secondaire agéostrophique ou à des instabilités de la couche mélangée (Capet et al., 2008a). En raison de l'affaiblissement des effets de la rotation et de la stratification à ces échelles, les mouvements déséquilibrés peuvent interagir avec les mouvements équilibrés et favoriser un transfert d'énergie cinétique vers des échelles plus petites (cascade directe) (Molemaker et al., 2010; Capet et al., 2008a). Cependant, dans le même temps, les fronts de sous-mésoéchelle peuvent également dynamiser des échelles plus grandes grâce à leur interaction avec les tourbillons de mésoéchelle, étendant ainsi le régime de cascade d'énergie inverse vers la sous-mésoéchelle (Klein et al., 2008; Qiu et al., 2014; Schubert et al., 2020). Par conséquent, l'échelle à laquelle les flux inter-échelles changent de signe se situe à une échelle inférieure à la méso-échelle (environ 10 km selon Klein et al. 2008), mais la route de dissipation peut commencer à une échelle plus grande en suivant des transferts d'énergie potentielle (Figure 1).

Outre la route intérieure de dissipation de l'énergie, d'autres puits d'énergie ont été reconnus comme contribuant au budget énergétique de l'océan. Aux limites verticales de surface et de fond, deux processus de dissipation importante sont reconnus : (i) celle induite par la traînée de fond qui est causée par l'interaction entre la topographie et les courants de fond (Sen et al., 2008; Trossman et al., 2017); (ii) celle induite par la traînée de surface - également connue sous le nom d'effet de "Current Feedback" - causée par l'interaction entre les courants de surface et les vents de surface (Renault et al., 2016b). Le mélange vertical, en particulier dans la couche limite océanique planétaire, est également considéré comme un puits d'énergie très important (Wunsch and Ferrari, 2004). Enfin, les modèles océaniques génèrent également une dissipation numérique (implicitement ou explicitement) pour amortir les erreurs de dispersion résultant de la discrétisation spatiale et temporelle des équations, en particulier les termes d'advection (Soufflet et al., 2016; Marchesiello et al., 2011).

Le cycle de l'énergie cinétique décrit ci-dessus résulte d'une théorie générale, mais elle n'a pas été entièrement démontrée pour le GS. En outre, le rôle de mécanismes tels que les marées et les interactions air-mer n'est pas entièrement intégré dans la théorie. De plus, il n'y a pas de quantification de l'importance relative des différentes sources et puits d'énergie du GS. L'objectif principal de la thèse est donc de décrire les routes de l'énergie cinétique dans le système du GS ainsi que les mécanismes impliqués dans sa dissipation, en visant à quantifier et à comparer les différentes composantes. Ces analyses sont réalisées à l'aide de configurations de modèles numériques océaniques et atmosphériques développées dans le cadre de cette thèse.

Dans le Chapitre 1, nous décrivons la circulation régionale et les mécanismes qui modulent la dynamique du GS. Nous précisons également les principales difficultés des modèles océaniques à représenter le GS. Un résumé des théories expliquant le bilan d'énergie cinétique est donné dans le Chapitre 2. Dans le Chapitre 3, nous présentons la méthodologie mise en œuvre dans cette étude. En particulier, nous décrivons les principales caractéristiques des modèles numériques océaniques et atmosphériques utilisés (CROCO et WRF). En outre, nous décrivons la méthode du *coarse-graining* qui nous permet d'estimer le flux d'énergie cinétique traversant les échelles spatiales. Cette estimation sera une des clés de notre recherche.

Dans le Chapitre 4, nous analysons la cascade d'énergie cinétique dans le GS estimée par la méthode du *coarse-graining*, en utilisant une simulation océanique forcée qui permet le développement de sous-mésoéchelle. Cette méthode nous permet de décrire la variabilité spatiale et temporelle du flux d'énergie cinétique dans l'océan. Nous discutons ensuite des mécanismes impliqués dans la cascade directe, et démontrons la prépondérance de l'advection agéostrophique associée à la frontogénèse. La dissipation intérieure (via la cascade directe) est comparée quantitativement à la dissipation numérique ainsi qu'aux dissipations frictionnelles sur le fond et la surface. Nous démontrons que la dissipation intérieure est un ordre de grandeur inférieur aux autres puits d'énergie. Enfin, nous évaluons la sensibilité des puits d'énergie au schéma d'advection de la quantité de mouvement horizontale et montrons qu'une dissipation numérique plus faible dans un schéma d'ordre supérieur entraîne une augmentation compensatoire par les dissipations sur le fond et la surface.

La marée est un acteur pouvant moduler le cycle de l'énergie cinétique, de façon encore imparfaitement comprise. Son effet sur la cascade énergétique et les puits d'énergie sont examinés au Chapitre 5. En comparant une série de simulations à sous-mésoéchelle avec et sans marées, nous montrons que les marées internes modulent la cascade turbulente du GS grâce à l'interaction entre les ondes internes et les courants, tandis que les marées externes augmentent la traînée de fond de la circulation dans l'océan profond.

Le Chapitre 6 vise à étudier le cycle énergétique complet du GS à sous-mésoéchelle (énergie cinétique et potentielle). Pour ce faire, nous développons et utilisons une simulation couplée océan-atmosphère à haute résolution sur le GS. Nous estimons alors un diagramme de Lorenz décrivant la génération, la conversion et la dissipation de l'énergie potentielle et cinétique, y compris les effets des interactions entre l'océan et l'atmosphère. Les principaux résultats obtenus sont que les réservoirs d'énergie cinétique sont alimentés à toutes les échelles (mésoéchelle et sous-mésoéchelle) par des transferts d'énergie potentielle, et drainés par la friction aux limites verticales, le mélange vertical de surface et la dissipation numérique. En outre, la cascade inverse d'énergie cinétique s'étend à la sous-mésoéchelle, jusqu'à environ 10 km, et seule une petite quantité suit une cascade directe en dessous de 10 km.

Enfin, le Chapitre 7 présente les conclusions et les perspectives de notre étude.



# The Gulf Stream System

---

## Contents

---

<b>1.1</b>	<b>Introduction</b>	<b>10</b>
<b>1.2</b>	<b>General Description</b>	<b>12</b>
1.2.1	Atmospheric Conditions	12
1.2.2	The Gulf Stream Circulation	15
<b>1.3</b>	<b>Classical models of wind-driven gyre circulation</b>	<b>16</b>
1.3.1	Sverdrup model	16
1.3.2	Western intensification and the Stommel model	19
1.3.3	Munk model	20
<b>1.4</b>	<b>The role of topography and eddies</b>	<b>21</b>
1.4.1	Topographic steering	21
1.4.2	Mesoscale eddy-mean flow interaction	24
1.4.3	Submesoscale fronts and eddies	24
<b>1.5</b>	<b>Gulf Stream representation in numerical ocean models</b>	<b>25</b>

---

## 1.1 Introduction

Western Boundary Currents (WBCs) are located on the western side of the subtropical gyres and are characteristically fast, intense, and narrow current compared to their eastern counterparts. WBCs include the Brazil Current in the South Atlantic, the Kuroshio in the North Pacific, the East Australia Current in the South Pacific, the Agulhas Current in the southern Indian Ocean and the Gulf Stream in the North Atlantic. These regions have been identified as the most energetic regions in the global ocean (Figure 1.1), reaching two orders of magnitude higher than the eastern boundary currents. Additionally, the meridional transport of warm water by WBCs induces a vigorous heat flux exchange between the ocean and atmosphere. This results in considerable heat loss from the ocean to the atmosphere (Figure 1.2).

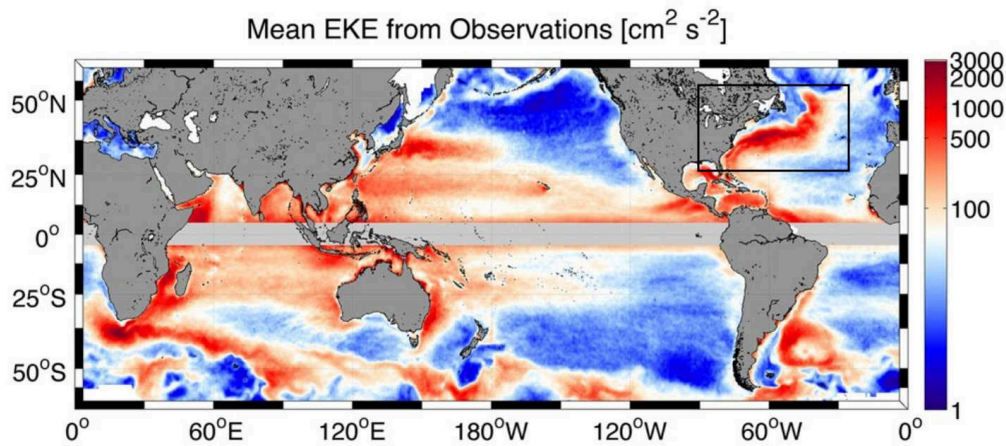


Figure 1.1: Eddy kinetic energy (EKE) estimated from the AVISO geostrophic currents. Black outlines indicate the GS region. Reprinted and adapted from Renault et al. (2017).

The Gulf Stream (GS) has garnered significant interest due to its vigorous circulation and role in the Atlantic Meridional Ocean Circulation (AMOC). The AMOC is unique in the global ocean, transporting warm and salty water northward into the upper layers of the ocean and exporting cold and dense water southward into the deep Atlantic (Buckley and Marshall, 2016; Tréguier et al., 2012) (Figure 1.3), resulting in about 25% of the poleward atmosphere-ocean transport in the Northern Hemisphere (Bryden and Imawaki, 2001). The AMOC plays a central role in global climate through its heat and freshwater transports (Buckley and Marshall, 2016) and contributes significantly to the temperate climate of the ocean and continental Europe (Bryden et al., 2005).

Understanding the dynamics of the GS is crucial. The GS is a complex system with multiple mechanisms exerting a significant influence over a wide range of temporal and spatial scales. This chapter describes the main atmospheric and oceanic features of the GS region, beginning with an account of the primary atmospheric and oceanic circulation conditions. Additionally, the difficulties encountered by numerical ocean models in representing the GS are thoroughly discussed.

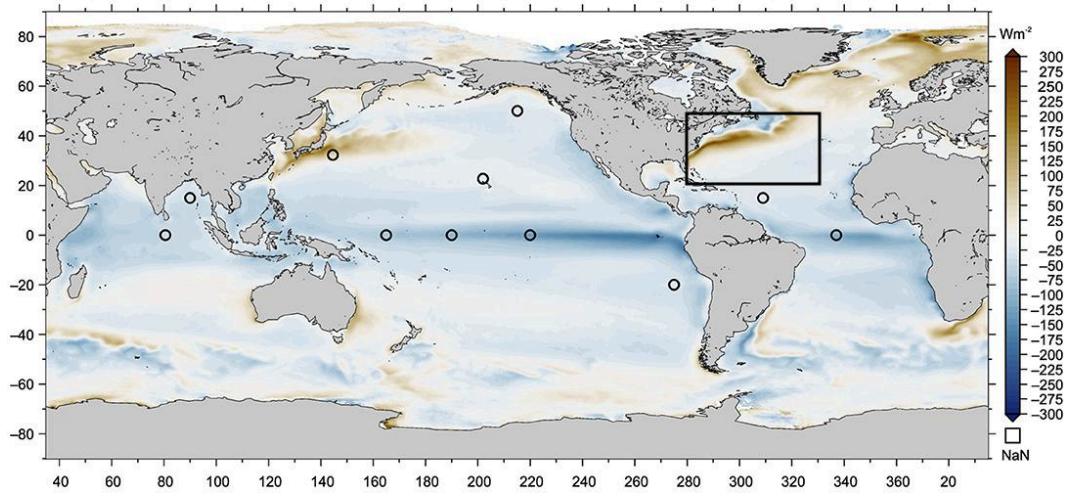


Figure 1.2: Time-mean (1988-2017) global surface net heat flux obtained from J-OFURO3 V1.1. Positive values are upward heat flux. Unit in  $\text{W m}^{-2}$ . Black outlines indicate the GS region. Reprinted and adapted from Tomita et al. (2021)

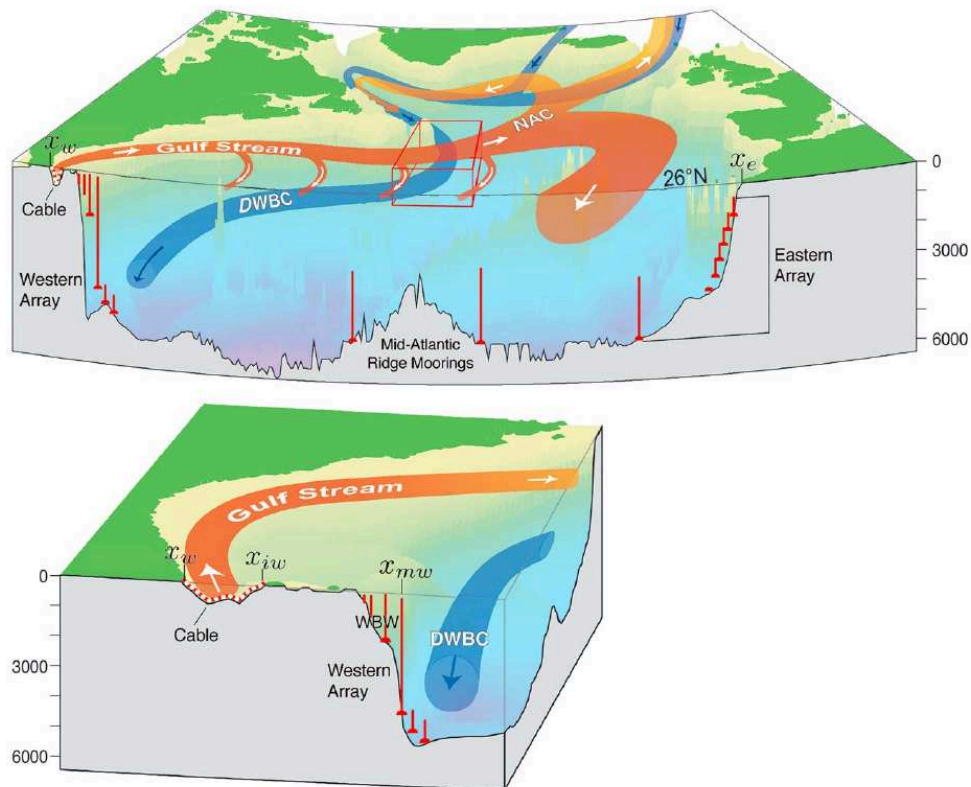


Figure 1.3: A schematic of the North Atlantic Ocean circulation: (top) the entire basin and (bottom) a close-up of the western boundary region. Surface currents, including the Gulf Stream, the North Atlantic Current (NAC), and Labrador Current, are shown in red, and the deep western boundary current (DWBC) is shown in blue. Reprinted from Buckley and Marshall (2016).

## 1.2 General Description

### 1.2.1 Atmospheric Conditions

The energy input from the winds, along with the tides, is the main source of energy for large-scale ocean circulation. The North Atlantic circulation is driven by the trade winds and the westerlies (Figure 1.4a). These winds are mainly determined by the Azores High, a semi-permanent high pressure center located in the subtropical North Atlantic (about  $30^{\circ}\text{W}$  and  $34^{\circ}\text{N}$ ) (Figure 1.4a) and associated with an anticyclonic atmospheric circulation (Figure 1.4b). In winter, the Azores High is less pronounced and is located in the eastern part of the North Atlantic at lower latitudes. At the same time, a low-pressure center located between Iceland and southern Greenland, called the Icelandic Low (Figure 1.4a), intensifies. As a result, the westerly winds are strengthened, with a tendency to veer northward to the east of  $54^{\circ}\text{W}$ , and the trade winds are slightly stronger in winter (Figure 1.4c). The Icelandic low is weak in summer, and the Azores high is most pronounced, located in the western North Atlantic and dominating the North Atlantic. This produces a distinct anticyclonic wind circulation (Figure 1.4d). Along the east coast of North America, the direction of the wind has an important seasonal variability with offshore winds for most of the year.

An important exchange of total heat fluxes between the GS and the atmosphere is produced by the interaction of warm water advected poleward by the GS, and cold and dry air. Observational data show that the annual mean heat transfer from the ocean to the atmosphere is about  $200\text{ Wm}^{-2}$  (Figure 1.5a) (da Silva et al., 1994). In winter, these values can reach more than  $400\text{ Wm}^{-2}$  over the GS (Figure 1.5b), but they are less than  $100\text{ Wm}^{-2}$  in summer (Figure 1.5c).

The influence of the GS on climate has been studied extensively. It has been shown that the loss of heat and moisture in the region is associated with the development of storm tracks (Nakamura et al., 2004). Using atmospheric models, Kuo et al. (1995) show that latent heat release is important for cyclogenesis. Minobe et al. (2010) found that the GS can affect the whole troposphere, showing a relationship between mesoscale rain bands and cloud formation over the GS. The authors observe that atmospheric pressure adjusts to the sea surface temperature (SST) gradient leading to the convergence of surface winds, which anchors a narrow rain band along the GS. In this rain band, upward motion and cloud formation extend into the upper troposphere. Climate model biases in GS simulation can affect atmospheric circulation in the North Atlantic (Keeley et al., 2012), but also in distant regions via a planetary Rossby wave response (Lee et al., 2018) and the AMOC, which is also critical for large-scale climate response (Hewitt et al., 2017). The interaction between the atmosphere and the ocean is complex as the atmosphere not only supplies but also depletes energy from the ocean. A more detailed explanation can be found in Chapter 2.

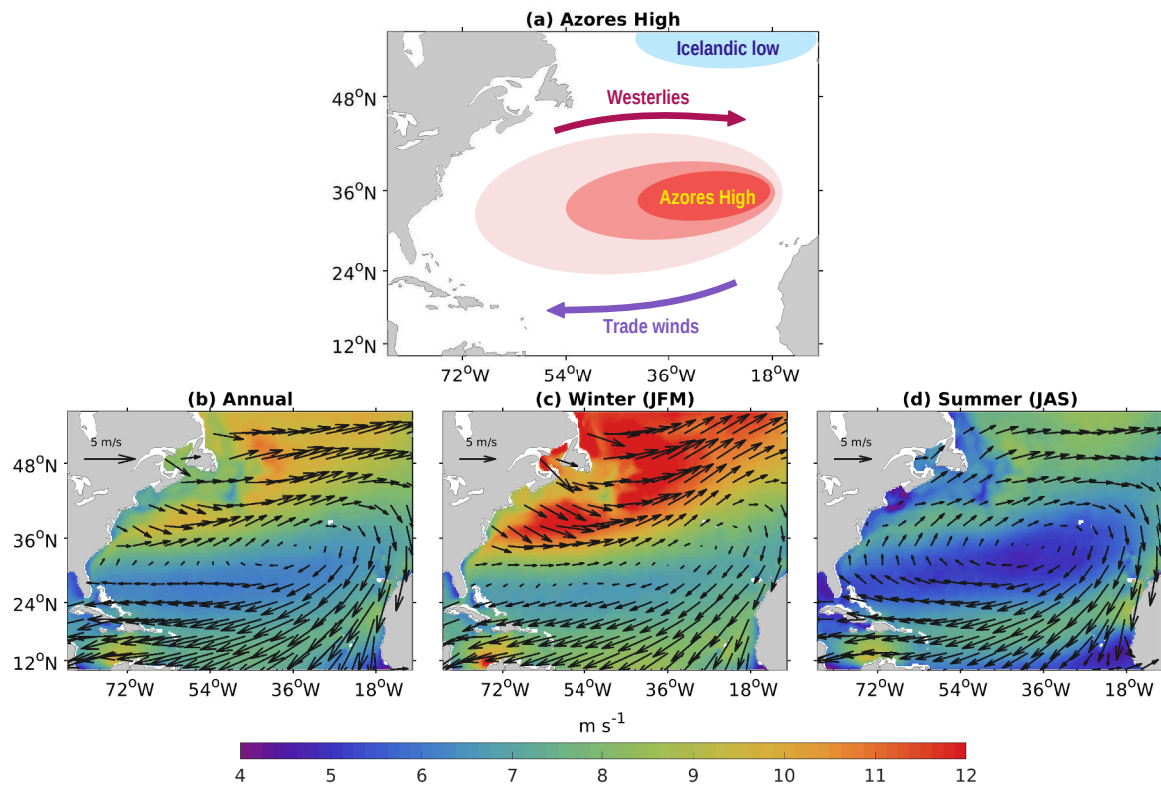


Figure 1.4: (a) Representation of the Azores High (red ellipses) and the Icelandic Low (shaded light blue) along with the westerlies and trade winds. (b) Annual (c) Winter (January, February, and March) (d) Summer (July, August, and September) means of the wind (vectors) and its magnitude (shaded). Data were obtained from SCOW (Chelton et al., 2000).

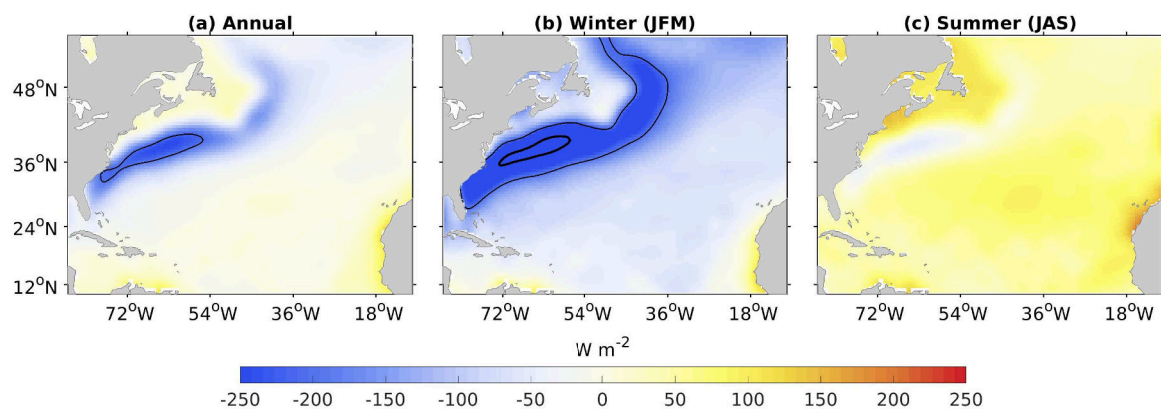


Figure 1.5: (a) Annual (b) Winter (January, February, and March) (c) Summer (July, August, and September) total heat flux. Thick and thin lines represent the 200 and 400  $\text{W m}^{-2}$  contours, respectively. Data were obtained from COADS05 (da Silva et al., 1994).

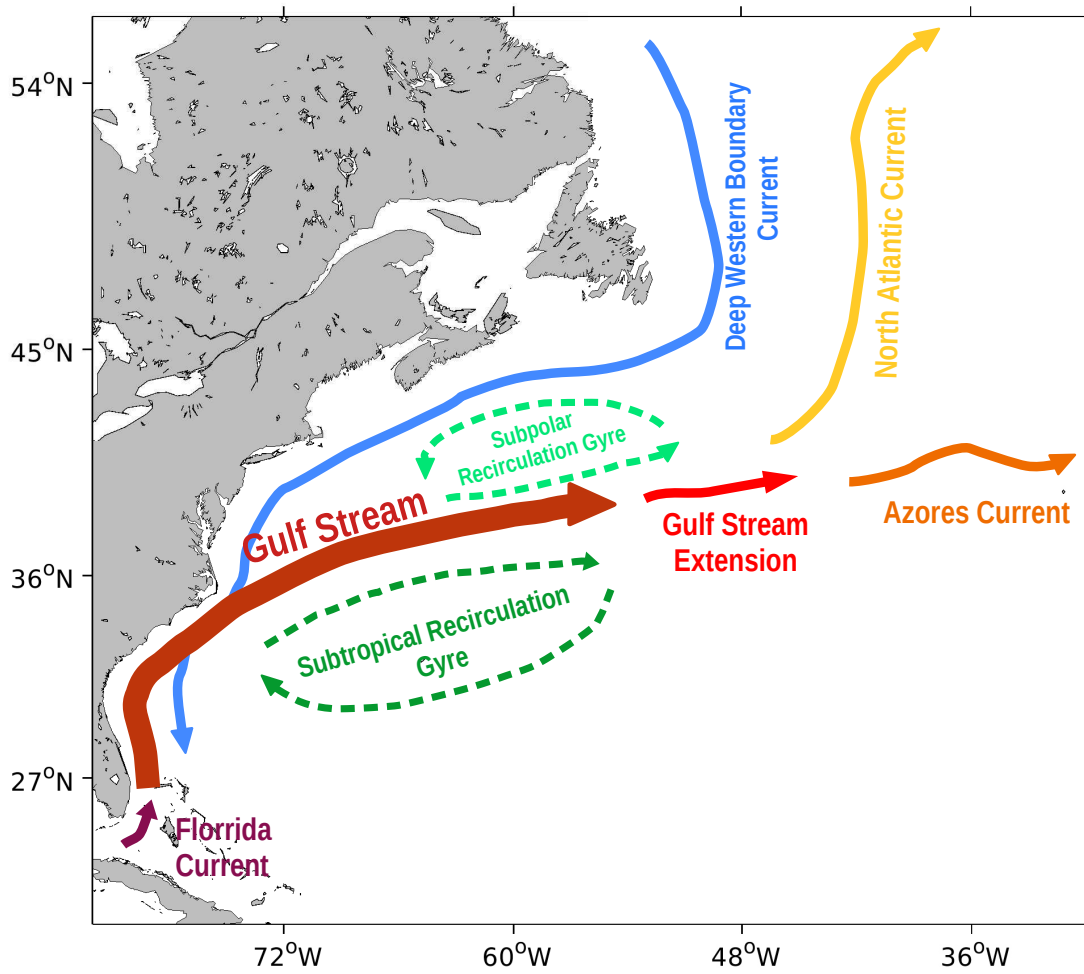


Figure 1.6: Scheme of the currents in the North Atlantic Ocean.

### 1.2.2 The Gulf Stream Circulation

The GS originates north of the Florida Straits and separates from the coast at Cape Hatteras. It flows eastward until it reaches  $50^\circ$  W longitude (Figure 1.6). Between the Florida Straits and Cape Hatteras, its course aligns with the Blake Plateau, following the contours of the continental slope (see Figure 1.7). The width of the current in this area is constrained by the 800-meter isobath, as documented by Colling (2001). Notably, the GS in this region receives contributions not only from the Antilles Current, but also from water circulation within the Sargasso Sea, as reported by Colling (2001).

After reaching Cape Hatteras, the GS leaves the continental slope and veers northeastward, reaching a depth of about 5000 meters. In this region, the current undergoes a process of widening and diffusion, unimpeded by significant topographic features, until it reaches the New England Seamount Chain. To the west of Cape Hatteras, the GS exhibits instability and produces a distinctive type of mesoscale eddy known as "*GS Ring*", resulting from the detachment of meandering GS segments, as demonstrated by Robinson (2012) (see Figure 1.13).

After separating at  $50^\circ$  W, the current is referred to as the *GS Extension* and is divided into three branches (Tomczak and Godfrey, 2003): (i) the North Atlantic Current (NAC), which flows northeastward toward Scotland to feed the Norwegian Current and eventually contribute to the formation of the Arctic Bottom Water; (ii) the Azores Current; and (iii) the Sargasso Sea Recirculation.

The GS is part of a double gyre system. The anticyclonic gyre, known as the Subtropical Recirculation Gyre and located at  $65^\circ$ W, consists of a deep current whose transport capacity is two to three times greater than that of the wider subtropical gyre (Stewart, 2008). The cyclonic gyre, called the Subpolar Recirculation Gyre and located at  $63^\circ$ W, is mainly bounded by the New England seamount chain and the Grand Banks, and contributes only around 20 Sverdrup (Sv) of water to GS transport (Hogg et al., 1986).

The GS exhibits remarkable transport, increasing as it flows towards the north (Colling, 2001). In the Florida Straits, the current flows at a velocity of  $1.8 \text{ m s}^{-1}$  and transports approximately 30 Sv. At Cape Hatteras, the current reaches a transport of 70-100 Sv. After the GS separates from the coast, higher magnitudes are reached around  $65^\circ$ W, with a transport of approximately 150 Sv and velocities close to  $1.5 \text{ m s}^{-1}$ . The transport decays east of  $65^\circ$ W (Colling, 2001). The GS system is characterized by strong local variation and lacks correlation with other regions where the current flows (Heiderich and Todd, 2020). Observations spanning 16 years indicate that the variation in transport of the Florida Current is primarily explained by frequencies lower than one year (70%) (Meinen et al., 2010). In the Florida Strait, the current displays maximum strength during March and transports 11 Sv more than during November (Tomczak and Godfrey, 2003). The Florida Strait's volume transport measurement and the Cape Hatteras's downstream transport exhibit no correlation (Sanchez-Franks et al., 2014).

Based on more than 50 years of *in situ* observations, Seidov et al. (2019) demonstrate

that the GS's location remains highly stable with minimal migration occurring between Cape Hatteras and the Grand Banks. In contrast, the GS extension displays greater variability (Seidov et al., 2019). During fall, the current is located farthest north, while in the winter and early spring, it is located farthest south. (Auer, 1987; Kelly and Gille, 1990; Hogg et al., 1986). Geosat altimetry data indicates that the highest (lowest) transport is generated in autumn (spring) (Kelly and Gille, 1990).

Finally, the GS transports warm and salty water northward. As it travels, it evaporates water and releases heat to the atmosphere, increasing the salinity and density of the water. At the Norwegian Current, the salinity is approximately 35.2 PSU. At this latitude, the water is cooler, which increases its density and induces the formation of deep water. The dense water flows south along the western boundary from the Labrador Sea to the equator due to the buoyancy gradient. It is then called the Deep Western Boundary Current (DWBC), which carries around 15 Sv (Spall, 1996).

### 1.3 Classical models of wind-driven gyre circulation

As stated earlier, the wind is the primary source of surface ocean circulation. The seminal studies establishing this were conducted by Sverdrup (1947), followed by Stommel (1948) and Munk (1950). These theories not only explain - albeit qualitatively - the circulation of deep, narrow, energetic currents at the western border of the basin, but also that of slow, wide currents along the eastern border. We will provide a brief overview of wind-driven gyre models, drawing on references such as Colling (2001), Cushman-Roisin and Beckers (2011), and Stewart (2008). For an in-depth review, we recommend Pedlosky (2013).

#### 1.3.1 Sverdrup model

The first study showing a relationship between oceanic surface circulation and wind stress was proposed by Sverdrup in 1947 (Sverdrup, 1947). The theory is formulated from the equation of horizontal motion,

$$\frac{\partial \mathbf{u}_h}{\partial t} + \mathbf{u} \cdot \nabla \mathbf{u}_h + f \hat{\mathbf{k}} \times \mathbf{u}_h + \frac{1}{\rho_0} \nabla_h P = F_h, \quad (1.1)$$

where  $\mathbf{u}$  is the velocity vector,  $f = 2\Omega \sin \theta$  is the Coriolis parameter,  $\Omega$  is the Earth rotation period,  $\theta$  is the latitude,  $\hat{\mathbf{k}}$  is the vertical unit vector,  $\rho_0$  is the reference density,  $P$  is the pressure,  $F_h$  is the friction force per unit mass, and the subindex  $h$  represents the horizontal component. The Sverdrup theory assumes the following:

1. A stationary flow.
2. Negligible advection and friction.

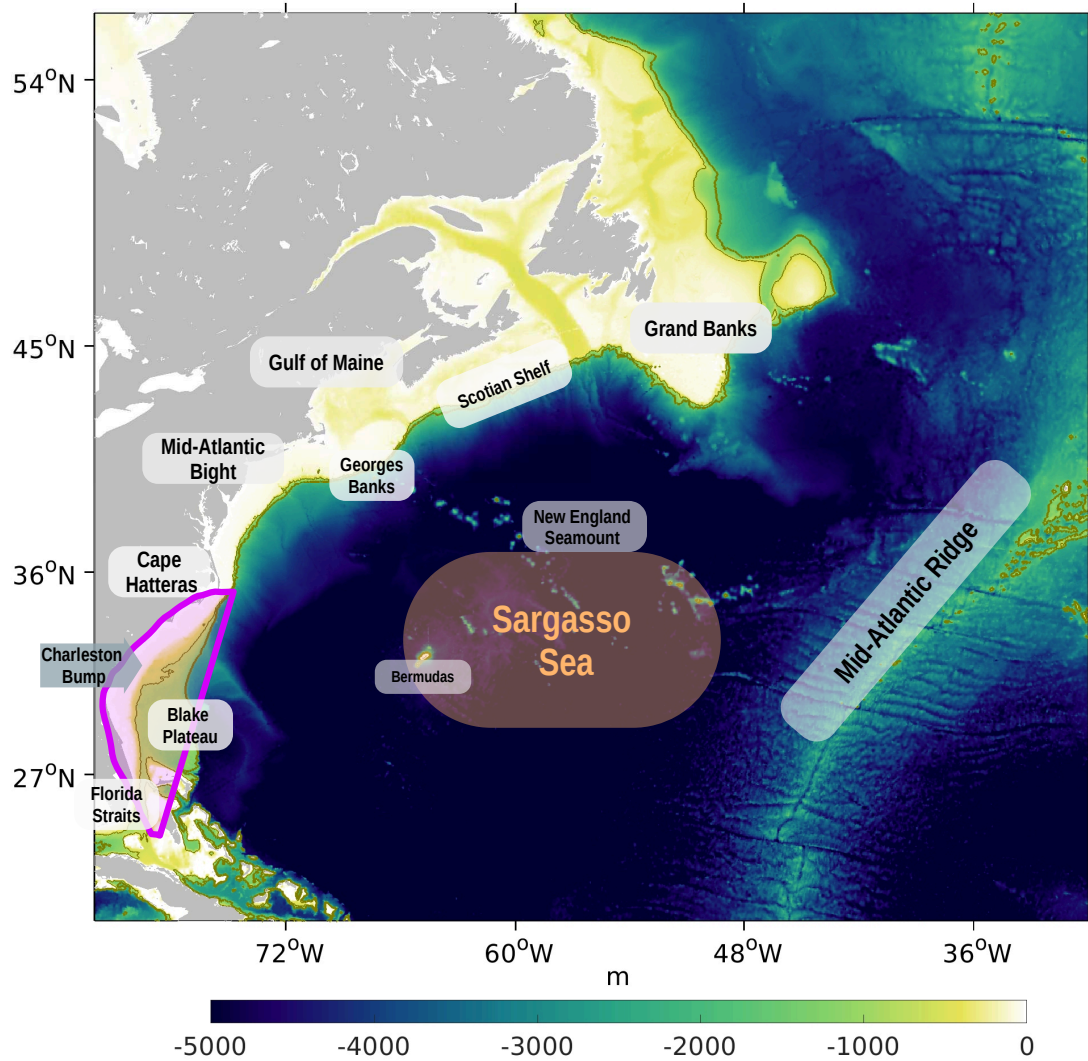


Figure 1.7: Topography (m) of the North Atlantic. The area marked with a magenta border represents the South Atlantic Bight. Data were obtained from ETOPO2 (<https://doi.org/10.7289/V5J1012Q>).

3. The wind-driven circulation vanishes at depths where there is no motion.
4. The Coriolis parameter  $f$  depends linearly on the latitude  $y$ , *i.e.*  $f = f_0 + \beta y$ , where  $f_0$  is the reference Coriolis parameter and  $\beta = \partial f / \partial y$  is the beta parameter that represents the rate of change of the Coriolis parameter with latitude.

With these assumptions, a simple linearized barotropic vorticity equation for steady flow emerges by taking the curl of the vertically integrated horizontal momentum equation (Eq. 1.1), where only the Coriolis and wind-forcing terms remain, giving a relationship between meridional transport  $V$  and the curl of wind stress  $\tau = (\tau_x, \tau_y)$ :

$$V = \int_H^0 v dz = \frac{1}{\rho_0 \beta} \nabla_h \times \tau, \quad (1.2)$$

where  $H$  is the ocean bottom. Eq. 1.2 is the *Sverdrup balance* that expresses a barotropic vorticity balance between the wind-stress curl and the planetary vorticity advection (the  $\beta$  term). Applying it to an idealized zonal wind in the Northern Hemisphere, with westerlies and trade winds (Figure 1.8a), the negative wind stress curl ( $\tau_y = 0$  and  $-\partial \tau_x / \partial y < 0$ ), and positive  $\beta$  results in an equatorward transport ( $V < 0$ ). Since  $V$  is strongest at  $30^\circ\text{N}$ , as is the wind stress curve, and weakest around this latitude, flow continuity requires zonal transport and therefore gyre circulation.

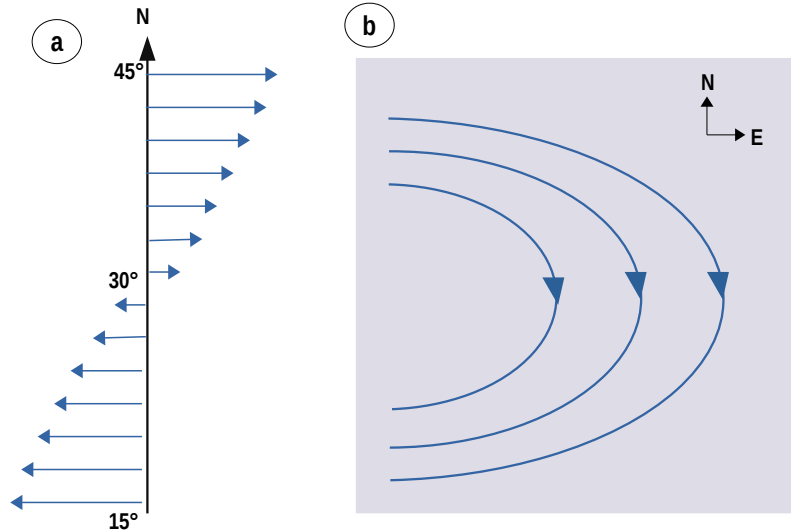


Figure 1.8: (a) Idealized zonal wind pattern, where westerlies winds (trade winds) blow in the north (south). (b) Representation of the transport generated by the winds of (a) estimated from Sverdrup's theory. Reprinted and adapted from Colling (2001).

We can derive the zonal transport  $U = \int_H^0 u dz$  by replacing Eq. 1.2 in the vertically

integrated continuity equation ( $\partial U/\partial x + \partial V/\partial y = 0$ ),

$$U = -\frac{1}{\rho_0\beta} \int_{x_0}^x \frac{\partial}{\partial y} \left( \frac{\partial \tau_y}{\partial x} - \frac{\partial \tau_x}{\partial y} \right) dx \quad (1.3)$$

A solution for Eq. 1.3 is found by choosing  $x_0 = 0$  at the eastern boundary and assuming no flow into the boundary ( $U(x_0) = 0$ ). To verify these equations, Sverdrup estimated the transport using wind data from the eastern tropical Pacific and compared it with hydrographic observations. The results show that the zonal transport of equatorial currents calculated from the Sverdrup relation is accurate, not only in direction but also in magnitude (Figure 1.9).

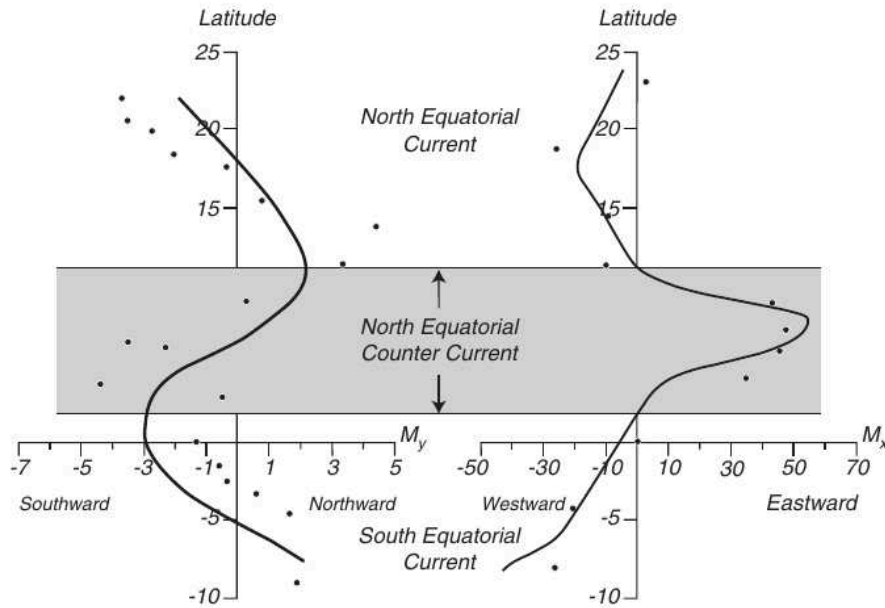


Figure 1.9: Transport in the eastern Pacific calculated from Eq. 1.2 and 1.3 using observed winds (solid lines) and pressure calculated from hydrographic data from ships (dots). Reprinted from [Stewart \(2008\)](#).

However, the Sverdrup model has important limitations, particularly when it comes to representing the observed intense WBCs. In terms of vorticity conservation, the eastern side of the gyre has a balance between negative wind stress curl and positive  $\beta$  term, but at the western side, both vorticity terms are negative and must be balanced by another term (not present in the Sverdrup equation), which should be positive.

### 1.3.2 Western intensification and the Stommel model

Stommel proposed a model that accounts for WBCs ([Stommel, 1948](#)) by incorporating a source of friction (bottom stress) into the analysis. In a rectangular basin of uniform depth, Stommel showed a relationship between WBCs and the Earth's differential rotation. He first calculated a solution with constant Earth rotation, presenting a symmetrical gyre with

no WBC (Figure 1.10b), then added differential Earth rotation to produce an asymmetrical circulation with a strong WBC (Figure 1.10c).

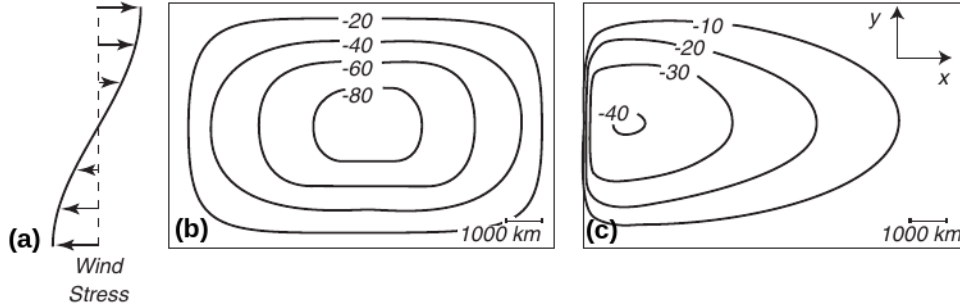


Figure 1.10: (a) Wind Stress used by Stommel to estimate the circulation. Streamfunction solution for (b) constant Earth rotation and (c) differential Earth rotation (varying linearly with latitude). Reprinted from Stewart (2008).

The addition of a friction term solved the problem of vorticity conservation. If the WBC is confined within a narrow frictional layer, a strong shear appears that can balance in the west the added negative vorticity of the wind curl and  $\beta$  term.

### 1.3.3 Munk model

Munk proposed a more realistic model in 1950 (Munk, 1950) by including lateral eddy viscosity as the necessary source of friction in the west. Using the streamfunction  $\psi$ <sup>1</sup>, the new solution is written:

$$A_h \nabla^4 \psi - \beta \frac{\partial \psi}{\partial x} = -\nabla \times \tau, \quad (1.4)$$

where  $A_h$  is the constant eddy friction coefficient and  $\nabla^4 = \frac{\partial^4}{\partial x^4} + 2 \frac{\partial^4}{\partial x^2 \partial y^2} + \frac{\partial^4}{\partial y^4}$ . Eq. 1.4 is similar to Eq. 1.2 but with the addition of the lateral friction term. The latter is only of importance at the western boundary, while the basin interior is in Sverdrup balance.

To find a solution to Eq. 1.4 for a rectangular basin extending from  $x = 0$  to  $x = r$  and from  $y = -s$  to  $y = +s$ , Munk considers that:

1. the flow at a boundary runs parallel to it so that there is no normal flow (Neumann condition):  $\psi = 0$  and  $\frac{\partial \psi}{\partial n} = 0$ , where  $n$  is normal to the boundary.
2. the wind stress is zonal and described as  $T = a \cos ny + b \sin ny + c$  with  $n = j\pi/s$  and  $j = 1, 2, \dots$

<sup>1</sup>Streamfunction ( $\psi$ ) is a scalar function depending on space and time. Its derivative with respect to any direction gives the component perpendicular to that direction of the velocity for an incompressible two-dimensional flow.

Munk's solution is consistent with Sverdrup's near the eastern boundary but also allows an intense western boundary current. Nevertheless, the WBC transport in Munk's theory is much weaker than observed and the GS separation and eastward penetration is not properly predicted. Moreover, the theory cannot explain the GS separation. These simple models predict that the current separation takes place where the Sverdrup transport vanishes at the western boundary near 48°N (Zhang and Vallis, 2007). The difference between the circulation predicted by the theory and the observations can be explained by regional and local mechanisms involving topographic steering and eddy-mean flow interaction, which will be described in the following section.

## 1.4 The role of topography and eddies

If simple wind-driven models may qualitatively describe the large-scale ocean surface circulation, they cannot explain the dynamics of the GS. Regional and local processes are essential and this is a brief overview of these processes.

### 1.4.1 Topographic steering

Bottom topography, in particular the continental slope, has proven to be a key element in the balance of vorticity in the GS (Holland, 1967; Warren, 1963; Özgökmen et al., 1997; Gula et al., 2015a; Debreu et al., 2022; Renault et al., 2023a). Topographic steering is the effect of conservation of potential vorticity  $(f + \zeta)/H$  (where  $\zeta$  is the relative vorticity and  $H$  is the bathymetry) on the motion of a fluid parcel, which thus tends to follow  $f/H$  contours. Its importance is generally assessed by the complete barotropic vorticity budget, which complements the Sverdrup balance (Holland, 1973; Hughes and De Cuevas, 2001; Couvelard et al., 2008; Schoonover et al., 2016; Debreu et al., 2022; Gula et al., 2015b), and calculated by taking the curl of the vertically integrated lateral momentum equation (the complete equation this time) :

$$\frac{\partial \bar{\zeta}}{\partial t} = \frac{J(P_b, h)}{\rho_0} - \mathcal{A} - \nabla \cdot (f\mathbf{U}) + \frac{\nabla \times \tau}{\rho_0} - \frac{\nabla \times \tau_b}{\rho_0} + \mathcal{D}, \quad (1.5)$$

where  $\bar{\zeta} = (\nabla \times \mathbf{U}) \cdot \hat{\mathbf{k}}$  is the barotropic vorticity,  $\mathbf{U}$  the barotropic current,  $J$  is the Jacobian operator,  $P_b$  is the bottom pressure, and  $\tau_b$  is the bottom stress. The right-hand-side terms of Eq. 1.5 are the bottom pressure torque ( $J(P_b, h)/\rho_0$ ), the advection torque ( $-\mathcal{A}$ ) representing the advection of vorticity by the mean and eddy flow, the planetary vorticity advection ( $-\nabla \cdot (f\mathbf{U})$ ), the wind stress curl ( $\nabla \times \tau/\rho_0$ ), the bottom stress curl ( $-\nabla \times \tau_b/\rho_0$ ), and the viscous torque ( $\mathcal{D}$ ).

The bottom pressure torque is a measure of the topographic steering of the flow and a major component of the barotropic vorticity balance (Holland, 1973; Hughes and De Cuevas, 2001). In fact, at the gyre scale (including the western border), the main balance is between the bottom pressure torque and the wind stress curl, and at the GS scale, it is between the bottom pressure torque and the planetary vorticity advection (Schoonover et al., 2016; Debreu

et al., 2022). Consequently, at all scales, topographical steering is essential to the western boundary current, equivalent to Munk's friction layer in classical wind-driven gyre models, but with a better physical basis (Hughes and de Cuevas, 2001).

The GS separation has been extensively studied (Tansley and Marshall, 2000; Marshall and Tansley, 2001; Spall, 1996; Chassignet and Xu, 2017; Schoonover et al., 2016, 2017; Debreu et al., 2022). The barotropic vorticity balance generally indicates that the bottom pressure torque is the mechanism that maintains the flow over the continental slope. However, a steep slope curvature can relax this steering effect and produce flow separation by planetary vorticity advection. Separation occurs when the ratio of current and beta ( $U/\beta$ ) is significantly larger than the radius of curvature of the coastline (Marshall and Tansley, 2001). Schoonover et al. (2017) analyzing various numerical experiments found that GS separation is favored by a steepening of the continental slope between the Charleston bump and Cape Hatteras. Debreu et al. (2022) confirm that the steeper the slope, the more inertia the GS has and the easier it is to separate. They also find that the slope plays a role in maintaining GS stability along the southeastern U.S. coast (weakening eddy-driven advection torque  $-\mathcal{A}$ ), which also contributes to greater mean flow inertia.

Yet, despite the stabilizing slope effect, the GS acceleration along the continental slope produces horizontal shear instability that can generate high variability, particularly at the Charleston Bump (Gula et al., 2015b). In the South Atlantic Bight, it produces significant meanders and eddies observed on the cyclonic side of the GS (Figure 1.11). These are "frontal eddies" with negative temperature anomalies, typically surrounded by warm streamers of water referred to as "shingles" (Von Arx et al., 1955). Frontal eddies measuring approximately 100-250 km in diameter propagate along the shelf and are smaller than those observed in the post-separation region (Glenn and Ebbesmeyer, 1994; Gula et al., 2015b).

The Charleston Bump is a region that has attracted a great deal of interest because it is a preferred area for the generation of eddies (Gula et al., 2015a). Initial observations were recorded in Webster (1961) and later documented in Olson et al. (1983) and Bane Jr and Dewar (1988), describing the seaward deflection of the GS near the Charleston Bump (Figures 1.7 and 1.12). According to Gula et al. (2015a), when the GS encounters the bump, the flow is disrupted and deflected to the east, triggering baroclinic and barotropic instabilities that produce the frontal eddies (Gula et al., 2015b,a) (Figure 1.12). As eddy energy feeds the mean flow downstream of the Charleston Bump, through eddy-mean flow interaction, eddy activity tends to weaken.

Another region of interest is the New England seamount chain (see Figure 1.7), as it has been suggested to have a major influence on the trajectory and eastward penetration of GS, although the results are uncertain. The New England seamount chain exerts strong bottom friction on the flow via form drag (Renault et al., 2023a), while on the other hand it can trigger baroclinic instability and increase eddy activity (Chassignet et al., 2023).

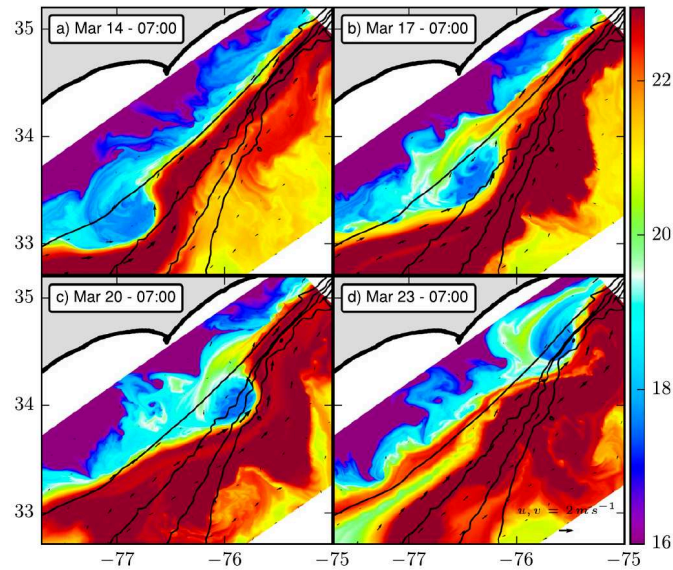


Figure 1.11: Simulated SST downstream of the Charleston Bump and to the south of the Gulf Stream separation point reveals the propagation of a large frontal eddy, which is visible as a cold anomaly. The surface velocities are represented by black vectors, while the topography is depicted through black contours at levels of -200, -600, -1000, and -2000 meters. Reprinted from Gula et al. (2016).

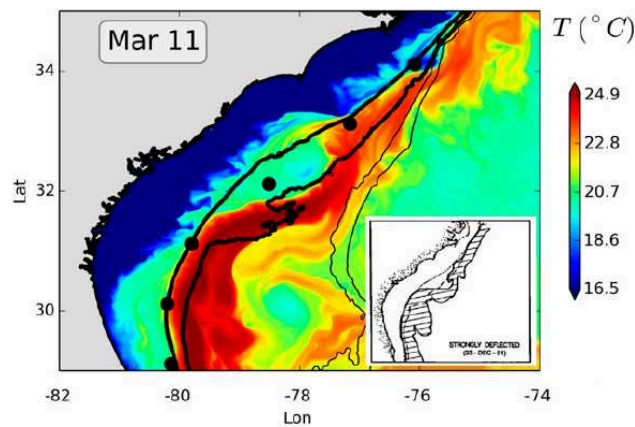


Figure 1.12: Simulated SST for the Gulf Stream showing a typical GS deflection at the Charleston bump. Inserts show corresponding sketches, retraced from AVHRR SST image, taken from Bane Jr and Dewar (1988). Topography is shown in black contours by the 0-, 200-, 600-, 1000-, and 2000-m isobaths. Reprinted from Gula et al. (2015b).

### 1.4.2 Mesoscale eddy-mean flow interaction

Munk's model predicts a GS transport around 36 Sv, significantly less than what hydrographic measurements show (the transport can reach maximum values close to 150 Sv around 65°W; see Section 1.2.2). The difference between linear wind-driven circulation models and observations may be due to energization by subpolar and subtropical recirculation, involving nonlinear effects (Stewart, 2008; Hogg et al., 1986). One of the first studies on recirculating gyres was conducted by Fofonoff (1981). It demonstrated the importance of incorporating the advection term in the momentum equations to elucidate the GS dynamics (see also Jamet et al. 2021). The recirculations are mainly driven by the potential energy of the GS thermocline, which produces strong mesoscale eddy activity that feeds back on the mean flow.

The process starts with baroclinic instability<sup>2</sup>, which converts potential energy to kinetic energy. Both baroclinic and barotropic instabilities — the latter associated with horizontal shear that extracts energy from the mean kinetic energy — are active after the GS separation (Hogg and Johns, 1995). The destabilization of the mean flow leads to the formation of meanders and eddies at the scale of the internal Rossby radius wavelength, *i.e.*, the oceanic mesoscale (Kang and Curchitser, 2015). As mentioned in Section 1.2.2, mesoscale eddy activity significantly increases in the post-separation region. Cyclonic eddies are characterized as "cold-core" eddies, whereas anticyclonic eddies are "warm-core" eddies (Figure 1.13). They typically range from 150 to 300 km in diameter. Warm core eddies are often located to the north of the current as they originate in the unproductive Sargasso Sea, while cold-core eddies transport nutrient-rich water into the Sargasso Sea.

Previous studies using satellite data and observations show that eddies can exchange energy and momentum through eddy-mean flow interactions (Webster, 1961; Dewar and Bane, 1989; Greatbatch et al., 2010a; Kang and Curchitser, 2015; Renault et al., 2019b). Mesoscale eddies interact with the GS, providing additional energy and increasing the GS flow rate. GS re-energization from mesoscale eddies is attenuated by friction with the bottom topography (Greatbatch et al., 2010b) and with the atmosphere at the ocean surface (Renault et al., 2019b).

### 1.4.3 Submesoscale fronts and eddies

The advection of warm water by the GS into colder water regions promotes the formation of strong temperature and density gradients at the ocean surface, ranging from meters to kilometers. As defined by McWilliams (2021), fronts refer to areas that exhibit a strong gradient, typically density, in the horizontal direction with a weak gradient perpendicular to it. Fronts play a significant role in the energy balance as they convert potential energy into kinetic energy that may follow a forward cascade to smaller scales in route to dissipation.

---

<sup>2</sup>These instabilities are explained in Vallis (2017): a disturbance in unstable conditions adds to the outgrowth of a wave until it produces a vortex. Baroclinic instability occurs in rotating stratified fluids with a horizontal buoyancy gradient.

Fronts can be found throughout the GS (Callies et al., 2015; Thomas et al., 2013; McWilliams et al., 2019), but one region that stands out for its high activity is the northern wall of the GS (McWilliams et al., 2019; Wenegrat et al., 2020; Thomas et al., 2013). McWilliams et al. (2019) using an idealized model shows that the variability of the jet is modulated by these structures. The South Atlantic Bight is another region with high frontogenesis activity, but also with filamentogenesis <sup>3</sup> (Gula et al., 2014).

Associated with fronts, submesoscale motions (ageostrophic secondary circulation, inertia-gravity waves and eddies) are mostly unbalanced and carry a substantial ageostrophic component. They are smaller and more rapidly evolving than mesoscale eddies and with vertical velocities one or two orders of magnitude larger (Capet et al., 2008b; Su et al., 2020; Siegelman, 2020; McWilliams, 2021). They can affect momentum, buoyancy, nutrient transport and biogeochemistry (Lévy et al., 2018; Uchida et al., 2019; Kessouri et al., 2020), and gas exchange between the ocean and atmosphere (Su et al., 2018). In addition, submesoscale currents have various impacts on the energy budget through distinct mechanisms, which are explained in detail in Section 2.4.3.

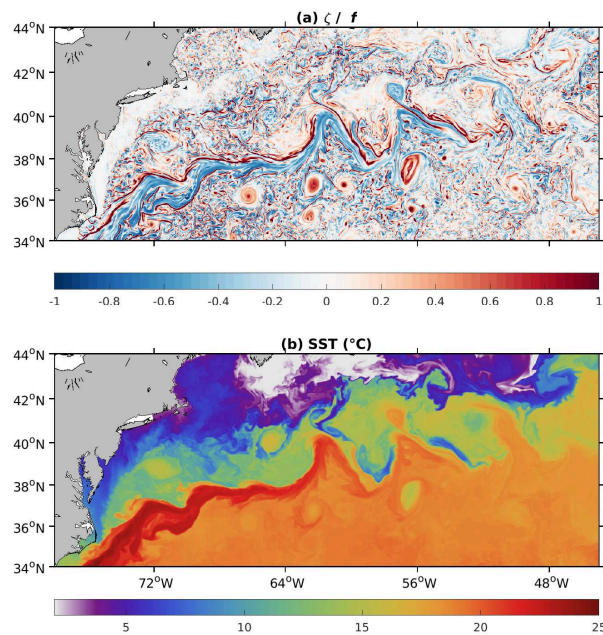


Figure 1.13: Simulated (a) surface relative vorticity (normalized by  $f$ ) and (b) sea surface temperature in March 2007. Adapted from Contreras et al. (2023b)

## 1.5 Gulf Stream representation in numerical ocean models

Satellite data, *in situ* observations, and ocean models have all contributed to our understanding of GS dynamics. Ocean models, in particular, have been useful in verifying theories. How-

<sup>3</sup>dual frontogenetic process, along the lines understood for a single front (Gula et al., 2014).

ever, simulating GS dynamics with numerical models has long been a challenge. Generally, coarse ocean models fail to adequately reproduce the basic features of the mean circulation. For instance, the GS tends to overshoot Cape Hatteras, *i.e.*, its separation from the coast occurs northward of the observed location and results in the formation of a large, stationary anticyclonic eddy (Bryan et al., 1995; Özgökmen et al., 1997). These models also feature insufficient eddy variability, feeble recirculation gyres and weak eastward GS penetration (Hurlburt and Hogan, 2000; Smith et al., 2000; Chassignet and Xu, 2017).

Inaccurate representation of GS dynamics can have various impacts on the North Atlantic circulation, *e.g.*, the Azores Current, the North Atlantic Current, and the overall AMOC (Bryan et al., 2007; Özgökmen et al., 1997; Hewitt et al., 2017). In particular, GS overshoot leads to a warm sea surface temperature bias on the cold Subpolar Recirculation Gyre (Talandier et al., 2014), and overestimation of heat transport (Maltrud and McClean, 2005). Heat flux biases can affect the atmospheric circulation in the North Atlantic (Keeley et al., 2012), but also in distant regions via a planetary Rossby wave response (Lee et al., 2018). This can have significant consequences in global warming projections (Saba et al., 2016) and on the spatial distribution of coastal sea-level rise (Ezer et al., 2013).

Coarse models of the North Atlantic, just like the Munk model, fail to reproduce the GS path between Cape Hatteras and Grand Banks, as observed from space. Therefore, as indicated in the Sections 1.3 and 1.4, the essential processes that are best expressed at high resolution must be taken into account in the models: mesoscale activity and eddy mean flow interaction, topographic steering, frontogenesis, etc. The representation of these processes is sensitive to different model choices: type of coordinate systems, numerical methods, parameterizations, grid resolution, etc. It can be difficult to understand how these choices affect a simulation due to their possible complex interactions. In the following, we will review the most significant model choices.

- Vertical coordinate systems: these determine how the bottom topography interacts with ocean currents. Terrain-following (sigma,  $\sigma$ - or s-) vertical coordinate systems provide the most natural bottom boundary conditions. However, they require bathymetry smoothing to avoid excessive numerical errors in discretized horizontal derivatives on steep slopes, particularly the pressure gradient (Shchepetkin and McWilliams, 2003) and lateral diffusion tensor — leading to spurious diapycnal diffusion (Marchesiello et al., 2009). The degree of smoothing required increases with topographic slope, but decreases with grid scale. Consequently, resolutions finer than  $1/12^\circ$  are required to ensure that the topographic slope is sufficiently realistic to strain the GS and give it enough inertia to separate from the coast at the observed location (Debreu et al., 2022). Debreu et al. (2022) show that correcting the topographic smoothing by a volume penalization method (a form of immersed boundary condition) significantly increases the bottom pressure torque, enabling realistic GS separation with a resolution as coarse as  $1/8^\circ$ .

Geopotential (z-level) coordinate systems are another classic choice, but more for global climate models. They avoid errors in horizontal derivatives, but give a staircase representation of bottom topography, requiring both a bottom condition and a lateral

boundary condition, the latter being an artifact of the model (Nasser et al., 2023). A few studies show that sigma models provide superior results to z-level models in reproducing the GS separation (Schoonover et al., 2016; Ezer, 2016). Ezer (2016) uses a generalized coordinate system model to compare sigma-level and z-level approaches. The result highlights the shortcomings of a staircase representation of the continental slope, which tends to produce grid-scale noise that interferes with flow-topography interactions. This is why higher resolution seems to be needed in z-level models than in sigma models to reproduce GS dynamics. However, even at resolutions of 1 to 3 km, a diversity of solutions for the GS seems to persist with these models (Uchida et al., 2022).

As mentioned, lateral boundary conditions are an artifact of z-level models, but we briefly present the issues involved, as they are the subject of much discussion in the literature. Two types of lateral boundary conditions are studied, namely the no-slip boundary condition, where normal and tangential velocities are zero, and the free-slip boundary condition, where only the normal component of velocity is zero. The no-slip condition is generally considered more realistic for the GS separation than the free-slip condition (Chassignet and Marshall, 2008; Haidvogel et al., 1992; Dengg, 1993). However, these results are sensitive to many aspects of the model, including grid orientation, which increases the form drag created by a staircase representation (Adcroft and Marshall, 1998). The results are also sensitive to the choice of advection schemes. For example, enstrophy and energy conserving momentum advection schemes appear to lessen the sensitivity of the GS representation to the staircase effect (Nasser et al., 2023). Again, only high resolution z-level models can reduce the adverse effects of a staircase representation to allow realistic GS dynamics (Uchida et al., 2022).

- Subgrid-scale parameterization: horizontal parameterizations of eddy viscosity and diffusivity have received particular attention in the literature. Bryan et al. (2007) observed a positive impact on GS trajectory when eddy viscosity is made scale-aware, with a dependence on resolution. GS dynamics seems sensitive to the type of dissipation operator, Laplacian or biharmonic. A biharmonic operator may disrupt the GS separation (Chassignet and Marshall, 2008; Smith et al., 2000), while a Laplacian operator has a significant damping effect on its eastward penetration. Consequently, various combinations have been proposed (Chassignet and Marshall, 2008), but the physical justification remains weak since a positive eddy viscosity is inconsistent with upscaled KE fluxes in the inverse cascade. Instead, Renault et al. (2019b) show that the missing dissipation process in models, necessary to stabilize the GS system, can be provided by surface drag to the atmosphere (air-sea interaction). These processes will be examined in detail in Chapter 2.

Studies concur that increasing the horizontal resolution beyond  $1/10^\circ$  greatly enhances the dynamics of the GS, regardless of the differing proposals for an accurate depiction of the GS (Bryan et al., 2007; Özgökmen et al., 1997; Chassignet and Xu, 2017; Smith et al., 2000). High-resolution simulations have been suggested to improve the representation of baroclinic instabilities by resolving the first baroclinic Rossby radius (Paiva et al., 1999; Smith et al.,

2000; Chassignet and Marshall, 2008). In addition, high-resolution models can improve the inertia of the GS, and thus better represent its separation from the coast, by enhancing the topographic slope (Debreu et al., 2022) and Reynolds number (Dengg, 1993; Tansley and Marshall, 2000). In other words, a better definition of bottom slopes and an explicit representation of mesoscale eddy activity, made possible by increased resolution, are essential for reproducing realistic GS dynamics (Hallberg, 2013; Debreu et al., 2022).

However, a high diversity of solutions remain even at high-resolution and the realism of the simulations is not guaranteed (Chassignet and Marshall, 2008; Bryan et al., 2007). For example, using a simulation with a resolution of  $1/10^\circ$ , Maltrud and McClean (2005) found that despite improvements over coarse resolution simulations, separation still presented overshoot problems. Uchida et al. (2022) compares several submesoscale-permitting simulations (1-3 km resolution) and finds that the reproduction of the GS separation is sensitive to other model parameters such as advection/diffusion schemes, atmospheric and tidal forcing, and/or vertical coordinates (Figure 1.14). In addition, the authors show a poor representation of the GS in an unstructured, high-resolution grid model (Figure 1.14d). Özgökmen and Chassignet (2002) observed that eddy-resolving models of the GS system (and WBC systems in general) exhibited an excess of kinetic energy. Consequently, a correct representation of the GS may depend on its energy balance, with appropriate sources and sinks represented.

An overlooked aspect of ocean modeling is air-sea interaction, in particular the interaction between wind stress and ocean surface currents, known as current feedback (CFB) and forming a top drag, akin to a bottom drag (Renault et al., 2016a, 2019b). The details of this mechanism are explained in Chapter 2. Renault et al. (2016a) and Renault et al. (2018) demonstrate that this interaction damps the (sub)mesoscale activity by around 30% through an eddy-killing mechanisms, *i.e.*, a sink of energy from (sub)mesoscale eddies to the atmosphere. The inclusion of top drag in ocean models enables a more realistic simulation of oceanic mesoscale activity (without the need to tamper with eddy viscosity).

CFB can be incorporated into air-sea coupled simulations (Renault et al., 2019b) or parameterized in forced ocean simulations (Renault et al., 2020). The inclusion of CFB in numerical simulations of the GS has led to significant enhancements. In a coupled ocean-atmosphere simulation, Renault et al. (2019b) shows that damping mesoscale activity reduces the eddy-mean flow interaction and hence the inverse kinetic energy cascade that feeds recirculation gyres. Stabilization of the GS follows on from this process, providing a more accurate representation of its separation (Figure 1.15). According to Renault et al. (2023a), top drag affects the kinetic energy balance by redistributing the different sinks. When top drag is neglected, bottom drag takes over, increasing in magnitude to partially compensate for the missing dissipation. As a result, the GS system is oversensitive to bottom drag when top drag is neglected. A natural question arising from these studies is whether all dissipation processes are correctly simulated in our models, or whether other processes, possibly in the turbulent cascade, are not properly accounted for, or even whether the numerical dissipation error is properly considered. In the next chapter, we will review kinetic energy balance theories.

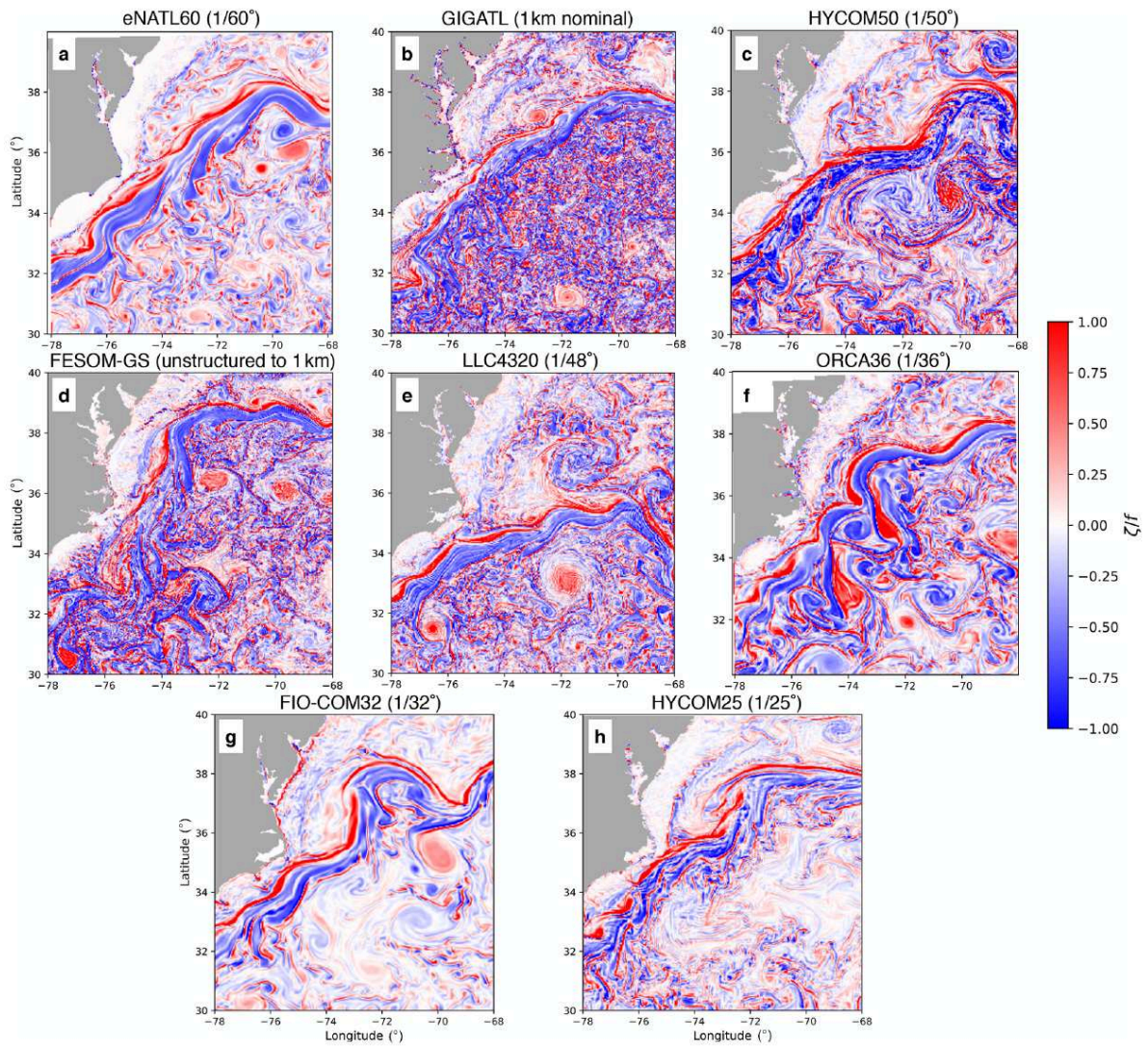


Figure 1.14: Snapshot of surface relative vorticity normalized by the local Coriolis parameter on 1 February at 00:00 from several model run over the Gulf Stream. Reprinted from Uchida et al. (2022).

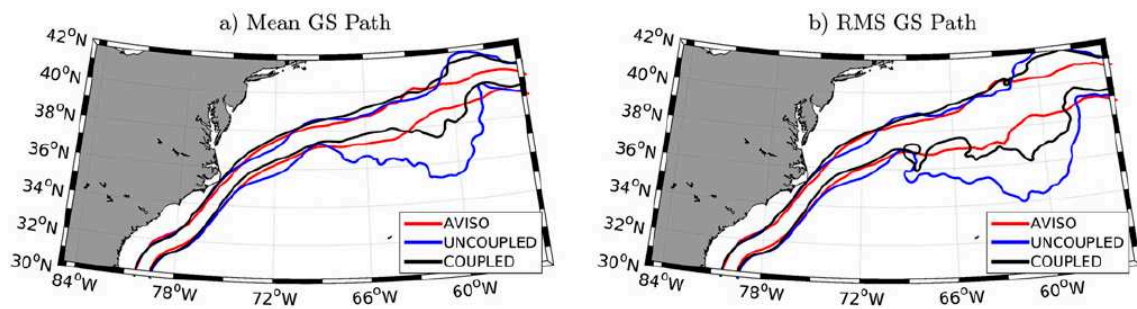


Figure 1.15: Mean (a) and RMS (b) GS trajectory estimated by mean geostrophic currents (contour  $0.6 \text{ m s}^{-1}$ ): from AVISO (red), a forced oceanic simulation without top drag parameterization (blue), and a coupled air-sea simulation (black), for the period 2000-04. Reprinted from Renault et al. (2016a).

# Kinetic energy pathway

---

## Contents

---

<b>2.1</b>	<b>Introduction</b>	<b>32</b>
<b>2.2</b>	<b>Description of spatial and temporal kinetic energy distribution</b>	<b>32</b>
<b>2.3</b>	<b>External kinetic energy sources</b>	<b>36</b>
<b>2.4</b>	<b>Ocean scale interactions</b>	<b>36</b>
2.4.1	Geostrophic turbulence	36
2.4.2	Evidence of inverse KE cascade	37
2.4.3	Role of submesoscale motions	38
2.4.3.1	Frontogenesis	40
2.4.3.2	Surface Baroclinic Instabilities	41
2.4.3.3	Frontal Instabilities	42
2.4.3.4	Internal Gravity Waves (IGW)	43
<b>2.5</b>	<b>Kinetic energy dissipation</b>	<b>43</b>
2.5.1	Boundary dissipation	43
2.5.1.1	Bottom Drag	44
2.5.1.2	Top Drag	44
2.5.2	Interior Dissipation and vertical mixing	45
<b>2.6</b>	<b>Final comments</b>	<b>47</b>

---

## 2.1 Introduction

To understand the kinetic energy (KE) budget of the ocean, we need to answer the following questions: What are the sources of energy? How is the energy distributed in time and space, and how is the energy dissipated (which is essential to maintain the energy balance)? The scientific community has paid great attention to these questions, with the last two still under debate. This chapter reviews the main references to provide possible answers. The study in this thesis will build on this previous work, in the hope of providing a more complete and quantitative answer.

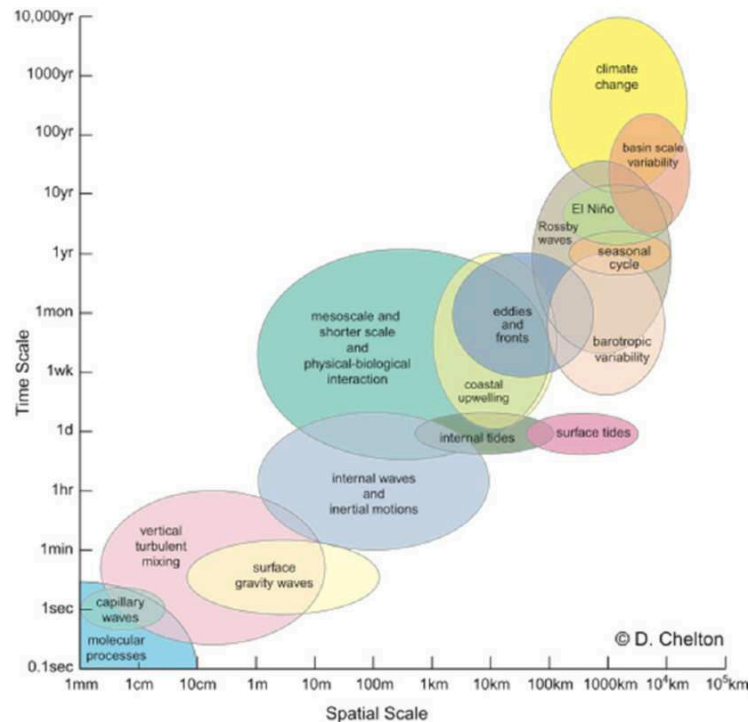


Figure 2.1: Time and space scales of the ocean processes. Reprinted from Dickey (2001) and adapted by Chelton (2011).

## 2.2 Description of spatial and temporal kinetic energy distribution

Figure 2.1 illustrates the main oceanic processes, providing the corresponding spatial and temporal scales. These processes have a wide range, from millimeters to thousands of kilometers in spatial extent and from seconds to thousands of years in temporal duration. With a few exceptions, such as the tides, there is a correlation between the spatial and temporal scales that determine the dynamic regime, as shown in the following Table 2.1.

At large scale and mesoscale ( $> \mathcal{O}(100\text{km})$ ), oceanic motions are quasi-horizontal with

	Length Scale	Timescale	Description
Large-scale	> 500 km	Seasonal to permanent	Balanced motions ( $u \sim v \gg w$ )
Mesoscale	25-500 km	10 to 100 days	Balanced motions ( $u \sim v \gg w$ )
Submesoscale	0.1-25 km	Hours to days	Transition to unbalanced motions ( $u \sim v > w$ )
Microscale	< 1 km	$\leq$ hours	Unbalanced motions ( $u \sim v \sim w$ )

Table 2.1: Classification of oceanic dynamical regimes from temporal and spatial scales.

only weak vertical velocities inhibited by Earth rotation and stratification, as expressed by Rossby and Froude numbers well below 1 ( $R_o = U/fL$  and  $F_r = U/NH$ , respectively, with  $L$  and  $H$  the horizontal and vertical length scales, and  $N$  the buoyancy or Brunt–Vaisala frequency). This so-called balanced or quasi-balanced flows refer to a balance between Coriolis, pressure gradient and buoyancy forces, and often described by quasi-geostrophic theory. However, at submesoscale, the effect of rotation weakens and the dynamical regime transitions between balanced and unbalanced motions, with larger vertical velocities (Klein et al., 2008). At microscale, unbalanced motions manifest themselves either as totally nonlinear turbulence or as internal gravity waves. The currents become three-dimensional with vertical velocities similar in magnitude to the horizontal velocities. Further down the scale, viscosity becomes important and leads to energy dissipation. Nonlinear interactions between currents at different scales are responsible for cross-scale energy fluxes (concerning both potential and kinetic energy), helping to create the broad dynamic spectrum observed in the ocean.

To describe the spatial and temporal variability of KE in the ocean, KE spectra have been extensively employed. *In situ* observations, satellite data, and numerical ocean models show the presence of a significant regional variability in the distribution of KE. For example, Figure 2.2 presents a KE spatial spectrum estimated from winter currents observed across the GS at 50 m depth (Oleander section around 36°N). The KE is concentrated at mesoscale (> 100 km) and decreases at small scales. Mesoscale eddies represent the main reservoir of energy in the ocean, capturing about 80% of the total KE (Klein et al., 2019; Chelton et al., 2011; Ferrari and Wunsch, 2009; Morrow and Le Traon, 2012). The slope at which the KE spectra decays typically varies between  $k^{-2}$  and  $k^{-3}$ , depending on the processes involved in cross-scale energy fluxes (Callies et al., 2015; Klein et al., 2008). In the following section, we will focus on those processes.

Figure 2.3 shows a near-surface KE temporal spectrum produced from a mooring in the Mid-Atlantic Ridge near 27°N. As expected from the relationship between the spatial and temporal scales mentioned above, KE generally decreases at higher frequency, with a few exceptions. An intense energy peak is present at inertial frequency  $f$  (*i.e.*, the Coriolis frequency), corresponding to the near-inertial internal gravity waves produced by winds and tides (Alford et al., 2016). We also observe a peak at a period of 12.42 hours, which aligns

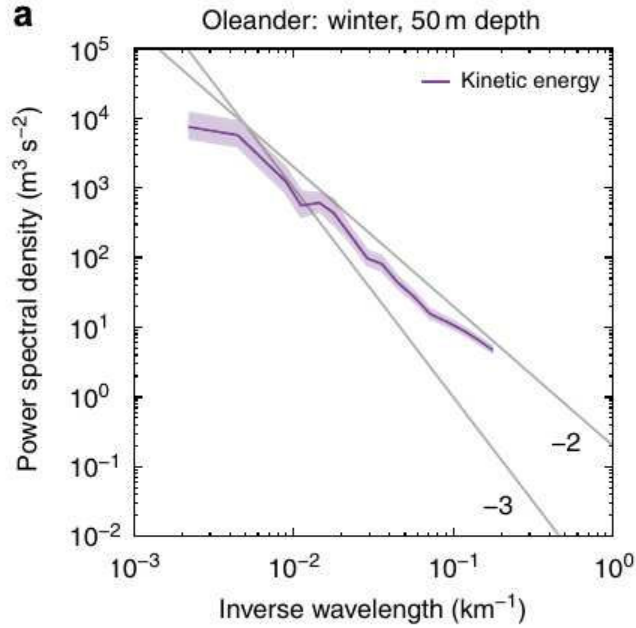


Figure 2.2: KE spectrum estimated from winter currents observed across the GS at 50 m depth. The light shading is the 95% confidence interval and the lines are the reference for the slopes  $k^{-2}$  and  $k^{-3}$ . Reprinted and adapted from Callies et al. (2015).

with the semi-diurnal M2 tidal component, recognized as the most powerful tidal mode.

Frequency-wavenumber spectra can also be used to characterize the various dynamical regimes. An example is given in the figure extracted from Torres et al. (2018) (see their Figure 3; here Figure 2.4). Figure 2.4 shows the frequency-wave number KE spectrum estimated using winter currents in a numerical ocean model over the Kuroshio Extension (Figure 2.4a) and a more schematic spectrum to describe the different dynamical regimes. Dispersive modes of internal gravitational waves (IGWs) are apparent at high frequencies (Rocha et al., 2016; Alford et al., 2016; Arbic et al., 2013), whereas horizontal frequency bands close to tidal (semidiurnal and diurnal) and inertial frequency  $f$  span a wide range of wavenumbers. The region of maximum energy that follows a nondispersive line below the IGW frequencies is not associated with wave dynamics, but corresponds to quasi-equilibrium motions: mesoscale (MBM) and submesoscale (SBM). Submesoscale motions above the inertial frequency are unbalanced (USM). Unbalanced submesoscale motions and internal gravity waves appear to share similar temporal and spatial scales, which complicates their decomposition. Note also that this spectrum varies seasonally and regionally (Qiu et al., 2017; Sasaki et al., 2014).

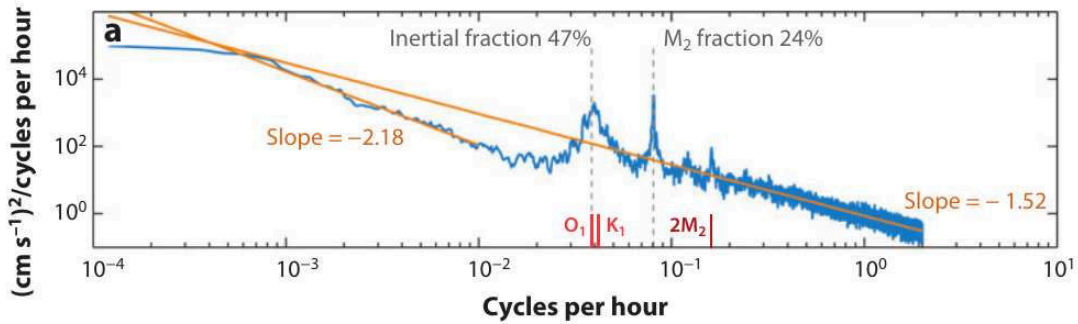


Figure 2.3: KE spectrum estimated from a current meter at 128 m depth on a mooring located over the Mid-Atlantic Ridge near 27°N. The peaks showing the inertial frequency, principal lunar semidiurnal M2, and diurnal O1, K1 tidal are represented, along with the percentage of KE concentrated around these peaks. Reprinted and adapted from Ferrari and Wunsch (2009).

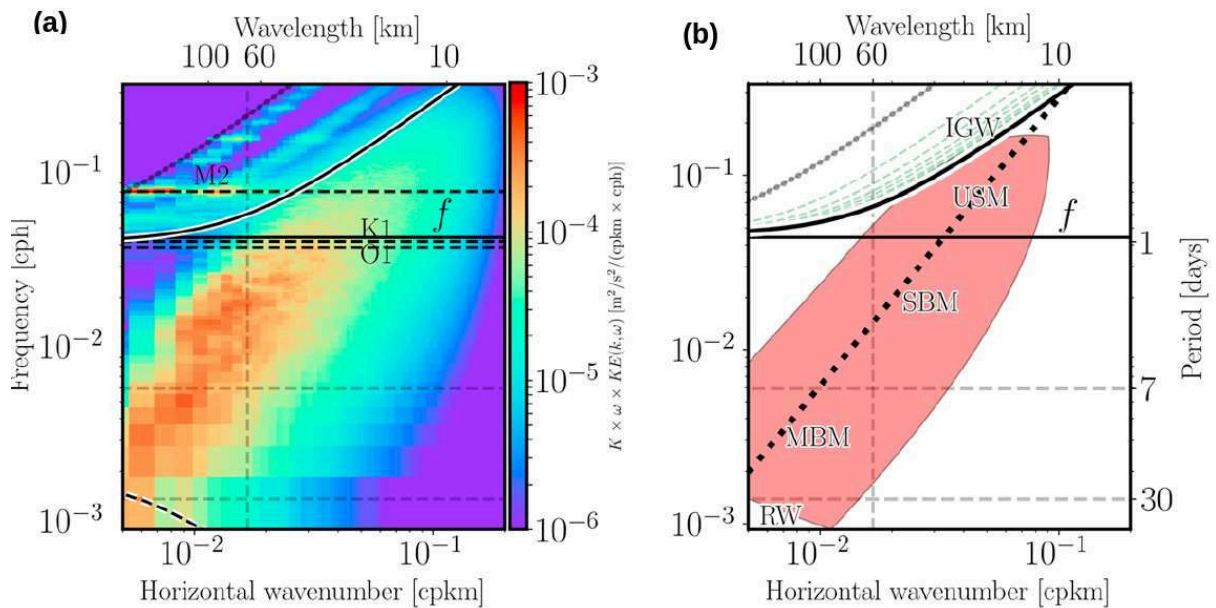


Figure 2.4: (a) Frequency-wave number spectrum of KE in the Kuroshio-Extension, during January-February-March winter season. (b) schematic frequency-wave number spectrum, where is displays the multiple dynamical regimes: RW stands for Rossby waves, MBM for mesoscale balanced motions, SBM for submesoscale balanced motions, USM for unbalanced submesoscale motions, and IGW for internal gravity waves. The schematic spectrum shows the dispersion relation of the first ten baroclinic modes: mode-1 in gray dotted line, mode-2 to mode-9 green dashed lines, and mode-10 in black. The nondispersive line,  $\omega - ck = 0$ , is drawn with  $c$  corresponding to an eddy speed of 8.5 km/day (10 m/s). Reprinted and adapted from Torres et al. (2018).

## 2.3 External kinetic energy sources

The main source of mechanical energy for the ocean is atmospheric forcing, *i.e.* wind stress — a parallel energy budget is provided by the tides with a transfer to the wind-driven circulation budget. The wind applies stress on the surface of the ocean, directly transferring KE (Ekman drift) that builds up potential energy (PE) via Ekman pumping. The wind-generated energy can then be transferred to depth through geostrophic adjustment (transfer of large-scale potential to kinetic energy) (Gill et al., 1974; Wunsch and Ferrari, 2004; Ferrari and Wunsch, 2009).

Satellite data have been used to estimate wind-generated energy, with uncertainties due to the estimation of wind stress and geostrophic rather than total currents. Wunsch and Ferrari (2004) suggested that the contribution is around 1 TW, which is consistent with Scott and Xu (2009) and Rai et al. (2021). When total currents are used (Von Storch et al., 2012), the wind-generated energy may be closer to 4 TW.

Tides are caused by the gravitational pull of the moon and the sun, as well as the centrifugal force generated by Earth rotation (Stewart, 2008). They consist of hundreds of harmonic constituents that arise from the six fundamental frequencies driving them. Of these constituents, the M2 tide, with a period of 12.42 hours, is the most energetic (Figure 2.3). According to satellite data, the primary 8 tidal constituents produce an energy of 3.5 TW, with M2 being responsible for 2.4 TW (Le Provost and Lyard, 1997; Munk and Wunsch, 1998). Part of the tidal energy is used to generate strong barotropic currents (70%), especially in coastal waters, and the remaining energy is used to generate internal tides, which are internal waves generated by the interaction of barotropic tides with the topography under stratified conditions (Egbert and Ray, 2000). Tides can influence the wind-driven energy budget through the action of barotropic tides, which modify bottom drag, and baroclinic tides, which trigger non-linear interactions between waves and currents.

## 2.4 Ocean scale interactions

The theoretical framework known as geostrophic turbulence explains the nonlinear interaction between various scales while in a state of hydrostatic and quasi-geostrophic (QG) balance. *In situ* observations, as well as satellite data and ocean model simulations, indicate that quasi-geostrophic equations do not fully account for the interaction between spatial scales. Here, we present a brief review of ocean scale interactions.

### 2.4.1 Geostrophic turbulence

Geostrophic turbulence is defined as the nonlinear motion of fluids that are near to a state of geostrophic and hydrostatic balance (Charney, 1971; Rhines, 1977; Salmon, 1980; Fu and Flierl, 1980; Hua and Haidvogel, 1986). It describes the fate of mesoscale eddies emerging

from baroclinic and barotropic instabilities. Mesoscale eddies are quasi-two-dimensional (2D), *i.e.*,  $u \sim v \gg w$ , but in Charney's theory, they initially follow a forward cascade from the injection scale in a process called barotropization, where baroclinic modes transfer energy to the barotropic mode. The barotropic mode then drives the inverse cascade as in 2D turbulence. However, in the ocean, barotropization is incomplete and both the barotropic and first baroclinic modes are involved in the inverse cascade, via merging processes (Scott and Arbic, 2007). On the opposite side of the injection scale starts a forward enstrophy cascade to smaller scales. This involves the stretching of vorticity filaments leading to gradient enhancement, but with very little downscale KE transfer.

Geostrophic turbulence predicts a limit to the growth in size of mesoscale eddies given by the Rhines scale,  $l_R \sim \sqrt{u/\beta}$  (Rhines, 1975). The eddies radiate as Rossby waves at this scale where the  $\beta$  effect is important, and the inverse cascade is arrested. This process generates alternating zonal jets of width  $l_R$  as the eddies elongate anisotropically in the zonal direction and their growth slows in the meridional direction (Rhines, 1975; Vallis, 2017). Note that a similar effect is expected from a topographic slope, *i.e.*, the topographic  $\beta$  effect.

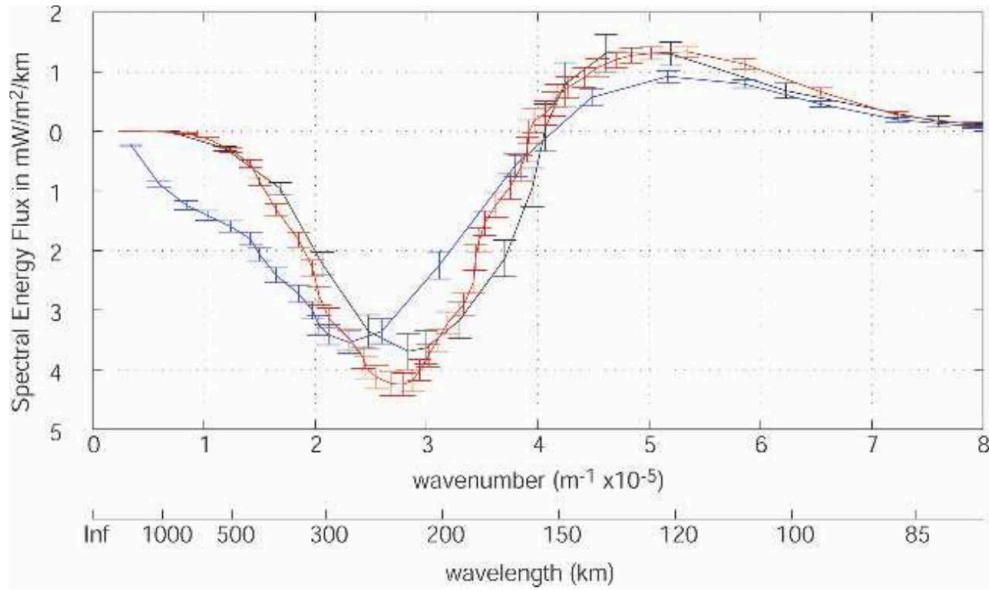


Figure 2.5: Spectral KE flux estimated from altimeter data over the Antarctic Circumpolar Current: the black curve using SSH on a  $32 \times 32$  grid, red curve using SSH on a  $64 \times 64$  grid, blue curve using velocity on a  $64 \times 64$  grid. Error bars represent standard error. Reprinted from Scott and Wang (2005).

### 2.4.2 Evidence of inverse KE cascade

The launch of the Topex/Poseidon (T/P, CNES/NASA) altimetry satellite made it possible to observe sea level in a spatial range from 100 km to over 5,000 km, marking a significant advance for oceanographic science. In particular, these observations made it possible to check

part of the theory of geostrophic turbulence. The existence of a large reservoir of mesoscale energy was confirmed, as well as the presence of zonal jets, although not necessarily verifying the Rhines scale, depending on the region (Maximenko et al., 2005). Satellite altimetry data, giving access to the first baroclinic mode (Smith and Vallis, 2001), have enabled a calculation of cross-scale (spectral) KE fluxes, that appeared to confirm also the occurrence of an inverse cascade that carries energy to the scales of the most energetic eddies around 250-300 km (Tulloch et al., 2011; Klein et al., 2019).

Nevertheless, contradictions between theory and observation were also found (Klein et al., 2019). The assumption that the KE inverse cascade starts around the injection scale (50-100 km) was first contradicted by Scott and Wang (2005) (Figure 2.5), but Arbic et al. (2013) attributed the discrepancy to a lack of resolution in the satellite data. Applying filters on a high-resolution global model solution (Figure 2.6) to obtain a signal representative of the AVISO data<sup>1</sup> (Ducet et al., 2000), they reproduced a spectral energy flux similar to that of Scott and Wang (2005). Without the filters, the model energy flux shows a wider range of inverse cascade. In fact, this range is even wider than predicted by geostrophic turbulence, extending to the submesoscale (Schubert et al., 2020; Klein et al., 2008; Capet et al., 2008d).

Another discrepancy is in Charney's prediction of a wavelength spectrum slope of  $k^{-3}$  in the enstrophy inertial range, whereas satellite data and in situ observations indicate seasonal and regional variability in this slope. The slope ranges from  $k^{-3}$  to  $k^{-2}$ , and even flatter in some low KE regions. The discrepancy is not due to noise in the observations, as first suggested by Fu (1983), but to mechanisms other than those implicated in geostrophic turbulence (Dufau et al., 2016; Xu and Fu, 2012).

These discrepancies between geostrophic turbulence and observations has stimulated many questions, and modeling studies over the last two decades have highlighted the role of submesoscale processes — not observed by current satellites (Scott and Wang, 2005; Morrow and Le Traon, 2012; Klein et al., 2019) — in the energy pathway.

### 2.4.3 Role of submesoscale motions

Using a high-resolution simulation ( $1/30^\circ$ ) over the Subtropical Countercurrent, Qiu et al. (2014) compares geostrophic eddy kinetic energy (EKE) from the model and AVISO data and observes two main differences (Figure 2.7a): (i) the model has higher EKE levels than AVISO, and (ii) the peak of model EKE occurs in April, which is 1.5 months earlier than AVISO. Using sea surface height (SSH) at wavelengths longer than 150 km, the model EKE becomes consistent with satellite observations (Figure 2.7b). These results, as those in the previous section, suggest that the AVISO data miss a substantial part of the mesoscale eddy energy, which extends to a lower scale than that expected from geostrophic turbulence. The excess energy appears to be associated with underestimated energy at submesoscale (Figure 2.7b).

<sup>1</sup>Archiving, Validation and Interpretation of Satellite Oceanographic data (AVISO) distributes altimeter data, which were post-processing, analysis and archiving for CNES.

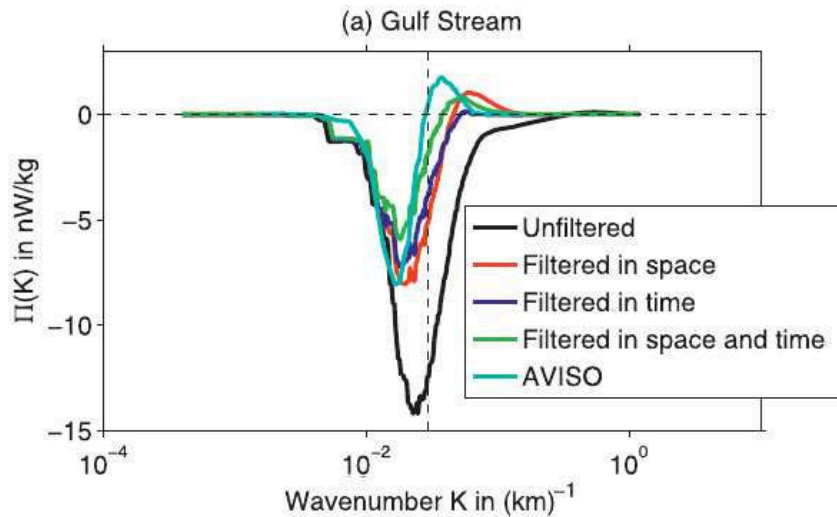


Figure 2.6: Spectral KE flux estimated from surface geostrophic ocean currents in the GS, using AVISO data (cyan curves) and four versions of estimation from a realistic ocean model simulation: unfiltered (black curves), spatially filtered (red curves), temporally filtered (blue curves), and spatially and temporally filtered (green curves). The vertical dashed line indicates the Rossby deformation wavenumber. Reprinted and adapted from [Arbic et al. \(2013\)](#).

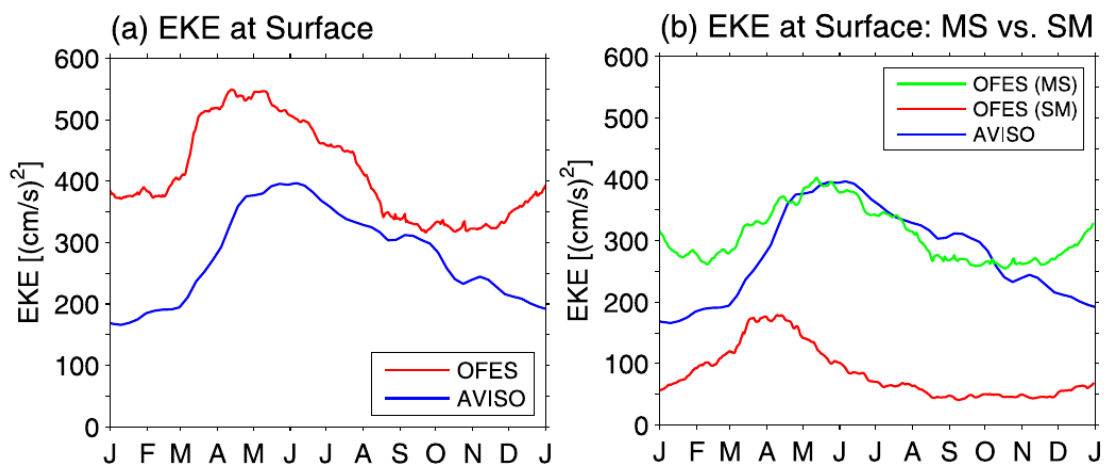


Figure 2.7: Surface EKE time series from the ocean simulation (OFES) over the Subtropical Countercurrent (red line) vs the AVISO SSH data (blue line) in 2001. (b) Time series of mesoscale EKE (green line) vs submesoscale EKE (red line) from the simulation. Blue line is same as that in (a). Reprinted and adapted from [Qiu et al. \(2014\)](#).

Increasing model resolution enables us to capture submesoscale processes. Ageostrophic (unbalanced) motions are favored as rotation and stratification become less dominant at finite Rossby and Froude numbers. Unbalanced motions are shown to be responsible for a forward cascade (Brüggemann and Eden, 2015) due to their strong divergent velocity component. By comparing QG and primitive equation models, Molemaker et al. (2010) show that, although unbalanced motions account for only a small fraction of the flow’s total KE, they are essential for a forward cascade of energy. According to Capet et al. (2008a), the very limited forward cascade of KE produced by surface quasi-geostrophic (SQG<sup>2</sup>) models is linked to the fact that the SQG (like interior QG) equations do not support momentum advection by ageostrophic currents. In short, it is the divergent component of the ageostrophic currents that leads to a forward cascade, while the inverse cascade is entirely due to balanced motions.

Note that SQG models, which can simulate frontogenesis, are able to predict a  $k^{-5/3}$  spectral slope, close to  $k^{-2}$  (Klein et al., 2008; Callies et al., 2016). In this case, the excess energy at submesoscale, compared with geostrophic turbulence, is provided by a conversion of potential to kinetic energy at the fronts, rather than a direct KE cascade (Capet et al., 2008a). It is therefore important to bear in mind that the PE cascade and conversion to KE are essential for understanding the KE spectrum at submesoscale.

Several mechanisms have been proposed to explain the emergence of submesoscale fronts and eddies. The following is a description of the main mechanisms involved.

### 2.4.3.1 Frontogenesis

Several studies have shown that a forward cascade is often associated with frontal regions (Hoskins, 1982; Thomas and Lee, 2005; Lapeyre and Klein, 2006; Capet et al., 2008a; Klein et al., 2008; Capet et al., 2008c; Molemaker et al., 2010; Schubert et al., 2020; McWilliams, 2021; Srinivasan et al., 2022). Fronts (described in the previous chapter) develop large vertical velocities that extend from the surface to a depth of a few hundred meters (Klein et al., 2019). Frontogenesis is the process that intensifies a front and occurs in regions where there is a horizontal buoyancy gradient in a background horizontal deformation flow (Figure 2.8). The deformation strengthens the horizontal buoyancy gradient and disrupts the geostrophic balance along the front. To restore balance, a secondary ageostrophic circulation (ASC) appears and acts by restratifying the subsurface. ASC causes the conversion of PE into KE through vertical vortex stretching (Hoskins and Bretherton, 1972), energizing submesoscale KE (Capet et al., 2008c). Capet et al. (2008a) suggested that ASC generates the ageostrophic advection responsible for a forward cascade. Recently, Srinivasan et al. (2022), using asymptotic theory and submesoscale simulations of a North Atlantic region between Greenland and Iceland, concluded that the primary mechanism for forward energy flow at fronts is frontogenesis. Frontogenesis and ASC are particularly active processes in the GS North Wall, where ASC appears to enhance frontogenesis in a positive feedback (McWilliams et al., 2019).

---

<sup>2</sup>SQG equations describe a flow with non-zero surface density and uniform potential vorticity in the interior; interior QG equations is for a flow with non-uniform potential vorticity in the interior.

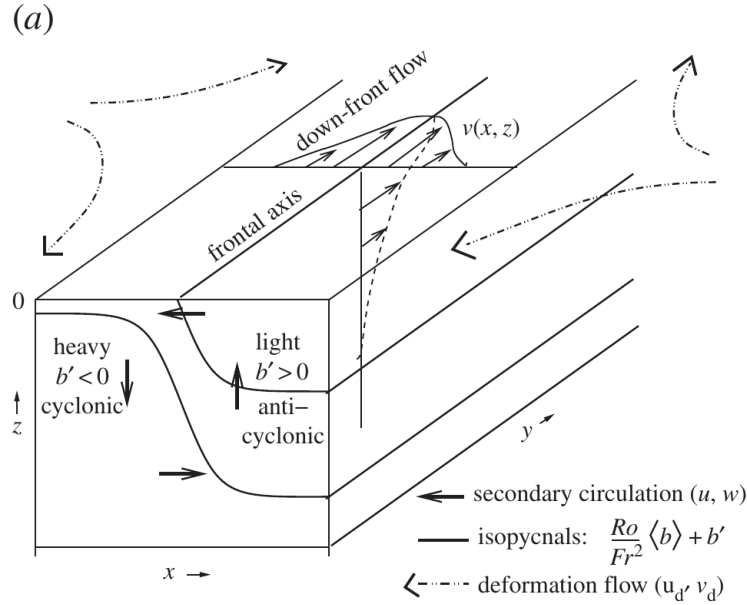


Figure 2.8: Schematic presentation of an intensifying surface front (frontogenesis) caused by a large-scale straining flow. The downfront flow  $v(x)$  is approximately geostrophic, and variables with primes are local perturbations presenting the ageostrophic secondary circulation across the front. Reprinted and adapted from McWilliams (2016).

QG models show no significant difference in energy distribution with increasing spatial resolution (McWilliams, 1989). In contrast, SQG models are more sensitive to resolution since they allow the development of frontogenesis that energizes the submesoscale (Blumen, 1978). However, the frontogenesis produced by SQG models is weaker than that of the primitive equations models (Capet et al., 2008a), due to the absence of advection by ageostrophic motions (which reinforce straining deformation), not included in QG and SQG equations. However, as mentioned earlier, SQG models produce a flatter slope of KE spectrum than QG models, showing that frontogenesis (even without ageostrophic enhancement) can produce much of the observed submesoscale energy.

For more information on the mathematics of frontogenesis, including all contributing terms, see Hoskins (1982), Capet et al. (2008c), and McWilliams (2021) for a general review.

### 2.4.3.2 Surface Baroclinic Instabilities

Submesoscale quasigeostrophic instabilities at finite Rossby number draw KE from the mesoscale PE, similarly to ASC. For example, mixed-layer instabilities (MLIs) are generated when the mixed layer is weakly stratified (associated with weak potential vorticity) and in the presence of horizontal buoyancy gradients. MLIs are similar to QG baroclinic instabilities that develop in the pycnocline, but on a much smaller scale given by the mixed layer Rossby radius

$NH/f$ , with  $H$  here the mixed layer depth (Boccaletti et al., 2007). Their horizontal scale range between 1-10 km and time scale is of days. An important role of MLIs, like ASC, is to restratify the mixed layer by extracting energy from the horizontal buoyancy gradients, *i.e.*, conversion from potential to kinetic energy (restoring balance at the front). The mixed layer eddies (MLEs) generated in the process contribute to energizing submesoscale KE and mesoscale eddies as well, via a process of absorption, therefore producing larger upscale fluxes (Khatri et al., 2021; Qiu et al., 2014; Schubert et al., 2020).

Another type of submesoscale baroclinic instabilities is the Charney instability (Capet et al., 2016). These have a temporal and spatial scale similar to that of MLIs, but develop in the presence of a surface buoyancy gradient and interior velocity shear (a coupled surface/interior baroclinic instability) (Roulet et al., 2012), and also result in a conversion of potential into kinetic energy.

These instabilities have important seasonal variability (Callies et al., 2015; Qiu et al., 2014). In winter, the mixer layer is deeper and the horizontal buoyancy gradient stronger, allowing for intensified MLIs. Strengthening of mesoscale eddies can be expected in this case as mentioned before, but a delay of a few weeks to a couple of month seems to be observed between the peak of MLE and that of mesoscale activity (Qiu et al., 2014; Schubert et al., 2020; Khatri et al., 2021). Schubert et al. (2020) suggest that this delay corresponds to the time needed by the absorption process.

### 2.4.3.3 Frontal Instabilities

Frontal instability can disrupt frontogenesis (McWilliams, 2021). It occurs when straining deformation by mesoscale eddies, enhanced by submesoscale motions, drives the process toward frontal collapse (Callies et al., 2016; Hoskins and Bretherton, 1972). Hoskins (1974) points out that small-scale instabilities can develop when the Ertel potential vorticity ( $PV$ )<sup>3</sup> has an opposite sign to the planetary vorticity ( $fPV < 0$ ). The instabilities that satisfy this condition can be classified into (Thomas et al., 2013; Haine and Marshall, 1998):

- Gravitational instability due to the extraction of available potential energy by the buoyancy flux.
- Symmetric instability due to the extraction of mean KE by vertical shear.
- Inertial (Centrifugal) instability due to the extraction of mean KE by horizontal shear.

In situ observations (Thomas et al., 2013; D’Asaro et al., 2011), numerical models (Klein et al., 2008; Capet et al., 2008c; Schubert et al., 2020) show that these instabilities drive a forward cascade to dissipation.

---

<sup>3</sup>Ertel potential vorticity is defined as  $(\zeta + f\mathbf{k}) \cdot \nabla b$ , where  $\zeta$  is the relative vorticity and  $b$  is the buoyancy

### 2.4.3.4 Internal Gravity Waves (IGW)

Recent studies suggest that near-inertial internal gravity waves (IGWs) contribute to the forward cascade through nonlinear interactions. IGWs can be produced by (i) tides (internal tides) with diurnal and semidiurnal frequencies, (ii) winds (near-inertial waves, NIWs) with frequencies close to  $f$ , and (iii) spontaneous emission by loss of balance, nonlinear wave-wave interactions, or lee-wave formation by geostrophic flows on the seafloor (Alford et al., 2016).

IGW contribute to the forward cascade by extracting energy from balanced motions, either from the mean flow or from mesoscale eddies and fronts (Barkan et al., 2015; Thomas, 2012; Shakespeare and Taylor, 2014; Bühler and McIntyre, 2005). Once IGWs are generated, it is not clear how they affect the energy cascade, but Barkan et al. (2017) suggested two mechanisms: wave turbulence (the direct energy cascade of internal waves; see Alford et al. 2016); and stimulated cascade (or imbalance), whereby internal waves trigger a transfer of energy from the mesoscale to the submesoscale.

Additional studies have been carried for internal tides, specifically. The mechanisms are similar to those of other internal waves: wave-wave interaction (MacKinnon and Winters, 2005); reflection, refraction, and scattering by interaction with the mean flow (Duda et al., 2018; Kelly et al., 2016) or with mesoscale eddies (Rainville and Pinkel, 2006).

## 2.5 Kinetic energy dissipation

In order to maintain the energy balance of the ocean, it is necessary to dissipate the energy provided by atmospheric and tidal forces. For a long time, the community has wondered how energy is dissipated in the ocean, considering that it tends to concentrate energy on a large scale where viscosity is negligible.

Dissipation is understood as the rate of loss of turbulent KE to heat through eddy viscosity. In large-scale geophysical flows, dissipation is provided by the frictional forces generated by turbulent flows near boundaries. Due to the complexity of turbulence, the estimation of frictional forces uses the eddy viscosity hypothesis proposed by Boussinesq, where the turbulent stress is assumed to be proportional to the velocity gradient field (Kundu et al., 2015). The idea of an interior route to dissipation through a forward cascade of energy starting at submesoscale is recent and there is no attempt at quantifying this process compared with boundary processes. This question is at the core of the present PhD thesis study.

The mechanisms at work in an ocean basin are briefly described below.

### 2.5.1 Boundary dissipation

In the ocean, frictional forces are usually neglected except for a thin boundary layer ( $\mathcal{O}(10m)$ ). In the bottom boundary layer, the velocity slows from values typical of the interior to zero

at a solid boundary. In contrast, at the surface, the velocity changes rapidly to catch up with the wind speed on the other side of the boundary. The effect of friction therefore differs between the bottom and surface layers, as explained below.

### 2.5.1.1 Bottom Drag

An important energy sink is given by the bottom drag exerted by the seafloor on bottom currents. On a rough topography, the mechanisms involved are: *skin friction*, *i.e.*, the reduction of flow to zero at an static boundary due to viscous forces; and *form drag* resulting pressure differences on either side of roughness elements (Thorpe, 2005; Belcher and Wood, 1996). Form drag is also associated with *wave drag* resulting from lee-wave breaking (Klymak, 2018; Trossman et al., 2017).

Sen et al. (2008) found that the dissipation of geostrophy currents by a quadratic bottom drag (increasing with squared bottom velocity) is about 0.2 - 0.8 TW, in agreement also with Arbic et al. (2009). The dissipation rate due to bottom drag is large, especially in energetic regions such as the GS (Sen et al., 2008), and can nearly balance the wind input (Weatherly, 1984). The absence of bottom friction in the models can have important consequences for ocean dynamics, as barotropization is uncontrolled and intensifies the inverse energy cascade (Trossman et al., 2017). Using a two-layer quasi-geostrophic turbulence model, Arbic and Flierl (2004) shows that a minimum of bottom friction is required to reproduce the observed amplitudes, vertical structure and horizontal scales of mid-latitude eddies.

Bottom drag also provides dissipation for barotropic tides, corresponding to 70% of the total tidal energy, especially in the coastal region where the currents are more intense (Egbert and Ray, 2000).

Recently, more attention has been paid to wave drag. The generation of lee waves on rough topography results in the direct conversion of energy from large-scale, geostrophically balanced flows to unbalanced internal waves, which can subsequently transfer their energy to small scales through wave turbulence and and breaking (Nikurashin et al., 2013). Nikurashin and Ferrari (2010) found that globally 20% of the wind energy input (about 0.2 TW) is converted into internal lee waves as geostrophic eddies flow over small-scale topography. Wave drag can also have local effect on momentum and vorticity, as on the Charleston bump along the GS path (de Marez et al., 2020).

### 2.5.1.2 Top Drag

Similar to bottom drag, frictional dissipation occurs near the surface ocean. As mentioned in Chapter 1, the interaction between surface ocean currents and wind stress, *i.e.*, current feedback (CFB) or top drag, produces an energy dissipation that dampens (sub)mesoscale activity by about 30% (Renault et al., 2016a, 2018). This eddy killing effect has been assessed using coupled air-sea models (Renault et al., 2016a,b, 2023a) and satellite data (Renault

et al., 2017; Rai et al., 2021), for the global ocean (Renault et al., 2017; Rai et al., 2021), and for regional circulation systems such as the GS (Renault et al., 2016b), California Current (Renault et al., 2016a), Agulhas Current (Renault et al., 2019b), Gulf of Mexico (Larrañaga et al., 2022) and western Mediterranean (Renault et al., 2021).

Using satellite altimetry and scatterometry, Rai et al. (2021) shows that eddy killing removes KE at scales smaller than 260 km at an average rate of 50 GW over the global ocean.

To understand the eddy killing process, we can analyze, as in Renault et al. (2016b), the ideal case of a southward uniform wind blowing over an anticyclonic eddy (Figure 2.9). Without CFB (Figure 2.9a), the wind stress is defined as  $\tau = C_d \rho_a U_a^2$ , where  $C_d$  is the drag coefficient,  $\rho_a$  the atmospheric density and  $U_a$  the surface wind. We can estimate the wind work, *i.e.*, the energy transferred by surface winds to the mesoscale eddy, as  $F_e K_e = \tau U_o$ , where  $U_o$  is the surface current. Since  $\tau$  is constant and  $U_o$  changes sign on either side of the eddy, the ocean gains energy from wind stress on one side and loses it on the other, but over the entire surface of the eddy, the result is zero wind work:  $F_e K_e = 0$ .

For the case where CFB is included (Figure 2.9b), the wind stress is defined as  $\tau = C_d \rho_a (U_a - U_o)^2$ . Assuming  $U_o \ll U_a$ , the sign of  $F_e K_e$  on either side of the eddy is the same as in the case without CFB, but the amplitude is now greater on the east side than on the west side, so that integration over the whole eddy area gives  $F_e K_e < 0$ , *i.e.*, the oceanic eddy is transferring energy to the atmosphere. A third case is where the CFB affects not only wind stress, but also the wind itself (Figure 2.9c). In this case, the wind reacts to variations in drag  $\tau$  and increases when drag is reduced by CFB (and vice versa). As a result, the difference in wind work on either side of the eddy is less than in the previous case, but not so much as to change the sign of the integral.

## 2.5.2 Interior Dissipation and vertical mixing

Energy dissipation in the interior of the ocean is possible through turbulent motions. These are due to loss of hydrostatic and geostrophic or gradient wind momentum balance (Brüggemann and Eden, 2015; Klein et al., 2008; Molemaker et al., 2010). Unbalanced motions enable a forward cascade of energy to the smallest scales, down to isotropic microscale turbulence until dissipated by molecular viscosity. The mechanisms leading to this possible interior route to dissipation have been discussed in Section 2.4.3.

In addition, oceanic currents can lose energy through instabilities of their vertical shear, a process that occurs mainly in the surface and bottom planetary boundary layers (PBLs) of  $\mathcal{O}(100m)$ , and for a wide range of scales (Marchesiello et al., 2011), but also in the ocean interior. Atmospheric forcing is a main source of vertical mixing in the oceanic surface boundary layer due to wind-induced shear flow or convection due to heat and freshwater fluxes (Large et al., 1994). A similar mixing process is attributed to the shear flow induced by bottom stress (Wunsch and Ferrari, 2004). Surface shear flow and vertical mixing do not only affect the large horizontal scales of ocean currents, but are in fact present at mesoscale and submesoscale, where they constitute an important sink (Marchesiello et al., 2011; McWilliams,

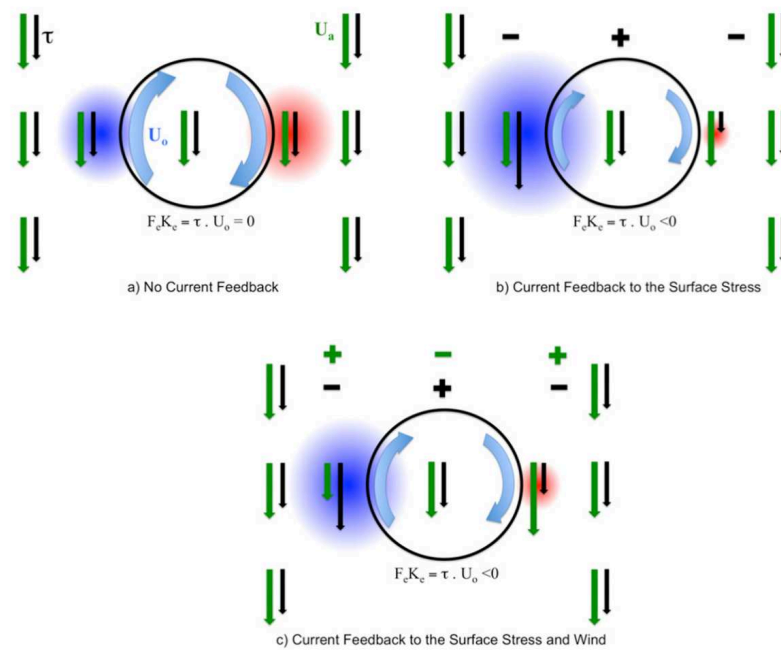


Figure 2.9: Schematic representation of the current feedback effects over an anticyclonic eddy, considering a uniform southward wind. The arrows represent the wind (green), surface stress (black), and surface current (blue). The red (blue) shade indicates a positive (negative)  $F_e K_e$ . The black (green) +/- signs indicate the current-induced stress (wind) curl. Reprinted from Renault et al. (2016b).

2016). In addition, wave generation and subsequent breaking is recognized as an important source of mixing and energy sink (Wunsch and Ferrari, 2004; Ferrari and Wunsch, 2009).

Vertical mixing is associated with downscale KE fluxes, but also with redistribution of PE. It is a diabatic process that converts part of the available potential energy (APE)<sup>4</sup> into potential energy that is no longer available to generate motion (Winters et al., 1995).

## 2.6 Final comments

By way of summary, answering the questions presented at the beginning of the chapter, we can conclude that:

1. The main external sources of KE are wind and tides, which provide energy at large scale.
2. Mesoscale eddies generated by instability of the large-scale circulation concentrate much of the energy input. These eddies interact with each other and transfer back their energy to the large scale.
3. The direction of energy transfer can be reversed when unbalanced motions are at work. The interaction of balanced and unbalanced motions can lead to a forward cascade of energy, somewhere in the submesoscale range.
4. The PE of mesoscale eddies can be transferred to smaller scales through eddy stirring, and converted by frontal processes to submesoscale KE.
5. Several ways of dissipating energy have been proposed. First, energy is dissipated at the boundaries by bottom and top drag. Second, interior dissipation can result from a forward cascade of energy — transferring energy to scales where molecular viscosity is significant. Finally, shear-induced vertical mixing can be an important player in planetary boundary layers, dissipating energy at all horizontal scales (with some degree of nonlocality).

It should be noted that many studies of oceanic KE budget mentioned in this chapter are based on idealized models, and not all processes have been confirmed or their contribution quantified in realistic simulations. This is an objective of the present thesis, focusing on the GS system. Also, if the KE budget is our main focus, close attention must be paid to the APE, which is a source or sink of KE across the entire spectrum. Processes such as Ekman pumping or barotropic tides are a source of APE. APE produced at large scale can be carried downscale, especially through eddy stirring (Klein et al., 2019). Then, as mentioned above, processes such as interior baroclinic instabilities, frontogenesis, submesoscale baroclinic instabilities are all APE sinks. In addition, the APE reservoir can be modified by air-sea interactions (Ma

---

<sup>4</sup>In geophysical flows, only a small fraction of the PE is available for transfer to KE, the available potential energy.

et al., 2016; Bishop et al., 2020; Renault et al., 2023b). The influence of the APE budget on the GS energy pathway will be examined in greater detail in Chapter 6.

# Methodology

## Contents

<b>3.1</b>	<b>Numerical Models</b>	<b>50</b>
3.1.1	CROCO	50
3.1.1.1	Current Feedback Parameterization	51
3.1.1.2	Bottom Drag Parameterization	51
3.1.1.3	Horizontal advection schemes and numerical dissipation	52
3.1.2	WRF-ARW	53
3.1.3	Models Configuration	54
<b>3.2</b>	<b>Post-processing</b>	<b>56</b>
3.2.1	Coarse-graining method	56
3.2.1.1	Decomposition	56
3.2.1.2	Derivation	58
3.2.1.3	Comparison with other methods	59

## 3.1 Numerical Models

In this study, we used the Coastal and Regional Ocean Community model (CROCO) (Shchepetkin and McWilliams, 2005; Debreu et al., 2012), and the Weather Research and Forecasting (WRF) model (Skamarock et al., 2008) to simulate the Gulf Stream dynamics and the overlying atmosphere. Below is a brief description of these models.

### 3.1.1 CROCO

CROCO is a modeling platform for the regional and coastal ocean, addressing realistic or idealized multiscale circulation problems. CROCO was born from different codes developed in France (ROMS\_AGRIF, MARS3D, SNBQ), supported by a consortium between IRD, Inria, Ifremer, CNRS and SHOM, and assembled through a GdR (Groupement de Recherche) since 2016. It is built around the kernel of ROMS (AGRIF version), supported for years by IRD and Inria, with the new addition of a nonhydrostatic solver, and with coupling capabilities for the atmosphere (WRF, MesoNH), surface waves (WKB, WW3), sediment dynamics (USGS, MUSTANG), ocean biogeochemistry and ecosystems (PISCES, BioEBUS). Information on the CROCO model can be found on <https://www.croco-ocean.org/>.

CROCO can be used either as a Boussinesq/hydrostatic (primitive equations) model, or a non-hydrostatic/non-Boussinesq model. In the present study, the model solves the primitive equations in an Earth-centered rotating environment, assuming free-surface, Boussinesq, incompressibility and turbulent closure. The equations are discretized using high-order numerical methods in terrain-following (generalized sigma) vertical coordinates, and horizontal curvilinear coordinates on an Arakawa C grid. The model uses a split-explicit time-stepping algorithm, *i.e.* a short time step is used for surface elevation and barotropic momentum, while a much larger time step is used for temperature, salinity, and baroclinic momentum (Shchepetkin and McWilliams, 2005).

In our simulations, for momentum, we use a 5th-order upstream biased horizontal advection scheme (UP5) or in some sensitivity tests a 3rd-order scheme (UP3). For tracers, we use a 3rd-order horizontal advection scheme with rotated diffusion along isopycnal surfaces (RSUP3) to avoid spurious diapycnal mixing and loss of water mass properties (Marchesiello et al., 2009; Lemarié et al., 2012). For open boundaries, we use an active-passive radiation condition for tracers and baroclinic velocities, and flather conditions for barotropic velocities (Marchesiello et al., 2001).

A large set of numerical schemes and parameterizations are available in CROCO and described on the model's website ([https://croco-ocean.gitlabpages.inria.fr/croco\\_doc/](https://croco-ocean.gitlabpages.inria.fr/croco_doc/)). In the following, we describe the parameterizations used in this thesis for bottom and top drag. More details on the model configurations are also available in the published paper presented in the fourth chapter.

### 3.1.1.1 Current Feedback Parameterization

In the stand-alone oceanic simulations, the current feedback is parameterized using the stress-correction approach described and tested in Renault et al. (2017) and Renault et al. (2020). It allows mimicking the wind response to CFB for a realistic representation of momentum exchange between the ocean and the atmosphere. The wind stress is defined as:

$$\boldsymbol{\tau} = \boldsymbol{\tau}_{NOCFB} + s_\tau \mathbf{U}_o, \quad (3.1)$$

where  $\boldsymbol{\tau}$  is the wind stress that includes the CFB effect,  $\boldsymbol{\tau}_{NOCFB}$  is the wind stress that does not include the CFB effect,  $\mathbf{U}_o$  is the surface ocean current, and  $s_\tau$  is a coupling coefficient between surface current vorticity and wind stress curl defined in Renault et al. (2017),

$$s_\tau = \begin{cases} \alpha |\mathbf{U}_{10\text{abs}}| + \beta, & \text{if } |\mathbf{U}_{10\text{abs}}| \geq 3 \text{ m/s} \\ -0.0007 \text{ N s/m}^3, & \text{otherwise.} \end{cases}$$

where  $\alpha = 2.9 \times 10^{-3} \text{ N s}^2 \text{ m}^{-4}$  and  $\beta = 0.008 \text{ N s m}^{-3}$ ,  $|\mathbf{U}_{10\text{abs}}|$  is the magnitude of the absolute wind at 10 m.  $\alpha$  and  $\beta$  were derived from the linear regression between  $|\mathbf{U}_{10\text{abs}}|$  and  $s_\tau$ .

In the coupled simulation, CFB is accounted for in the atmospheric model by introducing the surface current in both the tridiagonal matrix system solved in the vertical turbulent diffusion scheme and in the surface layer scheme following Lemarié (2015) and Renault et al. (2019a).

### 3.1.1.2 Bottom Drag Parameterization

Bottom drag is computed assuming that the flow in the bottom boundary layer has a classic vertical logarithmic profile, defined by a friction velocity  $u_*$  and a bottom roughness length  $Z_{0b}$  (m):

$$|\mathbf{u}_b| = \sqrt{u_b^2 + v_b^2} = \frac{u_*}{\kappa} \log \frac{z_b}{Z_{0b}}, \quad (3.2)$$

where log is the natural logarithm,  $u_b$  and  $v_b$  are the oceanic near-bottom currents in the log layer at a height  $z_b$  above bed (here corresponding to the first vertical grid level);  $u_* = \sqrt{\tau_b}$  with  $\tau_b$  the bottom stress;  $\kappa = 0.41$  the von Karman constant;  $Z_{0b}$ , the bottom roughness length, is given a default constant value of  $10^{-2}$ . The zonal and meridional components of bottom stress are then calculated as:

$$[\tau_{bx}, \tau_{by}] = C_d |\mathbf{u}_b| [u_b, v_b], \quad (3.3)$$

with the drag coefficient:

$$C_d = \frac{\kappa^2}{\log^2 \frac{z_b}{Z_{0b}}}. \quad (3.4)$$

### 3.1.1.3 Horizontal advection schemes and numerical dissipation

The spectral characteristics of numerical energy dissipation in ocean models has been presented in [Marchesiello et al. \(2011\)](#) and [Soufflet et al. \(2016\)](#). CROCO generally uses numerical methods with diffusion-dominated truncation error to optimally damp dispersion (phase) errors (without the need for explicit dissipation). The magnitude and extent of dissipation depend on the accuracy of the scheme, which is generally related to the order at which the error decreases with mesh size. The advection terms in the primitive equations are particularly important. CROCO proposes 3rd and 5th-order upstream-biased horizontal advection schemes (UP3 and UP5, respectively). The horizontal advection calculated by UP3 and UP5 (denoted by  $A_{UP3}$  and  $A_{UP5}$ ) can be written as the sum of a purely advective term and a purely diffusive term:

$$A_{UP3} = A_{C4} + D_{UP3}, \quad (3.5)$$

$$A_{UP5} = A_{C6} + D_{UP5}, \quad (3.6)$$

where  $A_{C4}$  and  $A_{C6}$  represent horizontal advection calculated from non-diffusive centered 4th- and 6th-order schemes, respectively, and  $D_{UP3}$  and  $D_{UP5}$  are the hyperdiffusive terms with velocity-dependent hyperviscosity. For more details, see Numeric Section in CROCO tutorial ([https://croco-ocean.gitlabpages.inria.fr/croco\\_doc/model/model.numerics.advec.html](https://croco-ocean.gitlabpages.inria.fr/croco_doc/model/model.numerics.advec.html))

Centered advection schemes are non-diffusive, but the dispersion of poorly resolved Fourier components are allowed to propagate throughout the solution without amplitude loss ([Durrant, 2010](#)), and with nonlinear growth that can be very detrimental to the solution. Upstream advection schemes provide a more accurate solution overall, even though diffusion can be in excess in a range of scales that defines the effective resolution of the model ([Soufflet et al., 2016](#)). This range is controlled by the order of hyper-diffusion and hyperviscosity is given by the truncation error derived from a Taylor expansion as a function of  $\Delta x$ , the mesh size ([Durrant, 2010](#); [Soufflet et al., 2016](#)). For the one-dimensional case in the  $x$  direction, the UP3 truncation error is :

$$\frac{|u|\Delta x^3}{12} \frac{\partial^4 u}{\partial x^4}, \quad (3.7)$$

and for UP5

$$\frac{|u|\Delta x^5}{60} \frac{\partial^6 u}{\partial x^6}, \quad (3.8)$$

where the hyperdiffusion operators are of order 4 and 6 for UP3 and UP5, respectively, with hyperviscosity  $|u|\Delta x^3/12$  and  $|u|\Delta x^5/60$ . Equations 3.7 and 3.8 indicate that increasing the order of the scheme results in a faster decrease in numerical diffusion with resolution. Higher-order schemes entail higher computational costs, but a significant gain in terms of effective resolution. For example, UP5 is 6% more expensive than UP3 in CROCO, but can double

the effective resolution, as in the case presented by [Menesguen et al. \(2018\)](#).

Effective resolution can be defined by the highest wavenumber at which simulated waves do not differ from an ideal solution (e.g., theoretical KE spectral slopes) or by the spectral range of the main energy dissipation term ([Marchesiello et al., 2011](#)). It can also be deduced from the theoretical amplitude error spectrum of an advection scheme ([Soufflet et al., 2016](#)). The effective resolution in CROCO is approximately  $10\delta x$  when using UP3 ([Soufflet et al., 2016](#)) and as low as  $5\delta x$  with UP5 ([Menesguen et al., 2018](#)). In this study, the simulations analyzed in Chapters 4, 5, and 6 use UP5 as the default scheme.

### 3.1.2 WRF-ARW

WRF is a state-of-the-art atmospheric modeling system with application in a broad range of scales ranging from tens of meters to thousands of kilometers. We used the Advanced Research WRF (WRF-ARW) version, and more precisely the version 4.2.1 modified to be coupled with CROCO (available at <https://github.com/wrf-croco/WRF>).

As described on the official WRF web site (<https://www2.mmm.ucar.edu/wrf/users/>), the model resolves the fully compressible, eulerian and nonhydrostatic equations with a runtime hydrostatic option. It is conservative for scalar variables. The model uses terrain-following, hybrid sigma-pressure vertical coordinate, with the top of the model being a constant pressure surface. The horizontal grid is the Arakawa-C grid. The time integration scheme in the model uses the third-order Runge-Kutta scheme, and the spatial discretization employs 5th-order upstream schemes (as CROCO). The model supports both idealized and real-data applications with various lateral boundary condition options.

WRF-ARW integrates several physics schemes with different options. The physics schemes interact during model simulations to emulate physical processes in the Earth's atmosphere (Figure 3.1).

As described on the official WRF website, the physics scheme included are:

1. Microphysics: resolve cloud and precipitation processes. Some schemes account for ice and/or mixed-phases processes.
2. Cumulus and shallow convection: represent the subgrid-scale effects of convective and/or shallow clouds. Implementation of this scheme is necessary for horizontal resolution coarser than 10 km. For spatial resolutions finer than 3 km, it is not strictly necessary. The spatial resolution between 3 km and 10 km are in a grey-zone, cumulus parameterization may or may not be necessary.
3. Planetary boundary layer (PBL): distribute surface fluxes with boundary layer eddy fluxes, and allow for PBL growth by entrainment. They are also responsible for any vertical mixing above the boundary layer.

4. Surface Layer: determine surface layer diagnostics, which includes exchange and transfer coefficients for heat and moisture to Land Surface. Also provide friction stress and water-surface fluxes of heat and moisture to the PBL.
5. Land Surface: predict soil temperature and soil moisture in 3 or 4 layers, depending on the scheme, as well as snow water equivalent on the ground.
6. Longwave radiation: estimate the longwave radiation emitted and absorbed by the surface and clouds, and gases such as water vapor and CO<sub>2</sub>.
7. Shortwave radiation: estimated incoming solar fluxes that may be reflected by the surface or clouds, or absorbed by gases, such as water vapor and ozone, and aerosols

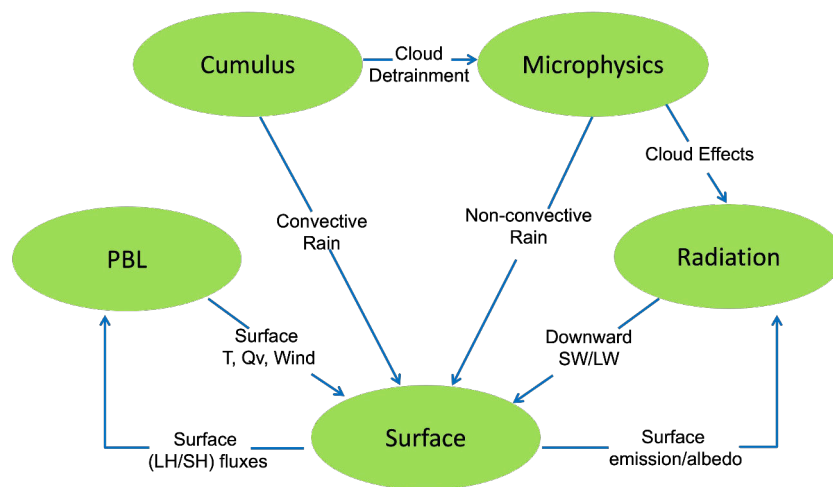


Figure 3.1: Representation of the physics schemes included in WRF. Reprinted from [https://www2.mmm.ucar.edu/wrf/users/wrf\\_users\\_guide/build/html/physics.html](https://www2.mmm.ucar.edu/wrf/users/wrf_users_guide/build/html/physics.html).

### 3.1.3 Models Configuration

We performed three submesoscale permitting forced oceanic simulations ( $\sim 2$  km) with CROCO over the GS region (Figure 3.2). These simulations have a similar configuration, but differ in the following: (i) the first simulation (NTD-UP5) has no tides and the horizontal momentum advection is fifth-order upstream (UP5); (ii) the second simulation (NTD-UP3) is similar but with UP3 momentum advection; (iii) the third simulation is tidally forced and uses the UP5 momentum advection scheme (TD-UP5). The first and second simulations are analyzed in Chapter 4 and the third simulation is analyzed in Chapter 5.

We also implemented and ran a coupled ocean-atmosphere simulation that is used in Chapter 6. The oceanic CROCO simulation is run with a horizontal resolution of 700 m. The initial state and lateral boundary forcing are derived from the submesoscale-permitting (2 km) TD-UP5 simulation (including tides). The atmospheric WRF simulation is run with a horizontal resolution of 2 km. The initial state and lateral boundary forcing are derived

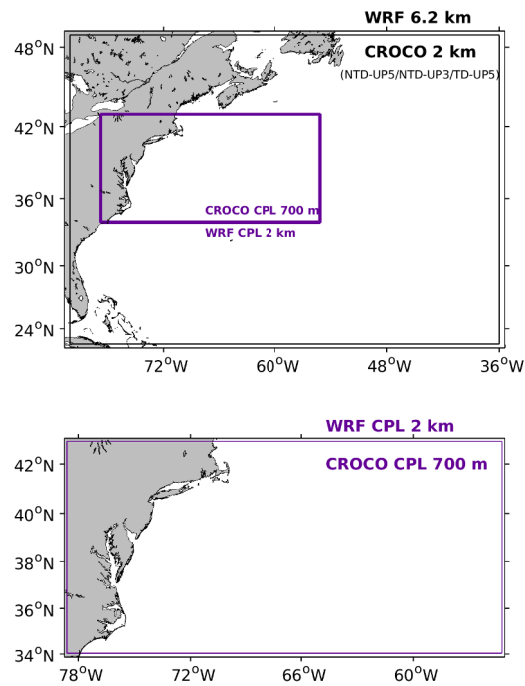


Figure 3.2: (Top) Domain of the 6 km atmospheric simulation. The black line indicates the area covered by the 2 km oceanic simulation. The purple lines indicate the domains of high-resolution simulations for both the atmosphere (2 km) and the ocean (700 m). (Bottom) The domain for the 2 km atmospheric simulation is depicted, with the purple line indicating the domain for the 700 m oceanic simulation.

from a coarser resolution (6.2 km) WRF simulation, which we previously ran. The models are coupled through the OASIS3-MCTV3 coupler (Craig et al., 2017), which exchanges hourly-averaged surface flux information between CROCO and WRF. A brief description of the configuration of these simulations is given in Figure 3.3. The details of the configuration and validations are described in each chapter where the simulation is analyzed.

## 3.2 Post-processing

### 3.2.1 Coarse-graining method

To understand the oceanic kinetic energy pathways between large-scale and small-scale flow, spectral analysis has generally been used (*e.g.*, Scott and Wang 2005; Capet et al. 2008d; Marchesiello et al. 2011; Renault et al. 2019b) and confirmed the presence of direct or inverse energy cascades. However, this approach assumes a statistically homogeneous field (Schubert et al., 2020), and does not give access to the spatial distribution of cross-scale energy fluxes.

The coarse-graining method (Leonard, 1975; Germano, 1992) is an alternative to evaluate cross-scale KE fluxes in the ocean. This method was introduced by Leonard (1975) in the context of the study of turbulence using a large-eddy simulation (LES) model, and then developed mathematically by Eyink (1995a,b, 2005). Applications in computational fluid dynamics followed (*e.g.*, Piomelli et al., 1991; Vreman et al., 1994; Aluie and Eyink, 2009; Chen et al., 2006; Kelley and Ouellette, 2011) but its application to the ocean circulation is relatively new. Aluie et al. (2018) is the first to apply coarse-graining to ocean dynamics, followed by Schubert et al. (2020) and Srinivasan et al. (2019), to specifically address the interior route to dissipation. The coarse-graining approach has several advantages over spectral analysis, including relaxing the homogeneous and isotropic field assumption, avoiding windowing procedures, and, most importantly, having access to spatial patterns of energy fluxes.

#### 3.2.1.1 Decomposition

The coarse-graining approach is based on a “filtering” framework, which separates the signal into large and small scales around a given scale  $l$ . Following Aluie et al. (2018) and Schubert et al. (2020), a low-pass spatial filter is defined using the convolution of a horizontal field  $\overline{F(x, y)}$  as  $\overline{F(x, y)} = C * F(x, y)$  where  $C$  is a top-hat kernel defined as

$$C(r) = \begin{cases} 1/A, & \text{if } |r| < l/2, \\ 0, & \text{otherwise} \end{cases}$$

where  $A = \pi l^2/4$  is the circular normalization area of diameter  $l$  and  $r$  is the radial vector. Note that  $C$  is normalized so that  $\int d^2r C(r) = 1$ . Other filters can be applied, but they must

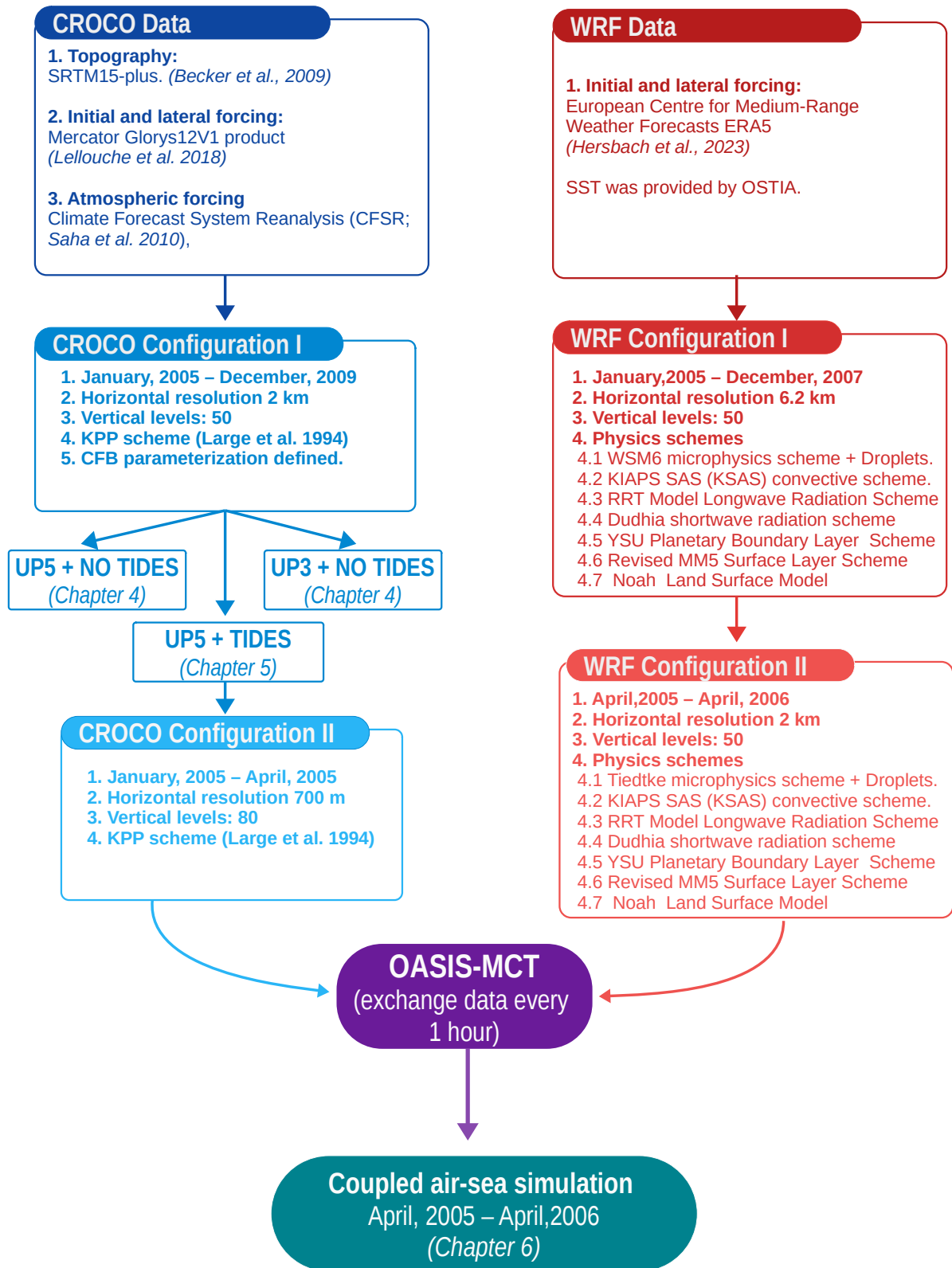


Figure 3.3: Summary of the oceanic and atmospheric simulations used throughout the thesis.

satisfy  $\nabla \cdot \bar{\mathbf{u}} = \overline{\nabla \cdot \mathbf{u}}$ , to ensure that the filtered flow remains incompressible. It is crucial for the decomposition to maintain the essential physical attributes of the flow, including its incompressibility, geostrophic character, and vorticity at various scales.

### 3.2.1.2 Derivation

A momentum equation for scales large than  $l$  is derived by applying the convolution to the primitive equations:

$$\frac{\partial \bar{\mathbf{u}}}{\partial t} + \bar{\mathbf{u}} \cdot \nabla \bar{\mathbf{u}} = -\frac{1}{\rho_o} \nabla \bar{p} - f \times \bar{\mathbf{u}} - \nabla \cdot \bar{\tau}_l(\mathbf{u}, \mathbf{u}) + \nu \nabla^2 \bar{\mathbf{u}} + \frac{\bar{\rho}}{\rho_0} g + \bar{F}, \quad (3.9)$$

where  $\mathbf{u} = (u, v, w)$  are the zonal, meridional, and vertical oceanic components of the surface current,  $p$  the pressure,  $f$  the Coriolis frequency,  $\nu$  the viscosity,  $\rho_0$  the reference density, and  $F$  the forcing. Note that Eq. 3.9 is similar to classical PE, but with the additional term  $\nabla \cdot \bar{\tau}_l(\mathbf{u}, \mathbf{u})$ , where

$$\bar{\tau}_l = \overline{\mathbf{u}\mathbf{u}} - \bar{\mathbf{u}} \bar{\mathbf{u}}, \quad (3.10)$$

is the subgrid-scale (SGS) stress tensor (as in LES literature) that represents the dynamical coupling between large and small scales (around  $l$ ).

From Eq. 3.9, we can derive the kinetic energy equation for motions larger than  $l$ :

$$\frac{\rho_0}{2} \frac{\partial |\bar{\mathbf{u}}|^2}{\partial t} + \nabla \cdot \mathbf{J} = -\Pi - \rho_0 \nu |\nabla \bar{\mathbf{u}}|^2 + \bar{\rho} g \cdot \bar{\mathbf{u}} + \rho_0 \bar{F} \cdot \bar{\mathbf{u}}, \quad (3.11)$$

where

$$J = \rho_0 \frac{\partial |\bar{\mathbf{u}}|^2}{2} \bar{\mathbf{u}} + \bar{p} \bar{\mathbf{u}} - \rho_0 \nu \nabla \frac{|\bar{\mathbf{u}}|^2}{2} + \rho_0 \bar{\mathbf{u}} \cdot \bar{\tau}_l(\mathbf{u}, \mathbf{u}), \quad (3.12)$$

$J$  represents the spatial transport of large-scale KE by the sum of advection (first term), pressure work (second term), diffusion due to molecular viscosity (third term), and transport by SGS stress (fourth term). The second term to the right hand side of Eq. 3.11 is the dissipation of kinetic energy by molecular viscosity, the third term is the conversion of gravitational potential into kinetic energy, the last is the contribution to kinetic energy by forcing. The first term represents the cross-scale kinetic energy flux and is defined as follows :

$$\Pi = -\rho_0 [(\overline{u^2} - \bar{u}^2) \bar{u}_x + (\overline{uv} - \bar{u} \bar{v})(\bar{u}_y + \bar{v}_x) + (\overline{v^2} - \bar{v}^2) \bar{v}_y], \quad (3.13)$$

This term quantifies the energy transferred across scale  $l$  to larger or smaller scales, due to nonlinear interactions.

### 3.2.1.3 Comparison with other methods

Aluie et al. (2018) compare the estimation of cross-scale KE flux with other methods that assume homogeneous flows and are derivatives of the momentum equation, such as the method proposed by Frisch (1995) or that used by Molemaker and McWilliams (2010). They find that the latter methods give ambiguous results for inhomogeneous flows. Aluie et al. (2018) explain that the difference in performance between the methods is due to the infinite number of ways to rearrange the terms associated with  $\nabla \cdot J$  and  $\Pi$  in the budget 3.11, and thus an infinite number of possible definitions for the transfer of kinetic energy across scales. Furthermore, the authors explain that the definition 3.13 is an appropriate measure of the cross-scale kinetic energy flux, since it is Galilean invariant <sup>1</sup>, which is not true for the other methods. Eyink and Aluie (2009) and Aluie and Eyink (2009) show that Galilean invariance is necessary for the so-called scale locality of the cascade <sup>2</sup>.

In addition to the mathematical aspects of the kinetic energy balance, we also note problems associated with the windowing procedure in the spectral method. Windowing can induce an underestimation of cross-scale KE fluxes. In addition, Aluie et al. (2018) indicate that it can introduce artificial gradients, length scales, spurious acceleration, and flow features not present in the original data, although in some circumstances these effects may be negligible. (Schubert et al., 2020) compared spectral and cross-graining methods to compute cross-scale fluxes in the Agulhas current system and found consistency in the results.

One of the caveats of the coarse-graining method is the treatment of the coastline, where the application of the filter can have an effect on boundary currents. Schubert et al. (2020) and Aluie et al. (2018) recommend representing the land as zero flows.

---

<sup>1</sup>It is the requirement that a determination of the amount of energy cascading at any given point  $x$  should not depend on the velocity of the observer.

<sup>2</sup>Only modes near a given scale contribute to transfer across that scale (Eyink, 2005).



# Understanding energy pathways in the Gulf Stream.

---

## Contents

---

4.1	Preamble . . . . .	62
4.2	AMS Copyright Notice . . . . .	63
4.3	Article . . . . .	63
4.4	Conclusion . . . . .	82

---

## 4.1 Preamble

As mentioned in the introduction, there are still large gaps in our knowledge of ocean dynamics. Despite being controlled by coastline curvature and topographic slope, the emblematic features of the GS in ocean models are also tied to the resolution of mesoscale activity through eddy-mean-flow interaction (McWilliams, 2008). A spatial resolution of  $1/10^\circ$  is suggested as a minimum for the correct representation of GS separation (Bryan et al., 2007; Chassignet and Marshall, 2008), although higher resolutions are generally required, depending on the type of model (Chassignet and Xu, 2017; Uchida et al., 2022). Increasing the spatial resolution of the models has greatly improved the representation of the GS, but the simulated eddy energy in WBCs has become excessive. In particular, according to Özgökmen and Chassignet (2002), an excess of mesoscale activity at the separation point leads to unrealistic separation of the western boundary currents from the coastline. Therefore, an energy sink is needed in high resolution mesoscale resolving models. A direct energy transfer to dissipation is possible due to the loss of balance at the submesoscale. Top and bottom boundary dissipation can also provide an important energy sink. The goal of this chapter is therefore to understand the main processes and mechanisms that drive the forward cascade of energy, *aka*, the interior dissipation of energy, and to quantify it in comparison with other sinks of energy such as those of bottom drag, top drag (due to current feedback to the atmospheric momentum forcing), and numerical dissipation.

In this work, published in Journal of Physical Oceanography (Contreras et al. (2023b); <https://doi.org/10.1175/JPO-D-22-0146.1>), we developed and ran a submesoscale forced oceanic simulation for a period of 5 years. This simulation is then used to calculate the cross-scale KE flux using the coarse-graining method (described in Chapter 3) that provides spatial and temporal distributions. We also evaluate the mechanisms involved in the energy cascade. For this purpose, we used a Helmholtz decomposition method to decompose the surface flows into balanced (rotational) and unbalanced (divergent) flows, and calculated their cross-scale KE flux. We also documented the seasonal changes of the energy cascade.

To determine the importance of the forward cascade in the energy budget of the GS (which is never explicitly done in the literature), we compare the interior dissipation - the dissipation generated by the forward cascade - by vertically integrating the cross-scale KE flux at the scale where the forward cascade is dominant in the region (and at a wavelength close to the effective resolution of the simulation). The interior dissipation is then compared with both numerical and boundary dissipation processes (top drag and bottom drag). Finally, to assess the sensitivity of numerical dissipation to the choice of horizontal momentum advection schemes, we compared a set of two simulations that differ only in their advection scheme, namely a 3rd- and 5th-order discretization.

## 4.2 AMS Copyright Notice

©Copyright American Meteorological Society (AMS). For permission to reuse any portion of this Work, please contact [permissions@ametsoc.org](mailto:permissions@ametsoc.org). Any use of material in this Work that is determined to be “fair use” under Section 107 of the U.S. Copyright Act (17 U.S. Code § 107) or that satisfies the conditions specified in Section 108 of the U.S. Copyright Act (17 USC § 108) does not require the AMS’s permission. Republication, systematic reproduction, posting in electronic form, such as on a website or in a searchable database, or other uses of this material, except as exempted by the above statement, requires written permission or a license from the AMS. All AMS journals and monograph publications are registered with the Copyright Clearance Center (<https://www.copyright.com>). Additional details are provided in the AMS Copyright Policy statement, available on the AMS website (<https://www.ametsoc.org/PUBSCopyrightPolicy>).

## 4.3 Article

©American Meteorological Society. Used with permission

## Understanding Energy Pathways in the Gulf Stream

MARCELA CONTRERAS<sup>1</sup>,<sup>a</sup> LIONEL RENAULT,<sup>a</sup> AND PATRICK MARCHESIELLO<sup>a</sup>

<sup>a</sup> LEGOS, Université de Toulouse, CNES-CNRS-IRD-UPS, Toulouse, France

(Manuscript received 13 July 2022, in final form 7 November 2022)

**ABSTRACT:** The Gulf Stream (GS) is one of the strongest ocean currents on the planet. Eddy-rich resolution models are needed to properly represent the dynamics of the GS; however, kinetic energy (KE) can be in excess in these models if not dissipated efficiently. The question of how and how much energy is dissipated and in particular how it flows through ocean scales thus remains an important and largely unanswered question. Using a high-resolution (~2 km) ocean model [Coastal and Regional Ocean Community (CROCO)], we characterize the spatial and temporal distribution of turbulent cascades in the GS based on a coarse-grained method. We show that the balanced flow is associated with an inverse cascade while the forward cascade is explained by ageostrophic advection associated with frontogenesis. Downscale fluxes are dominant at scales smaller than about 20 km near the surface and most intense at the GS North Wall. There is also strong seasonal variability in KE flux, with the forward cascade intensifying in winter and the inverse cascade later in spring. The forward cascade, which represents an interior route to dissipation, is compared with both numerical and boundary dissipation processes. The contribution of interior dissipation is an order of magnitude smaller than that of the other energy sinks. We thus evaluate the sensitivity of horizontal momentum advection schemes on energy dissipation and show that the decrease in numerical dissipation in a high-order scheme leads to an increase in dissipation at the boundaries, not in the downscale flux.

**KEYWORDS:** Nonlinear dynamics; Small-scale processes; Ocean models

### 1. Introduction

The Gulf Stream is a strong, deep, and persistent western boundary current. It is characterized by a separation near Cape Hatteras and penetration into the North Atlantic basin, where it acts as the main conduit for the upper branch of the meridional overturning circulation. According to Sverdrup's linear theory, the volume transport of western boundary currents should vary with the intensity of the basinwide wind curvature. However, many observations and high-resolution simulations contradict this simple picture, suggesting a more complex one with a large influence of topography and eddies (Spall 1996; Chassignet and Marshall 2008; Özgökmen and Chassignet 2002; Bryan et al. 1995, 2007; Couvelard et al. 2008; Gula et al. 2015, 2016; Renault et al. 2016b, 2019; Debreu et al. 2022). The limitations of low-resolution (>100 km) ocean models in reproducing Gulf Stream dynamics have been clearly demonstrated and significant biases have been observed near the separation of the Gulf Stream as well as in its northward penetration (Chassignet and Xu 2017; Bryan et al. 2007). On the other hand, if the refinement of the computational grid to reach an eddy-rich resolution largely improves the Gulf Stream representation and in particular its separation, a truly realistic representation seems only possible with adequate energy sinks.

At large scale, balanced motions dominate the ocean. Mesoscale eddies, generated by baroclinic and barotropic instabilities of the mean Gulf Stream (drawing energy from its potential energy), are also dominated by geostrophic balance. The quasigeostrophic theory then predicts that their kinetic

energy is essentially transferred to larger scales (i.e., an inverse cascade; Charney 1971; Arbic et al. 2013; Renault et al. 2019). To maintain the energy balance, the energy input in the Gulf Stream system must be dissipated. Some of the energy is dissipated at the surface (Renault et al. 2016b, 2019) and bottom boundaries (top and bottom drag, respectively), but another, more uncertain, portion may follow an interior route to dissipation when the momentum balance is broken—i.e., a direct transfer to smaller scales or forward cascade. For the models to produce a forward cascade, quasi-geostrophy must be relaxed (Molemaker et al. 2010), which is most likely to occur in the detached Gulf Stream jet (Jamet et al. 2021), allowing ageostrophic motions to reverse the spectral energy fluxes (e.g., Brüggemann and Eden 2015; Klein et al. 2008; Capet et al. 2008a; Molemaker et al. 2010). However, the persistence (in space and time) and effectiveness of this dissipation route is unclear.

Submesoscale oceanic fronts and eddies are mostly unbalanced motions and carry a substantial ageostrophic component. They are a relatively recent discovery, and their interest as a research topic has grown rapidly (McWilliams 2016). They occur on an intermediate scale of the order of 0.1–10 km horizontally, 10–100 m vertically, and from hours to days temporally, that is, smaller and more rapidly evolving than the mesoscale eddies and with vertical velocities that are one or two orders of magnitude larger (Capet et al. 2008b; Su et al. 2020; Siegelman 2020; McWilliams 2021). These can affect momentum, buoyancy, nutrient transport and biogeochemistry (Lévy et al. 2018; Uchida et al. 2019; Kessouri et al. 2020), and gas exchange between the ocean and atmosphere (Su et al. 2018). Important here, they may also provide an oceanic interior energy route to dissipation (Gula et al. 2016; Schubert et al. 2020), which may partially justify the use of a high turbulent viscosity to control Gulf Stream dynamics in eddy-rich models

Corresponding author: Marcela Contreras, marcela.contreras@legos.obs-mip.fr

(Chassignet et al. 2003; Chassignet and Marshall 2008; Chassignet and Xu 2017; Schoonover et al. 2016). The principle invoked is that, at submesoscales, the effect of rotation and stratification being weaker, the geostrophic or gradient-wind balance is disrupted, allowing the divergent flow component to transfer energy to smaller scales (Capet et al. 2008b; Klein et al. 2008). The proposed ageostrophic mechanisms are inertia-gravity wave emission by eddies (Barkan et al. 2015); frontogenesis (Capet et al. 2008c); submesoscale quasigeostrophic instabilities at finite Rossby number (Capet et al. 2016); and at even smaller scales, ageostrophic instabilities such as centrifugal, symmetric, gravitational, or Kelvin–Helmholtz instabilities (McWilliams 2016; Thomas et al. 2013; Haine and Marshall 1998).

However, submesoscale processes can also reinforce mesoscale eddies, extending the inverse kinetic energy (KE) cascade to a scale of a few tens of kilometers (Klein et al. 2019). This extension is particularly evidenced for frontogenesis (Klein et al. 2019) and for submesoscale quasigeostrophic instabilities that draw energy from the mesoscale potential energy at spatial scales of  $O(10)$  km and time scales of  $O(1)$  day<sup>-1</sup>, for example, mixed layer instabilities (MLIs; Schubert et al. 2020; Boccaletti et al. 2007) and Charney baroclinic instabilities (Capet et al. 2016). The broadening of the inverse cascade suggests that the KE of the ocean is less controlled by viscosity than one might think by considering only the effect of submesoscale processes on the forward cascade. In any case, the overall effect of submesoscales on the oceanic turbulent cascade is complex and may vary in space and time.

This study presents a submesoscale simulation at 2-km resolution, where strain-induced frontogenesis and mixed layer instabilities are resolved, but ageostrophic instabilities and associated secondary frontogenesis are not. The simulation is carried out over the Gulf Stream for a period of 5 years with three objectives. First, we assess the temporal and spatial distribution of cross-scale KE fluxes in the Gulf Stream. The evaluation is enabled by the use of a coarse-grained approach (Aluie et al. 2018). Second, we explore the submesoscale mechanisms and the contributions of rotational and divergent velocity components (associated with the balanced and unbalanced motions, respectively), in particular the extent to which they affect energy fluxes over the Gulf Stream. Last, we quantitatively evaluate the different energy dissipation processes. We compare the magnitude of the forward cascade with the dissipation by the top and bottom drag and by numerical discretization effects. Next, we analyze the sensitivity of horizontal momentum advection schemes on energy dissipation. The paper is organized as follows: section 2 describes the model configuration and method. In section 3, the spatial and season variability of cross-scale KE fluxes is assessed. Section 4 examines the possible mechanisms involved in the energy transfer. The quantification of energy pathways is discussed in section 5, followed by the conclusions.

## 2. Method

### a. Model configuration

The oceanic simulation is performed with the Coastal and Regional Ocean Community model (CROCO; Shchepetkin

and McWilliams 2005; Debreu et al. 2012). CROCO is a free-surface, terrain-following coordinate model with split-explicit time stepping. In the present study, the version with Boussinesq and hydrostatic approximations is used, and the equations are discretized with high-order computational methods. A third-order predictor–corrector time step algorithm, and fifth-order upstream biased momentum advection (instead of the more standard third-order scheme) allows reducing numerical dispersion and diffusion to achieve an effective resolution of about 5 times the horizontal resolution (Soufflet et al. 2016; Ménesguen et al. 2018). The advection of horizontal tracers is discretized using the rotated split third-order upstream scheme (Marchesiello et al. 2009; Lemarié et al. 2012). A nonlocal planetary  $K$ -profile boundary layer (KPP) scheme (Large et al. 1994) parameterizes the vertical subgrid-scale eddy effects at the surface, bottom, and interior of the ocean.

The simulation domain extends from 22.5° to 48.84°N and from 36° to 82°W (Fig. 1) with a horizontal resolution of 1/42° (~2.2 km). The topography is obtained from SRTM15-plus (Shuttle Radar Topography Mission), which is a global bathymetric dataset with a nominal resolution of 15 arc s (~0.5 km) ([http://topex.ucsd.edu/WWW\\_html/srtm30\\_plus.html](http://topex.ucsd.edu/WWW_html/srtm30_plus.html)). To reduce errors associated with the pressure gradient in a terrain-following coordinate model—in addition to the high-order correction scheme of Shchepetkin and McWilliams (2003)—the bottom topography is interpolated onto the model grid and its slope is selectively smoothed when the  $r$ -factor  $\delta h/h$  exceeds 0.2, where  $h$  is the bottom depth and  $\delta h$  is its horizontal variation between two grid points (Penven et al. 2005).

The simulation is performed over the period 2005–09 after a 5-yr spinup. The initial field and lateral boundary forcing are derived from the 1/12° daily mean Mercator Glorys12V1 product (Lellouche et al. 2018). The boundary forcing is introduced through open boundary conditions that consist of an active–passive 2D radiation scheme for the baroclinic mode (including temperature  $T$  and salinity  $S$ ) and a modified Flather-type scheme for the barotropic mode (Marchesiello et al. 2001). We use 50  $\sigma$  levels in the vertical direction (Shchepetkin and McWilliams 2009), with stretching parameters  $h_{\text{cline}} = 200$  m,  $\theta_b = 2$ , and  $\theta_s = 7$ .

Surface momentum, heat, and freshwater fluxes are estimated using the COARE bulk formula (Fairall et al. 2003). Surface atmospheric fields are derived from the hourly Climate Forecast System Reanalysis (CFSR; Saha et al. 2010), which has a spatial resolution of ~35 km. The surface ocean current feedback to the atmosphere (that controls the top drag) (Renault et al. 2016b) is parameterized using the stress-correction approach described in Renault et al. (2020), allowing realistic representation of the (sub)mesoscale momentum exchange between the ocean and the atmosphere. In our analysis, 3-h averaged output fields are used.

The simulation is generally in good agreement with the observations. As an example, Fig. 2 compares the simulated mean and mesoscale circulations with those observed by the AVISO product (Ducet et al. 2000) and drifters (Laurindo et al. 2017). To ensure a fair model–data comparison when comparing with AVISO, we first apply a 50-km Gaussian spatial filter and a 7-day average on the simulated Absolute

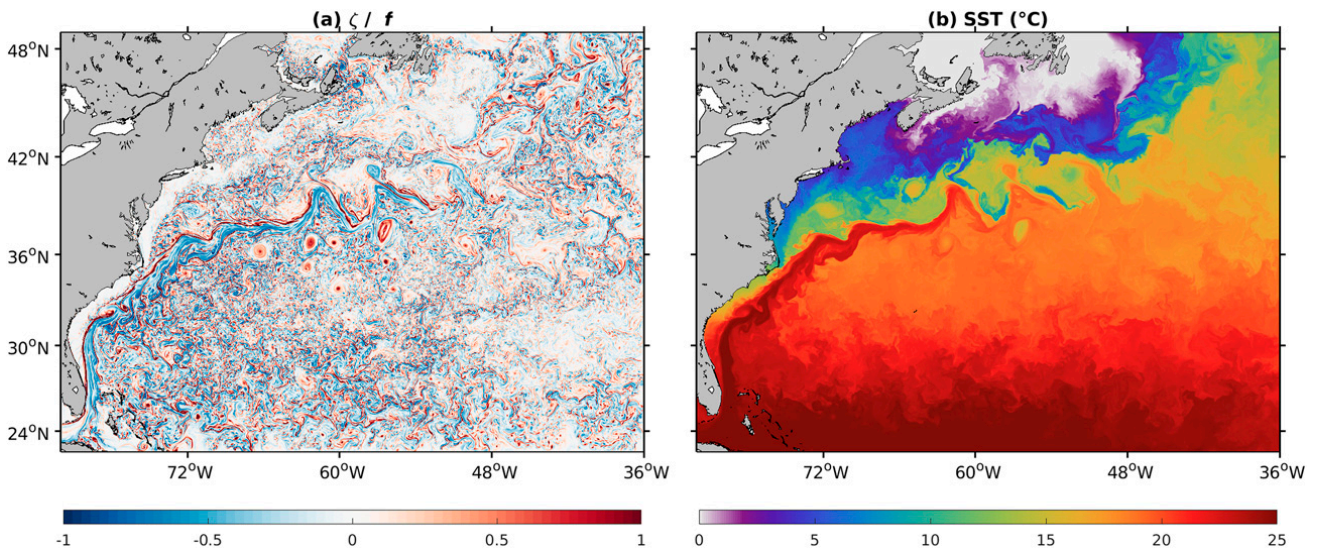


FIG. 1. Snapshots of (a) surface relative vorticity (normalized by  $f$ ) and (b) sea surface temperature in March 2007 from CROCO.

Dynamic Topography (ADT; [Arbic et al. 2013](#)). [Figures 2a](#) and [2b](#) show the mean ADT as estimated from CROCO and AVISO as well as the mean Gulf Stream path highlighted using the contour of  $0.5 \text{ m s}^{-1}$  of the mean geostrophic currents. The mean circulation is well reproduced by the model and in particular the Gulf Stream path shows very good agreement with the observations.

The surface geostrophic eddy kinetic energy [ $\text{EKE}(u_g)$ ] is computed as a proxy of the mesoscale activity from daily geostrophic surface current perturbations in CROCO and AVISO ([Figs. 2b,c](#)). The perturbations are estimated as the deviation of the 3-month average. The Gulf Stream path stability is associated with the EKE: the larger the EKE, the more unstable the Gulf Stream trajectory. In agreement

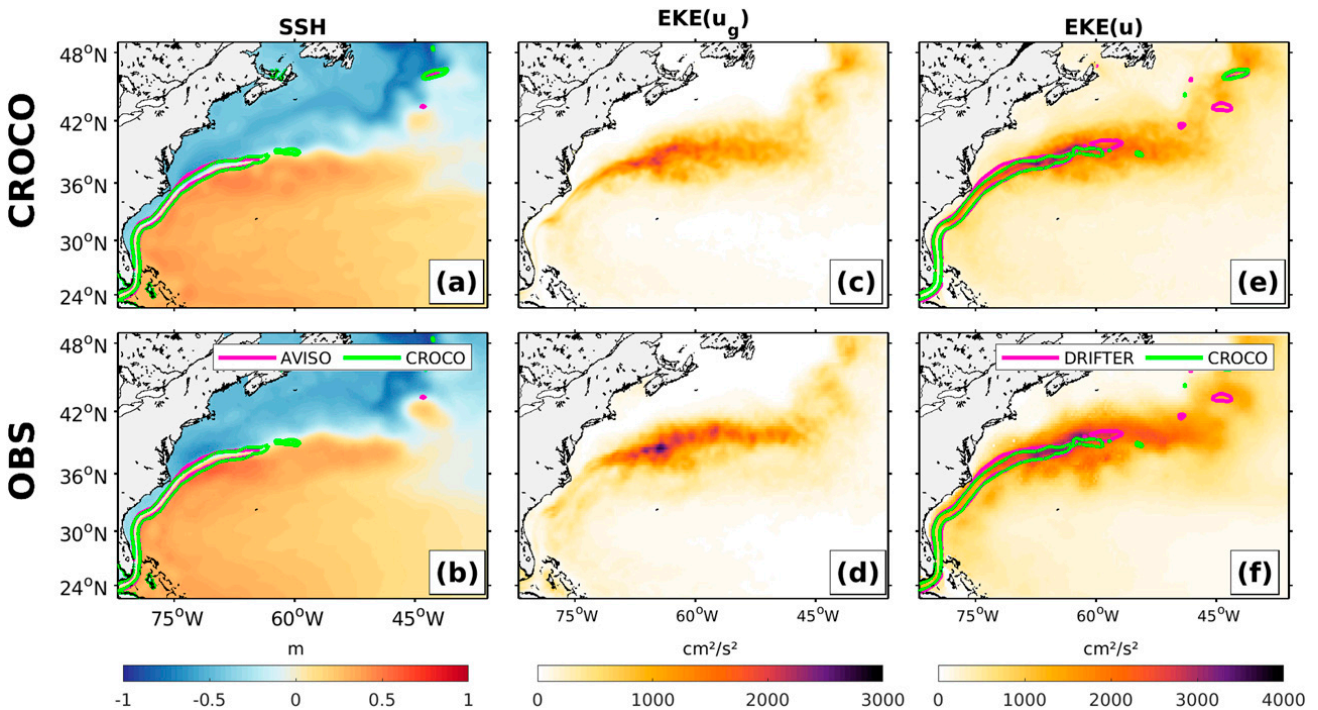


FIG. 2. (a),(b) Mean dynamic topography and (c),(d) EKE estimated using geostrophic currents from (top) CROCO and (bottom) AVISO. The magenta and green contours represent the mean Gulf Stream path ( $0.5 \text{ m s}^{-1}$  contour of the mean geostrophic current) from AVISO and CROCO, respectively. Also shown is the time average of EKE estimated using the surface total currents from (e) CROCO and (f) drifter data. The magenta and green contours again represent the mean Gulf Stream path but from the mean total currents ( $0.5 \text{ m s}^{-1}$  contour) from drifters and CROCO, respectively.

with previous studies, CROCO and observations show a stable trajectory separating straight from Cape Hatteras, with a larger EKE magnitude over the Gulf Stream core after separation. The simulated  $EKE(u_g)$  shows very close spatial patterns and amplitudes to those observed by AVISO (Figs. 2c,d). Similar results are found when comparing the model EKE [ $EKE(u)$ ] estimated from the total surface currents with drifter observations from the Global Drifter Program (Laurindo et al. 2017) (Figs. 2e,f)—note that the drifters are also included in the AVISO estimate of the mean dynamic topography.

### b. Coarse-grained method

In the literature, the cross-scale KE flux in the ocean is generally evaluated using a spectral analysis (e.g., Scott and Wang 2005; Arbic et al. 2013; Marchesiello et al. 2011; Renault et al. 2019). Based on this approach, several studies demonstrate the existence of direct or inverse energy cascades. However, it has several drawbacks. First, it assumes a statistically homogeneous field and a value for the small-scale flux (Schubert et al. 2020). Second, the spectral approach underestimates the energy flux due to the windowing required, and the result is very sensitive to the resolved scales of the model or altimeter data and the filtering methods used on these data (Arbic et al. 2013).

The coarse-grained method (Leonard 1975; Germano 1992) is an interesting alternative to assess the cross-scale KE fluxes in the ocean. Aluie et al. (2018) are the first to apply this method to ocean dynamics, followed by Schubert et al. (2020) and Srinivasan et al. (2019) to specifically address the interior route to dissipation. The coarse-grained approach has several advantages over spectral analysis, including relaxing the homogeneous and isotropic field assumption, avoiding windowing procedures, and, most importantly, having access to spatial patterns of energy fluxes.

The coarse-grained approach is based on a “filtering” framework, which separates the signal into large and small scales around a given scale  $L$ . Following Aluie et al. (2018) and Schubert et al. (2020), a low-pass spatial filter is defined using the convolution of a horizontal field  $F(x, y)$  as  $F(x, y) = C \times F(x, y)$ , where  $C$  is a top-hat kernel defined as

$$C(r) = \begin{cases} 1/A & \text{if } |r| < L/2 \\ 0 & \text{otherwise} \end{cases},$$

$A = \pi L^2/4$  is the circular normalization area of diameter  $L$ , and  $r$  is the radial vector.

By applying this convolution to the equation of motion, we can estimate the term that represents the scale transfer of kinetic energy:

$$\Pi = -\rho_0[(\bar{u}^2 - \bar{u}^2)\bar{u}_x + (\bar{u}\bar{v} - \bar{u}\bar{v})(\bar{u}_y + \bar{v}_x) + (\bar{v}^2 - \bar{v}^2)\bar{v}_y], \quad (1)$$

where  $\rho_0$  is the reference density and  $\mathbf{u} = (u, v, w)$  are the oceanic components of the surface current in the zonal, meridional, and vertical direction [see Aluie et al. (2018) for the full derivation]. This term quantifies the energy transferred from

the  $L$  scale to larger or smaller scales (i.e., a cross-scale flux at  $L$ ), due to nonlinear interactions.

In this study, the coarse-grained approach is applied to the total surface current as well as its rotational ( $\mathbf{u}_r$ ) and divergent ( $\mathbf{u}_d$ ) components using the Helmholtz decomposition. The latter consists of a separation of the total currents in terms of the streamfunction  $\psi$  and potential velocity  $\phi$ :

$$u = u_r + u_d = \psi_y + \phi_x \quad \text{and} \quad v = v_r + v_d = -\psi_x + \phi_y.$$

We obtain  $\mathbf{u}_d$  by solving  $\phi$  of a Poisson equation. We then estimate  $\mathbf{u}_r$  as the difference between  $\mathbf{u}$  and  $\mathbf{u}_d$ . Components  $\mathbf{u}_r$  and  $\mathbf{u}_d$  are associated with the balanced and unbalanced motions, which allows us to separate the contributions of these components to the energy cascade.

## 3. Description of the turbulent cascade

### a. Cross-scale KE fluxes

The kinetic energy flux  $\Pi$  is estimated over the Gulf Stream region using the coarse-grained approach at scales of 9, 22, 61, and 105 km (Fig. 3). The 9-km scale is the closest wavelength to the effective resolution of the simulation, 22 km corresponds approximately to a transition scale between mesoscale and submesoscale currents in this region, and 61 and 105 km represent scales of high mesoscale activity. Positive (negative) values indicate a forward (inverse) cascade, i.e., a transfer of kinetic energy to smaller (larger) scales.

At the 9-km scale (Fig. 3a),  $\Pi$  is mostly positive, revealing the presence of a systematic forward cascade at this scale. In contrast, at the 22-km scale,  $\Pi$  is characterized by a dipole located right on the Gulf Stream path (Fig. 3b), with a stronger downscale flux on its northern edge and a weaker upscale flux on its southern edge. At larger scales (61 and 105 km), the inverse cascade becomes dominant (Figs. 3c,d), which is consistent with an intense mesoscale eddy–mean flow interaction (Arbic et al. 2013; Renault et al. 2019). However, at these scales, an intense narrow band of positive values remains near Cape Hatteras, where the Gulf Stream separates from the coast.

On all scales analyzed,  $\Pi$  is most intense over the Gulf Stream and its surroundings, i.e., where the eddy activity is important (Fig. 1a). However, the various mechanisms that drive the kinetic energy flux—barotropic and baroclinic instabilities, filamentation and frontogenesis, mixed layer and ageostrophic instabilities—may bring a spatial dependency. Of particular importance is the Gulf Stream North Wall where significant density and temperature gradients (Fig. 1b) would allow for an intense frontogenesis activity (McWilliams et al. 2019). In the South Atlantic Bight, the topography plays an additional role, favoring barotropic destabilization of the flow (Gula et al. 2015) and there is a prominent topographic feature called the Charleston Bump where mesoscale frontal eddies are generated (Olson et al. 1983; Gula et al. 2015). Over the Charleston Bump, Fig. 3 reveals a large forward cascade, not only at small scales (<22 km) but also at large scales (>61 km), even though the inverse cascade intensifies in other regions. The next section will focus on the different components of the

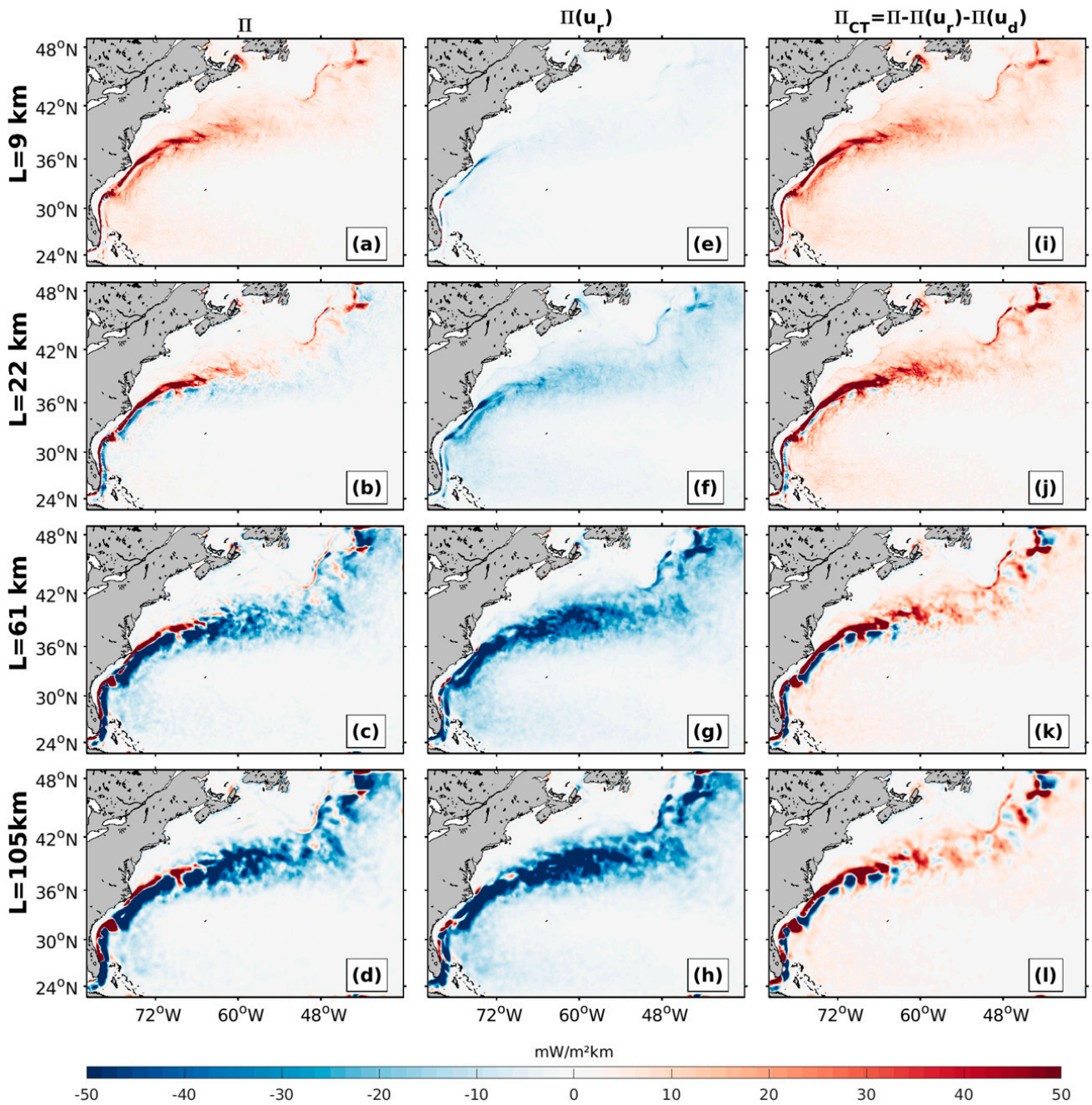


FIG. 3. Time-averaged (2005–09) cross-scale surface kinetic energy flux estimated from (left) total currents ( $\Pi$ ), (center) rotational (balanced) currents [ $\Pi(\mathbf{u}_r)$ ], and (right) the interaction of balanced and unbalanced flow [ $\Pi_{CT} = \Pi - \Pi(\mathbf{u}_r) - \Pi(\mathbf{u}_d)$ ]. The cross-scale fluxes are estimated at 9, 22, 61, and 105 km.

flow, particularly the role of unbalanced motions in the down-scale KE flux.

*b. Rotational and divergent components*

To understand the role of balanced and unbalanced motions in energy transfer at different scales, we decompose the surface currents into rotational and divergent components (i.e., Helmholtz decomposition, see section 2), where the rotational (divergent) velocity component is associated with the balanced (unbalanced) motion. Note that geostrophic currents

are nondivergent and included in the rotational component. Using these components, we estimated  $\Pi$  from (1) using rotational and divergent components.

Figures 3e–h depict the kinetic energy flux estimated using the rotational velocity component [ $\Pi(\mathbf{u}_r)$ ]. It reveals that, at all scales (stronger with increasing scale) and almost everywhere, the balanced kinetic energy flux is dominated by up-scale fluxes (Figs. 3e–h)—there are some exceptions where  $\Pi(\mathbf{u}_r)$  is positive for a few very localized regions such as near Cape Hatteras and over the Charleston Bump. These results

confirm the important role of balanced motions in the inverse cascade of kinetic energy. It is known that when balanced motions dominate, particularly the geostrophy that prevails at scales larger than 10 km, the effect of rotation and stratification is to inhibit vertical velocities and promote quasi-two-dimensional turbulence. However, even at small scales, the nondivergent part of the flow can hardly drive a forward cascade.

The KE flux  $\Pi(\mathbf{u}_d)$  estimated using the divergent velocity component alone (physically representing the advection of unbalanced motion by itself) is an order of magnitude smaller than both  $\Pi$  and  $\Pi(\mathbf{u}_r)$  (not shown). Therefore, the total cross-scale KE flux is not explained by the simple addition of rotational  $\Pi(\mathbf{u}_r)$  and divergent  $\Pi(\mathbf{u}_d)$  components, but by an additional cross term representing the interaction of balanced and unbalanced motions. The cross-term contribution to the kinetic energy flux of (1) is thus estimated as  $\Pi_{CT} = \Pi - \Pi(\mathbf{u}_r) - \Pi(\mathbf{u}_d)$ . In Figs. 3i–l,  $\Pi_{CT}$  is generally positive at all scales and the most intense values are located over the Gulf Stream. Note that patches of negative  $\Pi_{CT}$  are apparent, particularly along the southern edge of the Gulf Stream at large scale (>61 km; Figs. 3k,l).

To further quantify the contribution of  $\Pi(\mathbf{u}_r)$ ,  $\Pi(\mathbf{u}_d)$ , and  $\Pi_{CT}$  to the total KE flux, we calculate the percent contribution of each component as  $\% \Pi_X = |\Pi_X| / [|\Pi(\mathbf{u}_r)| + |\Pi(\mathbf{u}_d)| + |\Pi_{CT}|]$ , where  $\Pi_X$  can be  $\Pi(\mathbf{u}_r)$ ,  $\Pi(\mathbf{u}_d)$ , and  $\Pi_{CT}$ . Averaging  $\% \Pi_X$  over the entire domain shows that at scales greater than or equal to 22 km  $\Pi(\mathbf{u}_r)$  explains more than 50% of  $\Pi$  and  $\Pi_{CT}$  explains about 39%. At 9 km, the contribution of  $\Pi_{CT}$  increases to 68% and  $\Pi(\mathbf{u}_r)$  reduces to 26%. The contribution of  $\Pi(\mathbf{u}_d)$  to the total cross-scale KE flux is never larger than 6% at 9 km and falls below 4% at larger scales. Note that over areas of strong eddy activity in the Gulf Stream, the contribution of  $\Pi(\mathbf{u}_r)$  can be much higher than in the domain average (close to 90% at 105-km scales), whereas  $\Pi_{CT}$  has a stronger contribution over regions of weak eddy activity.

Previous studies have examined the origin of the forward cascade (Brüggemann and Eden 2015; Capet et al. 2008a; Molemaker et al. 2010). In particular, Capet et al. (2008a) note that in surface quasigeostrophic models that do not support momentum advection by ageostrophic currents, the forward cascade is weaker than in primitive equation models. They suggest that the forward cascade is associated with this missing part of the advection. Here, to confirm this hypothesis and extend it to balanced and unbalanced motions,  $\Pi_{CT}$  is further decomposed into the advection of rotational by divergent currents ( $\Pi_{CT_d}$ ) and the advection of divergent by rotational currents ( $\Pi_{CT_r}$ ), as follows:

$$\Pi_{CT_d} = X[(\mathbf{u}_d), (\mathbf{u}_d, \mathbf{u}_r)] \cdot (\overline{\mathbf{u}_{rx}}, \overline{\mathbf{u}_{ry}}) \quad \text{and} \quad (2)$$

$$\Pi_{CT_r} = Y[(\mathbf{u}_r), (\mathbf{u}_d, \mathbf{u}_r)] \cdot (\overline{\mathbf{u}_{dx}}, \overline{\mathbf{u}_{dy}}), \quad (3)$$

where  $X$  and  $Y$  are nonlinear operators, functions of  $\mathbf{u}_d$  or  $\mathbf{u}_r$  and their combinations. Note that  $\Pi_{CT}$  can be defined explicitly as  $\Pi_{CT} = \Pi_{CT_d} + \Pi_{CT_r}$  or implicitly as  $\Pi_{CT} = \Pi - \Pi(\mathbf{u}_d) + \Pi(\mathbf{u}_r)$ , both yielding the same result. The decomposition is applied at scales of 9, 22, and 61 km (Fig. 4; similar results are found at

105 km). Figure 4 reveals that  $\Pi_{CT}$  at 9, 22, and 61 km is primarily explained by  $\Pi_{CT_d}$  (Figs. 4a–c), i.e., by the advection of balanced momentum by unbalanced currents (unbalanced advection). The  $\Pi_{CT_d}$  shows dominant downscale fluxes at all scales, especially over the Gulf Stream North Wall, a region of strong density gradients. At large scale, upscale fluxes appear on the southern edge, while weaker positive and negative values are also present in  $\Pi_{CT_r}$  (Figs. 4d–f). Averaging over the entire region,  $\Pi_{CT_d}$  explains a large majority of  $\Pi_{CT}$  at all scales. Similar results were found with geostrophic and ageostrophic decompositions (not shown). Note that the advection of unbalanced by balanced currents may also play some role in specific regions such as the Charleston Bump. In summary, unbalanced advection has almost exclusive control over the forward cascade, while balanced motion drives the inverse cascade.

### c. Seasonal variability

A significant seasonal variability of the cross-scale KE flux has been estimated, based on high-resolution simulations, over the Agulhas Current (Schubert et al. 2020) and the subtropical western North Pacific (Qiu et al. 2014). Here, we estimate  $\Pi$  for the Gulf Stream system (Fig. 5) in winter (January–March) and summer (July–September). The fluxes are generally more intense in winter, and the patterns are similar to the annual mean during this season. This is particularly true at the 9- and 22-km scale (Figs. 5a–d), where the summer fluxes are much reduced. At 61 and 105 km, in winter, the narrow band of downscale fluxes stretching from Cape Hatteras is more evident than in the annual mean and actually disappears in summer.

The inverse cascade given by  $\Pi$  has a lesser seasonal cycle than appears from  $\Pi(\mathbf{u}_r)$  (Fig. 6). This difference is explained by a compensation between  $\Pi(\mathbf{u}_r)$  and  $\Pi_{CT}$ , which are respectively responsible for upscale and downscale fluxes. In winter, the inverse cascade driven by  $\Pi(\mathbf{u}_r)$  is intensified (Figs. 6a–d) but the forward cascade due to  $\Pi_{CT}$  is also intensified (Figs. 6i–l), balancing part of the upscale fluxes. The opposite is true in summer [weakening of both  $\Pi(\mathbf{u}_r)$  in Figs. 6e–h and  $\Pi_{CT}$  in Figs. 6m–p] with a similar moderate effect on upscale fluxes.

Previous studies suggest that seasonal variability not only alters the intensity of KE fluxes, but may also affect other indicators of seasonality. For example, Schubert et al. (2020) observe that the scale at which the peak upscale fluxes occur varies with the season, as does the scale at which the change of sign of the KE flux occurs (cross-over scale between downscale and upscale fluxes). To better analyze the temporal and spatial variability of  $\Pi$ , we focus on two regions, north and south of the Gulf Stream (Fig. 7; the areas of integration are drawn in Fig. 5). These two regions are representative of differences observed on the maps, focusing on them allows assessing the evolution of  $\Pi$  as a function of wavelength (as in a wavelength spectrum). Figure 7 reveals that  $\Pi$  has lower values in the southern region than in the northern region. In the northern region, the cross-over scale is also higher than in the southern region (~30–50 and ~10–30 km, respectively).

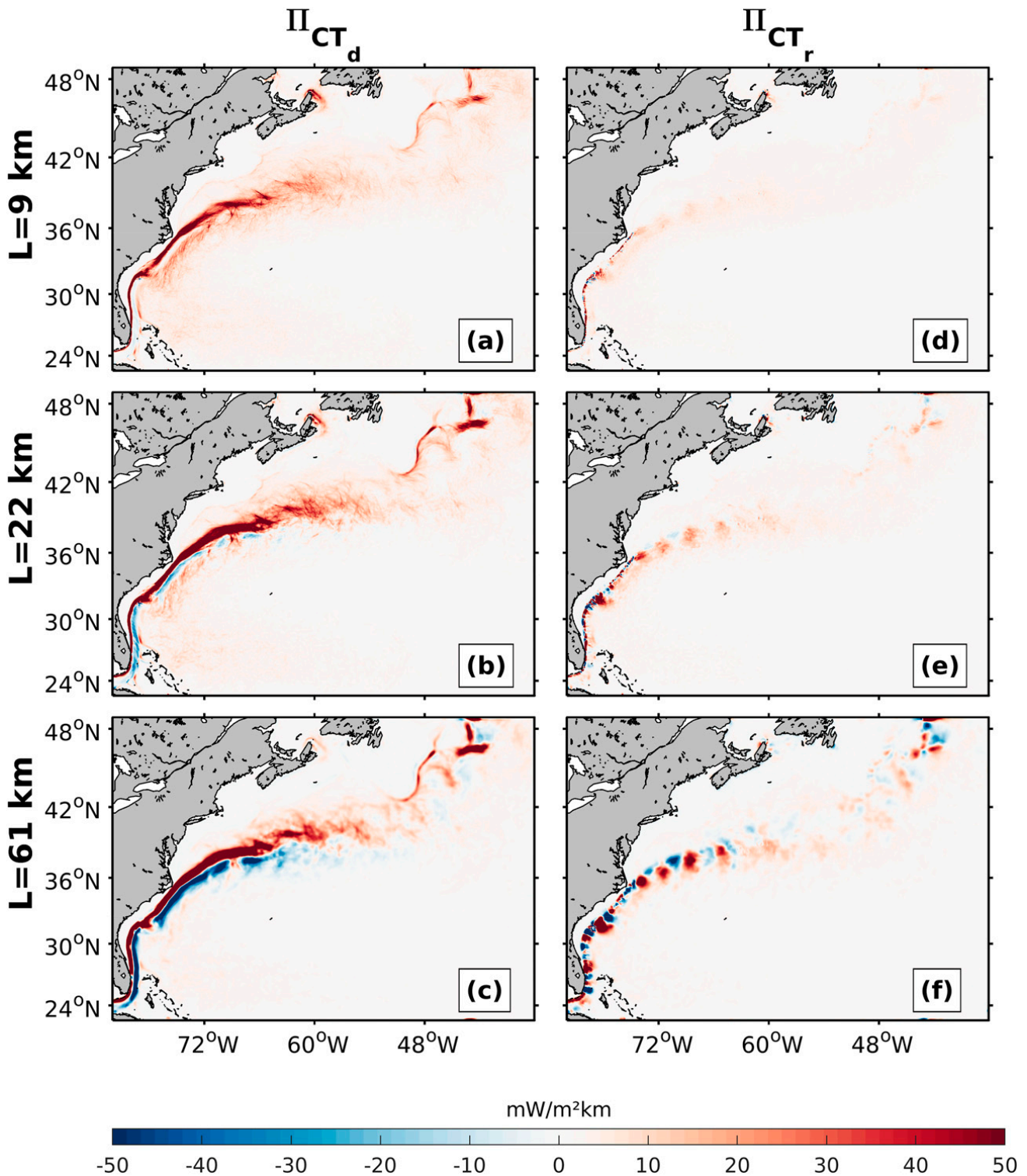


FIG. 4. Time-averaged (2005–09) cross-term contribution to the cross-scale KE flux, decomposed into terms associated with the (a)–(c) advection by unbalanced flow ( $\Pi_{CT_d}$ ) and (d)–(f) advection by balanced flow ( $\Pi_{CT_r}$ ). The cross-scale flux is estimated at (top) 9, (middle) 22, and (bottom) 61 km.

The cross-over scale shows seasonal variability: in the northern region, it is shorter in spring and longer in winter; in contrast, in the southern region, it is shorter in fall–winter and longer in summer.

In both regions, the forward cascade peaks in winter, while the inverse cascade has its larger values in spring. However, in the northern region, the inverse cascade is similar in winter, summer, and fall. In contrast, in the southern region, at scales

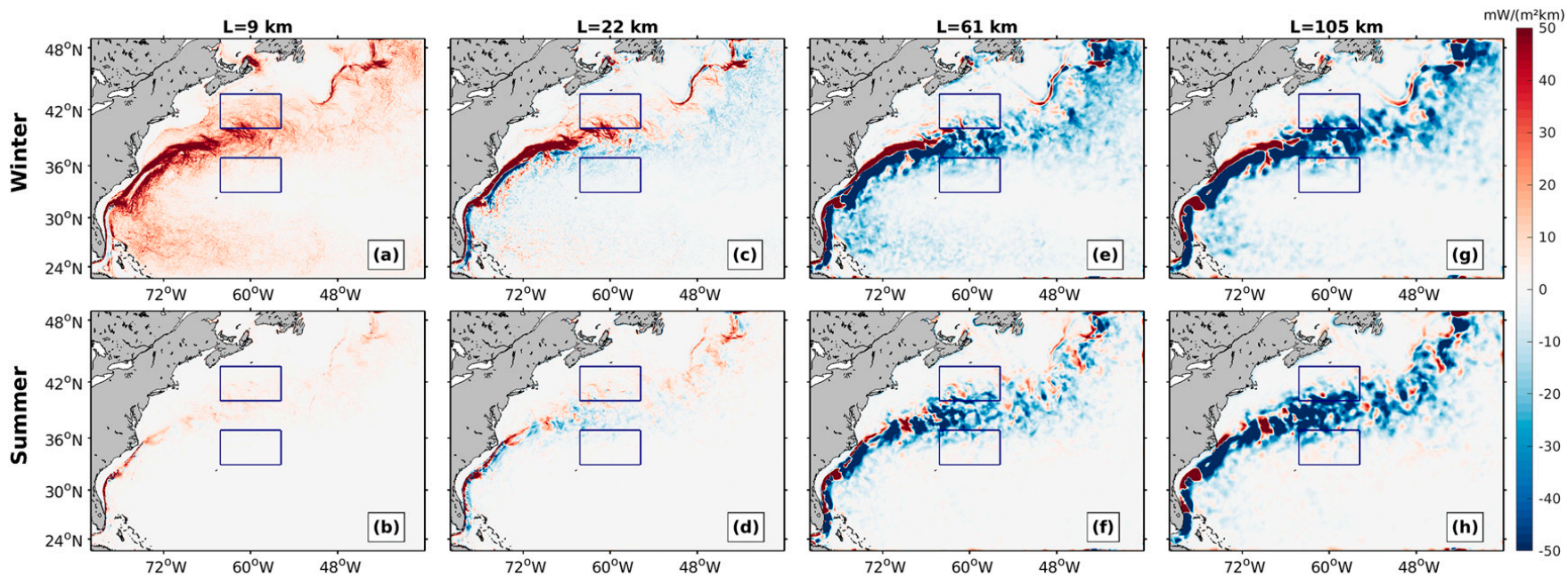


FIG. 5. (top) Winter [January–March (JFM)] and (bottom) summer [July–September (JAS)] averaged cross-scale kinetic energy fluxes estimated from total surface currents at (a),(b) 9; (c),(d) 22; (e),(f) 61; and (g),(h) 105 km. Blue outlines indicate the northern and southern regions analyzed in Fig. 7, below.

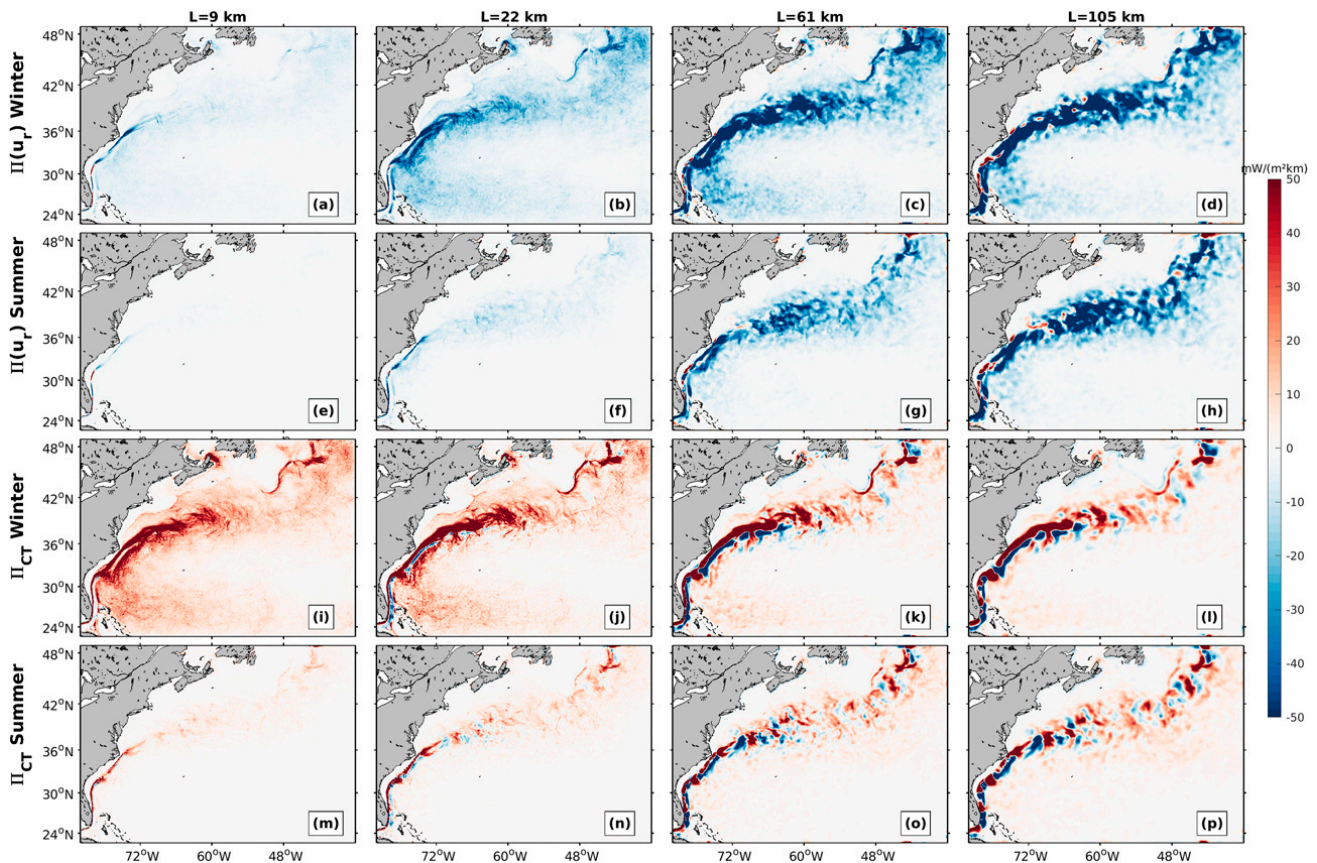


FIG. 6. Winter (JFM) mean of (a)–(d)  $\Pi(\mathbf{u}_r)$  and (i)–(l)  $\Pi_{CT}$ , and summer (JAS) mean of (e)–(h)  $\Pi(\mathbf{u}_r)$  and (m)–(p)  $\Pi_{CT}$ . Cross-scale energy fluxes are estimated at (left) 9, (left center) 22, (right center) 61, and (right) 105 km.

larger than 62 km, the upscale flux is weaker in autumn, and in summer it shows a more marked decrease toward smaller scales. Interestingly, in the northern region, the inverse cascade peaks at  $\approx 150$  km and does not have significant seasonal variation. In the southern region, the peak scale is larger in summer (101-km scale) and smaller in winter and autumn (62-km scale). These results suggest that the mechanisms involved in the kinetic energy flux are different in the two regions (this will be further discussed in section 4).

#### 4. Mechanisms

The objective of this section is to evaluate the mechanisms that determine the temporal and spatial variability of  $\Pi$ , as a measure of the KE cascade. We will be particularly interested in the mechanisms of forward cascade.

##### a. Frontogenesis

As shown in section 3, the forward cascade is produced primarily by the interaction between balanced and unbalanced motions ( $\Pi_{CT}$ ), and in particular by the advection of momentum by unbalanced flows ( $\Pi_{CT_d}$ ).

Frontogenesis occurs in regions where there is a horizontal buoyancy gradient in a background horizontal deformation flow. The deformation intensifies the horizontal buoyancy

gradient and disrupts the geostrophic balance along the front. To restore balance, a secondary ageostrophic circulation appears, which acts by restratifying the subsurface. The secondary circulation mechanism involves the generation of cyclonic vorticity and downwelling in the cold region and anticyclonic vorticity and upwelling of weaker amplitude in the warm region (McWilliams 2016). Based on submesoscale permitting simulations, Capet et al. (2008a,d); Klein et al. (2008) suggest that the forward cascade is essentially associated with this frontogenetic process.

The Gulf Stream presents favorable conditions for frontogenesis due to intense temperature gradients, especially at the North Wall and strong deformation flow (McWilliams et al. 2019). Figures 8a–c represent the annual, winter, and summer mean relative vorticity (i.e., normalized by the Coriolis parameter  $f$ ). From the Charleston Bump to the Gulf Stream postseparation, the vorticity is characterized by the presence of a dipole. On the northern (southern) edge of the Gulf Stream, the water masses are denser (lighter) and a cyclonic (anticyclonic) band is present, which is consistent with the observed frontal structure. Interestingly, the cyclonic side is spatially collocated with the  $60 \text{ mW m}^{-2} \text{ km}^{-1}$  contour of  $\Pi_{CT_d}$  at the 22-km scale (the contour shows the maximum values of  $\Pi_{CT_d}$ ). Note that similar consistency is found using contours of the same magnitude for  $\Pi_{CT_d}$  at the scales of 9 and 61 km.

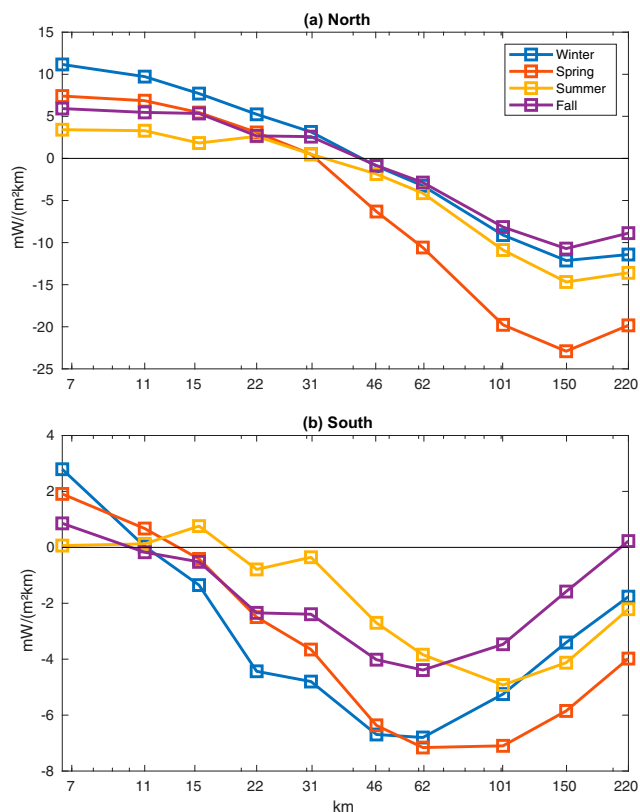


FIG. 7. Spatially averaged surface kinetic energy fluxes in the (a) northern and (b) southern regions, defined by the blue outlines in Fig. 5.

Following Hoskins and Bretherton (1972), the frontogenesis function is defined as  $F_s = \mathbf{Q} \cdot \nabla_h \rho$ , where  $\mathbf{Q}$  is the  $\mathbf{Q}$  vector. This function quantifies the rate of increase in the horizontal buoyancy gradient at the surface. Positive values indicate the development of frontogenesis and negative values indicate the development of frontolysis, i.e., a decrease of the buoyancy gradient. Figures 8d–f show that frontogenesis dominates in the region, especially at the North Wall of the Gulf Stream.  $F_s$  also presents a strong spatial and temporal coherence with the  $60 \text{ mW m}^{-2} \text{ km}^{-1}$  contour of  $\Pi_{CT_d}$  at the 22-km scale.

These results are in agreement with previous studies. In particular, Capet et al. (2008a) associate the ageostrophic advection responsible for the forward cascade with the secondary circulation generated by frontogenesis. Here, we confirm and extend their proposition to unbalanced (nondivergent) rather than ageostrophic motions. Recently, Srinivasan et al. (2022) use submesoscale-resolving simulations of a North Atlantic region between Greenland and Iceland and compute as we do the cross-scale energy flux using a Helmholtz decomposition. They find similar results to ours and conclude, with the help of an asymptotic theory, that the primary mechanism for the forward energy flux at fronts is frontogenesis.

While frontogenesis is an effective means of transferring energy to smaller scales, other processes can be considered, such as ageostrophic frontal instabilities (Molemaker et al. 2010;

Gula et al. 2016; Thomas et al. 2013). Frontal instabilities occur when chaotic advection by mesoscale eddies, intensified by submesoscale strain (due, for example, to MLI), drives the process to frontal collapse (Callies et al. 2016; Hoskins and Bretherton 1972). Because our simulations lack the spatial resolution to adequately reproduce these instabilities, we cannot analyze their role in the forward cascade. We expect their contribution to be significant, but perhaps not by increasing the energy flux as much as by taking over, at finer scales, the processes at work in finite Rossby number quasigeostrophic dynamics (McWilliams 2016). This hypothesis is also suggested by Marchesiello et al. (2011), whose model solutions from submesoscale-permitting to submesoscale-resolving show a continuation of the forward cascade but no increase in flux intensity.

North of the Gulf Stream, the relation between  $F_s$  and  $\Pi_{CT_d}$  appears to be lost:  $F_s$  has large values (especially in summer; Fig. 8f) while  $\Pi_{CT_d}$  is weak (Fig. 4b). One possible explanation is that in this region, the mesoscale EKE is weak relative to the Gulf Stream region and the frontogenesis function may reflect other processes than mesoscale confluent flow deformation.

#### b. Ekman buoyancy flux

Downstream of the Charleston Bump along the Gulf Stream, both the forward cascade ( $\Pi$  positive) and frontogenesis ( $F_s$ ) show strong seasonal variability. However, it is unclear why frontogenesis intensifies so strongly in winter, which raises the question: what processes explain the seasonal variability of frontogenesis? Atmospheric forcing and, in particular, wind may be good candidates to explain such a variability. Thomas and Lee (2005) suggest that, depending on wind direction, wind-driven Ekman currents can alter the ageostrophic secondary circulation. In particular, when the winds blow in the direction of the frontal jet (downfront winds), they can lead to an intensification of the front. To assess this hypothesis, following Thomas and Taylor (2010), the Ekman buoyancy flux (EBF) is defined as  $\text{EBF} = \mathbf{M}_e \cdot \nabla_h b_{z=0}$ , where  $\mathbf{M}_e = \boldsymbol{\tau} \times \mathbf{z}/(\rho_0 f)$  is the Ekman transport and  $\boldsymbol{\tau}$  is the wind stress vector. A positive EBF indicates an intensification of frontogenesis by Ekman transport.

Figures 8g–i reveal the presence of a dipolar structure in EBF downstream of the Charleston Bump, where positive and negative values are observed on the northern and southern edges, respectively, of the Gulf Stream. This structure correlates well with that of  $\Pi_{CT_d}$  and  $F_s$ , not only in space but also in time. In particular, EBF is positive over the Gulf Stream North Wall in the area covered by the  $60 \text{ mW m}^{-2} \text{ km}^{-1}$  contour of  $\Pi_{CT_d}$  at the 22-km scale (Fig. 8g). Therefore, wind-driven mixing contributes here to the transfer of energy to smaller scales. On the other hand, EBF is negative on the southern edge of the Gulf Stream, where  $\Pi_{CT_d}$  is small or even weakly negative (Figs. 4a–c). These trends are stronger in winter, when the wind and associated EBF are more intense than in summer, when the dipole disappears (Figs. 8h–i).

The Ekman buoyancy flux may also have a role in driving instabilities that promote or continue the forward cascade initiated by frontogenesis. Thomas et al. (2013) show for the

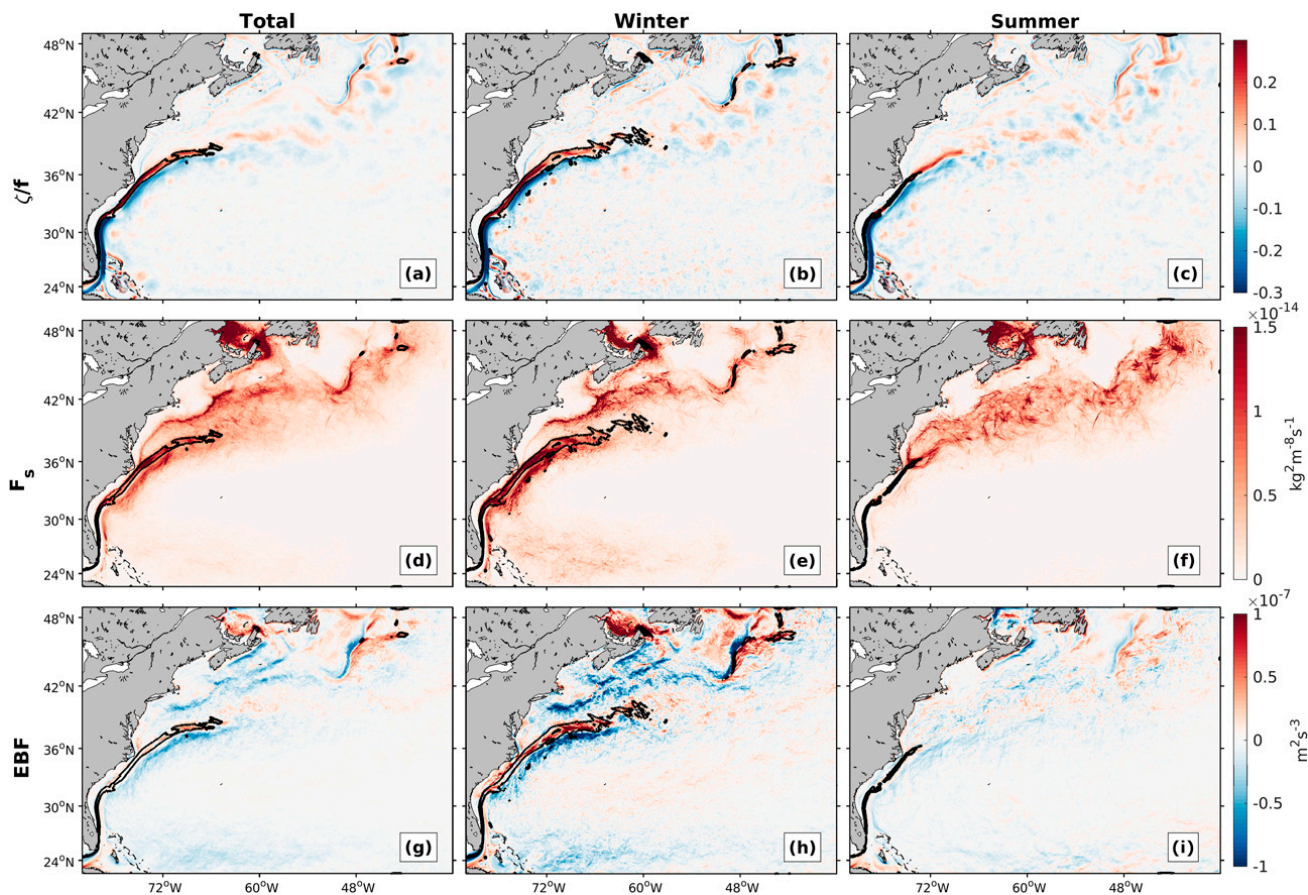


FIG. 8. Time-averaged (2005–09) surface (a)–(c) relative vorticity (normalized by  $f$ ), (d)–(f) frontogenesis function ( $F_s$ ;  $\text{kg}^2 \text{m}^{-8} \text{s}^{-1}$ ), and (g)–(i) Ekman buoyancy flux (EBF). The black contour represents the  $60 \text{ mW m}^{-2} \text{ km}^{-1}$  value of  $\Pi_{\text{CT}_d}$  at 22 km.

Gulf Stream that a cross-front advection by the Ekman flow of negative potential vorticity favors the development of symmetric instabilities that would drive energy farther toward the dissipation scale. D’Asaro et al. (2011) had drawn similar conclusions for the Kuroshio current. Again, due to the resolution of our model, we cannot verify these results.

### c. Upscaling effect of submesoscale eddies

In geostrophic turbulence theory, an inverse cascade is produced by the merging of mesoscale coherent eddies starting from the scales of eddy sources (Vallis 2017). However, submesoscale-permitting models reveal that the inverse cascade is intensified by submesoscale processes and extended to scales down to tenths of a kilometer (Klein et al. 2019). MLIs are a particularly effective example, and the intensification of mixed layer eddies in winter due to mixed layer deepening can be absorbed by mesoscale eddies, strengthening the latter and producing larger upscale fluxes (Khatri et al. 2021; Qiu et al. 2014; Schubert et al. 2020).

To investigate the submesoscale effect on the mesoscale activity, we use the seasonal analyses presented in section 3c. In the southern region, the seasonality of  $\Pi$  in Fig. 7b suggests two possible mechanisms related to MLIs and their role in the inverse cascade. First, consistent with Schubert et al. (2020), the maximum upscale flux occurs at smaller scales in winter as

compared with summer ( $\sim 50$  vs  $\sim 100$  km, respectively). Second, the cross-over scale between downscale and upscale fluxes is  $\sim 13$  km, which is similar to the most unstable MLI wavelength (15 km; Fox-Kemper et al. 2008). The cross-over scale of KE fluxes increases in summer to about 30 km, a seasonality perhaps weaker than reported by Schubert et al. (2020) for the Agulhas system. In the northern region, the upscale flux is more intense and its seasonality shows a significantly stronger flux in spring and cross-over scale varying from about 30 km in spring–summer to about 50 km in fall–winter.

These results agree with Schubert et al. (2020) and their interpretation that submesoscale flows affect the mesoscale seasonal cycle. The peak of MLI activity occurs in winter when the mixed layer is deeper, but the effect on mesoscale eddies (an absorption effect according to Schubert et al. 2020) develops during this season to peak in spring. We thus confirm for the Gulf Stream a phase shift of a few months in the effect of submesoscales on mesoscale activity.

## 5. Quantification of energy pathways

Mesoscale-resolving simulations were associated in the past with excessive mesoscale activity, reflecting a missing energy sink (e.g., Renault et al. 2019). Two mechanisms that may

have been underestimated can explain this: (i) interior dissipation driven by a forward energy cascade and (ii) boundary layer dissipation produced by top and bottom drag. In addition to these mechanisms, numerical models impose another energy sink, which is the dissipation required to dampen numerical dispersion errors. Since no explicit momentum dissipation operator is used in our simulation, numerical dissipation is essentially handled by the diffusive part of an upstream momentum advection scheme, whose viscosity varies with velocity powers (Soufflet et al. 2016). In what follows, the respective roles of interior, boundary, and numerical dissipation are evaluated, followed by a sensitivity analysis to advection schemes.

### a. Interior, boundary, and numerical dissipation

Dissipation of mesoscale currents by top drag can be estimated using the eddy geostrophic wind work  $F_e K_e = \langle \mathbf{u}'_g \boldsymbol{\tau}' \rangle - \Pi_{\tau_{22\text{km}}}$  where angle-bracket and prime operators indicate the average over 3 months and its fluctuation, respectively, and  $\Pi_{\tau_{22\text{km}}} = \overline{\boldsymbol{\tau} \cdot \mathbf{u}_g} - \overline{\boldsymbol{\tau}} \cdot \overline{\mathbf{u}_g}$  is the coarse-grained wind work at 22-km scale. The  $F_e K_e$  is calculated with geostrophic currents, excluding the Ekman or any ageostrophic contribution. Subtracting  $\Pi_{\tau_{22\text{km}}}$  from  $F_e K_e$  allows us to remove also the contribution of submesoscale currents and thus to further isolate the energy transfer from the mesoscale field to the atmosphere. Note, however, that  $\Pi_{\tau_{22\text{km}}}$  is only about 10% of  $F_e K_e$ . Dissipation by bottom drag is computed from the covariance of the bottom currents and bottom stress anomalies  $F_b K_b = \langle \mathbf{u}'_b \boldsymbol{\tau}'_b \rangle$ . Last, the numerical dissipation is  $H_{\text{Diff}} = \int_{\text{bottom}}^{\text{surface}} \mathbf{u} \cdot D dz$ , where the horizontal momentum diffusion  $D$  is diagnosed as either  $A_{\text{UP5}} - A_{\text{C6}}$ , that is, the difference between the UP5 advection term and an analogous advection term computed with a centered sixth-order nondissipative scheme, or  $A_{\text{UP3}} - A_{\text{C4}}$ , that is, the difference between the UP3 advection term and an analogous advection term computed with a centered fourth-order nondissipative scheme. Negative values of  $F_e K_e$ ,  $F_b K_b$ , and  $H_{\text{Diff}}$  indicate a dissipation of energy. These terms are directly comparable to the downscale flux at 9 km integrated between 100-m depth and the surface:  $I_{\text{Diss}} = -\int_{-100\text{m}}^{\text{surface}} \Pi_{9\text{km}} dz$ , that is, where the forward cascade dominates. Note that  $I_{\text{Diss}}$  is defined with a negative sign for downscale fluxes to represent a dissipation of energy. We consider 9 km to calculate the energy flux to better compare it with the numerical dissipation, which occurs mostly below this scale [the effective resolution of the model defined in Soufflet et al. (2016)].

Figures 9a–d depict the four energy sinks described above. The largest energy dissipation is from the top drag (negative  $F_e K_e$ ), i.e., the transfer from oceanic mesoscale currents to the atmosphere, over the Gulf Stream (Fig. 9a), consistent with Renault et al. (2016a). The positive values of  $F_e K_e$  over the shelf areas represent the generation of wind-driven shallow water currents (e.g., Renault et al. 2009). Not surprisingly,  $F_b K_b$  is negative everywhere, with higher magnitudes in regions where strong currents interact with the topography, e.g., over the Charleston Bump and New England Seamounts

(Fig. 9b). The numerical dissipation  $H_{\text{Diff}}$  is generally smaller than  $F_e K_e$  and  $F_b K_b$  and, like  $F_b K_b$ , tends to be larger over the rugged topography along the Gulf Stream path. Finally, the interior dissipation  $I_{\text{Diss}}$  is one order of magnitude smaller than the other energy sinks (note the scale factor applied in Fig. 9d) and, consistent with our previous results, has its largest values in the Gulf Stream North Wall (see Fig. 3a).

For a more quantitative comparison, Fig. 10 presents the spatial average of  $F_e K_e$ ,  $F_b K_b$ ,  $H_{\text{Diff}}$ , and  $I_{\text{Diss}}$  over the entire domain, the Gulf Stream region after separation (black contour in Fig. 9 using the  $500 \text{ cm}^2 \text{ s}^{-2}$  EKE contour estimated from AVISO) and the Gulf Stream before separation (yellow contour in Fig. 9 delineating the area between isobaths 200 and 780 m and between  $28.6^\circ$  and  $36.5^\circ\text{N}$ ). Averaging is performed over regions deeper than 200 m (thick dark green line in Fig. 9) to represent only mesoscale eddy dissipation. In the full domain,  $F_b K_b$  is the main dissipation process, while  $H_{\text{Diff}}$  and  $F_e K_e$  represent 74% and 43% of  $F_b K_b$ , respectively, and  $I_{\text{Diss}}$  is one order of magnitude smaller. On the Gulf Stream after separation (where the largest energy sinks are located),  $F_e K_e$  has a similar magnitude to  $F_b K_b$  due to strong mesoscale activity at the surface, while  $H_{\text{Diff}}$  is smaller with 53% of  $F_b K_b$ . Again, the forward cascade is an order of magnitude smaller than the other terms. West of Cape Hatteras, in the region around the Charleston Bump, dissipation by bottom drag is the main energy sink as expected.  $H_{\text{Diff}}$  is still high with about 30% of  $F_b K_b$ , due to the presence of strong currents, but both  $F_e K_e$  and  $I_{\text{Diss}}$  are one order of magnitude smaller than these two terms. The low values of  $F_e K_e$  can be explained by a re-energization of the ocean by the wind over the Charleston Bump (see Fig. 9).

### b. Sensitivity to momentum advection schemes

In our simulation (as in Ménesguen et al. 2018), horizontal momentum advection is discretized with a fifth-order (UP5) rather than the more usual third-order (UP3) upstream-biased advection (Shchepetkin and McWilliams 1998). UP3 has the advantage of a lower computational cost due to a decrease in the required computations and exchanges between parallel subdomains due to a relatively compact stencil. However, this is achieved at the cost of a higher truncation error, and thus higher numerical dissipation and lower effective resolution relative to UP5 (Soufflet et al. 2016; Ménesguen et al. 2018).

In a little more detail, the dominant truncation error term of UP3 for a one-dimensional problem in the  $x$  direction is

$$\frac{|u| \Delta x^3}{12} \frac{\partial^4 u}{\partial x^4},$$

which appears as a hyperdiffusion operator of order 4 and hyperviscosity  $|u| \Delta x^3 / 12$  ( $\Delta x$  is the mesh size). Soufflet et al. (2016) demonstrate that this numerical diffusion has the ability to precisely dampen the second-largest error term, which is dispersive and would produce unwanted and potentially explosive noise in the solution. The same qualities are found for UP5, but in this case the dominant error is

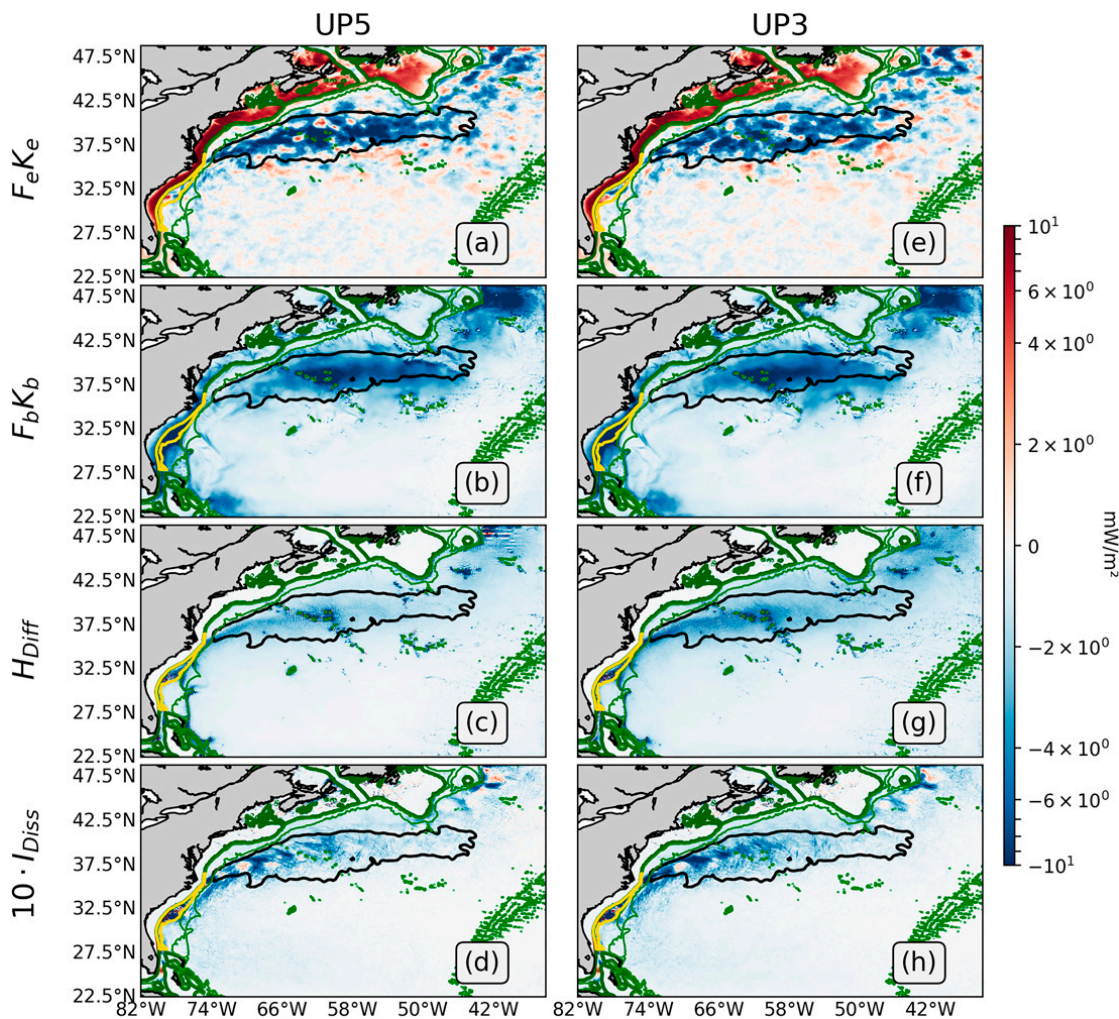


FIG. 9. Time-averaged (2005–09) kinetic energy dissipation: (top)  $F_e K_e$ , (top middle)  $F_b K_b$ , (bottom middle)  $H_{Diff}$ , and (bottom)  $10 \cdot I_{Diss}$ , computed from simulations with (a)–(d) UP5 and (e)–(h) UP3 numerical advection schemes. The eastern Gulf Stream region is bounded by the  $500 \text{ cm}^2 \text{ s}^{-2}$  EKE contour from AVISO (black contour). The western region is the area between the 200- and 780-m isobaths and between  $28.6^\circ$  and  $36.5^\circ \text{N}$  (yellow contour). The green contours indicate the 1000-, 3000-, and 200-m (thicker line) isobaths. Note that the energy dissipation color bar is nonlinear.

$$\frac{|u| \Delta x^5}{60} \frac{\partial^6 u}{\partial x^6},$$

that is, a hyperdiffusion of order 6 and hyperviscosity  $|u| \Delta x^5/60$ . In this case, numerical diffusion decreases faster with resolution and concentrates at scales closer to the grid scale, that is, about  $5\Delta x$  instead of  $10\Delta x$ , according to the dispersion relation of these schemes and the KE spectra performed with the idealized simulations of Ménesguen et al. (2018).

In the following, to evaluate the impact of the momentum horizontal advection schemes on the different energy sinks, the very same simulation (initially with UP5) is performed for a period of 5 years but using UP3.  $F_e K_e$ ,  $F_b K_b$ ,  $H_{diff}$ , and  $I_{Diss}$  are then estimated from that simulation and compared with the UP5 simulation. Figures 9e–h show that the spatial patterns of the different energy sinks are relatively similar in UP5 and UP3 simulations. However, as expected, the average

over the entire domain (excluding the shelf seas) indicates that the numerical dissipation in the UP3 simulation increases by 17.5% relative to UP5 (Fig. 10). The effect on the mean EKE is milder, with only about 3% decrease (Figs. 10a,b). The reason is that the numerical schemes also indirectly modify the other energy sinks, with compensation effects. Going from UP5 to UP3, the domain-average  $F_e K_e$  and  $F_b K_b$  are reduced by about 5% and 3%, respectively (Fig. 10c). This decrease is related to the greater damping of the eddies, which results in a lower loss by top drag and bottom drag. Similar results are found over the Gulf Stream boxes, with  $F_e K_e$  particularly affected after GS separation.

Quite surprisingly, the dissipation associated with the forward cascade ( $I_{Diss}$ ) increases by 24% with the more diffusive UP3 scheme. This is counterintuitive, as we would expect less resolved energy to produce less energy flux. A possible explanation is that the reduction of mean currents with UP3 (by

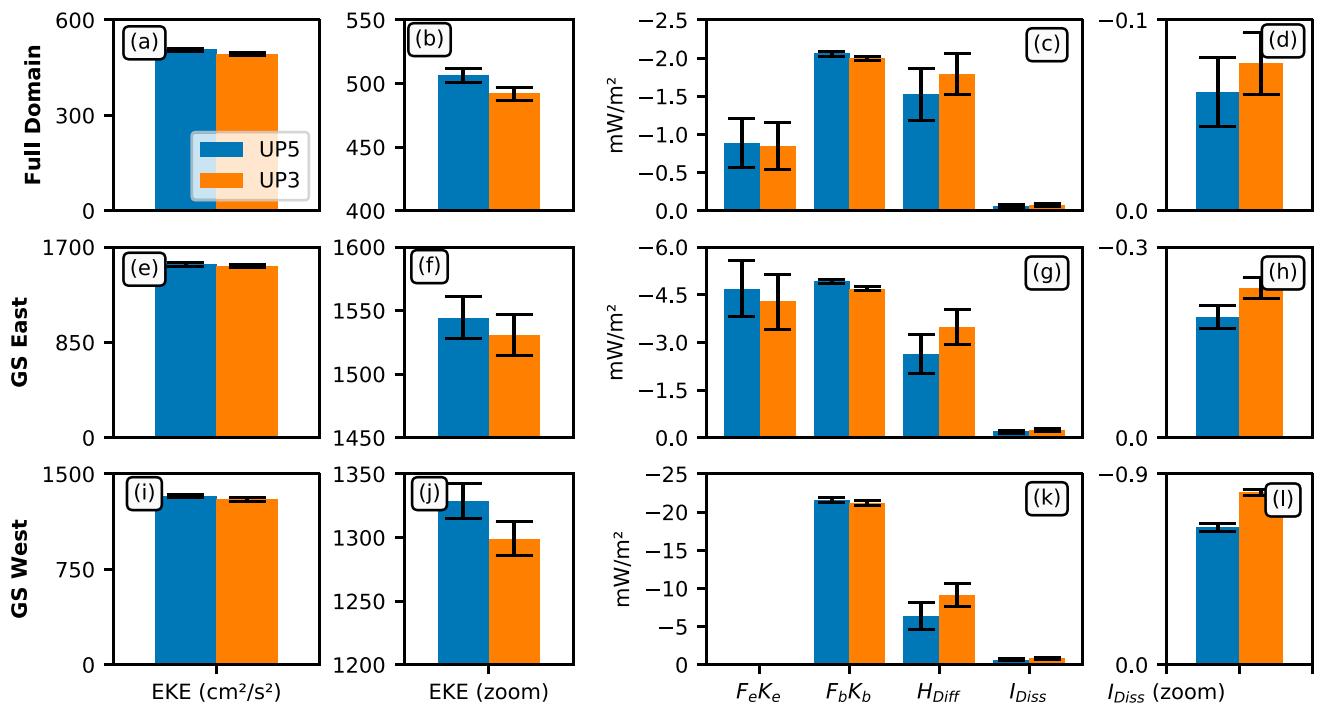


FIG. 10. Time-averaged (2005–09) (left),(left center) EKE and (right center),(right) KE dissipation computed from simulations with UP5 (blue bar) and UP3 (orange bar), and spatially averaged over (a)–(d) the entire domain, (e)–(h) the eastern GS region of the Gulf Stream defined by the black outline in Fig. 9, and (i)–(l) the western GS region defined by the yellow outline in Fig. 9; (b), (f), and (j) are zoomed-in panels of (a), (e), and (i) respectively, and (d), (h), and (l) are zoomed-in panels of  $I_{Diss}$  in (c), (g), and (k), respectively. In each panel, the error bar shows the standard error estimated by the bootstrap method. Note that the y axis is different in each region.

about 1.5%) also reduces the current feedback effect, resulting in a stronger mean surface stress. As mentioned in section 4b, a larger surface stress would favor frontogenesis, and thus enhance the forward cascade. EBF was estimated and found to be 5% higher with UP3 than UP5 over the entire domain and more than 6% in the Gulf Stream region. However, other explanations for a more intense downscale flux when numerical dissipation is increased are possible. In Marchesiello et al. (2011), for example, an increase of grid resolution extends the spectrum range of forward cascade to smaller scales, but its intensity tends to decrease slightly. In this case, there is no current feedback to the atmosphere, and the system behaves as if an extradissipation near the grid scale creates a vacuum for cross-scale fluxes. We leave this question for further studies in more idealized framework.

The general conclusion of this section is that numerical dissipation, even at a relatively high order of discretization, is still much larger than the resolved downscale flux. We would expect them to be similar for numerical dissipation to act as turbulent dissipation at the grid scale. Considering depths below 100 m, where the kinetic energy more generally follows an inverse cascade (e.g., Klein et al. 2008; Schubert et al. 2020), the problem is even more challenging and would require not only further reduction of numerical errors in advection schemes, but also consideration of subgrid-scale backscatter models to inject the missing energy.

## 6. Conclusions

In this study, we analyze the cross-scale kinetic energy flux in the Gulf Stream, using a coarse-grained approach on a submesoscale permitting (2 km) ocean model. This method allows us to describe the spatial and temporal variations of energy fluxes. From our results, a forward cascade tends to dominate everywhere near the surface at scales below 22 km, while the inverse cascade, generally associated with geostrophic turbulence, extends down to scales of at least 30 km. At larger scales, the inverse cascade dominates everywhere except on a narrow band extending from the Charleston Bump to the separation region along the Gulf Stream North Wall. To better understand what drives the kinetic energy flux, the total surface current was decomposed into its rotational (balanced) and divergent (unbalanced) components using a Helmholtz decomposition. The results show that the inverse and forward cascades are driven by the balanced and unbalanced flow, respectively. The forward cascade is temporally and spatially consistent with strong frontogenesis on the GS North Wall and associated ageostrophic secondary circulation. Next, we show that the kinetic energy flux is marked by seasonal variability. In winter, the forward cascade at 22 km is intensified everywhere, possibly due to the development of mixed layer instabilities, whereas the inverse cascade is intensified later in spring as submesoscales reinforce the mesoscale activity, consistent with previous studies.

Eddy-rich resolution models can exhibit excessive kinetic energy if not dissipated efficiently. How much energy is dissipated and how it flows through ocean scales is still an open question. In this study, we compare various energy sinks associated with boundary processes (top and bottom drag) and the interior route with dissipation through a downscale flux of resolved energy (forward cascade). Another process, numerical dissipation, is spurious in the sense that its role is to provide numerical integrity to the model, possibly at the expense of physical accuracy, but we generally assume that it is not a dominant process. It turns out that, in our model, the interior route to dissipation is one order of magnitude smaller than the dissipation produced by boundary processes and numerical discretization. Two important conclusions for numerical modeling can be drawn from these results. (i) The main energy dissipation processes in the real ocean are at the boundaries, and both top and bottom drags must be carefully accounted for in the models. Neglecting, in particular, the top drag process leads to an excess of eddy kinetic energy by  $\approx 30\%$  and overestimation of the inverse cascade (Renault et al. 2019; Aluie et al. 2018). (ii) The turbulent viscosity used in the explicit or implicit diffusion operators of current models largely overestimates the dissipation required by the physical mechanisms.

We tested the sensitivity of numerical momentum advection schemes using fifth- and third-order upstream-biased schemes. As expected, UP3 is more dissipative than UP5, but the difference is somewhat compensated by a reduced dissipation in the boundary layers. Weaker surface dissipation with UP3 can even enforce the mean surface stress, increase frontogenesis and the forward cascade. Therefore, efforts to reduce numerical dissipation to more physically meaningful values (with higher-order schemes and higher resolution) may give more weight to both the top drag and the bottom drag, perhaps simultaneously increasing the inverse cascade, but not necessarily the forward cascade. However, another dissipation process that UP5/UP3 may account for (besides eddy damping) is the breaking of internal waves generated by storms or tides. This process is not included in our estimate of downscale fluxes but may be important, although it is also probably greatly overestimated by current advection schemes (Jouanno et al. 2016).

Previous studies have estimated the rate of energy dissipation in symmetrically unstable fronts through observations. Using wintertime surveys of the Gulf Stream, Thomas et al. (2013) estimate that the dissipation associated with symmetric instabilities—following larger-scale energy-draining processes—is between  $O(1)$  and  $O(10)$   $\text{mW m}^{-2}$  depending on the intensity of the front. In the Kuroshio region, D'Asaro et al. (2011) found dissipation rates to be  $O(100)$   $\text{mW m}^{-2}$  for a symmetrically unstable front, the high intensity explained by conditions favorable to a large EBF. Using the winter snapshot of our simulation, we observe that the downscale energy flux in the front, which would be dissipated by symmetric instabilities if the resolution allowed, is consistent with the magnitudes estimated by Thomas et al. (2013) and can sometimes be as high as  $O(100)$   $\text{mW m}^{-2}$  (not shown). These magnitudes are comparable to the dissipation produced by bottom and top drag and numerical dissipation, so the interior dissipation may be locally substantial. However, due to the large spatial and temporal variability of the

fronts, the interior dissipation decreases significantly when estimating its long-term average contribution (i.e., greater than one month), making it significantly lower than other energy sinks.

Our study has several caveats. The spatial resolution of our simulations is too coarse to allow for ageostrophic submesoscale instabilities. Previous studies have suggested that symmetric (Dong et al. 2021; Thomas et al. 2013) or centrifugal (Gula et al. 2016) instabilities may contribute to the forward cascade. However, this would occur below the 20-km scale that appears to mark the beginning of a pseudodissipation range associated with frontogenesis. It is therefore unclear whether frontal instabilities would simply take over the direct cascade initiated by frontogenesis without much change in the dissipation rate, or whether they would restructure the turbulent forward cascade and the associated dissipation rate. Second, we do not explicitly consider the effects of air–sea interactions, but rather rely for our simulation on a parameterization of the current feedback. Considering that top and bottom drags are key processes for mesoscale energy dissipation, a coupled model could improve the representation of air–sea exchanges and their effect on mesoscale and submesoscale activity. However, our validation of mean and eddy flows against satellite and drifter data seems already beyond the accuracy of these observations, and it is unclear how much improvement can be gained or how to evaluate it with current observations.

Current satellite observations do not allow for an accurate characterization of the turbulent cascade (Klein et al. 2019). Satellite products such as AVISO are highly smoothed and can only resolve eddies with a radius greater than about 40 km and a lifetime greater than one week (Chelton et al. 2011). Arbic et al. (2013) and Renault et al. (2019) show that this limitation strongly affects the representation of the turbulent cascade, with a large underestimation of the cross-scale KE fluxes and a shift to lower wavenumbers of the forward cascade. Progress should be made as mesoscale and submesoscale motions with scales down to 30 km should be observable by the upcoming SWOT (Surface Water and Ocean Topography) altimetry mission (Morrow et al. 2019). However, the ageostrophic flow will be incompletely monitored and entangled with internal gravity waves (Klein et al. 2019). Future satellite missions—such as Odysea (Bourassa et al. 2016; Rodríguez et al. 2018)—will aim to consistently measure total surface currents (geostrophic and ageostrophic currents) and surface stress. This may contribute to our understanding of the energy pathways in the ocean.

*Acknowledgments.* Author Contreras was supported by Becas Chile (CONICYT-PFCHA/Doctorado Becas Chile/2020-72210196). We appreciate support from the Centre National d'Étude Spatial through the TOSCA projects I-CASCADE and CARAMBA, the LEFE VENUS project, and from the GdR and GdRI CROCO. The model and calculations were executed at GENCI (project 13051).

*Data availability statement.* The data to reproduce the figures are available online (<https://doi.org/10.6084/m9.figshare.20193092.v2>).

## REFERENCES

- Aluie, H., M. Hecht, and G. K. Vallis, 2018: Mapping the energy cascade in the North Atlantic Ocean: The coarse-graining approach. *J. Phys. Oceanogr.*, **48**, 225–244, <https://doi.org/10.1175/JPO-D-17-0100.1>.
- Arbic, B. K., K. L. Polzin, R. B. Scott, J. G. Richman, and J. F. Shriver, 2013: On eddy viscosity, energy cascades, and the horizontal resolution of gridded satellite altimeter products. *J. Phys. Oceanogr.*, **43**, 283–300, <https://doi.org/10.1175/JPO-D-11-0240.1>.
- Barkan, R., K. B. Winters, and S. G. L. Smith, 2015: Energy cascades and loss of balance in a reentrant channel forced by wind stress and buoyancy fluxes. *J. Phys. Oceanogr.*, **45**, 272–293, <https://doi.org/10.1175/JPO-D-14-0068.1>.
- Boccaletti, G., R. Ferrari, and B. Fox-Kemper, 2007: Mixed layer instabilities and restratification. *J. Phys. Oceanogr.*, **37**, 2228–2250, <https://doi.org/10.1175/JPO3101.1>.
- Bourassa, M. A., E. Rodriguez, and D. Chelton, 2016: Winds and currents mission: Ability to observe mesoscale air/sea coupling. *2016 IEEE Int. Geoscience and Remote Sensing Symp.*, Beijing, China, Institute of Electrical and Electronics Engineers, 7392–7395, <https://doi.org/10.1109/IGARSS.2016.7730928>.
- Brüggemann, N., and C. Eden, 2015: Routes to dissipation under different dynamical conditions. *J. Phys. Oceanogr.*, **45**, 2149–2168, <https://doi.org/10.1175/JPO-D-14-0205.1>.
- Bryan, F. O., C. W. Böning, and W. R. Holland, 1995: On the midlatitude circulation in a high-resolution model of the North Atlantic. *J. Phys. Oceanogr.*, **25**, 289–305, [https://doi.org/10.1175/1520-0485\(1995\)025<0289:OTMCI>2.0.CO;2](https://doi.org/10.1175/1520-0485(1995)025<0289:OTMCI>2.0.CO;2).
- , M. W. Hecht, and R. D. Smith, 2007: Resolution convergence and sensitivity studies with North Atlantic circulation models. Part I: The western boundary current system. *Ocean Modell.*, **16**, 141–159, <https://doi.org/10.1016/j.ocemod.2006.08.005>.
- Callies, J., G. Flierl, R. Ferrari, and B. Fox-Kemper, 2016: The role of mixed-layer instabilities in submesoscale turbulence. *J. Fluid Mech.*, **788**, 5–41, <https://doi.org/10.1017/jfm.2015.700>.
- Capet, X., P. Klein, B. L. Hua, G. Lapeyre, and J. C. McWilliams, 2008a: Surface kinetic energy transfer in surface quasi-geostrophic flows. *J. Fluid Mech.*, **604**, 165–174, <https://doi.org/10.1017/S0022112008001110>.
- , J. C. McWilliams, M. J. Molemaker, and A. F. Shchepetkin, 2008b: Mesoscale to submesoscale transition in the California Current system. Part I: Flow structure, eddy flux, and observational tests. *J. Phys. Oceanogr.*, **38**, 29–43, <https://doi.org/10.1175/2007JPO3671.1>.
- , —, —, and —, 2008c: Mesoscale to submesoscale transition in the California Current system. Part II: Frontal processes. *J. Phys. Oceanogr.*, **38**, 44–64, <https://doi.org/10.1175/2007JPO3672.1>.
- , —, —, and —, 2008d: Mesoscale to submesoscale transition in the California Current system. Part III: Energy balance and flux. *J. Phys. Oceanogr.*, **38**, 2256–2269, <https://doi.org/10.1175/2008JPO3810.1>.
- , G. Roullet, P. Klein, and G. Maze, 2016: Intensification of upper-ocean submesoscale turbulence through Charney baroclinic instability. *J. Phys. Oceanogr.*, **46**, 3365–3384, <https://doi.org/10.1175/JPO-D-16-0050.1>.
- Charney, J. G., 1971: Geostrophic turbulence. *J. Atmos. Sci.*, **28**, 1087–1095, [https://doi.org/10.1175/1520-0469\(1971\)028<1087:GT>2.0.CO;2](https://doi.org/10.1175/1520-0469(1971)028<1087:GT>2.0.CO;2).
- Chassignet, E. P., and D. P. Marshall, 2008: Gulf Stream separation in numerical ocean models. *Ocean Modeling in an Eddy Regime*, *Geophys. Monogr.*, Vol. 177, Amer. Geophys. Union, 39–62, <https://doi.org/10.1029/177GM05>.
- , and X. Xu, 2017: Impact of horizontal resolution (1/12° to 1/50°) on Gulf Stream separation, penetration, and variability. *J. Phys. Oceanogr.*, **47**, 1999–2021, <https://doi.org/10.1175/JPO-D-17-0031.1>.
- , L. T. Smith, G. R. Halliwell, and R. Bleck, 2003: North Atlantic simulations with the Hybrid Coordinate Ocean Model (HYCOM): Impact of the vertical coordinate choice, reference pressure, and thermobaricity. *J. Phys. Oceanogr.*, **33**, 2504–2526, [https://doi.org/10.1175/1520-0485\(2003\)033<2504:NASWTH>2.0.CO;2](https://doi.org/10.1175/1520-0485(2003)033<2504:NASWTH>2.0.CO;2).
- Chelton, D. B., M. G. Schlax, and R. M. Samelson, 2011: Global observations of nonlinear mesoscale eddies. *Prog. Oceanogr.*, **91**, 167–216, <https://doi.org/10.1016/j.pocean.2011.01.002>.
- Couvelard, X., P. Marchesiello, L. Gourdeau, and J. Lefèvre, 2008: Barotropic zonal jets induced by islands in the southwest Pacific. *J. Phys. Oceanogr.*, **38**, 2185–2204, <https://doi.org/10.1175/2008JPO3903.1>.
- D'Asaro, E., C. Lee, L. Rainville, R. Harcourt, and L. Thomas, 2011: Enhanced turbulence and energy dissipation at ocean fronts. *Science*, **332**, 318–322, <https://doi.org/10.1126/science.1201515>.
- Debreu, L., P. Marchesiello, P. Penven, and G. Cambon, 2012: Two-way nesting in split-explicit ocean models: Algorithms, implementation and validation. *Ocean Modell.*, **49–50**, 1–21, <https://doi.org/10.1016/j.ocemod.2012.03.003>.
- , N. K.-R. Kevlahan, and P. Marchesiello, 2022: Improved Gulf Stream separation through brinkman penalization. *Ocean Modell.*, **179**, 102121, <https://doi.org/10.1016/j.ocemod.2022.102121>.
- Dong, J., B. Fox-Kemper, H. Zhang, and C. Dong, 2021: The scale and activity of symmetric instability estimated from a global submesoscale-permitting ocean model. *J. Phys. Oceanogr.*, **51**, 1655–1670, <https://doi.org/10.1175/JPO-D-20-0159.1>.
- Ducet, N., P.-Y. Le Traon, and G. Reverdin, 2000: Global high-resolution mapping of ocean circulation from TOPEX/Poseidon and ERS-1 and-2. *J. Geophys. Res.*, **105**, 19477–19498, <https://doi.org/10.1029/2000JC900063>.
- Fairall, C. W., E. F. Bradley, J. E. Hare, A. A. Grachev, and J. B. Edson, 2003: Bulk parameterization of air-sea fluxes: Updates and verification for the COARE algorithm. *J. Climate*, **16**, 571–591, [https://doi.org/10.1175/1520-0442\(2003\)016<0571:BPOASF>2.0.CO;2](https://doi.org/10.1175/1520-0442(2003)016<0571:BPOASF>2.0.CO;2).
- Fox-Kemper, B., R. Ferrari, and R. Hallberg, 2008: Parameterization of mixed layer eddies. Part I: Theory and diagnosis. *J. Phys. Oceanogr.*, **38**, 1145–1165, <https://doi.org/10.1175/2007JPO3792.1>.
- Germano, M., 1992: Turbulence: The filtering approach. *J. Fluid Mech.*, **238**, 325–336, <https://doi.org/10.1017/S0022112092001733>.
- Gula, J., M. J. Molemaker, and J. C. McWilliams, 2015: Gulf Stream dynamics along the southeastern U.S. seaboard. *J. Phys. Oceanogr.*, **45**, 690–715, <https://doi.org/10.1175/JPO-D-14-0154.1>.
- , —, and —, 2016: Submesoscale dynamics of a Gulf Stream frontal eddy in the South Atlantic bight. *J. Phys. Oceanogr.*, **46**, 305–325, <https://doi.org/10.1175/JPO-D-14-0258.1>.
- Haine, T. W. N., and J. Marshall, 1998: Gravitational, symmetric, and baroclinic instability of the ocean mixed layer. *J. Phys. Oceanogr.*, **28**, 634–658, [https://doi.org/10.1175/1520-0485\(1998\)028<0634:GSABIO>2.0.CO;2](https://doi.org/10.1175/1520-0485(1998)028<0634:GSABIO>2.0.CO;2).
- Hoskins, B. J., and F. P. Bretherton, 1972: Atmospheric frontogenesis models: Mathematical formulation and solution. *J. Atmos.*

- Sci.*, **29**, 11–37, [https://doi.org/10.1175/1520-0469\(1972\)029<0011:AFMMFA>2.0.CO;2](https://doi.org/10.1175/1520-0469(1972)029<0011:AFMMFA>2.0.CO;2).
- Jamet, Q., B. Deremble, N. Wienders, T. Uchida, and W. Dewar, 2021: On wind-driven energetics of subtropical gyres. *J. Adv. Model. Earth Syst.*, **13**, e2020MS002329, <https://doi.org/10.1029/2020MS002329>.
- Jouanno, J., X. Capet, G. Madec, G. Rouillet, and P. Klein, 2016: Dissipation of the energy imparted by mid-latitude storms in the Southern Ocean. *Ocean Sci.*, **12**, 743–769, <https://doi.org/10.5194/os-12-743-2016>.
- Kessouri, F., D. Bianchi, L. Renault, J. C. McWilliams, H. Frenzel, and C. A. Deutsch, 2020: Submesoscale currents modulate the seasonal cycle of nutrients and productivity in the California Current system. *Global Biogeochem. Cycles*, **34**, e2020GB006578, <https://doi.org/10.1029/2020GB006578>.
- Khatri, H., S. M. Griffies, T. Uchida, H. Wang, and D. Menemenlis, 2021: Role of mixed-layer instabilities in the seasonal evolution of eddy kinetic energy spectra in a global submesoscale permitting simulation. *Geophys. Res. Lett.*, **48**, e2021GL094777, <https://doi.org/10.1029/2021GL094777>.
- Klein, P., B. L. Hua, G. Lapeyre, X. Capet, S. Le Gentil, and H. Sasaki, 2008: Upper ocean turbulence from high-resolution 3D simulations. *J. Phys. Oceanogr.*, **38**, 1748–1763, <https://doi.org/10.1175/2007JPO3773.1>.
- , and Coauthors, 2019: Ocean-scale interactions from space. *Earth Space Sci.*, **6**, 795–817, <https://doi.org/10.1029/2018EA000492>.
- Large, W. G., J. C. McWilliams, and S. C. Doney, 1994: Oceanic vertical mixing: A review and a model with a nonlocal boundary layer parameterization. *Rev. Geophys.*, **32**, 363–403, <https://doi.org/10.1029/94RG01872>.
- Laurindo, L. C., A. J. Mariano, and R. Lumpkin, 2017: An improved near-surface velocity climatology for the global ocean from drifter observations. *Deep-Sea Res. I*, **124**, 73–92, <https://doi.org/10.1016/j.dsr.2017.04.009>.
- Lellouche, J.-M., and Coauthors, 2018: Recent updates to the Copernicus Marine Service global ocean monitoring and forecasting real-time 1/12° high-resolution system. *Ocean Sci.*, **14**, 1093–1126, <https://doi.org/10.5194/os-14-1093-2018>.
- Lemarié, F., L. Debreu, A. Shchepetkin, and J. C. McWilliams, 2012: On the stability and accuracy of the harmonic and biharmonic isoneutral mixing operators in ocean models. *Ocean Modell.*, **52–53**, 9–35, <https://doi.org/10.1016/j.ocemod.2012.04.007>.
- Leonard, A., 1975: Energy cascade in large-eddy simulations of turbulent fluid flows. *Adv. Geophys.*, **18**, 237–248, [https://doi.org/10.1016/S0065-2687\(08\)60464-1](https://doi.org/10.1016/S0065-2687(08)60464-1).
- Lévy, M., P. J. S. Franks, and K. S. Smith, 2018: The role of submesoscale currents in structuring marine ecosystems. *Nat. Commun.*, **9**, 4758, <https://doi.org/10.1038/s41467-018-07059-3>.
- Marchesiello, P., J. C. McWilliams, and A. Shchepetkin, 2001: Open boundary conditions for long-term integration of regional oceanic models. *Ocean Modell.*, **3**, 1–20, [https://doi.org/10.1016/S1463-5003\(00\)00013-5](https://doi.org/10.1016/S1463-5003(00)00013-5).
- , L. Debreu, and X. Couvelard, 2009: Spurious diapycnal mixing in terrain-following coordinate models: The problem and a solution. *Ocean Modell.*, **26**, 156–169, <https://doi.org/10.1016/j.ocemod.2008.09.004>.
- , X. Capet, C. Menkes, and S. C. Kennan, 2011: Submesoscale dynamics in tropical instability waves. *Ocean Modell.*, **39**, 31–46, <https://doi.org/10.1016/j.ocemod.2011.04.011>.
- McWilliams, J. C., 2016: Submesoscale currents in the ocean. *Proc. Roy. Soc.*, **472A**, 20160117, <https://doi.org/10.1098/rspa.2016.0117>.
- , 2021: Oceanic frontogenesis. *Annu. Rev. Mar. Sci.*, **13**, 227–253, <https://doi.org/10.1146/annurev-marine-032320-120725>.
- , J. Gula, and M. J. Molemaker, 2019: The Gulf Stream north wall: Ageostrophic circulation and frontogenesis. *J. Phys. Oceanogr.*, **49**, 893–916, <https://doi.org/10.1175/JPO-D-18-0203.1>.
- Ménèsquen, C., S. Le Gentil, P. Marchesiello, and N. Ducousso, 2018: Destabilization of an oceanic meddy-like vortex: Energy transfers and significance of numerical settings. *J. Phys. Oceanogr.*, **48**, 1151–1168, <https://doi.org/10.1175/jpo-d-17-0126.1>.
- Molemaker, M. J., J. C. McWilliams, and X. Capet, 2010: Balanced and unbalanced routes to dissipation in an equilibrated Eady flow. *J. Fluid Mech.*, **654**, 35–63, <https://doi.org/10.1017/S0022112009993272>.
- Morrow, R., and Coauthors, 2019: Global observations of fine-scale ocean surface topography with the Surface Water and Ocean Topography (SWOT) mission. *Front. Mar. Sci.*, **6**, 232, <https://doi.org/10.3389/fmars.2019.00232>.
- Olson, D. B., O. B. Brown, and S. R. Emmerson, 1983: Gulf Stream frontal statistics from Florida straits to Cape Hatteras derived from satellite and historical data. *J. Geophys. Res.*, **88**, 4569–4577, <https://doi.org/10.1029/JC088iC08p04569>.
- Özgökmen, T. M., and E. P. Chassignet, 2002: Dynamics of two-dimensional turbulent bottom gravity currents. *J. Phys. Oceanogr.*, **32**, 1460–1478, [https://doi.org/10.1175/1520-0485\(2002\)032<1460:DOTDTB>2.0.CO;2](https://doi.org/10.1175/1520-0485(2002)032<1460:DOTDTB>2.0.CO;2).
- Penven, P., V. Echevin, J. Pasapera, F. Colas, and J. Tam, 2005: Average circulation, seasonal cycle, and mesoscale dynamics of the Peru Current system: A modeling approach. *J. Geophys. Res.*, **110**, C10021, <https://doi.org/10.1029/2005JC002945>.
- Qiu, B., S. Chen, P. Klein, H. Sasaki, and Y. Sasai, 2014: Seasonal mesoscale and submesoscale eddy variability along the North Pacific subtropical countercurrent. *J. Phys. Oceanogr.*, **44**, 3079–3098, <https://doi.org/10.1175/JPO-D-14-0071.1>.
- Renault, L., B. Dewitte, M. Falvey, R. Garreaud, V. Echevin, and F. Bonjean, 2009: Impact of atmospheric coastal jet off central Chile on sea surface temperature from satellite observations (2000–2007). *J. Geophys. Res.*, **114**, C08006, <https://doi.org/10.1029/2008JC005083>.
- , M. J. Molemaker, J. Gula, S. Masson, and J. C. McWilliams, 2016a: Control and stabilization of the Gulf Stream by oceanic current interaction with the atmosphere. *J. Phys. Oceanogr.*, **46**, 3439–3453, <https://doi.org/10.1175/JPO-D-16-0115.1>.
- , —, J. C. McWilliams, A. F. Shchepetkin, F. Lemarié, D. Chelton, S. Illig, and A. Hall, 2016b: Modulation of wind work by oceanic current interaction with the atmosphere. *J. Phys. Oceanogr.*, **46**, 1685–1704, <https://doi.org/10.1175/JPO-D-15-0232.1>.
- , P. Marchesiello, S. Masson, and J. C. McWilliams, 2019: Remarkable control of western boundary currents by eddy killing, a mechanical air-sea coupling process. *Geophys. Res. Lett.*, **46**, 2743–2751, <https://doi.org/10.1029/2018GL081211>.
- , S. Masson, T. Arsouze, G. Madec, and J. C. McWilliams, 2020: Recipes for how to force oceanic model dynamics. *J. Adv. Model. Earth Syst.*, **12**, e2019MS001715, <https://doi.org/10.1029/2019MS001715>.
- Rodríguez, E., A. Wineteer, D. Perkovic-Martin, T. Gál, B. W. Stiles, N. Niamsuwan, and R. R. Monje, 2018: Estimating ocean vector winds and currents using a Ka-band pencil

- beam Doppler scatterometer. *Remote Sens.*, **10**, 576, <https://doi.org/10.3390/rs10040576>.
- Saha, S., and Coauthors, 2010: The NCEP Climate Forecast System Reanalysis. *Bull. Amer. Meteor. Soc.*, **91**, 1015–1058, <https://doi.org/10.1175/2010BAMS3001.1>.
- Schoonover, J., and Coauthors, 2016: North Atlantic barotropic vorticity balances in numerical models. *J. Phys. Oceanogr.*, **46**, 289–303, <https://doi.org/10.1175/JPO-D-15-0133.1>.
- Schubert, R., J. Gula, R. J. Greatbatch, B. Baschek, and A. Biastoch, 2020: The submesoscale kinetic energy cascade: Mesoscale absorption of submesoscale mixed layer eddies and frontal downscale fluxes. *J. Phys. Oceanogr.*, **50**, 2573–2589, <https://doi.org/10.1175/JPO-D-19-0311.1>.
- Scott, R. B., and F. Wang, 2005: Direct evidence of an oceanic inverse kinetic energy cascade from satellite altimetry. *J. Phys. Oceanogr.*, **35**, 1650–1666, <https://doi.org/10.1175/JPO2771.1>.
- Shchepetkin, A. F., and J. C. McWilliams, 1998: Quasi-monotone advection schemes based on explicit locally adaptive dissipation. *Mon. Wea. Rev.*, **126**, 1541–1580, [https://doi.org/10.1175/1520-0493\(1998\)126<1541:QMASBO>2.0.CO;2](https://doi.org/10.1175/1520-0493(1998)126<1541:QMASBO>2.0.CO;2).
- , and J. McWilliams, 2003: A method for computing horizontal pressure-gradient force in an oceanic model with a non-aligned vertical coordinate. *J. Geophys. Res.*, **108**, 3090, <https://doi.org/10.1029/2001JC001047>.
- , and J. C. McWilliams, 2005: The Regional Oceanic Modeling System (ROMS): A split-explicit, free-surface, topography-following-coordinate oceanic model. *Ocean Modell.*, **9**, 347–404, <https://doi.org/10.1016/j.ocemod.2004.08.002>.
- , and —, 2009: Correction and commentary for “ocean forecasting in terrain-following coordinates: Formulation and skill assessment of the regional ocean modeling system” by Haidvogel et al., *J. Comp. Phys.* 227, pp. 3595–3624. *J. Comput. Phys.*, **228**, 8985–9000, <https://doi.org/10.1016/j.jcp.2009.09.002>.
- Siegelman, L., 2020: Energetic submesoscale dynamics in the ocean interior. *J. Phys. Oceanogr.*, **50**, 727–749, <https://doi.org/10.1175/JPO-D-19-0253.1>.
- Soufflet, Y., P. Marchesiello, F. Lemarié, J. Jouanno, X. Capet, L. Debret, and R. Benshila, 2016: On effective resolution in ocean models. *Ocean Modell.*, **98**, 36–50, <https://doi.org/10.1016/j.ocemod.2015.12.004>.
- Spall, M. A., 1996: Dynamics of the Gulf Stream/deep western boundary current crossover. Part I: Entrainment and recirculation. *J. Phys. Oceanogr.*, **26**, 2152–2168, [https://doi.org/10.1175/1520-0485\(1996\)026<2152:DOTGSW>2.0.CO;2](https://doi.org/10.1175/1520-0485(1996)026<2152:DOTGSW>2.0.CO;2).
- Srinivasan, K., J. C. McWilliams, M. J. Molemaker, and R. Barkan, 2019: Submesoscale vortical wakes in the lee of topography. *J. Phys. Oceanogr.*, **49**, 1949–1971, <https://doi.org/10.1175/JPO-D-18-0042.1>.
- , R. Barkan, and J. C. McWilliams, 2022: A forward energy flux at submesoscales driven by frontogenesis. *J. Phys. Oceanogr.*, **53**, 287–305, <https://doi.org/10.1175/JPO-D-22-0001.1>.
- Su, Z., J. Wang, P. Klein, A. F. Thompson, and D. Menemenlis, 2018: Ocean submesoscales as a key component of the global heat budget. *Nat. Commun.*, **9**, 775, <https://doi.org/10.1038/s41467-018-02983-w>.
- , H. Torres, P. Klein, A. F. Thompson, L. Siegelman, J. Wang, D. Menemenlis, and C. Hill, 2020: High-frequency submesoscale motions enhance the upward vertical heat transport in the global ocean. *J. Geophys. Res. Oceans*, **125**, e2020JC016544, <https://doi.org/10.1029/2020JC016544>.
- Thomas, L. N., and C. M. Lee, 2005: Intensification of ocean fronts by down-front winds. *J. Phys. Oceanogr.*, **35**, 1086–1102, <https://doi.org/10.1175/JPO2737.1>.
- , and J. R. Taylor, 2010: Reduction of the usable wind-work on the general circulation by forced symmetric instability. *Geophys. Res. Lett.*, **37**, L18606, <https://doi.org/10.1029/2010GL044680>.
- , —, R. Ferrari, and T. M. Joyce, 2013: Symmetric instability in the Gulf Stream. *Deep-Sea Res. II*, **91**, 96–110, <https://doi.org/10.1016/j.dsr2.2013.02.025>.
- Uchida, T., D. Balwada, R. Abernathy, G. McKinley, S. Smith, and M. Lévy, 2019: The contribution of submesoscale over mesoscale eddy iron transport in the open Southern Ocean. *J. Adv. Model. Earth Syst.*, **11**, 3934–3958, <https://doi.org/10.1029/2019MS001805>.
- Vallis, G. K., 2017: *Atmospheric and Oceanic Fluid Dynamics: Fundamentals and Large-Scale Circulation*. 2nd ed. Cambridge University Press, 946 pp., <https://doi.org/10.1017/9781107588417>.

## 4.4 Conclusion

In this chapter, we have described the spatial and temporal variations of energy fluxes using a submesoscale-permitting, forced oceanic simulation over the GS. The results are in agreement with theoretical predictions. The forward cascade dominates at small scales ( $<22$  km), while the inverse cascade dominates at larger scales ( $\geq 22$  km). We showed that the balanced motions are responsible for the inverse cascade, while their interactions with unbalanced motions (ageostrophic advection) drive the forward cascade. There is large spatial heterogeneity in the GS, and the forward cascade is largely explained by ageostrophic advection associated with frontogenesis on the North Wall. Ageostrophic advection has been studied previously in idealized simulations (Capet et al., 2008a; Molemaker et al., 2010; Brüggemann and Eden, 2015; Srinivasan et al., 2022), but our study allows characterization and quantification under realistic conditions. This has implications, for example, for satellite observation. In particular, SWOT data, which will provide high-resolution geostrophic currents, may be useful for monitoring the inverse KE cascade, but for the forward cascade, an estimate of ageostrophic motions will be required.

Consistent with the literature, we also demonstrate the presence of a strong seasonal variability in the KE cascade, with the forward cascade intensifying in winter and the inverse cascade intensifying later in spring, after a development phase in winter.

By comparing the different energy sinks in the GS an original part of our results are in the quantification of the interior route to dissipation. The direct KE cascade at submesoscale is an order of magnitude smaller than dissipation due to boundaries drags and to the numerical advection scheme. These results indicate that the main energy dissipation processes are at the boundaries, relying in both top and bottom drags. This calls into question the need to resolve submesoscales in order to have a realistic representation of the energy budget of the GS. However, there are clear advantages to increasing resolution. One is that a high resolution of the order of 1 km enables the range of numerical dissipation to be reduced to scales below the lower limit of the inverse cascade (around 10 km here), allowing full mesoscale energization. Another advantage is to enable better resolution of topographic slopes (although new improved topographic representations can operate at relatively coarse resolution; Debreu et al. 2022). Finally, submesoscale resolution enables more realistic vertical buoyancy fluxes to be obtained, contributing to the surface restratification induced by submesoscale processes.

# Tidal modulation of energy dissipation routes in the Gulf Stream

---

Contents

---

5.1	Preamble . . . . .	84
5.2	Article . . . . .	84
5.3	Supporting Information . . . . .	96
5.4	Conclusion . . . . .	101

---

## 5.1 Preamble

Ocean tides are mainly generated by the gravitational forces of the sun and moon, making them an important source of energy for the world's oceans (Munk and Wunsch, 1998). Tides can have a considerable impact on ocean circulation by increasing dissipation and mixing, making them an important subject of study in oceanography (Munk and Wunsch, 1998; Wunsch and Ferrari, 2004). On a global scale, it is estimated that bottom drag dissipates around 70% of the energy of barotropic tides, while the remaining 30% is transferred to internal tides (Egbert and Ray, 2000). However, the effects of tides on the energy balance of the GS is unknown.

In this chapter, the aim is to analyze the influence of tides on the energy budget of the wind circulation of the GS system, with particular emphasis on the forward transfer of KE. The configuration and methodology developed in the previous chapter were used as leverage for this purpose. A couple of submesoscale-permitting simulations were therefore carried out, one with tides (TD) and the other without tides (NTD, *i.e.*, the same as in the preceding chapter). The energy cascade is evaluated again using the coarse-graining method (outlined in Chapter 3) in both simulations, allowing to unravel the role of internal tides on the energy budget of the GS. Following the previous chapter, the role of balanced and unbalanced motions and their interactions with internal tides is analyzed with a Helmholtz decomposition. In addition, to emphasize the contribution of internal tides to the KE cascade, the current is further divided into low and high frequencies (with a frequency cut-off of one day).

Lastly, the effect of tides on GS KE dissipation is evaluated, including interior dissipation (via the forward cascade), bottom drag, and numerical dissipation.

These findings are published in Geophysical Research Letters (Contreras et al. (2023a); <https://doi.org/10.1029/2023GL104946>) and provided in the following.

## 5.2 Article

# Geophysical Research Letters®



## RESEARCH LETTER

10.1029/2023GL104946

### Key Points:

- Internal tides modulate the Gulf Stream (GS) turbulent cascade through wave-flow interaction
- External tides increase bottom drag of subtidal circulation in the deep ocean, intensifies the forward cascade
- Tide-induced increased dissipation pathways reduce GS mesoscale activity

### Supporting Information:

Supporting Information may be found in the online version of this article.

### Correspondence to:

M. Contreras,  
marcela-paz.contreras-contreras@univ-tlse3.fr

### Citation:

Contreras, M., Renault, L., & Marchesiello, P. (2023). Tidal modulation of energy dissipation routes in the Gulf Stream. *Geophysical Research Letters*, 50, e2023GL104946. <https://doi.org/10.1029/2023GL104946>

Received 19 JUN 2023  
Accepted 27 SEP 2023

### Author Contributions:

**Conceptualization:** L. Renault, P. Marchesiello  
**Investigation:** L. Renault, P. Marchesiello  
**Methodology:** M. Contreras, L. Renault, P. Marchesiello  
**Resources:** L. Renault  
**Supervision:** L. Renault, P. Marchesiello  
**Validation:** M. Contreras  
**Writing – original draft:** M. Contreras  
**Writing – review & editing:** L. Renault, P. Marchesiello

© 2023. The Authors.

This is an open access article under the terms of the [Creative Commons Attribution License](https://creativecommons.org/licenses/by/4.0/), which permits use, distribution and reproduction in any medium, provided the original work is properly cited.

## Tidal Modulation of Energy Dissipation Routes in the Gulf Stream

M. Contreras<sup>1</sup> , L. Renault<sup>1</sup> , and P. Marchesiello<sup>1</sup> 

<sup>1</sup>LEGOS, University of Toulouse, IRD, CNRS, CNES, UPS, Toulouse, France

**Abstract** The Gulf Stream (GS) is a powerful ocean current that is instrumental in regulating the global climate. While a correct reproduction of GS dynamics is contingent on an appropriate representation of energy dissipation, the specific role of tides in dissipation pathways of the wind-driven circulation is not well understood. Here, we present evidence, using high-resolution ocean simulations (~2 km grid spacing), that ocean tides, by generating internal gravity waves, increase the forward cascade of energy in the GS region. This effect is greatest in summer, when the intensity of internal tides increases. However, the dissipation route associated with the forward energy cascade remains an order of magnitude weaker than frictional dissipation near the surface and bottom boundaries.

**Plain Language Summary** Understanding the dynamics of the Gulf Stream (GS) is essential because of its influence on global climate and ocean circulation. Previous studies have shown that a realistic representation of this region using oceanic models depends on a correct representation of the energy balance and, in particular, how the system loses energy. Energy can be dissipated at the boundaries (bottom and surface ocean) and in the interior, but how tides affect energy dissipation in the GS is unknown. In this study, we found that the interior dissipation increases when tides are included, but this route remains small compared to the energy dissipated at the boundaries.

### 1. Introduction

The Gulf Stream (GS) is a Western Boundary Current recognized as one of the most powerful oceanic currents. It originates in the Gulf of Mexico and the Antilles Current and transports warm water toward the pole along the U.S. East Coast from the Straits of Florida to Cape Hatteras. At Cape Hatteras, the current separates from the coast and turns northeastward. The linear Sverdrup theory predicts that the GS volume transport varies with the intensity of basin-scale wind stress curl. Numerous studies have analyzed the energy balance of this region, showing a more complex dynamic where topography and eddies exert a strong influence over a wide range of temporal and spatial scales (Chassignet & Marshall, 2008; Contreras et al., 2023b; Gula et al., 2015, 2016; Renault, Molemaker, Gula, et al., 2016; Spall, 1996; Özgökmen & Chassignet, 2002).

However, despite numerous international programs devoted to observation and modeling, our understanding of GS dynamics still has significant gaps. The GS separation from the coast has long been understood as the result of coastal curvature and the inertia required to overcome topographic steering (Debreu et al., 2022; Spall, 1996). Modeling studies of the last two decades have linked emblematic features of the GS to the resolution of mesoscale activity through eddy-mean flow interaction (McWilliams, 2008), suggesting spatial resolution of  $1/10^\circ$  as a minimum for accurately representing the GS separation (Bryan et al., 2007; Chassignet & Marshall, 2008). Paradoxically, while the increase in grid resolution considerably improved the representation of the GS, the simulated eddy energy has become excessive, leading to biases in the separation of the GS as well as in its penetration of the North Atlantic basin (Chassignet & Xu, 2017; Chassignet et al., 2023; Renault, Molemaker, Gula, et al., 2016). This points to the need for a correct representation of the various energy sinks. How the energy is dissipated in the ocean has been one of the long unanswered questions. The recent literature shows that dissipation can be generated within turbulent boundary layers near the surface and bottom (Arbic et al., 2009; Ferrari & Wunsch, 2009; Renault, Molemaker, McWilliams, et al., 2016) or in the interior of the ocean (Capet et al., 2008; Contreras et al., 2023b; McWilliams, 2016; Molemaker et al., 2010).

Bottom drag represents the interaction between bottom currents and bathymetry. It is a major energy sink (Arbic et al., 2007, 2009; Nikurashin & Ferrari, 2010; Renault et al., 2023; Sen et al., 2008), controlling ocean dynamics, for example, the strength of barotropic flow and eddy-mean flow interaction (Renault et al., 2023; Trossman

et al., 2017). This is particularly true in high-energy regions like the GS (Sen et al., 2008), where bottom drag nearly balances the energy input from the wind (Weatherly, 1984). However, other dissipation processes are at work and models that fail to represent them tend to show solutions that are overly sensitive to the bottom drag parameterization (Renault et al., 2023).

Top drag is associated with frictional dissipation at the ocean surface. It actually represents the dissipation caused by the interaction between surface currents and wind stress, known as current feedback (CFB) (Renault et al., 2019; Renault, Molemaker, McWilliams, et al., 2016). CFB causes a large energy sink from (sub)mesoscale eddies to the atmosphere, damping (sub)mesoscale activity by about 30% (Renault et al., 2018; Renault, Molemaker, Gula, et al., 2016). Over the GS, the reduction of mesoscale activity weakens the eddy-flow interaction and stabilizes the mean flow, improving the representation of the GS dynamics (Renault et al., 2019).

Interior dissipation occurs with the loss of hydrostatic and geostrophic or gradient-wind momentum balances (large-scale balanced dynamics), allowing energy to be transferred to small scales (forward cascade) through to molecular dissipation (Brüggemann & Eden, 2015; Klein et al., 2008; Molemaker et al., 2010). The weakening of geostrophic balance occurs at the submesoscale, which is characterized by motions of the order of 0.1–10 km horizontally, 10–100 m vertically, and hours to days temporally (McWilliams, 2016). The associated mechanisms are: frontogenesis (Capet et al., 2008; Contreras et al., 2023b; Srinivasan et al., 2022); submesoscale quasigeostrophic instabilities at finite Rossby numbers (Capet et al., 2016); ageostrophic instabilities such as centrifugal, symmetric, gravitational, or Kelvin-Helmholtz instabilities (Contreras et al., 2019; Gula et al., 2016; Haine & Marshall, 1998; McWilliams, 2016; Thomas, 2012); and internal waves (Barkan et al., 2015; Bühler & McIntyre, 2005; Thomas, 2012). Using a 2-km resolution simulation, Contreras et al. (2023b) show that the most important energy sink for the GS is caused by top and bottom drags, and secondarily by the numerical dissipation of the model. The interior dissipation was an order of magnitude smaller than the other sinks. However, in their study, the potential effect of tides was neglected.

Internal waves can be forced by tides or winds (near-inertial waves, NIW), or generated by spontaneous emission through loss of balance, nonlinear wave-wave interactions, and lee-wave formation by geostrophic flow over sea-floor topography (Alford et al., 2016). Several studies have shown that internal waves extract energy from balanced motions, either from the mean flow or from mesoscale eddies or fronts (Barkan et al., 2015; Bühler & McIntyre, 2005; Shakespeare & Taylor, 2014; Thomas, 2012). Direct extraction is followed by wave-wave interaction, reinforcing the forward cascade (Alford et al., 2016).

Tides, more specifically, are a major source of energy for the ocean. They are caused by the gravitational forces exerted on the earth by the moon, and to a lesser extent, the sun (Stewart, 2008). The semi-diurnal M2 tide (period of 12.42 hr) is the most energetic component, accounting for around 2/3 of the energy produced by all constituents (Le Provost & Lyard, 1997; Munk & Wunsch, 1998). Tides generate strong barotropic currents, particularly in coastal waters, where around 70% of the barotropic tidal energy is dissipated by bottom drag (Egbert & Ray, 2000). The remaining 30% is transferred to internal tides in deep water over rough topography and under stratified conditions. Internal tides dissipate their energy by breaking, sometimes after traveling long distances (Garrett & Kunze, 2007). This is certainly true for semi-diurnal tides in the Atlantic, but diurnal tides are much weaker there and, because they are subinertial poleward of 30°, internal diurnal tides play only a minor role in this basin (Egbert & Ray, 2003). The transformation of internal tides during their propagation are similar to those of other internal waves: wave-wave interaction (MacKinnon & Winters, 2005); reflection, refraction and scattering by interaction with the mean flow (Duda et al., 2018; Kelly et al., 2016), or with mesoscale eddies (Rainville & Pinkel, 2006). These mechanisms suggest that internal tides can interact with the eddying wind-driven circulation and modify its energy budget, but a quantitative assessment for the entire GS system is not available. Barotropic tides, if strong enough, can also have an effect through an increase in nonlinear bottom drag, affecting both tidal and subtidal currents.

Recently, Barkan et al. (2021) has shown for a small area in the subpolar North Atlantic that internal tides tend to weaken the inverse energy cascade and strengthen the forward cascade (interior dissipation), thus reducing mesoscale kinetic energy (KE). They identify two main mechanisms: wave turbulence (the direct energy cascade of internal waves) and stimulated cascade (or imbalance), whereby internal waves trigger a transfer of energy from the mesoscale to the submesoscale. They also show that the tide-induced forward cascade is enhanced in summer, which they associate with greater M2 internal tide energy caused by increased stratification (Rocha et al., 2016). In winter, the forward cascade is stronger than in summer, but not because of internal tides, as

stratification is weakened by mixing due to winter winds and heat loss from the ocean, but because of submesoscale processes such as mixed layer instabilities that are favored by mixed layer deepening (Callies et al., 2015; Contreras et al., 2023b; Rocha et al., 2016; Schubert et al., 2020).

The main objective of this study is to analyze the effect of tides on the energy pathways of the wind-driven circulation of the GS. Firstly, we will assess the effect of tides on cross-scale KE fluxes and energy dissipation. Secondly, we will demonstrate the role of internal tides in modifying the forward cascade, but also that of surface tides in modifying bottom dissipation. A set of submesoscale-permitting simulations with tides (TD) and without tides (NTD) is analyzed for this purpose, and described in the next section.

## 2. Model Configuration

NTD and TD are performed with Coastal and Regional Ocean Community (CROCO; Debreu et al., 2012; Shchepetkin & McWilliams, 2005) over the period 2005–2009. The simulations are carried out in the GS region with a horizontal resolution of  $1/42^\circ$  ( $\sim 2.2$  km). The NTD configuration is described in Contreras et al. (2023b). TD is similar but is additionally forced by barotropic tides (height and currents) from the global tidal model TPXOv.7 (Egbert & Erofeeva, 2002), a global tidal model that best-fits the Laplace tidal equations and altimetry data. The 8 primary harmonic components of TPXO are prescribed at the open boundaries (Marchesiello et al., 2001). In addition, the tidal potential and the self-attraction and loading—due to redistribution of water masses over the solid earth (Hendershott, 1972)—are taken from GOT99.2b, which is a global ocean tide model based on TOPEX/Poseidon altimetry (Ray, 1999), and entered as a body force throughout the CROCO domain. For top drag, both TD and NTD simulations use a stress correction approach (Renault et al., 2020). Bottom drag is quadratic and parameterized through a logarithmic law of the wall with a roughness length of  $Z_{ob} = 10^{-2}$ . In our analysis, 3-hr averaged output fields are used. Both NTD and TD are in good agreement with observations. This is shown for NTD in Contreras et al. (2023b) and for TD in Supporting Information S1 (SI), where we also discuss the possible effects of spatial and temporal resolution in our analysis.

## 3. Cross-Scale Kinetic Energy Flux

The cross-scale KE flux ( $\Pi$ ) indicates the direction and intensity of KE transfer at a given spatial scale: positive values represent a forward cascade of energy from larger to smaller scales, while negative values represent an inverse cascade from smaller to larger scales (Aluie et al., 2018; Scott & Wang, 2005).  $\Pi$  is estimated here from surface currents using the coarse-graining approach (Aluie et al., 2018). Unlike the spectral analysis, the coarse-graining technique does not assume a homogeneous and isotropic field and avoids windowing procedures. In addition, this approach allows us to describe the spatial patterns of cross-scale fluxes. We follow the methodology proposed in Aluie et al. (2018) (see also Contreras et al. (2023b)) and estimate the energy flux across the spatial scales of 9, 22, and 61 km. The 9-km scale is near the effective resolution of the simulation—defined in Soufflet et al. (2016) as the dissipation wavelength below which the model KE departs from the assumed regime; 22-km marks roughly the transition between mesoscale and submesoscale in this region; and 61-km represents a peak in mesoscale activity.

Figures 1a–1c depicts the spatial average of  $\Pi$  in the GS region over the whole period (a), winter (b), and summer (c). The GS region is defined by the eddy kinetic energy (EKE) contour of  $500 \text{ cm}^2 \text{ s}^{-2}$  estimated from AVISO dataset (Archiving, Validation and Interpretation of Oceanographic Satellite data (Ducet et al., 2000); area denoted by the black contour in Figure 2). TD, the model produces a systematic increase in the annual forward cascade at the 9- and 22-km scales compared with NTD (by 32% and 171%, respectively) and a decrease of the inverse cascade at 61 km by 42%, revealing that tides favor downscale energy transfer. Consistent with Rocha et al. (2016) and Barkan et al. (2021), the largest differences occur in summer (July–September, JAS). In summer, at 9 km, the forward cascade dominates in both simulations, but is more intense (by 148%) in TD than in NTD (Figure 1c). At the 22-km scale, the forward cascade is present only in TD, but not in NTD (where a weak inverse cascade is observed). At the 61-km scale, the inverse cascade dominates in both simulations, but is more intense in NTD than in TD (reduction of 78%). In winter (January–March, JFM), the differences are smaller but still present, reaching up to 15%, 44% and  $-26\%$  at the 9, 22 and 61 km scales, respectively (Figure 1b).

In the following (and in subsequent analyses), the focus is on the summer period, that is, when the tidal influence is strongest. Similar results are obtained for the winter period or for the whole year. To better understand

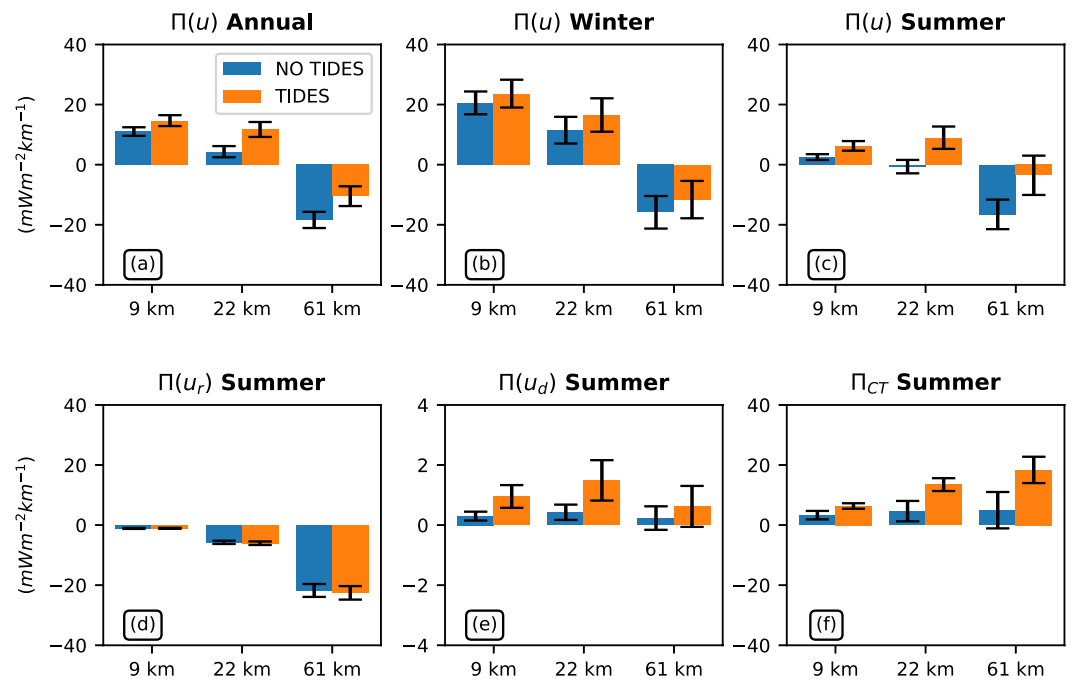


**Figure 1.** (a) Annual, (b) winter, and (c) summer mean cross-scale kinetic energy (KE) fluxes estimated from total surface currents in NTD and TD simulations. (d) Summer mean KE fluxes estimated from rotational currents, (e) divergent currents, and (f) the interaction of rotational and divergent currents ( $\Pi_{CT}$ ). Note that the y-axis in (e) differs from the other graphs. In panels (a)–(f), results were spatially averaged over the Gulf Stream region defined by the black contour in Figure 2. The cross-scale fluxes are estimated at 9, 22, and 61 km. The error-bar shows the standard error estimated by the bootstrap method.

the influence of tides on the forward and inverse cascades, the surface currents are decomposed into a balanced (rotational) component  $\mathbf{u}_r$  and an unbalanced (divergent) component  $\mathbf{u}_d$  (including waves), using the Helmholtz decomposition. Contreras et al. (2023b) show that the inverse cascade is mostly explained by balanced dynamics ( $\Pi(u_r)$ ), while the forward cascade results from unbalanced advection of balanced flow, computed as the cross-term contribution  $\Pi_{CT} = \Pi - \Pi(\mathbf{u}_d) - \Pi(\mathbf{u}_r)$ , where  $\Pi(\mathbf{u}_d)$  is the unbalanced advection of unbalanced flow.  $\Pi(\mathbf{u}_d)$  also contributes to the forward cascade, but by an order of magnitude less.

The spatial average over the GS region of the cross-scale KE flux estimated from balanced dynamics ( $\Pi(\mathbf{u}_r)$ ) shows only a weak tidal effect on the inverse cascade at all scales analyzed (compare TD with NTD). In contrast, the two terms associated with the forward cascade,  $\Pi(\mathbf{u}_d)$  and  $\Pi_{CT}$ , increase significantly from NTD to TD at all scales analyzed (Figures 1e and 1f). However, as with NTD, the contribution of  $\Pi(\mathbf{u}_d)$  remains well below that of  $\Pi_{CT}$  (note that in Figure 1e, the y-axis is an order of magnitude smaller than in Figure 1f). The increase in  $\Pi_{CT}$  due to the tide is 91%, 189% and 270% at scales of 9, 22 and 61 km respectively. This means that the apparent reduction in the inverse cascade at 61 km and the increase in the forward cascade at 9 and 22 km are due to ageostrophic advection.

Maps of mean summer  $\Pi$  values in NTD and TD simulations at 9, 22, and 61 km scales are shown in Figures 2a–2c and 2d–2f, respectively. The intensification of the forward cascade in TD at all scales analyzed is produced at the GS North Wall, but mainly in the area around 40°N and 60°W, and around the Gulf of Maine (GoM). South of the GS, there is no significant change in cross-scale KE flux.

Although the GoM is not the focus here, it deserves attention because of its possible influence on the GS via tides. This region is dominated by the semi-diurnal M2 tide, greatly amplified by its unique shape, achieving one of the world's highest magnitudes. Energetic internal tides are generated by topographic interaction along the flanks of Georges Bank and propagate both onshore and offshore (Chen et al., 2011; Kelly et al., 2016). They vary with seasonal stratification changes and peak in summer, fueled by a robust pycnocline forming around 15 m deep due to solar radiation (Brown, 2011; Katavouta et al., 2016; Loder & Greenberg, 1986). The internal tides radiating

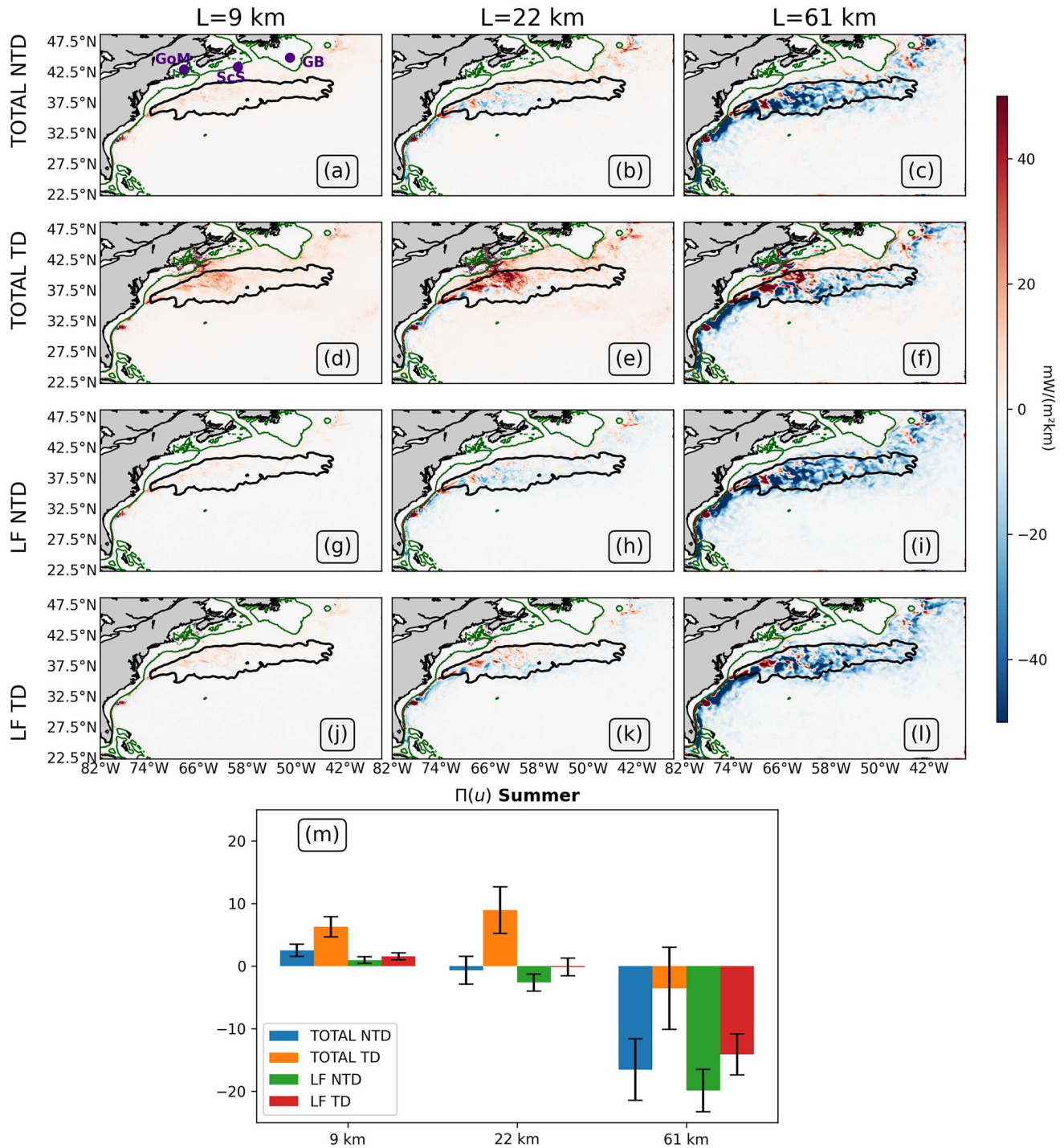


**Figure 2.** Maps of summer mean cross-scale kinetic energy (KE) fluxes estimated from total currents in NTD (a–c); in TD (d–f); low-frequency (>1 day) currents in NTD (LF NTD) (g–i); and in TD (LF TD) (j–l). The cross-scale fluxes are estimated at 9, 22, and 61 km. The black contour is the  $500 \text{ cm}^2 \text{ s}^{-2}$  AVISO EKE contour and defines the Gulf Stream (GS) region. The green contour is the 200 m isobath. The purple dots indicate the geographic region of the Gulf of Maine, Scotian Shelf (ScS) and Grand Banks (GB). (m) Summer mean cross-scale KE fluxes estimated from TOTAL NTD (blue), TOTAL TD (orange), LF NTD (green) and LF TD (red), spatially averaged over the GS region. The error-bar in m shows the standard error estimated by the bootstrap method.

offshore can experience strong reflection and refraction by the GS (Duda et al., 2018), and tidal scattering by the mean flow that promotes energy conversion to higher modes (Dunphy & Lamb, 2014; Kelly et al., 2016). Noteworthy, the region where the forward cascade is greatest in TD (around 40°N and 60°W), coincides with the location of GS-altered non-coherent internal tides reported by Kelly et al. (2016) (see their Figure 12).

#### 4. Role of Internal Tides

The increase of the forward KE cascade from NTD to TD simulations could be explained by the generation of internal tides. To verify this hypothesis, we decomposed the TD surface currents into their high-frequency and low-frequency components, assuming that high-frequency currents are associated with internal tides (off the shelf). To obtain the low-frequency component ( $\hat{\mathbf{u}}$ ), we apply a temporal Butterworth low-pass filter with a cutoff period of 1-day. The high-frequency component is defined as  $\mathbf{u}'' = \mathbf{u} - \hat{\mathbf{u}}$ . Comparison of the spectra indicates that the filter effectively eliminates the tidal signal (not shown). However, one of the main caveats of this methodology is that it also suppresses waves generated by other mechanisms and probably some high-frequency submesoscale currents.

As in the previous section, our analysis focuses on summer. Using  $\hat{\mathbf{u}}$  from TD, we estimated the associated KE flux ( $\Pi(\hat{\mathbf{u}})$ ).  $\Pi(\hat{\mathbf{u}})$  shows a weaker forward cascade than the total flux  $\Pi$  (Figures 2d–2f), especially over the GoM and around 40°N and 60°W. Interestingly, the magnitude of  $\Pi(\hat{\mathbf{u}})$  in TD is comparable to  $\Pi$  in NTD at all scales (Figures 2a–2c). This confirms that the internal tides are responsible for the intensification of the forward cascade.

Comparison of filtered and unfiltered KE fluxes in TD shows that  $\Pi(\hat{\mathbf{u}})$  (Figure 2j) is reduced by 75% compared to  $\Pi$  (Figure 2d) at the 9 km scale. At the 22-km scale, the reduction is 101% (Figures 2e and 2k). At this scale,  $\Pi$  shows an intense forward cascade, which is higher than that at the 9 km scale, in stark contrast to  $\Pi(\hat{\mathbf{u}})$  which shows a weak inverse cascade.

Although the filtered KE flux in TD is similar to the total flux in NTD, as mentioned above,  $\Pi(\hat{\mathbf{u}})$  in TD (Figure 2j) is, however, 38% lower than  $\Pi$  in NTD at the 9 km scale (Figure 2a). At the 22 and 61 km scales,  $\Pi(\hat{\mathbf{u}})$  in TD also shows a reduction in the inverse cascade of 74% and 14% compared to NTD, respectively. This difference is explained by the removal of internal waves generated by non-tidal mechanisms, which are present in both TD and NTD. The contribution of non-tidal mechanisms can be revealed by calculating  $\Pi(\hat{\mathbf{u}})$  in NTD with the same filters. In summer, in the GS region, the forward cascade at 9-km scale given by  $\Pi(\hat{\mathbf{u}})$  in NTD is reduced by 62% compared to  $\Pi$ . At 22 and 61-km scales, the inverse cascade given by  $\Pi(\hat{\mathbf{u}})$  in NTD is increased by 299% and 20%, respectively. These results suggest that non-tidal waves contribute significantly to the forward cascade. However, note that some of the filtered high-frequency currents belong to submesoscale eddies rather than transient features such as wind-generated NIWs.

In summary, high-frequency currents are relevant to explain the forward cascade induced by tides. It seems that the intensification of the forward cascade around 40°N and 60°W results from the interaction between the internal tides generated in the GoM and the mean GS flow (see previous section). It should be noted that the forward cascade is also intensified by high-frequency currents in areas close to the Scotian Shelf and Grand Banks (indicated in Figures 2a–2f). However, this enhancement is less significant than that observed around 40°N and 60°W, possibly due to weaker tides and currents.

#### 5. Energy Sink

Here, we evaluate the overall impact of tides on the energy sinks following the methodology proposed in Contreras et al. (2023b):

- Dissipation of mesoscale currents by top drag can be estimated using the eddy geostrophic wind work  $F_e K_e = \langle \mathbf{u}_g' \tau' \rangle - \Pi_{\tau_{22km}}$  where  $\langle \rangle$  and  $'$  operators indicate the average over 3-month and its fluctuation, respectively, and  $\Pi_{\tau_{22km}} = \overline{\tau \cdot \mathbf{u}_g} - \overline{\tau} \cdot \overline{\mathbf{u}_g}$  is the coarse-grained wind work at 22-km.
- Dissipation by bottom drag is computed from the covariance of the bottom currents and bottom stress anomalies  $F_b K_b = \langle \mathbf{u}_b' \tau_b' \rangle$ .
- Interior dissipation is defined as  $I_{Diss} = - \int_{-100m}^{surface} \Pi_{9km} dz$ .

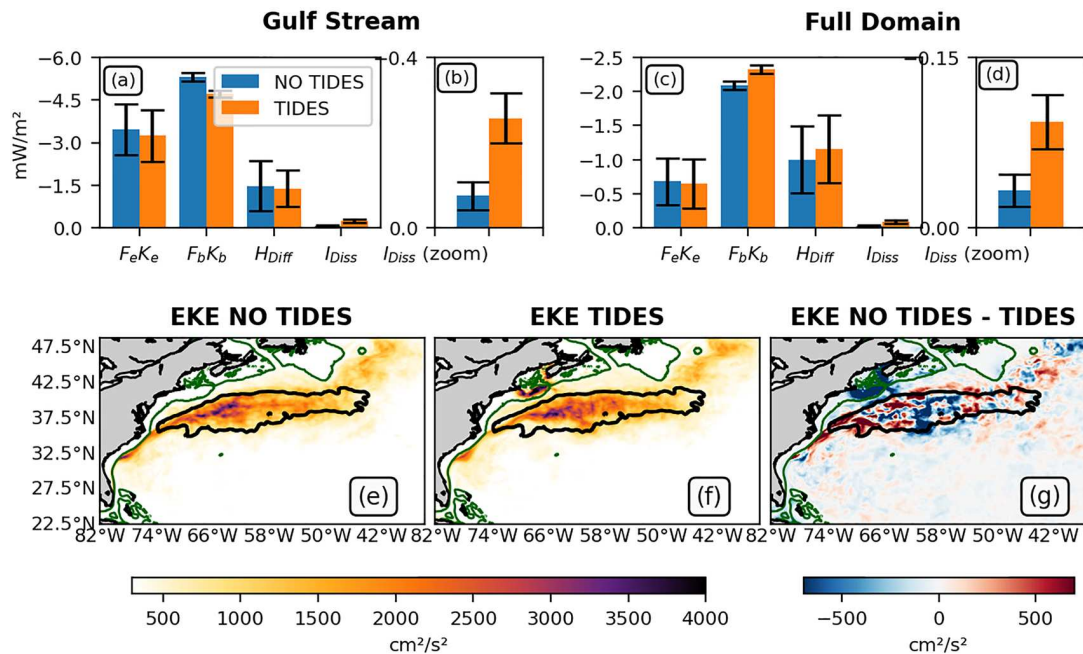


**Figure 3.** Summer mean kinetic energy dissipation computed from NTD (blue bar) and TD (orange bar) and spatially averaged over panels (a)–(b) the Gulf Stream region defined by the black outline in (e)–(g) and (c)–(d) the entire domain. Panels (b), (d) are zoom panels of panels (a) and (b) for  $I_{Diss}$ . In each panel, the error-bar shows the standard error estimated by the bootstrap method. Panels (e)–(g) Summer mean EKE estimated from NTD, TD, and their difference. The green contour is the 200 m isobath.

- We estimate numerical dissipation (from the fifth-order upstream scheme, UP5, used in the simulations)  $H_{Diff} = \int_{bottom}^{surface} \mathbf{u} \cdot \mathbf{D} dz$ , where  $D$  is the horizontal momentum diffusion diagnosed from the difference between UP5 and a non-dissipative sixth-order centered scheme (Contreras et al., 2023b).

Negative values of these diagnostics indicate a dissipation of energy. Again, the energy sink terms are estimated for summer (similar results are found for the other seasons or the whole year).

The average over the GS region (and over the whole domain) reveals that the major contribution to energy dissipation in TD and NTD is produced by top and bottom drag, followed by numerical dissipation (Figures 3a–3d). Consistent with Contreras et al. (2023b), the contribution of the interior dissipation is an order of magnitude smaller than the other energy sinks. Over the GS region,  $F_b K_b$  is reduced by 11% between NTD and TD (Figure 3a). A slight decrease of 6% in TD is also shown in both  $F_e K_e$  and  $H_{Diff}$ . As expected from our previous results, including the tides leads to an increase of  $I_{Diss}$  by 240% (stronger forward cascade; Figures 3a and 3b). However,  $I_{Diss}$  remains an order of magnitude smaller than the other sinks.

One possible reason for the decrease in energy dissipation over the GS region in TD is the decrease in eddy KE (EKE; where perturbations are measured as deviations from the 3-month mean), in particular from Cape Hatteras to 60°W (Figure 3g). Paradoxically, the reduction of EKE is caused by increased dissipation by barotropic tides over the entire domain, which stabilizes the GS and thus reduces energy conversion to mesoscale eddies. We noted a 2.35% reduction in EKE over the entire domain (and a 0.23% reduction over the GS). Although these percentages seem small, a strong correspondence is found between the NTD-TD EKE difference (Figure 1g) and the NTD-TD  $F_b K_b$  difference (not shown). A positive difference in EKE translates into a negative difference in  $F_b K_b$ , with an estimated correlation coefficient of  $-0.6$ . Over the entire deep ocean domain (i.e., the area deeper than 200 m, corresponding to the thick dark green line in Figure 2),  $F_b K_b$ ,  $H_{Diff}$  and  $I_{Diss}$  increase by 11%, 15%, and 182%, respectively, when tides are present (TD).

## 6. Discussion and Conclusion

In this study, we described the effects of tides on the KE pathway of the GS using two submesoscale permitting (2 km) ocean models, TD and NTD. We analyzed the cross-scale KE flux using a coarse-graining approach.

Although significant throughout the year, the impact of tides on energy transfer seems to be greatest in summer, which is in line with Rocha et al. (2016), Barkan et al. (2021). In summer, over the GS region, the cross-scale KE flux from the tidal simulation shows a decrease in the inverse cascade and an increase in the forward cascade, which is explained by an increase in unbalanced (ageostrophic) advection.

A decomposition between high-frequency and low-frequency currents ( $\geq 1$  day) shows that the intensification of the forward cascade in TD is mainly driven by internal tides. When the high-frequency currents are filtered out, the cross-scale KE flux in TD is much closer to that estimated in NTD. The remaining difference can be attributed to non-tidal features (NIW and high-frequency range of submesoscale eddies) and possibly, to a lesser extent, to the residual tidal signals, imperfectly eliminated by the temporal filter.

Previous studies have suggested that wave-wave and wave-flow interactions can both produce a forward cascade (Alford et al., 2016). If we associate  $\Pi_{CT}$  (unbalanced advection of balanced flow) with wave-flow interaction and  $\Pi(\mathbf{u}_d)$  (unbalanced advection of unbalanced flow) with wave-wave interaction, and since  $\Pi_{CT} \gg \Pi(\mathbf{u}_d)$ , we confirm here that wave-flow interaction has the greatest contribution to the forward cascade. This is also supported by the forward cascade intensification around 40°N and 60°W (Figure 2) where significant interaction between internal tides and the GS has been suggested by Kelly et al. (2016). The specific mechanisms involved in the wave-flow interaction are unclear, but  $\Pi_{CT}$  is consistent with the stimulated imbalance process proposed by Barkan et al. (2017), where externally forced internal waves stimulates a transfer of energy from mesoscale to submesoscale eddies. Future work should attempt to clarify this point.

In winter, the impact of the tides is the same as in summer, but less intense, that is, the intensification (weakening) of the forward (inverse) cascade is lower. The forward cascade without the contribution of internal waves (generated by both tides and winds) decreases by 47% and 26% at 9 and 22 km scales (where the forward cascade dominates). These numbers are lower than in summer, but are significant.

Early tidal models were decoupled to the wind-driven ocean general circulation (Hendershott, 1972; Hibiya et al., 2006; Simmons, 2008). It is now more common to use models that combine the two dynamics, such as CROCO (Barkan et al., 2021; Delpech et al., 2023; Renault & Marchesiello, 2022), Massachusetts Institute of Technology general circulation model (MITgcm; Rocha et al., 2016), and Hybrid Coordinate Ocean Model (HYCOM; Arbic et al., 2010). The inclusion of tides improves the representation of low-frequency ocean dynamics (Arbic et al., 2012; Chavanne et al., 2010; Padman et al., 2006; Park & Watts, 2006), but regional ocean models often fail to accurately reproduce high-frequency observations (Kumar et al., 2019; Mazloff et al., 2020; Nelson et al., 2020; Siyanbola et al., 2023). Here too, internal tides and their effects may be under-represented. One possible improvement is to include the forcing of remotely generated internal tides in the open boundary conditions (Nelson et al., 2020; Siyanbola et al., 2023). However, care must be taken when implementing the boundary conditions to avoid excessive reflection of internal waves from the interior, which would falsely increase the internal wave energy (Siyanbola et al., 2023).

Despite possible caveats in the methodology, the present results convincingly assess the role that tides would play in the energy balance of the GS circulation. They demonstrate a large change in the turbulent cascade, although the forward cascade as a dissipation pathway remains weaker than frictional dissipation near surface and bottom boundaries. Besides, bottom dissipation of the subtidal circulation is also increased by barotropic tides in the deep ocean, which may seem contradictory to the assumption that barotropic tides in the deep ocean decay mainly by conversion to baroclinic tides (Egbert & Ray, 2003). Overall, our results seem to confirm that the ocean's KE tends to dissipate mainly near its boundaries, and that ocean models should probably pay more attention to the treatment of bottom topography and friction, air-sea coupling processes and numerical dissipation.

### Data Availability Statement

CROCO model is available at Auclair et al. (2022). The data to reproduce the figures are available at Contreras et al. (2023a).

**Acknowledgments**

M. Contreras was supported by Becas Chile from ANID (Agencia Nacional de Investigación y Desarrollo; CONICYT-PFCHA/Doctorado Becas Chile/2020-72210196). We appreciate support from the Centre National d'Étude Spatial through the TOSCA projects I-CASCADE and M-ODYSEA, and from LEFE VENUS and the GdR CROCO and GdRI CROCO. The model and calculations were executed at GENCI (project 13051). We appreciate the suggestions of the two anonymous reviewers, which improved the quality of our manuscript.

**References**

Alford, M. H., MacKinnon, J. A., Simmons, H. L., & Nash, J. D. (2016). Near-inertial internal gravity waves in the ocean. *Annual Review of Marine Science*, 8(1), 95–123. <https://doi.org/10.1146/annurev-marine-010814-015746>

Aluie, H., Hecht, M., & Vallis, G. K. (2018). Mapping the energy cascade in the North Atlantic Ocean: The coarse-graining approach. *Journal of Physical Oceanography*, 48(2), 225–244. <https://doi.org/10.1175/jpo-d-17-0100.1>

Arbic, B. K., Flierl, G. R., & Scott, R. B. (2007). Cascade inequalities for forced–dissipated geostrophic turbulence. *Journal of Physical Oceanography*, 37(6), 1470–1487. <https://doi.org/10.1175/jpo3067.1>

Arbic, B. K., Richman, J. G., Shriver, J. F., Timko, P. G., Metzger, E. J., & Wallcraft, A. J. (2012). Global modeling of internal tides: Within an eddy ocean general circulation model. *Oceanography*, 25(2), 20–29. <https://doi.org/10.5670/oceanog.2012.38>

Arbic, B. K., Shriver, J. F., Hogan, P. J., Hurlburt, H. E., McClean, J. L., Metzger, E. J., et al. (2009). Estimates of bottom flows and bottom boundary layer dissipation of the oceanic general circulation from global high-resolution models. *Journal of Geophysical Research*, 114(C2), C02024. <https://doi.org/10.1029/2008jc005072>

Arbic, B. K., Wallcraft, A. J., & Metzger, E. J. (2010). Concurrent simulation of the eddy general circulation and tides in a global ocean model. *Ocean Modelling*, 32(3–4), 175–187. <https://doi.org/10.1016/j.ocemod.2010.01.007>

Auclair, F., Benschila, R., Bordoiso, L., Boutet, M., Brémond, M., Caillaud, M., et al. (2022). Coastal and regional ocean community model [Software]. Zenodo. <https://doi.org/10.5281/zenodo.7415343>

Barkan, R., Srinivasan, K., Yang, L., McWilliams, J. C., Gula, J., & Vic, C. (2021). Oceanic mesoscale eddy depletion catalyzed by internal waves. *Geophysical Research Letters*, 48(18), e2021GL094376. <https://doi.org/10.1029/2021gl094376>

Barkan, R., Winters, K. B., & McWilliams, J. C. (2017). Stimulated imbalance and the enhancement of eddy kinetic energy dissipation by internal waves. *Journal of Physical Oceanography*, 47(1), 181–198. <https://doi.org/10.1175/jpo-d-16-0117.1>

Barkan, R., Winters, K. B., & Smith, S. G. L. (2015). Energy cascades and loss of balance in a reentrant channel forced by wind stress and buoyancy fluxes. *Journal of Physical Oceanography*, 45(1), 272–293. <https://doi.org/10.1175/jpo-d-14-0068.1>

Brown, W. (2011). Winter variability in the western gulf of Maine: Part 1: Internal tides. *Dynamics of Atmospheres and Oceans*, 52(1–2), 224–249. <https://doi.org/10.1016/j.dynatmoce.2011.03.004>

Brügemann, N., & Eden, C. (2015). Routes to dissipation under different dynamical conditions. *Journal of Physical Oceanography*, 45(8), 2149–2168. <https://doi.org/10.1175/jpo-d-14-0205.1>

Bryan, F. O., Hecht, M. W., & Smith, R. D. (2007). Resolution convergence and sensitivity studies with North Atlantic circulation models. Part I: The western boundary current system. *Ocean Modelling*, 16(3–4), 141–159. <https://doi.org/10.1016/j.ocemod.2006.08.005>

Bühler, O., & McIntyre, M. E. (2005). Wave capture and wave–vortex duality. *Journal of Fluid Mechanics*, 534, 67–95. <https://doi.org/10.1017/s0022112005004374>

Callies, J., Ferrari, R., Klymak, J. M., & Gula, J. (2015). Seasonality in submesoscale turbulence. *Nature Communications*, 6(1), 6862. <https://doi.org/10.1038/ncomms7862>

Capet, X., McWilliams, J. C., Molemaker, M. J., & Shchepetkin, A. F. (2008). Mesoscale to submesoscale transition in the California current system. Part III: Energy balance and flux. *Journal of Physical Oceanography*, 38(10), 2256–2269. <https://doi.org/10.1175/2008jpo3810.1>

Capet, X., Roulet, G., Klein, P., & Maze, G. (2016). Intensification of upper-ocean submesoscale turbulence through charney baroclinic instability. *Journal of Physical Oceanography*, 46(11), 3365–3384. <https://doi.org/10.1175/jpo-d-16-0050.1>

Chassignet, E. P., & Marshall, D. P. (2008). Gulf stream separation in numerical ocean models. In *Geophysical Monograph Series* (Vol. 177).

Chassignet, E. P., & Xu, X. (2017). Impact of horizontal resolution (1/12 to 1/50) on gulf stream separation, penetration, and variability. *Journal of Physical Oceanography*, 47(8), 1999–2021. <https://doi.org/10.1175/jpo-d-17-0031.1>

Chassignet, E. P., Xu, X., Bozec, A., & Uchida, T. (2023). Impact of the New England seamount chain on gulf stream pathway and variability. *Journal of Physical Oceanography*, 53(8), 1871–1886. <https://doi.org/10.1175/jpo-d-23-0008.1>

Chavanne, C., Flament, P., Luther, D., & Gurgel, K. (2010). The surface expression of semidiurnal internal tides near a strong source at Hawaii. Part II: Interactions with mesoscale currents. *Journal of Physical Oceanography*, 40(6), 1180–1200. <https://doi.org/10.1175/2010jpo4223.1>

Chen, C., Huang, H., Beardsley, R. C., Xu, Q., Limeburner, R., Cowles, G. W., et al. (2011). Tidal dynamics in the gulf of Maine and New England shelf: An application of FVCOM. *Journal of Geophysical Research*, 116(C12), C12010. <https://doi.org/10.1029/2011jc007054>

Contreras, M., Pizarro, O., Dewitte, B., Sepulveda, H. H., & Renault, L. (2019). Subsurface mesoscale eddy generation in the ocean off Central Chile. *Journal of Geophysical Research: Oceans*, 124(8), 5700–5722. <https://doi.org/10.1029/2018jc014723>

Contreras, M., Renault, L., & Marchesiello, P. (2023a). Tidal modulation of cross-scale kinetic energy fluxes in the gulf stream [Dataset]. Figshare. <https://doi.org/10.6084/m9.figshare.23393267>

Contreras, M., Renault, L., & Marchesiello, P. (2023b). Understanding energy pathways in the gulf stream. *Journal of Physical Oceanography*, 53(3), 719–736. <https://doi.org/10.1175/jpo-d-22-0146.1>

Debreu, L., Kevlahan, N.-R., & Marchesiello, P. (2022). Improved gulf stream separation through brinkman penalization. *Ocean Modelling*, 179, 102121. <https://doi.org/10.1016/j.ocemod.2022.102121>

Debreu, L., Marchesiello, P., Penven, P., & Cambon, G. (2012). Two-way nesting in split-explicit ocean models: Algorithms, implementation and validation. *Ocean Modelling*, 49, 1–21. <https://doi.org/10.1016/j.ocemod.2012.03.003>

Delpach, A., Barkan, R., Renault, L., McWilliams, J., Siyanbola, O. Q., Buijsman, M. C., & Arbic, B. K. (2023). Wind-current feedback is an energy sink for oceanic internal waves. *Scientific Reports*, 13(1), 5915. <https://doi.org/10.1038/s41598-023-32909-6>

Ducet, N., Le Traon, P. Y., & Reverdin, G. (2000). Global high-resolution mapping of ocean circulation from TOPEX/Poseidon and ERS-1 and -2. *Journal of Geophysical Research*, 105(C8), 19477–19498. <https://doi.org/10.1029/2000jc900063>

Duda, T. F., Lin, Y.-T., Buijsman, M., & Newhall, A. E. (2018). Internal tidal modal ray refraction and energy ducting in baroclinic gulf stream currents. *Journal of Physical Oceanography*, 48(9), 1969–1993. <https://doi.org/10.1175/jpo-d-18-0031.1>

Dunphy, M., & Lamb, K. G. (2014). Focusing and vertical mode scattering of the first mode internal tide by mesoscale eddy interaction. *Journal of Geophysical Research: Oceans*, 119(1), 523–536. <https://doi.org/10.1002/2013jc009293>

Egbert, G. D., & Erofeeva, S. Y. (2002). Efficient inverse modeling of Barotropic Ocean tides. *Journal of Atmospheric and Oceanic Technology*, 19(2), 183–204. [https://doi.org/10.1175/1520-0426\(2002\)019<0183:eimob>2.0.co;2](https://doi.org/10.1175/1520-0426(2002)019<0183:eimob>2.0.co;2)

Egbert, G. D., & Ray, R. D. (2000). Significant dissipation of tidal energy in the deep ocean inferred from satellite altimeter data. *Nature*, 405(6788), 775–778. <https://doi.org/10.1038/35015531>

Egbert, G. D., & Ray, R. D. (2003). Semi-diurnal and diurnal tidal dissipation from topex/poseidon altimetry. *Geophysical Research Letters*, 30(17), 1907. <https://doi.org/10.1029/2003gl017676>

Ferrari, R., & Wunsch, C. (2009). Ocean circulation kinetic energy: Reservoirs, sources, and sinks. *Annual Review of Fluid Mechanics*, 41(1), 253–282. <https://doi.org/10.1146/annurev.fluid.40.1.11406.102139>

- Garrett, C., & Kunze, E. (2007). Internal tide generation in the deep ocean. *Annual Review of Fluid Mechanics*, 39(1), 57–87. <https://doi.org/10.1146/annurev.fluid.39.050905.110227>
- Gula, J., Molemaker, M. J., & McWilliams, J. C. (2015). Gulf stream dynamics along the southeastern us seaboard. *Journal of Physical Oceanography*, 45(3), 690–715. <https://doi.org/10.1175/jpo-d-14-0154.1>
- Gula, J., Molemaker, M. J., & McWilliams, J. C. (2016). Submesoscale dynamics of a gulf stream frontal eddy in the South Atlantic bight. *Journal of Physical Oceanography*, 46(1), 305–325. <https://doi.org/10.1175/jpo-d-14-0258.1>
- Haine, T. W. N., & Marshall, J. (1998). Gravitational, symmetric, and baroclinic instability of the ocean mixed layer. *Journal of Physical Oceanography*, 28(4), 634–658. [https://doi.org/10.1175/1520-0485\(1998\)028<0634:gsabio>2.0.co;2](https://doi.org/10.1175/1520-0485(1998)028<0634:gsabio>2.0.co;2)
- Hendershott, M. (1972). The effects of solid Earth deformation on global ocean tides. *Geophysical Journal International*, 29(4), 389–402. <https://doi.org/10.1111/j.1365-246x.1972.tb06167.x>
- Hibiya, T., Nagasawa, M., & Niwa, Y. (2006). Global mapping of diapycnal diffusivity in the deep ocean based on the results of expendable current profiler (XCP) surveys. *Geophysical Research Letters*, 33(3), L03611. <https://doi.org/10.1029/2005gl025218>
- Katavouta, A., Thompson, K. R., Lu, Y., & Loder, J. W. (2016). Interaction between the tidal and seasonal variability of the gulf of Maine and Scotian shelf region. *Journal of Physical Oceanography*, 46(11), 3279–3298. <https://doi.org/10.1175/jpo-d-15-0091.1>
- Kelly, S. M., Lermusiaux, P. F., Duda, T. F., & Haley, P. J., Jr. (2016). A coupled-mode shallow-water model for tidal analysis: Internal tide reflection and refraction by the gulf stream. *Journal of Physical Oceanography*, 46(12), 3661–3679. <https://doi.org/10.1175/jpo-d-16-0018.1>
- Klein, P., Hua, B. L., Lapeyre, G., Capet, X., Le Gentil, S., & Sasaki, H. (2008). Upper ocean turbulence from high-resolution 3d simulations. *Journal of Physical Oceanography*, 38(8), 1748–1763. <https://doi.org/10.1175/2007jpo3773.1>
- Kumar, N., Suanda, S. H., Colosi, J. A., Haas, K., Di Lorenzo, E., Miller, A. J., & Edwards, C. A. (2019). Coastal semidiurnal internal tidal incoherence in the Santa Maria basin, California: Observations and model simulations. *Journal of Geophysical Research: Oceans*, 124(7), 5158–5179. <https://doi.org/10.1029/2018jc014891>
- Le Provost, C., & Lyard, F. (1997). Energetics of the  $M_2$  Barotropic Ocean tides: An estimate of bottom friction dissipation from a hydrodynamic model. *Progress in Oceanography*, 40(1–4), 37–52. [https://doi.org/10.1016/s0079-6611\(97\)00022-0](https://doi.org/10.1016/s0079-6611(97)00022-0)
- Loder, J. W., & Greenberg, D. A. (1986). Predicted positions of tidal fronts in the gulf of Maine region. *Continental Shelf Research*, 6(3), 397–414. [https://doi.org/10.1016/0278-4343\(86\)90080-4](https://doi.org/10.1016/0278-4343(86)90080-4)
- MacKinnon, J. A., & Winters, K. (2005). Subtropical catastrophe: Significant loss of low-mode tidal energy at 28.9°. *Geophysical Research Letters*, 32(15), L15605. <https://doi.org/10.1029/2005gl023376>
- Marchesiello, P., McWilliams, J. C., & Shchepetkin, A. (2001). Open boundary conditions for long-term integration of regional oceanic models. *Ocean Modelling*, 3(1–2), 1–20. [https://doi.org/10.1016/s1463-5003\(00\)00013-5](https://doi.org/10.1016/s1463-5003(00)00013-5)
- Mazloff, M. R., Cornuelle, B., Gille, S. T., & Wang, J. (2020). The importance of remote forcing for regional modeling of internal waves. *Journal of Geophysical Research: Oceans*, 125(2), e2019JC015623. <https://doi.org/10.1029/2019jc015623>
- McWilliams, J. C. (2008). The nature and consequences of oceanic eddies. *Ocean Modeling in an Eddying Regime*, 177, 5–15.
- McWilliams, J. C. (2016). Submesoscale currents in the ocean. *Proceedings of the Royal Society A: Mathematical, Physical and Engineering Sciences*, 472(2189), 20160117. <https://doi.org/10.1098/rspa.2016.0117>
- Molemaker, M. J., McWilliams, J. C., & Capet, X. (2010). Balanced and unbalanced routes to dissipation in an equilibrated eddy flow. *Journal of Fluid Mechanics*, 654, 35–63. <https://doi.org/10.1017/s0022112009993272>
- Munk, W., & Wunsch, C. (1998). Abyssal recipes II: Energetics of tidal and wind mixing. *Deep Sea Research Part I: Oceanographic Research Papers*, 45(12), 1977–2010. [https://doi.org/10.1016/s0967-0637\(98\)00070-3](https://doi.org/10.1016/s0967-0637(98)00070-3)
- Nelson, A., Arbic, B., Menemenlis, D., Peltier, W., Alford, M., Grisouard, N., & Klymak, J. (2020). Improved internal wave spectral continuum in a regional ocean model. *Journal of Geophysical Research: Oceans*, 125(5), e2019JC015974. <https://doi.org/10.1029/2019jc015974>
- Nikurashin, M., & Ferrari, R. (2010). Radiation and dissipation of internal waves generated by geostrophic motions impinging on small-scale topography: Application to the southern ocean. *Journal of Physical Oceanography*, 40(9), 2025–2042. <https://doi.org/10.1175/2010jpo4315.1>
- Özgökmen, T. M., & Chassignet, E. P. (2002). Dynamics of two-dimensional turbulent bottom gravity currents. *Journal of Physical Oceanography*, 32(5), 1460–1478. [https://doi.org/10.1175/1520-0485\(2002\)032<1460:dotdtb>2.0.co;2](https://doi.org/10.1175/1520-0485(2002)032<1460:dotdtb>2.0.co;2)
- Padman, L., Howard, S., & Muench, R. (2006). Internal tide generation along the south scotia ridge. *Deep Sea Research Part II: Topical Studies in Oceanography*, 53(1–2), 157–171. <https://doi.org/10.1016/j.dsr2.2005.07.011>
- Park, J.-H., & Watts, D. R. (2006). Internal tides in the Southwestern Japan/East sea. *Journal of Physical Oceanography*, 36(1), 22–34. <https://doi.org/10.1175/jpo2846.1>
- Rainville, L., & Pinkel, R. (2006). Propagation of low-mode internal waves through the ocean. *Journal of Physical Oceanography*, 36(6), 1220–1236. <https://doi.org/10.1175/jpo2889.1>
- Ray, R. D. (1999). *A global ocean tide model from topex/poseidon altimetry: Got99*. 2. National Aeronautics and Space Administration, Goddard Space Flight Center.
- Renault, L., & Marchesiello, P. (2022). Ocean tides can drag the atmosphere and cause tidal winds over broad continental shelves. *Communications Earth & Environment*, 3(1), 70. <https://doi.org/10.1038/s43247-022-00403-y>
- Renault, L., Marchesiello, P., & Contreras, M. (2023). Coaction of top and bottom drags in gulf stream dynamics. *Journal of Geophysical Research: Oceans*, 128(3), e2022JC018939. <https://doi.org/10.1029/2022jc018939>
- Renault, L., Marchesiello, P., Masson, S., & McWilliams, J. C. (2019). Remarkable control of western boundary currents by eddy killing, a mechanical air-sea coupling process. *Geophysical Research Letters*, 46(5), 2743–2751. <https://doi.org/10.1029/2018gl081211>
- Renault, L., Masson, S., Arsouze, T., Madec, G., & McWilliams, J. C. (2020). Recipes for how to force oceanic model dynamics. *Journal of Advances in Modeling Earth Systems*, 12(2), e2019MS001715. <https://doi.org/10.1029/2019ms001715>
- Renault, L., McWilliams, J. C., & Gula, J. (2018). Dampening of submesoscale currents by air-sea stress coupling in the Californian upwelling system. *Scientific Reports*, 8(1), 1–8. <https://doi.org/10.1038/s41598-018-31602-3>
- Renault, L., Molemaker, M. J., Gula, J., Masson, S., & McWilliams, J. C. (2016). Control and stabilization of the gulf stream by oceanic current interaction with the atmosphere. *Journal of Physical Oceanography*, 46(11), 3439–3453. <https://doi.org/10.1175/jpo-d-16-0115.1>
- Renault, L., Molemaker, M. J., McWilliams, J. C., Shchepetkin, A. F., Lemarié, F., Chelton, D., et al. (2016). Modulation of wind work by oceanic current interaction with the atmosphere. *Journal of Physical Oceanography*, 46(6), 1685–1704. <https://doi.org/10.1175/jpo-d-15-0232.1>
- Rocha, C. B., Gille, S. T., Chereskin, T. K., & Menemenlis, D. (2016). Seasonality of submesoscale dynamics in the Kuroshio extension. *Geophysical Research Letters*, 43(21), 11–304. <https://doi.org/10.1002/2016gl071349>
- Schubert, R., Gula, J., Greatbatch, R. J., Baschek, B., & Biastoch, A. (2020). The submesoscale kinetic energy cascade: Mesoscale absorption of submesoscale mixed layer eddies and frontal downscale fluxes. *Journal of Physical Oceanography*, 50(9), 2573–2589. <https://doi.org/10.1175/jpo-d-19-0311.1>

- Scott, R. B., & Wang, F. (2005). Direct evidence of an oceanic inverse kinetic energy cascade from satellite altimetry. *Journal of Physical Oceanography*, 35(9), 1650–1666. <https://doi.org/10.1175/jpo2771.1>
- Sen, A., Scott, R. B., & Arbic, B. K. (2008). Global energy dissipation rate of deep-ocean low-frequency flows by quadratic bottom boundary layer drag: Computations from current-meter data. *Geophysical Research Letters*, 35(9), L09606. <https://doi.org/10.1029/2008gl033407>
- Shakespeare, C. J., & Taylor, J. (2014). The spontaneous generation of inertia–gravity waves during frontogenesis forced by large strain: Theory. *Journal of Fluid Mechanics*, 757, 817–853. <https://doi.org/10.1017/jfm.2014.514>
- Shchepetkin, A. F., & McWilliams, J. C. (2005). The regional oceanic modeling system (ROMS): A split-explicit, free-surface, topography-following-coordinate oceanic model. *Ocean Modelling*, 9(4), 347–404. <https://doi.org/10.1016/j.ocemod.2004.08.002>
- Simmons, H. L. (2008). Spectral modification and geographic redistribution of the semi-diurnal internal tide. *Ocean Modelling*, 21(3–4), 126–138. <https://doi.org/10.1016/j.ocemod.2008.01.002>
- Siyanbola, O. Q., Buijsman, M. C., Delpech, A., Renault, L., Barkan, R., Shriver, J. F., et al. (2023). Remote internal wave forcing of regional ocean simulations near the us west coast. *Ocean Modelling*, 181, 102154. <https://doi.org/10.1016/j.ocemod.2022.102154>
- Soufflet, Y., Marchesiello, P., Lemarié, F., Jouanno, J., Capet, X., Debreu, L., & Benshila, R. (2016). On effective resolution in ocean models. *Ocean Modelling*, 98, 36–50. <https://doi.org/10.1016/j.ocemod.2015.12.004>
- Spall, M. A. (1996). Dynamics of the gulf stream/deep western boundary current crossover. Part I: Entrainment and recirculation. *Journal of Physical Oceanography*, 26(10), 2152–2168. [https://doi.org/10.1175/1520-0485\(1996\)026<2152:dotgsw>2.0.co;2](https://doi.org/10.1175/1520-0485(1996)026<2152:dotgsw>2.0.co;2)
- Srinivasan, K., Barkan, R., & McWilliams, J. C. (2022). A forward energy flux at submesoscales driven by frontogenesis. *Earth and Space Science Open Archive*, 41.
- Stewart, R. H. (2008). *Introduction to physical oceanography*. Robert H. Stewart.
- Thomas, L. N. (2012). On the effects of frontogenetic strain on symmetric instability and inertia–gravity waves. *Journal of Fluid Mechanics*, 711, 620–640. <https://doi.org/10.1017/jfm.2012.416>
- Trossman, D. S., Arbic, B. K., Straub, D. N., Richman, J. G., Chassignet, E. P., Wallcraft, A. J., & Xu, X. (2017). The role of rough topography in mediating impacts of bottom drag in eddying ocean circulation models. *Journal of Physical Oceanography*, 47(8), 1941–1959. <https://doi.org/10.1175/jpo-d-16-0229.1>
- Weatherly, G. L. (1984). An estimate of bottom frictional dissipation by gulf stream fluctuations. *Journal of Marine Research*, 42(2), 289–301. <https://doi.org/10.1357/002224084788502729>

## References From the Supporting Information

- Caldwell, P., Merrifield, M., & Thompson, P. (2015). Sea level measured by tide gauges from global oceans—the joint archive for sea level holdings (NCEI accession 0019568), version 5.5, NOAA National Centers for Environmental Information, Dataset. *Centers Environ. Information, Dataset*, 10, V5V40S47W.
- Pawlowicz, R., Beardsley, B., & Lentz, S. (2002). Classical tidal harmonic analysis including error estimates in MatLab using t\_tide. *Computers & Geosciences*, 28(8), 929–937. [https://doi.org/10.1016/s0098-3004\(02\)00013-4](https://doi.org/10.1016/s0098-3004(02)00013-4)

### 5.3 Supporting Information

# Supporting Information for 'Tidal modulation of energy dissipation routes in the Gulf Stream'

M. Contreras<sup>1</sup>, L. Renault<sup>1</sup>, and P. Marchesiello<sup>1</sup>

<sup>1</sup>LEGOS, University of Toulouse, IRD, CNRS, CNES, UPS, Toulouse, France

## Contents of this file

1. Text S1 to S2
2. Figures S1

## Introduction

In this document we evaluate the reproduction of tidal simulations (TD) compared to hydrographic and satellite data. In addition, we discussed the effects of spatial and temporal resolution in our analysis.

## Text S1.

Our results may be impacted by spatial and temporal resolution. A 3-hour averaged output is the minimum frequency required to represent tidal dynamics. We expect that a higher frequency of model output would reveal more energetic internal and barotropic tides. As a result, the interaction between barotropic tides and bottom topography would increase bottom drag, while the increased internal tides would facilitate the interaction

---

with balanced motions, intensifying the forward cascade. Conversely, increasing spatial resolution should energize submesoscale processes (see Introduction) and internal gravity waves. This could also promote the interaction of internal tides with balanced motions and associated forward cascade. In summary, an increase in spatial and temporal resolution should amplify the magnitude of cross-scale kinetic energy fluxes and energy dissipation. However, we do not anticipate any major quantitative changes that would affect our interpretation of the mechanisms involved. We leave it to further studies to examine the sensitivity of both spatial and temporal resolution.

### **Text S2.**

To evaluate TD performance, we compared TD with AVISO altimetry data (Ducet et al., 2000) and data from three coastal tide gauges provided by the University of Hawaii Sea Level Center (Caldwell et al., 2015) (Tide gauges data are available at <https://uhs1c.soest.hawaii.edu/data/>. ) (Figure S1). The mean absolute dynamic topography and mean GS path (highlighted by the  $0.5 \text{ ms}^{-1}$  contour) from TD and AVISO indicate that the model reproduces the mean circulation well (Figure S1a-b). We also analyzed the tidal components for the period 2005-2009 using 3h-averaged of sea surface height (SSH) from TD and the tide gauges (purple dots in Figure S1a-b). SSH from the tide gauges were 3h-averaged to be comparable to the TD output. The SSH spectra estimated from TD and the tide gauges indicate that the main tidal components are well reproduced by the model, showing that the most energetic tidal components are M2 (12.42 hours), K1 (23.93 hours), and O1 (25.81 hours) (Figure S1c-e). For quantitative error estimation, we also performed harmonic analyses using the T-TIDES package (Pawlowicz et al., 2002), and

estimated the difference between observed and modeled harmonic amplitudes. The M2 normalized root mean square error for all stations is about 20%. This error is acceptable for our purpose, which is to assess the interplay between tides and wind-driven circulation.

## References

- Caldwell, P., Merrifield, M., & Thompson, P. (2015). Sea level measured by tide gauges from global oceans—the joint archive for sea level holdings (ncei accession 0019568), version 5.5, noaa national centers for environmental information, dataset. *Centers Environ. Information, Dataset, 10*, V5V40S47W.
- Ducet, N., Le Traon, P.-Y., & Reverdin, G. (2000). Global high-resolution mapping of ocean circulation from topex/poseidon and ers-1 and-2. *Journal of Geophysical Research: Oceans, 105*(C8), 19477–19498.
- Pawlowicz, R., Beardsley, B., & Lentz, S. (2002). Classical tidal harmonic analysis including error estimates in matlab using t\_tide. *Computers & Geosciences, 28*(8), 929–937.

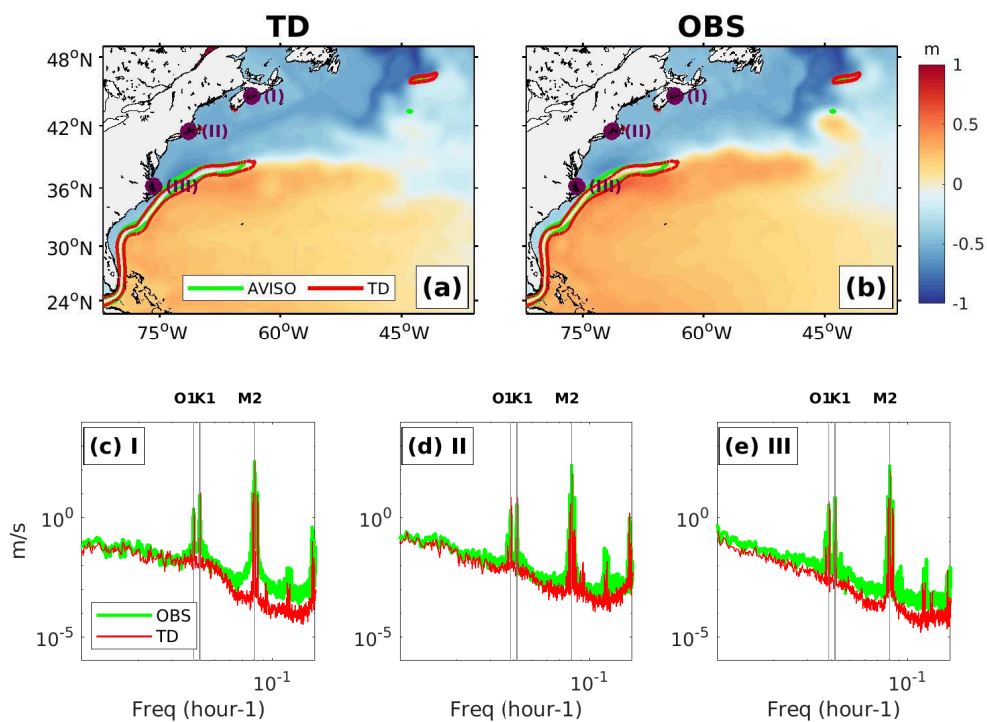


**Figure S1.** Mean dynamic topography from (a) TD and (b) AVISO. The red and green contours represent the mean GS path ( $0.5 \text{ m s}^{-1}$  contour of the mean geostrophic current) from AVISO and CROCO, respectively. The purple dots indicate the positions of the tide gauges used to evaluate the tidal signal in c-e. (c-e) SSH spectra from tide gauge data (green) and TD (red).

## 5.4 Conclusion

In this study, we used two submesoscale-permitting ocean model simulations (with tides (TD) and without tides (NTD)) to investigate the effects of tides on the KE budget of the GS. Our findings indicate that tides have an impact on cross-scale energy fluxes throughout the year, with the largest effect during the summer months. These results are consistent with previous research (Rocha et al., 2016; Barkan et al., 2021).

Compared to NTD, TD shows a decrease in the inverse cascade and an increase in the forward cascade. Chapter 4 shows that balanced motions drive the inverse cascade, whereas the forward cascade results from ageostrophic advection. The cross-scale KE flux using low-frequency currents from TD is comparable to that of NTD. This indicates that internal tides are responsible for intensifying the forward cascade.

Although the tidal increase in forward cascade is significant, it remains an order of magnitude smaller as a dissipation process than bottom and top drag or numerical dissipation, as shown in Chapter 4. Interestingly, TD shows a decrease in bottom drag across the GS. The good correlation between the patterns of EKE and bottom drag suggests that the latter's decrease is due to an increase in GS bottom dissipation due to barotropic tides throughout the domain, which stabilizes the current and reduces its energy conversion into mesoscale eddies. However, this hypothesis needs to be further investigated in future research.



# A full description of the Lorenz Energy Cycle over the Gulf Stream

---

## Contents

---

<b>6.1</b>	<b>Introduction</b>	<b>104</b>
<b>6.2</b>	<b>Models Configuration</b>	<b>105</b>
6.2.1	CROCO	106
6.2.2	WRF	107
<b>6.3</b>	<b>Energy budget equations</b>	<b>111</b>
6.3.1	Kinetic energy budget	114
6.3.2	Available Potential energy budget	115
6.3.3	Nonlocal interactions	116
6.3.4	Forcing and dissipation terms	116
6.3.5	Scale selection in the decomposition	117
<b>6.4</b>	<b>Submesoscale energy cycle</b>	<b>119</b>
6.4.1	Energy reservoirs	119
6.4.2	Lorenz Diagram	119
6.4.2.1	Background kinetic energy ( <i>BKE</i> )	119
6.4.2.2	Submesoscale kinetic energy ( <i>SKE</i> )	121
6.4.2.3	Submesoscale potential energy ( <i>SPE</i> )	123
6.4.2.4	Background potential energy ( <i>BPE</i> )	125
<b>6.5</b>	<b>Quasi-balanced and unbalanced submesoscale ranges</b>	<b>125</b>
<b>6.6</b>	<b>Seasonal Variability</b>	<b>128</b>
6.6.1	Winter	128
6.6.2	Summer	130
<b>6.7</b>	<b>Conclusion and Discussion</b>	<b>134</b>

---

### 6.1 Introduction

Understanding the GS's energy cycle is essential to improve its representation in numerical ocean models. However, the GS is a complex system in which multiple mechanisms such as that of wind-driven circulation, topographic steering, mesoscale eddy-mean flow interaction and air-sea coupling, have a significant impact on the system across different temporal and spatial scales (Spall, 1996; Chassignet and Marshall, 2008; Özgökmen and Chassignet, 2002; Gula et al., 2015b, 2016; Renault et al., 2016a). These mechanisms can convert potential to kinetic energy at injection scales, and transfer this energy either to smaller scales (forward cascade) or to larger scales (inverse cascade).

Intense mesoscale eddy activity is observed along the GS flowing eastward past its separation at Cape Hatteras. Mesoscale eddies are formed through baroclinic instabilities, which convert potential energy (PE) to kinetic energy (KE), and barotropic instabilities that extract kinetic energy from the mean flow (Kang and Curchitser, 2015). These vortices can interact with each other, merge, and transfer KE on a large scale. Mesoscale eddy stirring also modifies the surface density field and transfers PE to smaller scales via frontogenesis, which leads to submesoscale instabilities. These mechanisms can transfer PE across the submesoscale range and help its conversion to KE.

Recent studies have focused on submesoscale processes. At this scale, the effect of rotation and stratification are weak. As a result, vertical velocities associated with ageostrophic (unbalanced) motions become significant and affect the turbulent cascade. Unbalanced advection enables a downscale KE flux (Capet et al., 2008a; Molemaker et al., 2010; Srinivasan et al., 2022; Contreras et al., 2023b). The associated mechanisms are frontogenesis, mixed layer instabilities (MLIs), Charney instabilities, and a family of ageostrophic instabilities (Capet et al., 2008c; Klein et al., 2008; McWilliams, 2016). On the other hand, submesoscale motions may also contribute to mesoscale re-energization, *e.g.*, through absorption of mixed layer eddies (MLEs) (Qiu et al., 2014; Schubert et al., 2020). However, the overall importance of submesoscale processes in the energy budget is not fully documented.

Air-sea interactions can also modify the energy budget through two mechanisms: current feedback (CFB) and thermal feedback (TFB). CFB results from the interaction between surface currents and wind stress (top drag). This interaction results in a reduction of the KE by about 30% (Renault et al., 2016a, 2018), which affects the inverse cascade (Renault et al., 2019b). TFB is essentially the atmospheric boundary layer response to SST gradients (Small et al., 2008; Chelton et al., 2004; O'Neill et al., 2010; Seo et al., 2023). It has two main direct effects. First, it can affect wind stress in regions with strong SST gradients, such as frontal regions, as winds blowing over warm (cold) water are accelerated (decelerated). A linear relationship between the crosswind (downwind) SST gradient and mesoscale wind stress curl (divergence) is observed (Chelton et al., 2004; O'Neill et al., 2010). On the other hand, TFB can modulate the turbulent surface heat flux, and thus the PE reservoir. According to Ma et al. (2016), the interplay between SST and net heat flux over mesoscale eddies results in a depletion of eddy available potential energy (*EPE*), which translates into a reduction in eddy kinetic energy (*EKE*). This depletion of *EPE* was also noted by Bishop et al. (2020),

who attributes a 0.1 TW global sink of  $EPE$  to this mechanism. Recently, Renault et al. (2023b) confirmed the mechanism and showed that the reduction of  $EKE$  is mainly situated within the surface layer of the ocean and that a lack of TFB in models is partially offset by more negative eddy wind work.

Lorenz (1955) proposed a diagram to represent the energy cycle that summarizes the conversion, sink and source of KE and PE. The diagram was initially created for the atmospheric energy cycle, but has since been employed in oceanic contexts. Von Storch et al. (2012) estimate the terms of the Lorenz diagram using a global air-sea coupled simulation with a horizontal resolution of  $1/10^\circ$ . Chen et al. (2014) proposed a modification of the diagram to show the impact of non-local energy production on cross-scale energy transfer (more details in Section 6.3.3). A Lorenz energy diagram was also estimated for the GS region by Kang and Curchitser (2015) using a 7 km resolution forced ocean simulation. The results confirm the essential contribution of barotropic and baroclinic instabilities to balanced dynamics. More recently, Cao et al. (2021) described the submesoscale energy cycle over 2-week using a high-resolution oceanic simulation (0.5 km) over the Kuroshio current. The authors found that potential energy is a key source of submesoscale KE. However, to our knowledge, no study has included air-sea interactions in a complete Lorenz diagram describing balanced (planetary scale and mesoscale) and submesoscale energy cycles.

Our aim is to provide a comprehensive description of the submesoscale energy cycle under realistic high-energy conditions in the GS, including air-sea interaction. We use a 700-m resolution, coupled air-sea simulation (WRF-CROCO), described in Section 2. Then, in Section 3, we derive the terms of the Lorenz diagrams from the energy budget equation. Application to the GS is presented in Section 4. To analyze the dual role of submesoscale motions in the direct and inverse energy cascades, we analyze two definitions of the submesoscale range starting at 16 or 8 km (Section 5). In Section 6, we describe the seasonal variability of the energy budget. Finally, Section 7 presents our conclusions and a discussion.

## 6.2 Models Configuration

A coupled ocean-atmosphere model is used to perform an energy budget analysis across the GS. The Coastal and Regional Ocean Community (CROCO) model (Shchepetkin and McWilliams, 2005; Debreu et al., 2012) is used for the oceanic simulation, and the Weather Research and Forecasting (WRF) model (Skamarock et al., 2008) for the atmospheric simulation. The models are coupled through the OASIS3-MCTV3 coupler (Craig et al., 2017) and exchange data every hour. CROCO sends hourly averaged SST and surface currents to WRF, which sends in return freshwater, heat, and momentum fluxes to CROCO.

The CROCO domain extends from  $34^\circ$  to  $42.9^\circ\text{N}$  and from  $78.6^\circ$  to  $55.2^\circ\text{W}$  (Figure 3.2) with a horizontal resolution of  $1/126^\circ$  ( $\sim 700$  m). The WRF domain is extended by  $0.1^\circ$  around the CROCO domain to avoid coupling with the WRF sponge layer. The horizontal resolution of WRF is 2 km.

## Chapter 6. A full description of the Lorenz Energy Cycle over the Gulf Stream

The simulation is conducted for the period between April 2005 and April 2006 with a spin-up period in the first month. The analysis covers a full year, from May 2005 to April 2006, using 3-hour average output. The models and their setup are described below.

### 6.2.1 CROCO

CROCO is a free-surface, terrain-following coordinate model with split-explicit time stepping. The Boussinesq and hydrostatic approximation version is used, and the equations are discretized using high-order numerical methods. A third-order predictor-corrector time stepping algorithm and fifth-order upstream biased momentum advection allow reducing numerical dispersion and diffusion to achieve an effective resolution of about 5 times the horizontal resolution (Soufflet et al., 2016; Menesguen et al., 2018). The lateral advection of tracers is discretized with the rotated split third-order upstream scheme (Marchesiello et al., 2009; Lemarié et al., 2012). A nonlocal planetary K-profile boundary layer (KPP) scheme (Large et al., 1994) parameterizes the vertical subgrid-scale eddy viscosity at the surface, bottom, and interior of the ocean. The bottom drag is quadratic and parameterized through a logarithmic law of the wall with a roughness length of  $Z_{0b} = 5 \cdot 10^{-3}$ .

The topography is obtained from Shuttle Radar Topography Mission (SRTM15-plus), which is a global bathymetric dataset with a nominal resolution of 15 arc/s (0.5 km) ([http://topex.ucsd.edu/WWW\\_html/srtm30\\_plus.html](http://topex.ucsd.edu/WWW_html/srtm30_plus.html)). To reduce errors associated with the pressure gradient in a terrain-following coordinate model — in addition to the high-order correction scheme of Shchepetkin and McWilliams (2003) — the bottom topography is interpolated on the model grid and its slope is selectively smoothed when the  $r$ -factor  $\delta h/h$  exceeds 0.2, where  $h$  is bottom depth and  $\delta h$  is its horizontal variation between two grid points (Penven et al., 2005). We use 80  $\sigma$ -levels in the vertical direction, with stretching parameters  $h_{cline} = 200m$ ,  $\theta_s = 7$  and  $\theta_b = 2$  (Shchepetkin and McWilliams, 2009).

The initial and lateral boundary forcing for the simulation were obtained from a CROCO simulation at a submesoscale-permitting resolution of 2 km, including tidal forcing. This lower-resolution model domain is shown in Figure 3.2, and the configuration is described in Chapter 5 of this thesis or in Contreras et al. (2023b). Boundary forcing is introduced by open boundary conditions consisting of an active-passive 2D radiation scheme for the baroclinic mode and tracers (temperature  $T$  and salinity  $S$ ), and a modified Flather-type scheme for the barotropic mode (Marchesiello et al., 2001). Surface momentum, heat, and freshwater fluxes are received from WRF.

As the ocean model requires a longer spin-up than the atmospheric model, CROCO was run alone three months before the coupled model (from January 2005 to March 2005). This was done using surface atmospheric fields from the hourly ECMWF Reanalysis v5 (ERA5), at approximately 25 km resolution; (Heiderich and Todd, 2020) to estimate surface momentum, heat, and freshwater fluxes via the COARE bulk formula (Fairall et al., 2003) with a parameterized top drag (Renault et al., 2020).

The oceanic simulation is compared with observations for validation (see Chapter 5 for the

parent simulation at 2 km resolution). Figure 6.1 show the mean absolute dynamic topography from CROCO (averaged between May, 2005 - April, 2006) and AVISO data (Arbic et al., 2013). The model compares well with AVISO, but with greater spatial variability, probably due to the use of a single simulation year. We also compare the mean SST and currents with drifter data (Laurindo et al., 2017) (Figure 6.2). The mean GS path - highlighted by the contour of  $0.5 \text{ m s}^{-1}$  - is well reproduced by the model, although with more intense eastward penetration compared to the observations. In the deep water region, the model SST shows a maximum difference with drifters of less than  $2 \text{ }^\circ\text{C}$ . At the coast this difference increases to about  $3 \text{ }^\circ\text{C}$ , but this region is not the focus of our study.

### 6.2.2 WRF

The high-resolution atmospheric simulation (HR-W) of the coupled model (2 km) is a one-way offline nesting of a lower resolution simulation (LR-W). LR-W encompasses the region between  $22^\circ$  and  $49.1^\circ\text{N}$ , and  $82.5^\circ$  and  $35.4^\circ\text{W}$  (Figure 3.2) with a horizontal resolution of 6.2 km. In the vertical direction, 50 terrain-following model levels are considered with a model top pressure at 1000 Pa. The simulation is run between January 2005 and December 2007 with lateral boundary forcing from the ERA5 dataset at 1-hour intervals. SST is provided by the OSTIA satellite dataset (Donlon et al., 2012).

The physics schemes in this simulation are: WRF Single-moment 6-class (WSM6) micro-physics scheme (Hong and Lim, 2006) with the inclusion of droplet concentration (Jousse et al., 2016); KIAPS SAS (KSAS) convective scheme (Han and Pan, 2011; Kwon and Hong, 2017); Rapid Radiative Transfer Model Longwave Radiation Scheme (Mlawer et al., 1997); Dudhia shortwave radiation scheme (Dudhia, 1989); Yonsei University (YSU) Planetary Boundary Layer Scheme (Hong et al., 2006); Revised MM5 Surface Layer Scheme (Fairall et al., 2003); and Noah Land Surface Model (Mukul Tewari et al., 2004).

HR-W is forced with lateral conditions from LR-W 3-hourly averaged output. The HR-W configuration is very similar to LR-W, except for the cumulus parameterization. Due to the resolution of HR-W, which allows resolved mesoscale convection, we have utilized only the Tiedtke scheme (Tiedtke, 1989; Zhang et al., 2011) to parameterize the shallow convection.

We assessed LR-W for the period 2005-2007 by comparing heat fluxes with the OAFLUX dataset (Figure 6.3). Figure 6.3 shows that the heat fluxes are adequately reproduced by the model. The latent heat flux presents the largest difference with OAFLUX, especially to the south of the GS (Figures 6.3d-f). Differences in sensible heat flux (Figures 6.3a-c), shortwave radiation (Figures 6.3g-i), and longwave radiation (Figures 6.3j-l) are within expectations. The total heat flux shows a good match, with larger differences north of  $35^\circ\text{N}$  (Figures 6.3d-f). As a result, air temperature at 2m (T2m) is generally correctly reproduced compared to OAFLUX (Figure 6.4), with less than  $2 \text{ }^\circ\text{C}$  difference, the maximum differences being over the North American shelves, which are not a focus here.

As wind stress curl is important for GS dynamics, we also assess its reproduction in WRF in comparison with Scatterometer Ocean Wind Climatology (SCOW) estimates (Risien and

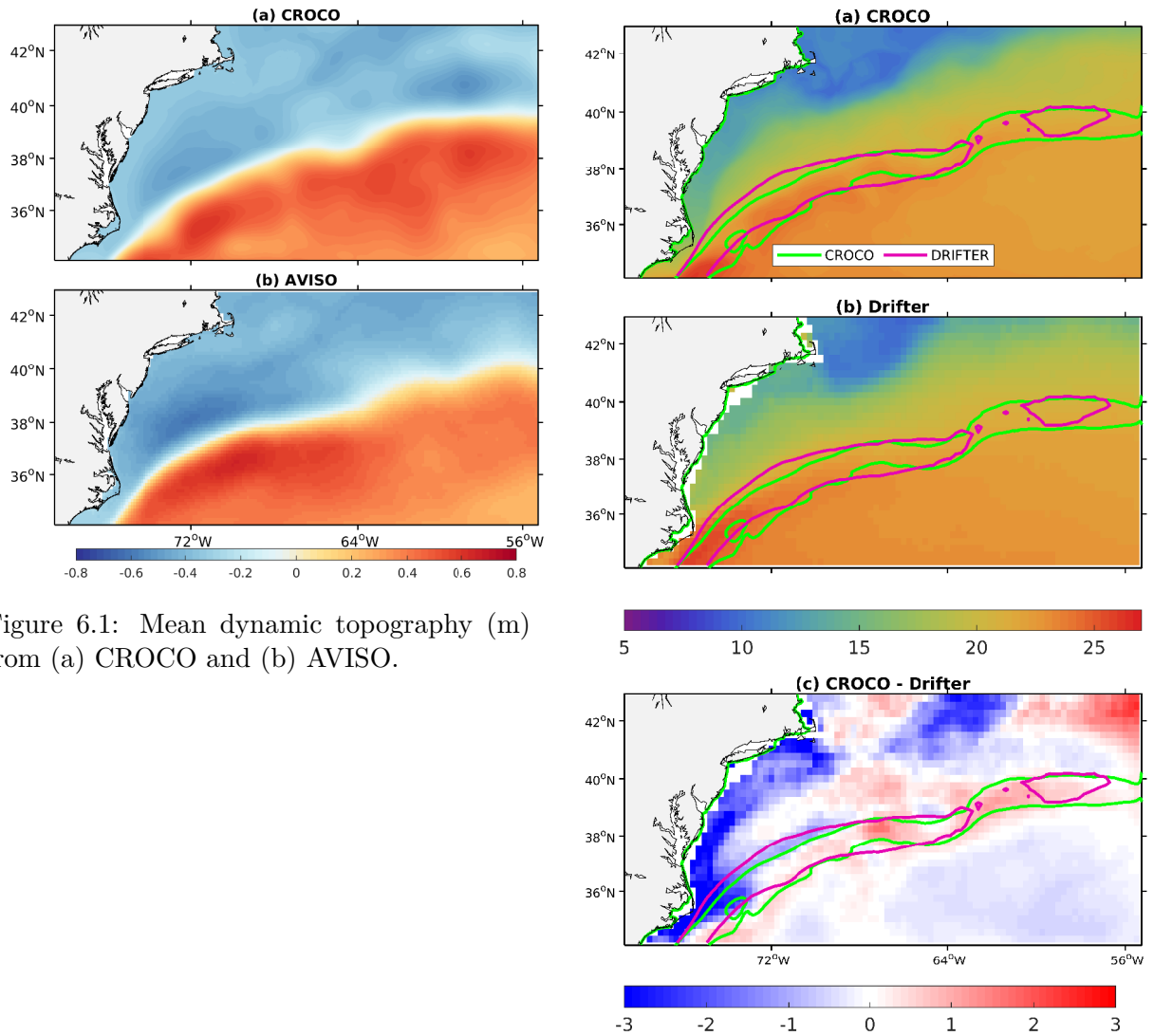


Figure 6.1: Mean dynamic topography (m) from (a) CROCO and (b) AVISO.

Figure 6.2: Sea surface temperature ( $^{\circ}C$ ) from (a) CROCO and (b) drifter data (Laurindo et al., 2017) and (c) their differences. Magenta and green contours represent the mean GS path ( $0.5 \text{ m s}^{-1}$ ).

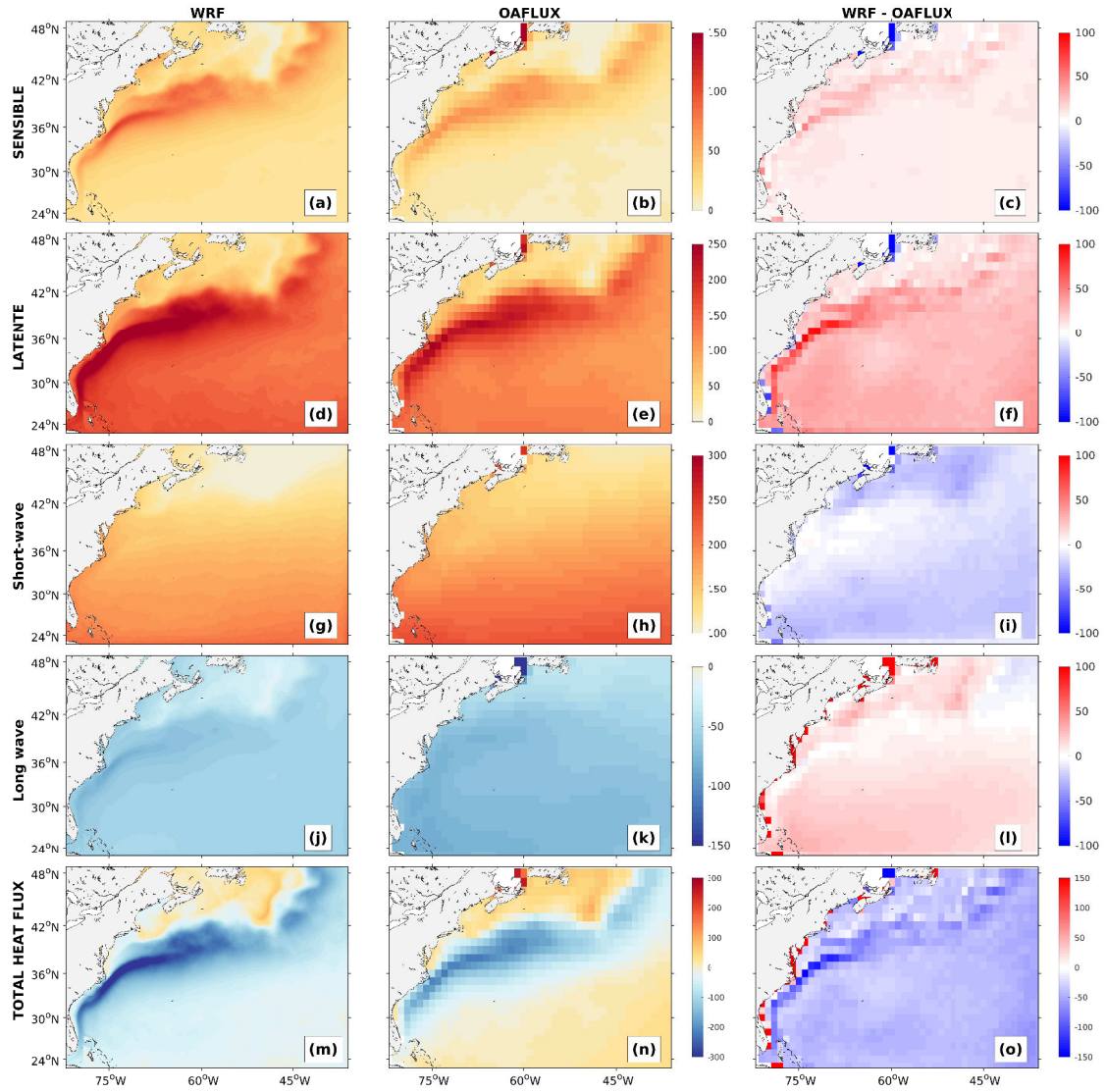


Figure 6.3: Annual-mean (2005-2007) heat fluxes ( $\text{mW m}^{-2}$ ) from: (left) low-resolution atmospheric simulation (LR-W); (middle) OAFLUX; and (right) their difference.

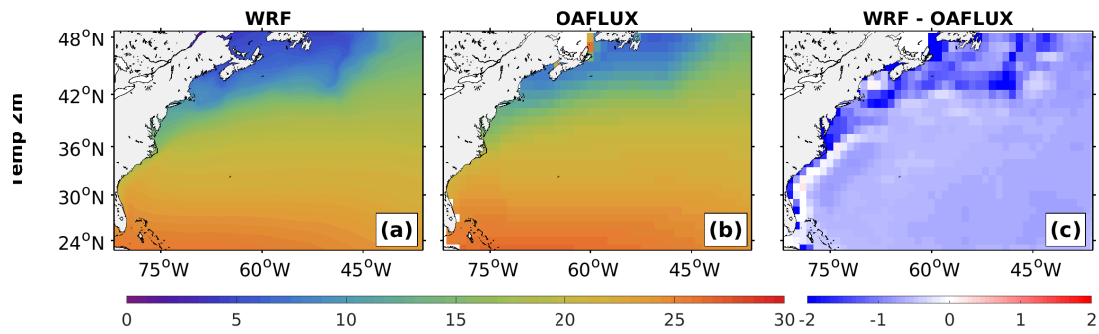


Figure 6.4: Annual-mean (2005-2007) air temperature at 2 m ( $^{\circ}\text{C}$ ) from: (a) low-resolution atmospheric simulation (LR-W); (b) OAFLUX data; and (c) their difference.

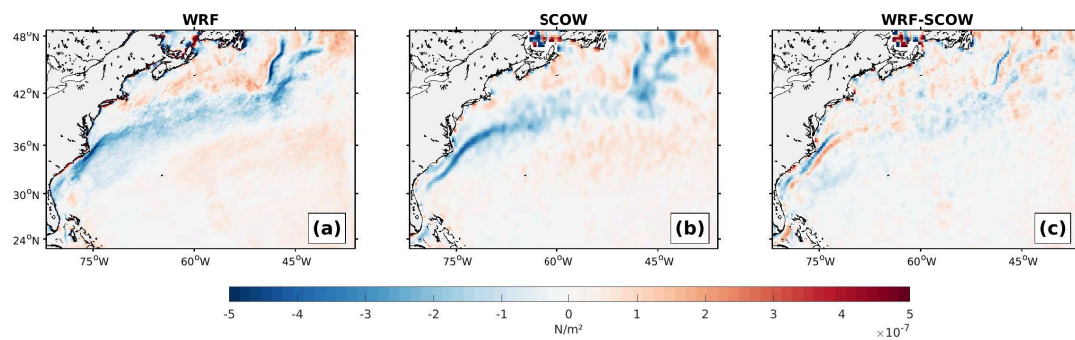


Figure 6.5: Annual-mean (2005-2007) wind stress curl ( $\text{N m}^{-2}$ ) from: (a) low-resolution atmospheric simulation (LR-W); (b) SCOW data; and (c) their difference.

Chelton, 2008). In Figure 6.5), WRF and SCOW show similar patterns and magnitude of mean wind stress curl.

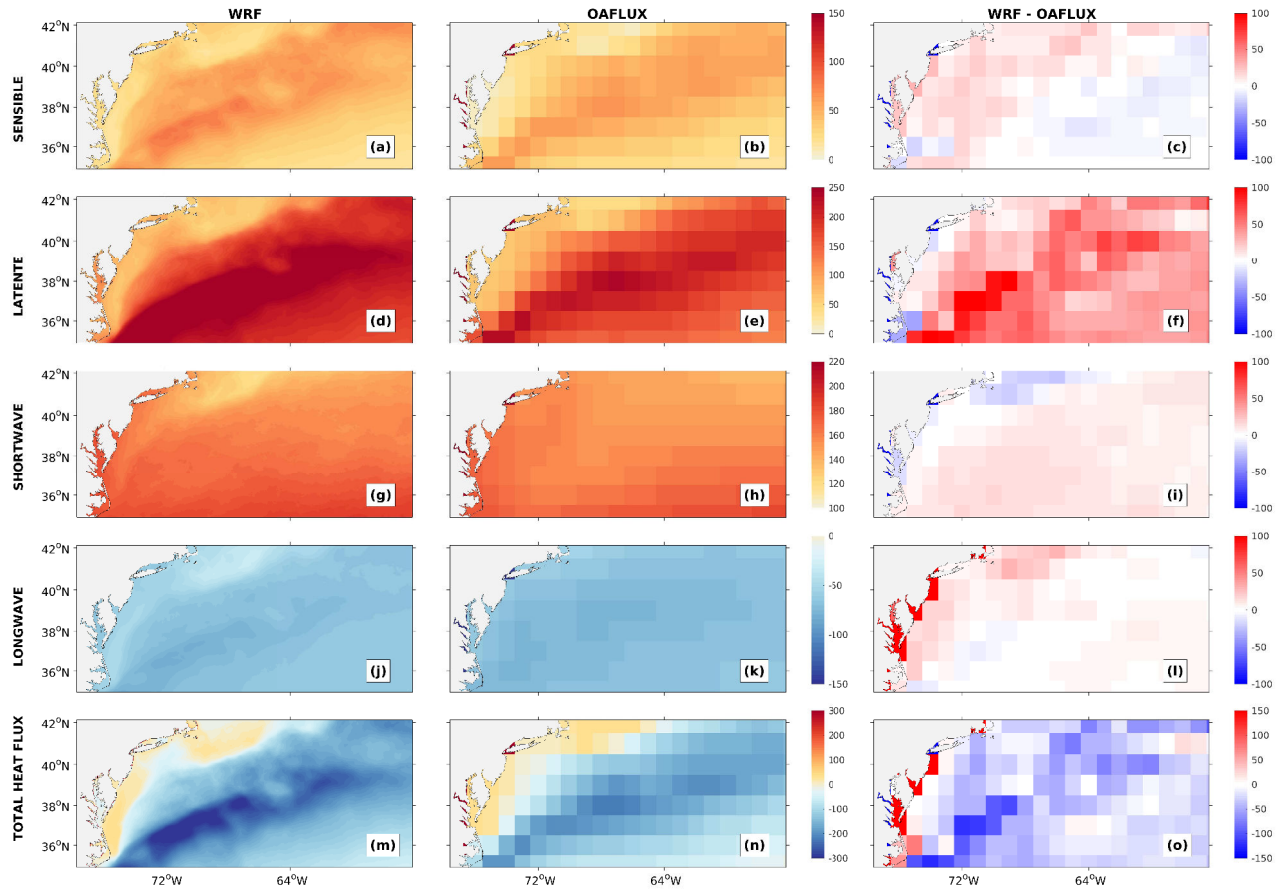


Figure 6.6: Annual-mean (May 2005-April 2006) heat fluxes ( $\text{mW m}^{-2}$ ) from: (left) high-resolution atmospheric simulation (HR-W); (middle) OAFLUX; and (right) their difference.

We reproduced the same comparison with the HR-W. Figures 6.6, 6.7 and 6.8 show that the nested simulation behaves rather similarly to the parent one. A notable exception is for solar radiation, as HR-W is cloud-resolving. HR-W appears to correct the underestimation of solar radiation in the low-resolution model (compare Figure 6.6i and 6.3i), with a slight overestimation. It should be noted that the low resolution of the observation data may affect the comparison, and small-scale differences should probably be ignored.

### 6.3 Energy budget equations

We follow previous studies that have evaluated the energy cycle through analysis of the KE and PE budgets (Kang and Curchitser, 2015; Cao et al., 2021; Von Storch et al., 2012; Chen

## Chapter 6. A full description of the Lorenz Energy Cycle over the Gulf Stream

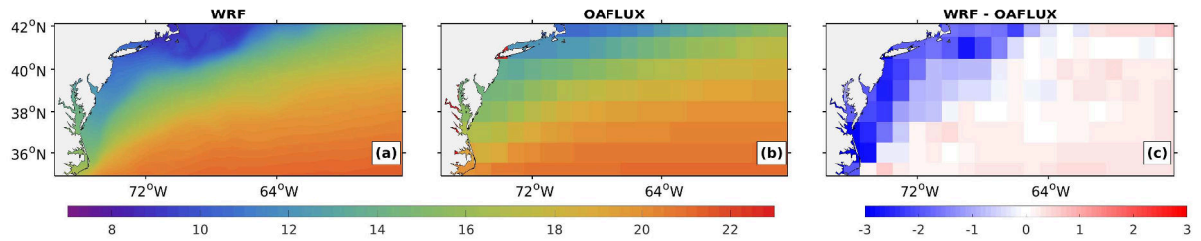


Figure 6.7: Annual-mean (May 2005-April 2006) air temperature at 2 m ( $^{\circ}\text{C}$ ) from: (a) high-resolution atmospheric simulation (HR-W); (b) OAFLUX; and (c) their difference.

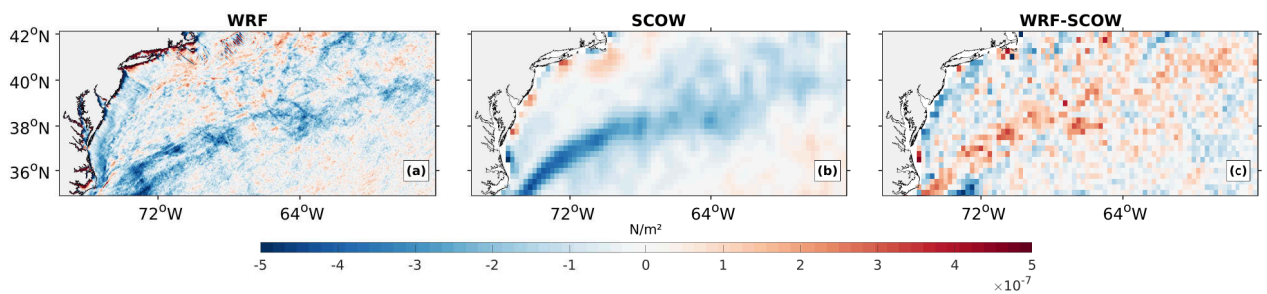


Figure 6.8: Annual-mean (May 2005-April 2006) wind stress curl ( $\text{N m}^{-2}$ ) from: (a) high-resolution atmospheric simulation (HR-W); (b) SCOW data; and (c) their difference.

et al., 2014), obtained from the hydrostatic Boussinesq (primitive) equations of motion:

$$\frac{\partial u}{\partial t} + \mathbf{u} \cdot \nabla u - fv = -\frac{1}{\rho_0} \frac{\partial p}{\partial x} + \mathcal{F}_x + \mathcal{D}_x, \quad (6.1)$$

$$\frac{\partial v}{\partial t} + \mathbf{u} \cdot \nabla v + fu = -\frac{1}{\rho_0} \frac{\partial p}{\partial y} + \mathcal{F}_y + \mathcal{D}_y, \quad (6.2)$$

$$\frac{\partial p}{\partial z} = -\rho g, \quad (6.3)$$

$$\nabla \cdot \mathbf{u} = 0, \quad (6.4)$$

$$\frac{\partial \rho}{\partial t} + \mathbf{u} \cdot \nabla \rho = \mathcal{F}_\rho + \mathcal{D}_\rho, \quad (6.5)$$

where  $\mathbf{u} = (u, v, w)$  is the velocity vector,  $f$  is Coriolis frequency,  $p$  is the pressure,  $g$  is the gravitational acceleration,  $\rho_0 = 1025 \text{ kg m}^{-3}$  is the constant reference density, and  $\mathcal{F}$  and  $\mathcal{D}$  are forcing and dissipation terms, respectively. Eq. 6.5 is a combination of the equations for temperature ( $T$ ) and salinity ( $S$ ) according to the equation of state  $\rho = \rho(T, S, z)$  defined by  $T$ ,  $S$  and depth ( $z$ ). We can decompose  $\rho$  as follows:

$$\rho(x, y, z, t) = \rho_r(z) + \rho_a(x, y, z, t), \quad (6.6)$$

where  $\rho_r$  and  $\rho_a$  are the reference and perturbation density, respectively. We define  $\rho_r$  as the density that remains constant at a specific depth and is determined by the area-mean and the time-mean values from May 2005 to April 2006.  $\rho_a$  is the residual between  $\rho$  and  $\rho_r$ . From Eq. 6.5, an equation for  $\rho_a$  is:

$$\frac{\partial \rho_a}{\partial t} + \mathbf{u} \cdot \nabla \rho_a = \frac{\rho_0 N^2}{g} w + \mathcal{F}_\rho + \mathcal{D}_\rho, \quad (6.7)$$

where  $N^2 = -\frac{g}{\rho_0} \frac{\partial \rho_r}{\partial z}$  is the buoyancy frequency.

Following Cao et al. (2021), we obtain the equations for the submesoscale kinetic and potential energy budgets by decomposing the motion between the background flow and its submesoscale perturbations (with a scale separation that will be variable here):

$$\mathbf{u} = \bar{\mathbf{u}} + \mathbf{u}', \quad (6.8)$$

where  $\bar{\mathbf{u}}$  and  $\mathbf{u}$  are the background and submesoscale component <sup>1</sup>, respectively. In the following sections, we develop the kinetic and potential energy budgets.

---

<sup>1</sup>In this chapter, the terms - and ' should not be confused with the definition of decomposition used in the coarse-graining method

### 6.3.1 Kinetic energy budget

The background kinetic energy (*BKE*) and submesoscale kinetic energy (*SKE*) are defined as:

$$BKE = \frac{1}{2}\rho_0(\bar{u}^2 + \bar{v}^2), \quad (6.9)$$

$$SKE = \frac{1}{2}\rho_0(\overline{u'^2 + v'^2}). \quad (6.10)$$

The *BKE* equation is derived by averaging the equations of motion for  $u$  and  $v$  (Eq. 6.1 and 6.2, respectively), then multiplying these results by their respective mean values ( $\bar{u}$  and  $\bar{v}$ ) and finally, adding the two equations:

$$\begin{aligned} \frac{\partial BKE}{\partial t} = \rho_0 & \underbrace{(-\nabla \cdot [\mathbf{u}BKE])}_{AK_B} - \underbrace{\frac{1}{\rho_0}\nabla \cdot (\bar{\mathbf{u}}\bar{p})}_{P_B} - \underbrace{\frac{1}{\rho_0}g\bar{\rho}_a\bar{w}}_{PK_B} \\ & + \underbrace{(u'\mathbf{u}' \cdot \nabla\bar{u} + v'\mathbf{u}' \cdot \nabla\bar{v})}_{-BSK} + BnK + DK_B + FK_B. \end{aligned} \quad (6.11)$$

The first and second terms on the right-hand side represent the transport of *BKE* due to advection ( $AK_B$ , including the horizontal and vertical terms) and pressure work ( $P_B$ ), respectively. Note that these terms can redistribute energy from one region to another, but they cannot generate or dissipate energy (Kundu et al., 2015). The third term,  $PK_B$ , converts energy from background available potential energy (*BPE*) to *BKE* through buoyancy production. The fourth term, represented by  $BSK$ , indicates the cross-scale transfer of energy between *BKE* and *SKE* resulting from Reynolds stress work, including vertical and horizontal shear terms.  $DK_B$  and  $FK_B$  are the dissipation and forcing terms for *BKE*, respectively.  $BnK$  can be interpreted as a nonlocal cross-scale flux term as proposed by Chen et al. (2014) (more details below).

The *SKE* equation is derived by subtracting the background KE Eq. 6.11 from the total KE equation:

$$\begin{aligned} \frac{\partial SKE}{\partial t} = \rho_0 & \underbrace{(-\nabla \cdot [\mathbf{u}SKE])}_{AK_S} - \underbrace{\frac{1}{\rho_0}\nabla \cdot (\bar{\mathbf{u}}'\bar{p}')}_{P_S} - \underbrace{\frac{1}{\rho_0}g\rho'_a\bar{w}'}_{PK_S} - \underbrace{-(u'\mathbf{u}' \cdot \nabla\bar{u} + v'\mathbf{u}' \cdot \nabla\bar{v})}_{BSK} \\ & + DK_S + FK_S. \end{aligned} \quad (6.12)$$

Similar to Eq. 6.11, the first two terms on the right-hand side denote the advection and pressure work contribution to the transport of *SKE*, represented by  $AK_S$  and  $P_S$ , respectively. The third term,  $PK_S$ , represents the energy transfer from submesoscale available potential energy (*SPE*) to *SKE* through buoyancy production. The fourth term,  $BSK$ , is identical to that in Eq. 6.11, but with an opposite sign. The dissipation and forcing terms of *SKE* are represented by  $DK_S$  and  $FK_S$ , respectively.

Note that the sum of the terms  $P_{B/S}$  and  $PK_{B/S}$  can be written as the product between

the current and the horizontal pressure gradient ( $PG_{B/S}$ ):

$$PG_B = P_B + PK_B$$

$$-\frac{\overline{\mathbf{u}_h}}{\rho_0} \cdot \nabla_h \bar{p} = -\frac{1}{\rho_0} \nabla \cdot (\overline{\mathbf{u}} \bar{p}) - \frac{g}{\rho_0} \overline{w} \bar{\rho}_a,$$

and

$$PG_S = P_S + PK_S$$

$$-\frac{\overline{\mathbf{u}_h'}}{\rho_0} \cdot \nabla_h p' = -\frac{1}{\rho_0} \nabla \cdot (\overline{\mathbf{u}'} p') - \frac{g}{\rho_0} \overline{w'} \rho_a',$$

where the sub-index  $h$  represents the horizontal terms. Due to the simplicity of estimating  $PG_{B/S}$  compared to  $P_{B/S}$ , the latter terms were calculated as the difference between  $PG_{B/S}$  and  $PK_{B/S}$ .

### 6.3.2 Available Potential energy budget

In the ocean's energy budget, only a small fraction of potential energy that can be converted into kinetic energy is relevant. This fraction is referred to as the *available potential energy* ( $APE$ ). The definition of  $APE$  was proposed by Lorenz (1955) for the atmosphere, but there is no exact definition for the ocean due to diapycnal mixing (Huang, 1999; Winters et al., 1995), but several useful definitions are available (Molemaker and McWilliams, 2010; Roulet Guillaume, 2009; Huang, 1999; Gill, 1982). Here, we used the linear definition proposed by Gill (1982) following others, *e.g.*, Kang and Curchitser (2015) and Cao et al. (2021):

$$APE = \frac{g^2 \rho_a^2}{2\rho_0 N^2}. \quad (6.13)$$

The background available potential energy ( $BPE$ ) and the submesoscale available potential energy ( $SPE$ ) are thus:

$$BPE = \frac{g^2 \bar{\rho}_a^2}{2\rho_0 N^2}, \quad (6.14)$$

and

$$SPE = \frac{g^2 \overline{\rho_a'^2}}{2\rho_0 N^2}. \quad (6.15)$$

The  $BPE$  and  $SPE$  equations are derived by multiplying Eq. 6.7 by  $g^2 \bar{\rho}_a / \rho_0 N^2$  and  $g^2 \rho_a' / \rho_0 N^2$ , respectively:

$$\frac{\partial BPE}{\partial t} = \underbrace{-\nabla \cdot [\overline{\mathbf{u} BPE}]}_{AP_B} + \underbrace{\frac{1}{\rho_0} g \bar{\rho}_a \overline{w}}_{-PK_B} + \underbrace{\frac{g^2}{\rho_0 N^2} (\overline{\rho_a' \mathbf{u}' \cdot \nabla \rho_a})}_{-BSP} + BnP + DP_B + FP_B, \quad (6.16)$$

## Chapter 6. A full description of the Lorenz Energy Cycle over the Gulf Stream

and

$$\frac{\partial SPE}{\partial t} = \underbrace{-\nabla \cdot [\mathbf{u}SPE]}_{AP_S} + \underbrace{\frac{1}{\rho_0} g \overline{\rho' w'}}_{-PK_S} - \underbrace{\frac{g^2}{\rho_0 N^2} \overline{(\rho'_a \mathbf{u}' \cdot \nabla \rho_a)}}_{BSP} + DP_S + FP_S. \quad (6.17)$$

The first term,  $AP_{B(S)}$ , represents the transport of  $BPE$  ( $SPE$ ) produced by advection.  $BSP$  refers to the transfer of  $APE$  from background to submesoscale reservoirs, due to eddy density fluxes. The terms  $PK_B$  ( $PK_S$ ) denote the conversion between potential and kinetic energy, already defined in equations 6.11 (6.12). Additionally, the terms  $DP_{B(S)}$  and  $FP_{B(S)}$  refer to the dissipation and forcing of potential energy.

### 6.3.3 Nonlocal interactions

$BnK$  and  $BnP$  represent energy released in one reservoir that is not locally used to sustain the growth of energy in the other reservoir (Chen et al., 2014). This interpretation as nonlocal cross-scale transfer terms is now generally adopted (Cao et al., 2021; Jamet et al., 2022; Kang and Curchitser, 2015).

Following the derivation of Chen et al. (2014), Cao et al. (2021) defined the contribution of non-local interactions as:

$$BnK = SBK + BSK, \quad (6.18)$$

and

$$BnP = SBP + BSP, \quad (6.19)$$

where  $SBK = \overline{-\bar{u} \nabla \cdot (\mathbf{u}' u') + \bar{v} \nabla \cdot (\mathbf{u}' v')}$  is the  $BKE$  change due to eddy momentum fluxes, and  $SBP = -\frac{g^2}{\rho_0^2 N^2} \overline{\bar{\rho} \nabla \cdot \mathbf{u}' \rho'_a}$  is the  $BPE$  change due to eddy density fluxes. We could expect  $SBK$  ( $SBP$ ) and  $BSK$  ( $BSP$ ) to be of equal magnitude but opposite sign, indicating local interaction. However, their sum  $BnK$  ( $BnP$ ) takes the form of a divergence that only cancels by integration in a closed area, suggesting the possibility of a non-local contribution.

### 6.3.4 Forcing and dissipation terms

Because horizontal diffusion of momentum and tracers are implicit in CROCO's advection schemes (Soufflet et al., 2016; Menesguen et al., 2018), they are not readily available, and we choose to have them as the residual to the budget equations. Therefore, the total dissipation terms are :

$$DK_B = \bar{\mathbf{u}} \cdot \frac{\partial}{\partial z} \left( A_v \frac{\partial \mathbf{u}}{\partial z} \right) + \text{residual}, \quad (6.20)$$

$$DK_S = \bar{\mathbf{u}}' \cdot \frac{\partial}{\partial z} \left( A_v \frac{\partial \mathbf{u}}{\partial z} \right)' + \text{residual}, \quad (6.21)$$

$$DP_B = \frac{g^2 \bar{\rho}_a}{\rho_0 N^2} \cdot \frac{\partial}{\partial z} \left( \kappa_e \frac{\partial \rho_a}{\partial z} \right) + \text{residual}, \quad (6.22)$$

$$DP_S = \frac{g^2 \overline{\rho_a'}}{\rho_0 N^2} \cdot \overline{\frac{\partial}{\partial z} \left( \kappa_e \frac{\partial \rho_a}{\partial z} \right)'} + \text{residual}, \quad (6.23)$$

where  $A_v$  and  $\kappa_e$  are the vertical eddy viscosity and diffusivity coefficients, respectively.

We will vertically integrate the energy budget equations from the surface to a depth of 150 meters. In this case, the forcing terms will lose a division by the top grid space:

$$FK_B = \overline{\tau} \cdot \overline{\mathbf{u}_h}, \quad (6.24)$$

$$FK_S = \overline{\tau'} \cdot \overline{\mathbf{u}_h'}, \quad (6.25)$$

$$FP_B = \frac{1}{\rho_0} \left( \frac{g \alpha_o}{n_o} \overline{\rho_a} \overline{J} - \frac{g \beta_o}{n_o} \overline{\rho_a} \overline{G} \right), \quad (6.26)$$

$$FP_S = \frac{1}{\rho_0} \left( \frac{g \alpha_o}{n_o} \overline{\rho_a'} \overline{J'} - \frac{g \beta_o}{n_o} \overline{\rho_a'} \overline{G'} \right), \quad (6.27)$$

where  $\tau$  is the wind stress,  $\alpha_0$  and  $\beta_0$  are values of expansion coefficients in the uppermost model layer,  $n_o = -\frac{\rho_0}{g} N^2$  represents the vertical gradient of the time-mean and area-mean local density.  $J = (1/\rho_0 c)H$  and  $G = S_0(E - P)$  are the temperature and salinity flux at the sea surface, where  $c = 4000 \text{ J}(\text{kg K})^{-1}$  is the specific heat of seawater,  $H$  the total heat flux at the sea surface (positive values represent a flux into the ocean),  $S_0$  the surface salinity, and  $E$  and  $P$  are the evaporation rate and the precipitation rate at the sea surface, respectively.

Previous studies (*e.g.*, Bishop et al. (2020)) suggest that freshwater flux has a smaller effect on potential energy than heat flux. Our results indicate that the contribution of freshwater flux to  $BPE$  is an order of magnitude smaller than that of heat flux (not shown). On the other hand, freshwater and heat fluxes have similar contributions to  $SPE$  (not shown).

### 6.3.5 Scale selection in the decomposition

To analyze the dual role of the submesoscale on the energy cascade, we selected two cutoff scales to define the perturbation: 8 and 16 km. The 8 km scale was chosen because it is where the forward cascade is most intense. On the other hand, 16 km represents the scale where the forward cascade starts declining. It also corresponds to the wavelength of MLI (Boccaletti et al., 2007; Fox-Kemper et al., 2008), which has been associated with submesoscale energization of the inverse cascade.

To get the background field  $\overline{(\ )}$ , we apply a Gaussian filter. The window is defined as  $(2 \cdot tr \cdot \sigma + 1) \times (2 \cdot tr \cdot \sigma + 1)$ , where  $\sigma$  is the standard deviation and  $tr$  is the truncation. We define  $tr = 4$ , and  $\sigma = 5.625$  for a filter cutoff of 16 km, and  $\sigma = 2.625$  for 8 km. We will first present our reference analysis with the 16 km cutoff filter. When presenting the 8 km cutoff filter analysis, the terms will appear with an index (*e.g.*,  $X_{8km}$ ).

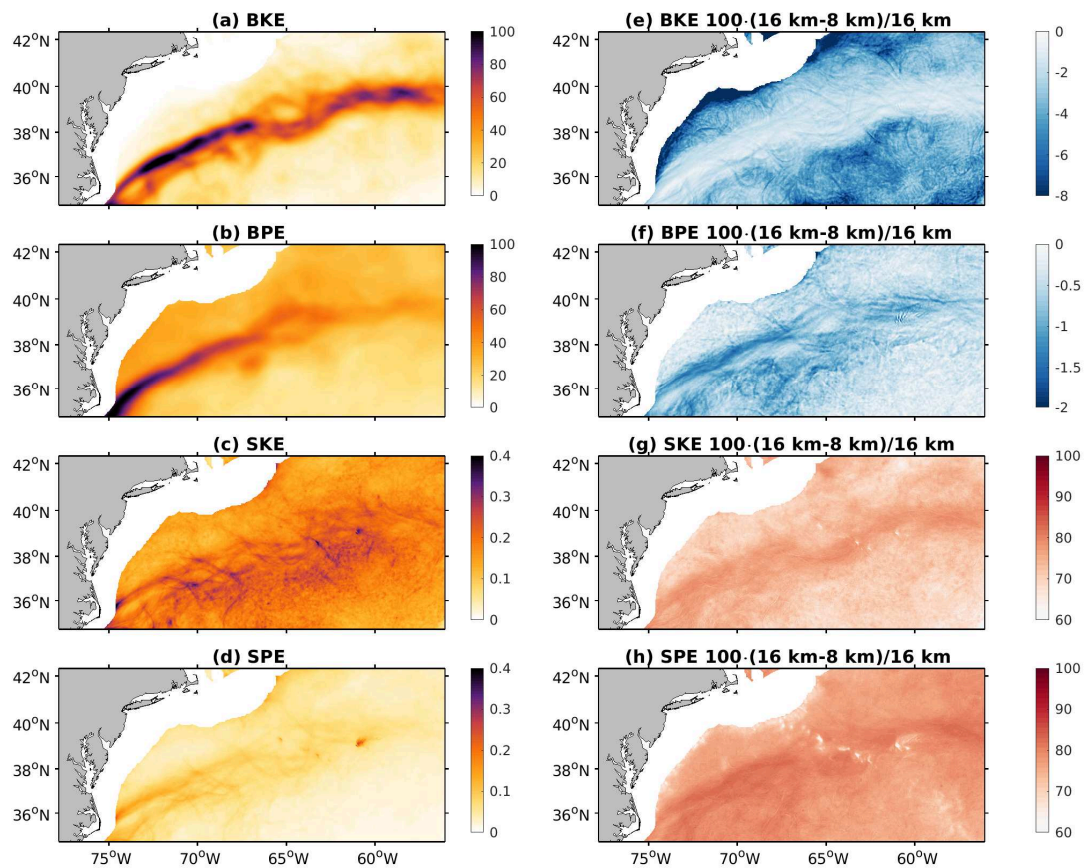


Figure 6.9: Annual-mean (May, 2005 - April, 2006) energy reservoirs: (a) *BKE*, (b) *BPE*, (c) *SKE* and (d) *SPE* integrated between 1 and 150 m. The units are  $1000 \cdot Jm^{-2}$ . (e-h) Relative difference (percentage) between energy reservoirs using 16 km and 8 km cutoff filters

## 6.4 Submesoscale energy cycle

### 6.4.1 Energy reservoirs

We calculated the background energy budget,  $BKE$  and  $BPE$ , and the submesoscale energy budget,  $SKE$  and  $SPE$ , using the oceanic simulation from May 2005 to April 2006 (Figure 6.9). The energy reservoirs were integrated vertically from a depth of 1 m to 150 m (we avoided the surface level to facilitate vertical derivation). The intensity of  $BKE$  and  $BPE$  is greatest along the mean GS path (Figure 6.9a-b). Both terms are particularly strong from Cape Hatteras to the New England seamount chain (NESC,  $\sim 65^\circ\text{W}$ ), at which point there is significant decline. However,  $BKE$  increases again eastward of the NESC, as opposed to  $BPE$ . The  $BKE$  and  $BPE$  averages over the entire domain (excluding shallow shelf areas below 150 m) are 23.03 and 29.2  $\text{kJm}^{-2}$  respectively.

In contrast, the magnitude of  $SKE$  is two orders smaller than that of  $BKE$ , and the magnitude of  $SPE$  is almost three orders smaller than that of  $BPE$  (Figure 6.9). The averages of  $SKE$  and  $SPE$  over the entire domain are 181.54 and 49.26  $\text{Jm}^{-2}$ , respectively. Figure 6.9c-d show that  $SKE$  and  $SPE$  present maxima on either sides of the mean GS path and  $SKE$  has generally larger values south of the mean GS path, where winter mixed layer eddies are generated.

### 6.4.2 Lorenz Diagram

The result of the energy budget, using a 16 km cut-off filter, is represented by the Lorenz diagram (Figure 6.10). The terms were integrated between 1 m and 150 m depth and averaged over the entire domain, excluding the shelf area, for the period May 2005 to April 2006. The energy fluxes for each reservoir are explained below.

#### 6.4.2.1 Background kinetic energy ( $BKE$ )

Figure 6.10 shows that the wind stress is the largest source of  $BKE$  ( $FK_B = 22.50 \text{ mW m}^{-2}$ ), generated mainly through its interaction with the GS circulation (Figure 6.11b).  $FK_B$  includes top drag, particularly the mesoscale eddy killing effect, which reduces the wind work (by about 30% according to Renault et al. 2016b).

The wind work is mostly balanced by dissipation  $DK_B$  ( $-20.41 \text{ mW m}^{-2}$ ), more precisely by vertical mixing in the surface boundary layer. Figure 6.11c confirms that  $DK_B$  is widespread negative everywhere, representing energy loss. These results confirm previous studies (Von Storch et al., 2012; Marchesiello et al., 2011; Chen et al., 2014). As proposed by Marchesiello et al. (2011), vertical mixing is mainly a response to the increase vertical shear generated by wind work. Other processes, such as instabilities, frontogenesis and breaking waves would also trigger vertical mixing, some of it at smaller scale, which will be further

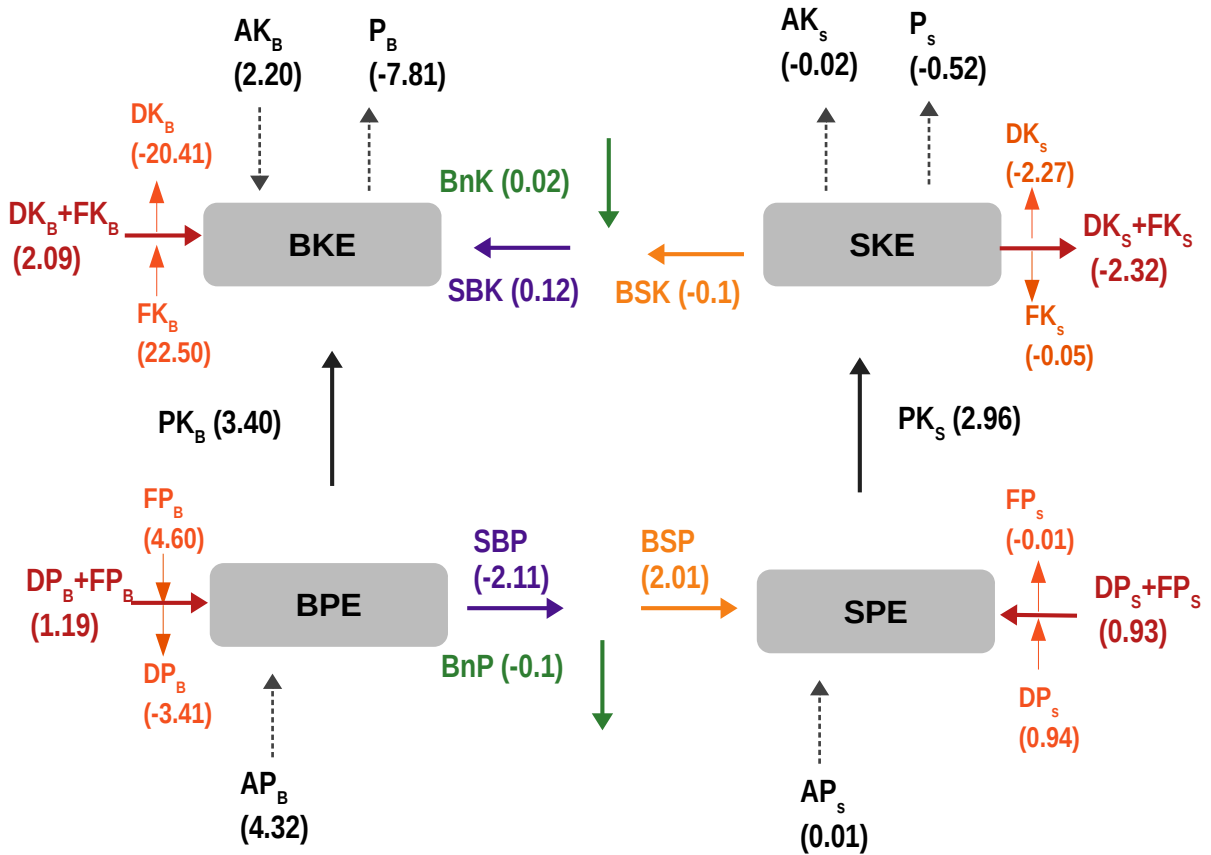


Figure 6.10: Lorenz diagram showing sources and sinks of the background and submesoscale potential and kinetic energy reservoirs. The terms are averaged for the period May 2005 to April 2006 and over the entire domain excluding the shelf zone, and integrated between 1 and 150 m depth. The arrows indicate the direction of energy transfer. The unit is in  $\text{mW m}^{-2}$ .

discussed in the following section.

$PK_B$  ( $3.40 \text{ mW m}^{-2}$ ) is an order of magnitude smaller than  $FK_B$ , but larger than  $FK_B+DK_B$  and thus constitutes a significant input to the background KE. Several mechanisms contribute to  $PK_B$ , most importantly baroclinic instability that converts PE to KE at mesoscale, but partly compensated by an opposite conversion at large scale due to Ekman pumping (Wunsch and Ferrari, 2004). Ferrari and Wunsch (2009) suggest that baroclinic instability can transfer at mesoscale 30% to 100% of the wind energy given to the large-scale circulation. Here, the conversion of  $BPE$  to  $BKE$  is positive and probably reflects that baroclinic instability dominates baroclinic conversion of the background circulation.  $PK_B$  is almost consistently positive throughout the GS area (Figure 6.11a).

$BKE$  increases due to energy transport by  $AK_B$  at a rate of  $2.20 \text{ mW m}^{-2}$  (Figure 6.10). The  $AK_B$  contribution is of the same order of magnitude as  $PK_B$ . The transport of  $BKE$  due to pressure work,  $P_B$  ( $-7.81 \text{ mW m}^{-2}$ ), removes the remaining energy not dissipated by  $DK_B$  by radiating it at depth and on either sides of the mean GS path.

$SBK$  contributes minimally to  $BKE$  at only  $0.12 \text{ mW m}^{-2}$  and is two orders of magnitude smaller than wind work. It corresponds to an inverse cascade from  $SKE$  to  $BKE$ , occurring through the energization of mesoscale eddies by submesoscale fronts or absorption of mixed-layer eddies (Klein et al., 2019; Schubert et al., 2020). Although  $BnK$  in the whole domain ( $0.02 \text{ mW m}^{-2}$ ) is an order of magnitude smaller than  $SBK$  and  $BSK$ , it is significant over the GS (Figures 6.12a-c), indicating that nonlocal interactions play some role in the energization of  $BKE$ .

#### 6.4.2.2 Submesoscale kinetic energy ( $SKE$ )

Buoyant production ( $PK_S = 2.96 \text{ mW m}^{-2}$ ) is the only source of energy for  $SKE$  (Figure 6.10 and 6.11d). Note that the contribution of baroclinic conversion  $PK_S$  is comparable to that of  $PK_B$ , even though the background energy reservoir is greater than the submesoscale energy reservoir. There is a compensation between the conversion PE/KE at planetary scale and mesoscale processes, which does not occur at submesoscale.

Several submesoscale processes may be involved in the conversion of potential to kinetic energy ( $SPE$  to  $SKE$ ), such as frontogenesis and surface-layer instability. Frontogenesis has been recognized as an important process driving the forward cascade in the GS (Contreras et al., 2023b). This process intensifies buoyancy gradients over a frontal region by mesoscale straining, enhanced by ageostrophic secondary circulation (McWilliams et al., 2019). Frontal intensification occurs also with downfront winds, via Ekman Buoyancy Flux ( $EBF$ ), a process triggered by cross-front density advection by Ekman flow (Thomas and Lee, 2005; Contreras et al., 2023b; D'Asaro et al., 2011). Nonlinear Ekman pumping, resulting from the cross-front gradient of vertical vorticity, can drive additional frontogenetic ageostrophic secondary circulations (Thomas and Lee, 2005).

Submesoscale baroclinic instabilities also contribute to  $PK_S$ , e.g., mixed-layer instabilities

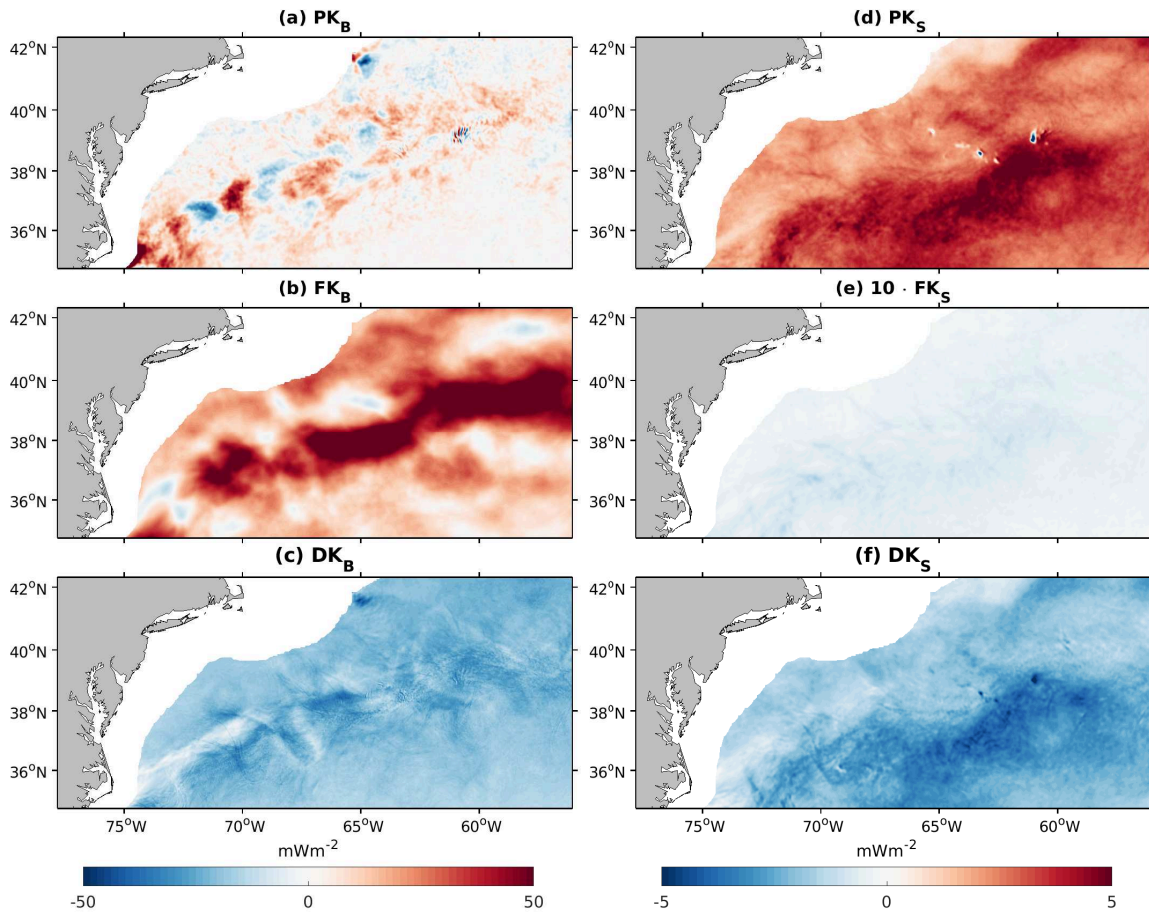


Figure 6.11: Annual-mean (May, 2005 - April, 2006) KE budget terms: (a)  $PK_B$ , (b)  $FK_B$ , (c)  $DK_B$  (d)  $PK_S$ , (e)  $10 \cdot FK_S$ , (f)  $DK_S$  integrated between 1 m and 150 m depth ( $\text{mW m}^{-2}$ ).

(Boccaletti et al., 2007; Fox-Kemper et al., 2008) and Charney instabilities (Capet et al., 2016). The former occur when the mixed layer is deep and weakly stratified and in the presence of horizontal buoyancy gradients, while the latter develop with surface buoyancy gradients and interior velocity shear (coupled surface/interior baroclinic instabilities) (Roulet et al., 2012).

*SKE* provided by  $PK_S$  is mostly dissipated by  $DK_S$  ( $-2.27 \text{ mW m}^{-2}$ ), at about 80%. The spatial distribution of  $DK_S$  and  $PK_S$  are strongly correlated (Figure 6.11d and), showing that these terms cancel each other locally (Marchesiello et al., 2011). The same observation in the energy spectrum led Capet et al. (2008d) and Marchesiello et al. (2011) to refer to the submesoscale range as a pseudo-inertial range.

Vertical mixing of horizontal submesoscales has drawn particular attention. The mechanisms in the surface layer can be inferred by the turbulent thermal wind (TTW), a balance between pressure gradient, Coriolis force and vertical mixing (Gula et al., 2014). TTW tends to regulate ageostrophic secondary circulation across dense filaments and fronts, linking buoyancy fluxes and vertical mixing (Gula et al., 2014; McWilliams, 2021). The generation and breakdown of internal gravity waves is also considered a major mixing process (Garrett and Kunze, 2007; Nikurashin et al., 2013; Ferrari and Wunsch, 2009; Wunsch and Ferrari, 2004).

Over the entire domain, *SKE* decreases due to pressure work ( $P_S = -0.52 \text{ mW m}^{-2}$ ), possibly arising from downward radiation of internal waves. However, this term is considerably smaller than both  $DK_S$  and  $PK_S$ .  $AK_S$  ( $-0.02 \text{ mW m}^{-2}$ ) also reduces *SKE*, but is an order of magnitude smaller than  $P_S$ .

As previously stated, *BSK* transfers energy from the submesoscale to the background kinetic energy (inverse cascade extended to the submesoscale range). However, this flux is an order of magnitude smaller than  $DK_S$  and  $PK_S$ .

The *SKE* budget indicates that the forcing term,  $FK_S$ , acts as an energy sink caused by submesoscale eddy killing through top drag (Renault et al., 2018), but its magnitude is two orders of magnitude lower than that of  $DK_S$ . This seems to contradict Renault et al. (2018), which show for the US West coast large submesoscale eddy killing due to top drag, damping *SKE* by 17%.

### 6.4.2.3 Submesoscale potential energy (*SPE*)

The main source of energy for *SPE* is  $BSP$  ( $2.01 \text{ mW m}^{-2}$ ; Figure 6.10), which transfers energy from *BPE* through horizontal eddy density fluxes. This is a forward cascade of potential energy created by horizontal mesoscale stirring near the surface that leads to frontogenesis (Klein et al., 2019; Molemaker and McWilliams, 2010). The transfer of energy from *BPE* to *SPE* is primarily a local conversion, as  $BnP$  is an order of magnitude smaller than  $BSP$  and  $SBP$ . The two terms also have a similar spatial distribution with opposite signs (Figure 6.12d-f). Thus, energy injection by  $BSP$  is transmitted to  $PK_S$ , which re-energizes *SKE*. Note that the spatial distributions of  $BSP$  and  $PK_S$  are comparable (see Figure 6.12d-e and

## Chapter 6. A full description of the Lorenz Energy Cycle over the Gulf Stream

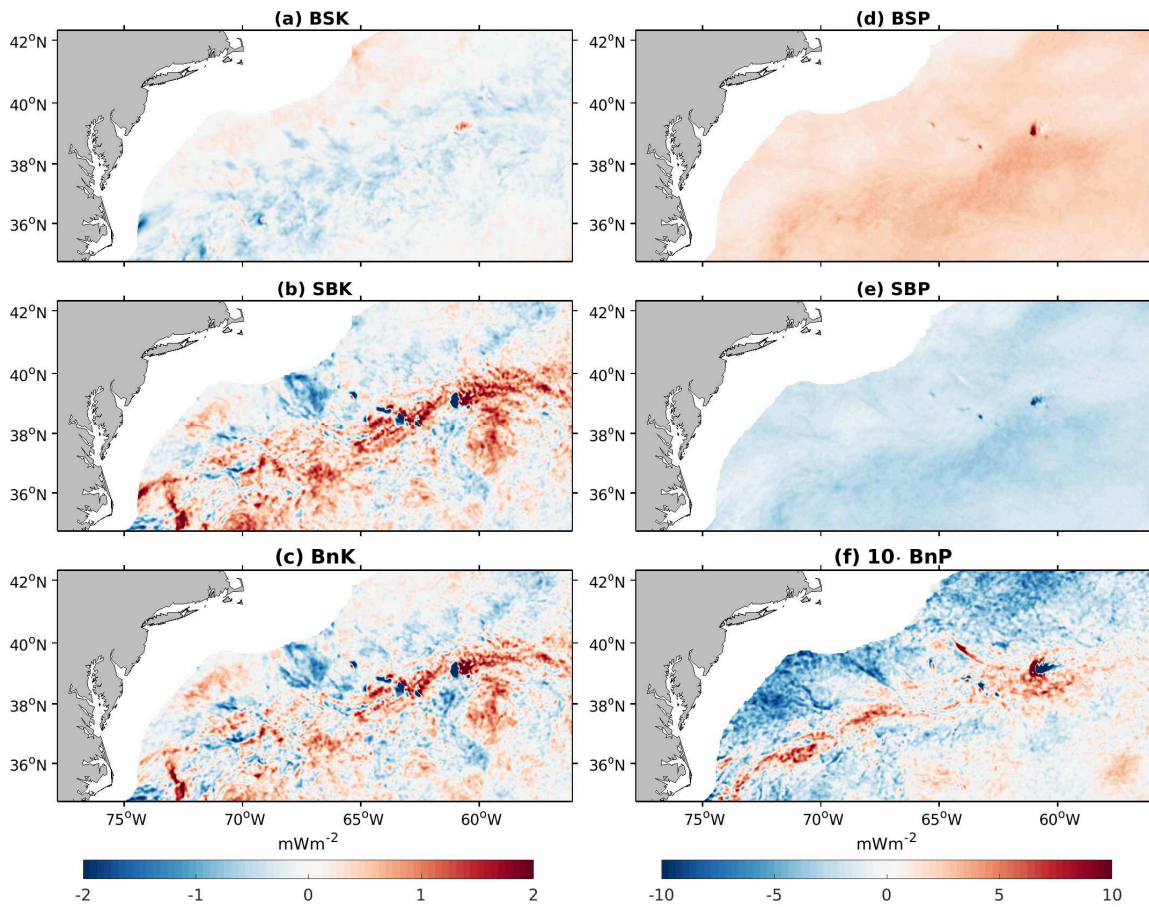


Figure 6.12: Annual-mean (May, 2005 - April, 2006) barotropic transfer terms of KE and APE budgets: (a)  $BSK$ , (b)  $SBK$ , (c)  $BnK$  (d)  $BSP$ , (e)  $SBP$ , (f)  $10 \cdot BnP$  integrated between 1 m and 150 m depth ( $\text{mW m}^{-2}$ ).

6.11d).

$DP_S$  also contributes to  $SPE$  (possibly through vertical mixing), albeit with smaller magnitudes compared to  $BSP$  ( $0.94 \text{ mWm}^{-2}$ ). Throughout the entire domain,  $DP_S$  exhibits a positive trend, except for the New England seamounts (Figure 6.13d). The forcing term,  $FP_S$ , contributes to a sink of  $SPE$  but only at a rate of  $0.01 \text{ mWm}^{-2}$  (Figure 6.13c).  $SPE$  advection  $AP_S$  injects energy into the domain, but with similar small magnitude to  $FP_S$  and opposite sign.

#### 6.4.2.4 Background potential energy ( $BPE$ )

Unlike other reservoirs, all terms in the  $BPE$  budget make a significant contribution (Figure 6.10). The main sources of  $BPE$  energy are atmospheric forcing ( $FP_B = 4.60 \text{ mWm}^{-2}$ ) and advection ( $AP_B = 4.32 \text{ mWm}^{-2}$ ).  $FP_B$  increases  $BPE$  across the entire domain except along the mean GS path (Figure 6.13a). The negative values are attributed to warm water transport causing heat loss, which generates unstable stratification that decreases potential energy.

$BPE$  injection by  $FB_P$  and  $AP_B$  is balanced by diffusion  $DP_B$  and  $SBP$ , *i.e.*, transfer to submesoscale PE by eddy stirring. Note that  $DP_B$  is mostly negative over the domain, except for the region near the GS separation.

## 6.5 Quasi-balanced and unbalanced submesoscale ranges

As previously stated, submesoscale motions can play two roles in the energy cascade. Submesoscale baroclinic instabilities and fronts can contribute to the inverse cascade (Klein et al., 2008; Qiu et al., 2014; Schubert et al., 2020; Capet et al., 2016), while frontogenetic secondary circulation, frontal instabilities, and IGW can drive a forward cascade (Capet et al., 2008a; Molemaker et al., 2010; Srinivasan et al., 2022; Contreras et al., 2023b). The forward cascade regime is only apparent at scales lower than about 10 km (at larger scale, the inverse cascade dominates). We can thus define a submesoscale range, characterized by quasi-balanced motions (small divergence) and an inverse KE cascade, and another range at smaller scales with unbalanced motions and a forward cascade of both KE and PE.

The Lorenz diagram presented above focuses on quasi-balanced submesoscales that extend the mesoscale inverse cascade, and here we present the same diagram for unbalanced submesoscales. To this end, we recalculated the budgets of Eqs. 6.11, 6.12, 6.16 and 6.17 using a cutoff filter of 8 km.

The bigger background energy reservoir has only slightly increased with the 8 km cutoff filter (Figure 6.9e-h).  $BKE_{8km}$  and  $BPE_{8km}$  over the entire domain are 23.56 and 29.37 kJ  $\text{m}^{-2}$ , *i.e.*, an increase of about 1% with respect to  $BKE$  and  $BPE$  (Figure 6.9e-f). A more significant difference is observed in the smaller unbalanced submesoscale reservoir (Figure

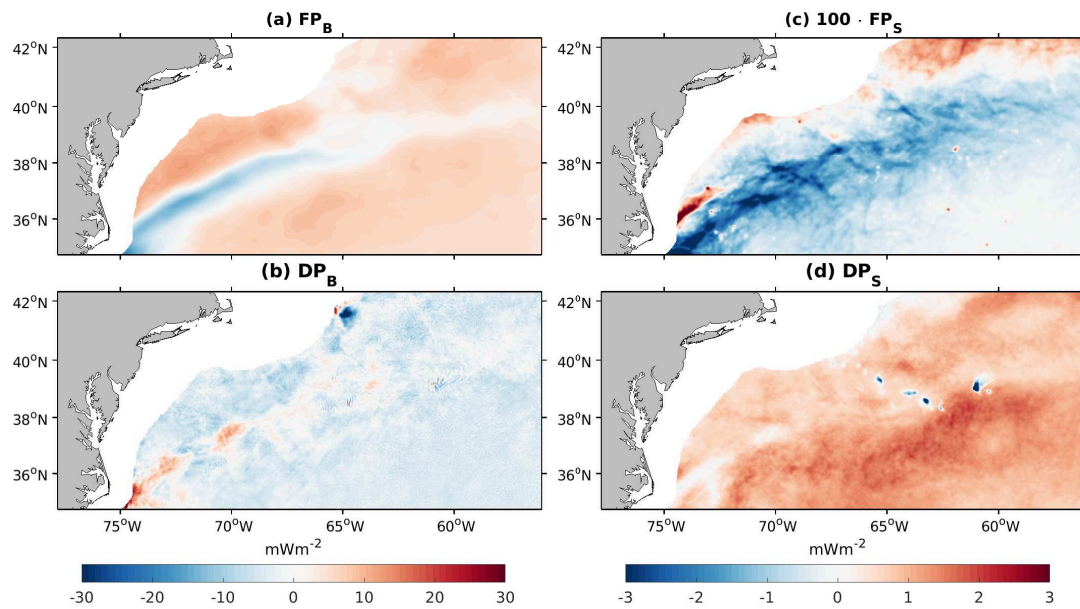


Figure 6.13: Annual-mean (May, 2005 - April, 2006) forcing and diffusion terms of APE budget: (a)  $FP_B$ , (b)  $DP_B$ , (c)  $100 \cdot FP_S$  and (d)  $DP_S$ , integrated between 1 m and 150 m depth ( $mW m^{-2}$ ).

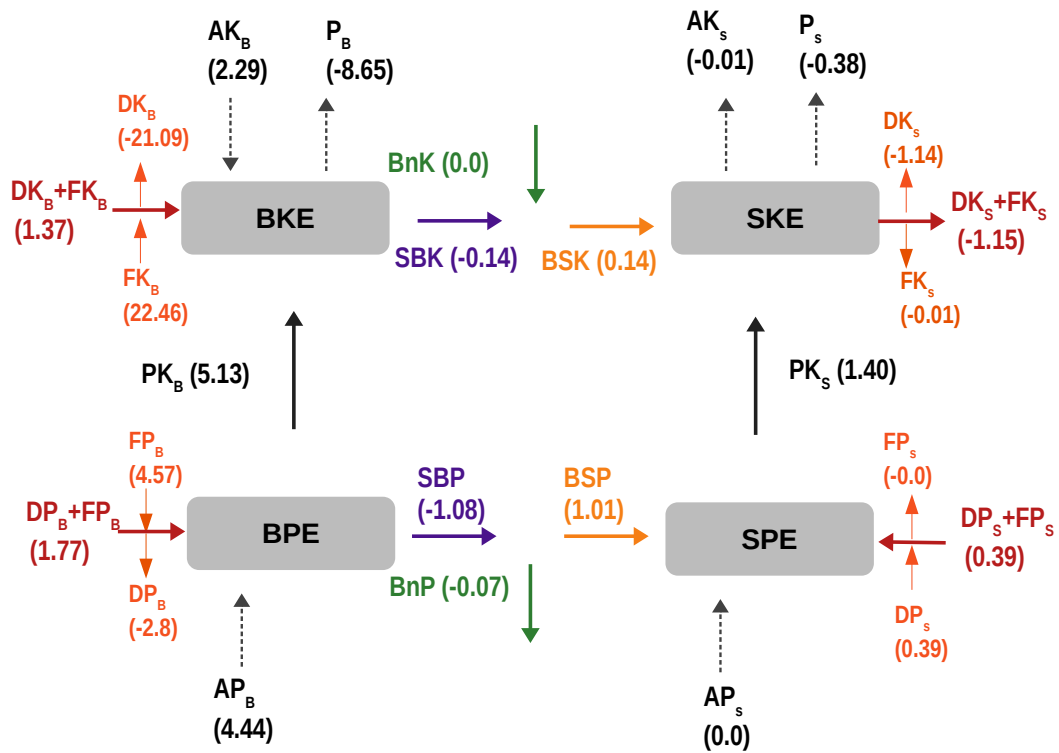


Figure 6.14: Schematic of the energy cycle, where the cutoff scale between background and submesoscales is taken at 8 km. The terms are averaged for the period May 2005 - April 2006 and over the whole domain (excluding the shelf zone), and integrated between 1 and 150 m depth. The arrow indicates the direction of energy transfer. The unit is in  $\text{mW m}^{-2}$ .

6.9g-h).  $SKE_{8km}$  and  $SPE_{8km}$  across the entire domain are  $49.11 \text{ J m}^{-2}$  and  $10.71 \text{ J m}^{-2}$ , *i.e.*, a reduction of 73% and 78% for  $SKE$  and  $SPE$ , respectively.

Figure 6.14 shows the Lorenz diagram estimated with the 8-km cutoff filter. A striking difference between the two diagrams is the sign of KE transfer between background and submesoscales. It shows an inverse KE cascade from quasi-balanced submesoscales to larger scales ( $BSK > 0/SBK < 0$ ; Figure 6.14), but a forward cascade to the unbalanced submesoscale ( $BSK_{8km} < 0/SBK_{8km} > 0$ ; Figure 6.14).

Previous studies suggest that the energization of scales larger than about 10 km is produced by the interaction of mesoscale eddies with submesoscale fronts (Klein et al., 2008; Schubert et al., 2020; Qiu et al., 2014; Capet et al., 2016), or submesoscale baroclinic instabilities (Schubert et al., 2020; Qiu et al., 2014). On the other hand, a forward cascade is permitted when ageostrophic advection is strong enough (Capet et al., 2008a; Molemaker et al., 2010; Srinivasan et al., 2022; Contreras et al., 2023b).

The Lorenz diagram for unbalanced submesoscales generally shows an increase in the magnitude of background energy budget terms and a decrease for submesoscale energy budget terms. There are exceptions, including  $FK_B$ ,  $AK_B$ ,  $FP_B$ , and  $DP_B$ , but not significant.

## 6.6 Seasonal Variability

Previous studies show that submesoscale processes exhibit significant seasonal variability, with submesoscale currents stronger in winter than in summer (Schubert et al., 2020; Qiu et al., 2014; Callies et al., 2015; Torres et al., 2018; Rocha et al., 2016; Contreras et al., 2023b). Our simulation concurs with these findings. Figure 6.15 illustrates a snapshot of the surface relative vorticity for both seasons, indicating a higher level of submesoscale activity during winter.

Interpretation of the annual mean terms in the Lorenz diagram can change due to the seasonal variation in submesoscale activity. The section below presents a revision of the Lorenz diagram for winter (January to March; Figure 6.16) and summer (July to September; Figure 6.18).

### 6.6.1 Winter

At large scales, the injection of energy through atmospheric forcing shows a significant increase during winter (Figure 6.16).  $FK_B$  and  $FP_B$  both experience significant increase of 101% and 341%, respectively, compared with the annual mean. Due to the increase in external energy flux, both background kinetic and potential energy dissipation ( $DK_B$  and  $DP_B$ ) increase by 91% and 201%, respectively.

The buoyancy production is also intensified at both background scale and submesoscale,

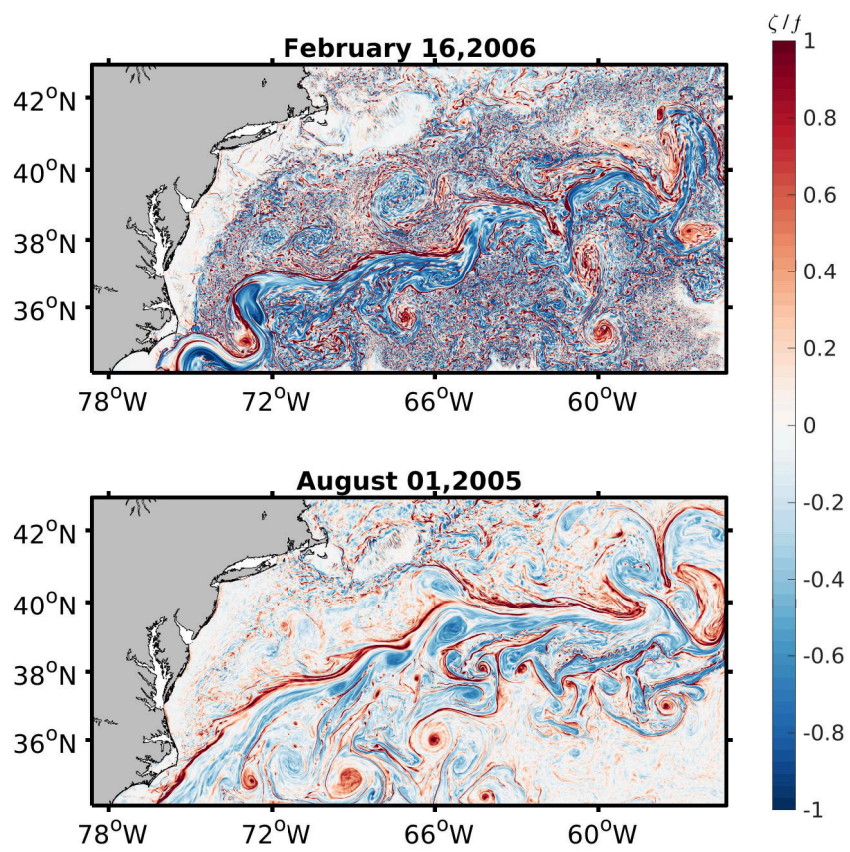


Figure 6.15: Snapshot of the surface relative vorticity (normalized by  $f$ ) on February 16, 2006 and August 01, 2005.

## Chapter 6. A full description of the Lorenz Energy Cycle over the Gulf Stream

with an increase of 133% for  $PK_S$  (68% for  $PK_B$ ) compared to the annual mean. The intensification of processes such as frontogenesis and submesoscale instabilities can explain this increase. Using *in-situ* observations, Callies et al. (2015) show winter intensification of frontogenesis and MLI around the GS northern wall.

Following the increase in KE injection ( $SPE$  to  $SKE$ ), the dissipation of submesoscale kinetic energy ( $DK_S$ ) intensifies also during winter (by 136%).  $DP_S$  increases by 159% while the contribution of the submesoscale forcing term remains small.

The values of  $AK_B$ ,  $P_B$ ,  $AK_S$ ,  $P_S$ ,  $AP_B$ , and  $SBP/BSP$  ( $BnP$ ) increase during winter and have a similar impact on the energy budget as observed in the annual mean, while  $AP_S$  remains constant. However, interestingly, the upscale KE flux  $BSK$  ( $SKE$  to  $BKE$ ) decreases by 30%. In line with Contreras et al. (2023b), this is the result of the strengthening of unbalanced motions, which increase the forward cascade and shift the crossover scale between downscale and upscale fluxes to a larger scale. The upscale effect of the absorption of mixed-layer eddies by mesoscale eddies develops during winter, but reaches its maximum later in spring. (Contreras et al., 2023b; Schubert et al., 2020).

Figure 6.17a-d show the winter energy reservoirs. Compared to the annual mean (Figure 6.9), we notice an increase in  $BKE$  and  $SKE$  by 6% and 66%, respectively, but a decrease in  $BPE$  and  $SPE$  by 16% and 37%, respectively. The decrease in APE and increase in KE can be explained by the intensification of processes favoring baroclinic conversion.

In summary, winter shows an increase in the magnitudes of the terms of the energy budget, with only a slight weakening of the KE inverse cascade. Similar findings are obtained with the 8-km cutoff filter, but in this case there is a slight increase of the KE forward cascade.

### 6.6.2 Summer

During summer, there is a general decrease in the magnitude of the energy budget terms (Figure 6.18).  $FK_B$  is 84% lower than the annual mean, causing  $DK_B$  to drop by 74%. Unlike in winter or the annual mean,  $FP_B$  acts as a sink of  $BPE$  in summer. However,  $DP_B$  increases by 87%.

In summer, the mechanisms that transform APE into KE are less effective, including frontogenesis and baroclinic instability. Consequently,  $PK_B$  and  $PK_S$  decreased by 71% and 90%, respectively, in comparison to the annual mean.

There is also a significant reduction in energy transfer between  $BPE$  and  $SPE$ , with nonlocal interactions becoming more relevant. In this case, the local transfer to  $BPE$  ( $SBP$ ) has opposite sign to that directed to  $SPE$  ( $-BSP$ ), and the nonlocal transfer  $BnP$  is dominant. In summer, KE follows an upscale flux from  $SKE$  to  $BKE$  as in the annual mean, but  $BSK/SBK$  are reduced by 17%/30%.

$AK_B$ ,  $AP_B$ , and  $AP_S$  show an input of energy as in the annual mean. However, in

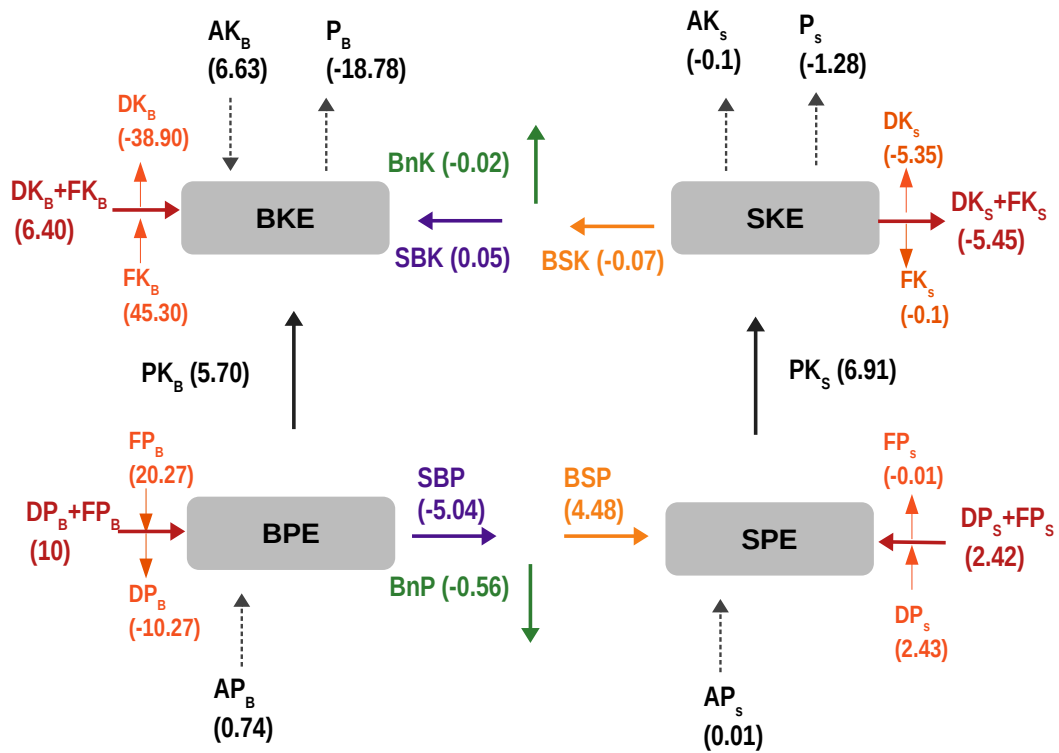


Figure 6.16: Schematic of the energy cycle, for the background scale and submesoscale reservoirs using a 16 km cutoff for scale separation. The terms are averaged for January 2006 - March 2006 and over the whole domain (excluding the shelf zone), and integrated between 1 and 150 m depth. The arrow indicates the direction of energy transfer. The unit is in  $\text{mW m}^{-2}$ .

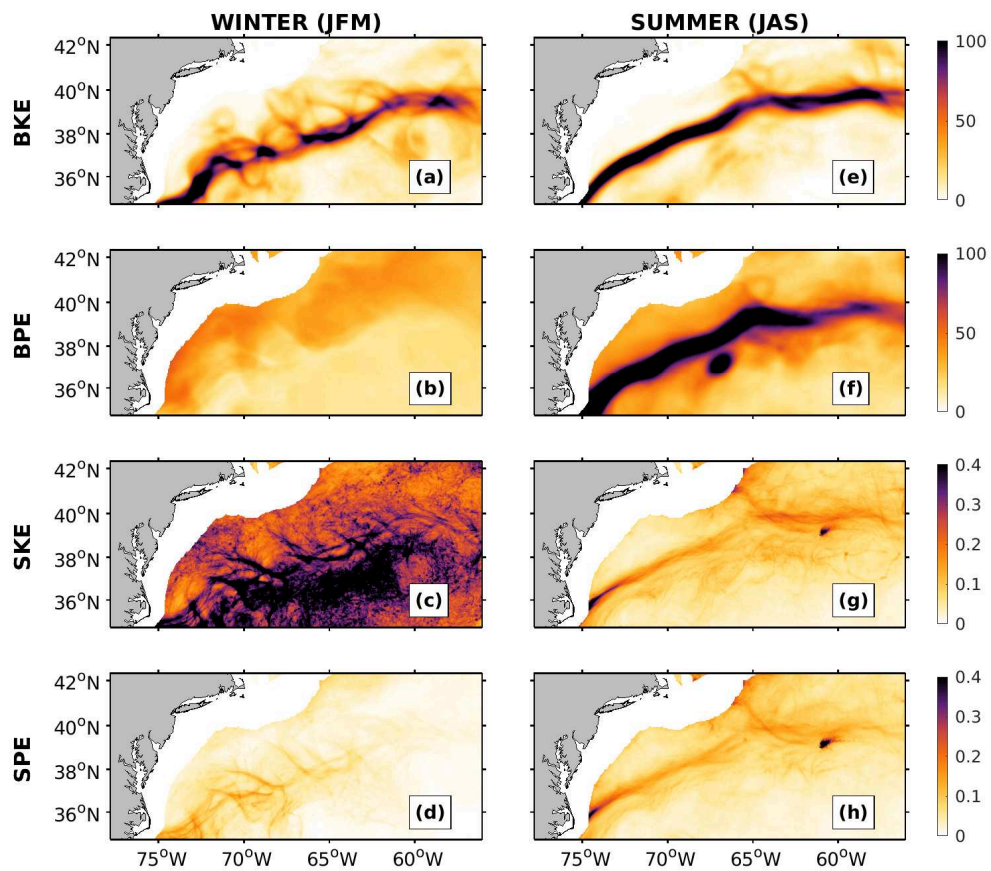


Figure 6.17: (a and e) *BKE*, (b and f) *BPE*, (c and g) *SKE* and (d and h) *SPE* integrated between 1 m and 150 m, and averaged in (left) winter and (right) summer. The units are  $1000 \cdot Jm^{-2}$ .

summer, the first term decreases by 14%, the second increases by 92%, and the last remains unchanged. In contrast to the annual mean,  $AK_S$  is a source of  $SKE$ , but its contribution is two orders of magnitude smaller than that of  $PK_S$ . As in the annual mean,  $P_B$  and  $P_S$  are energy sinks, but with magnitudes reduced by 84% and 96%, respectively.

Due to the decrease in submesoscale energy input,  $DK_S$  is reduced by 90%, but  $DP_S$  does not change significantly. The submesoscale forcing terms are negligible for both PE and KE.

The energy reservoirs are also changed in summer compared with the annual mean. Contrarily to winter,  $BKE$  and  $SKE$  decrease (by 4% and 57%), while  $BPE$  and  $SPE$  increase (by 53% and 29%; Figure 6.17e-h). Again, this can be explained by the weakening of processes driving baroclinic conversion.

In summary, the main difference between the summer annual mean budget is a decrease of transfer between the energy reservoirs. In addition, there is a substantial contribution of nonlocal interaction to the transfer from  $BPE$  to  $SPE$ . Similar findings were found with the 8-km cutoff filter.

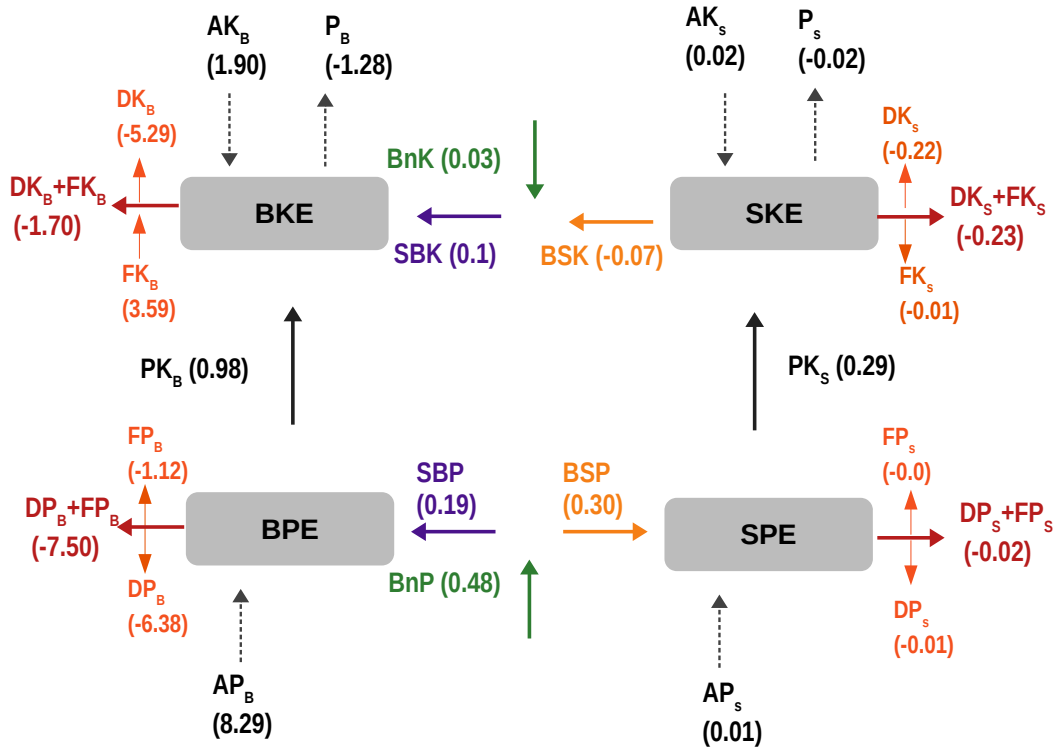


Figure 6.18: Schematic of the energy cycle, for the background scale and submesoscale reservoirs using a 16 km cutoff for scale separation. The terms are averaged for July - September 2005 and over the whole domain (excluding the shelf zone), and integrated between 1 and 150 m depth. The arrow indicates the direction of energy transfer. The unit is in  $\text{mW m}^{-2}$ .

## 6.7 Conclusion and Discussion

In this study, we examined the submesoscale energy cycle in the GS. The analysis is based on a 1-year (May 2005 to April 2006) high-resolution, coupled air-sea simulation (CROCO-WRF). The oceanic and atmospheric simulations have horizontal resolutions of 700 m and 2 km, respectively. From the oceanic simulation, we derive a set of equations for the background (planetary scale and mesoscale) and submesoscale energy budget defined by a cutoff scale of 16 km (reference) or 8 km.

The wind stress provides energy to background KE  $BKE$ , while large-scale heat and freshwater fluxes feed the background PE  $BPE$ . Submesoscale KE  $SKE$  gets energy by baroclinic conversion from  $SPE$ .  $BPE$  supplies energy to  $SPE$  through eddy stirring, in a forward cascade of potential energy. Potential and kinetic energy have different paths for energy loss.  $BKE$  and  $SKE$  are depleted by their dissipation terms, including vertical mixing. On the other hand, background and submesoscale potential energy ( $BPE$  and  $SPE$ ) lose energy by conversion to kinetic energy.

It is now understood that submesoscale motions play a dual role in the energy budget. On one hand, unbalanced motions favor a forward cascade through the ageostrophic advection (Capet et al., 2008a; Molemaker et al., 2010). On the other hand, submesoscale eddies and fronts can energize the mesoscale by absorption (Klein et al., 2008; Qiu et al., 2014; Schubert et al., 2020). Submesoscales can thus be split into quasi-balanced and unbalanced dynamical regimes, where flow divergence in either regime determines the sign of cross-scale fluxes. A Lorenz diagram using a filter cutoff of 8 km reveals the unbalanced submesoscale energy budget ( $SKE$ ). In this regime, shear production produces a downscale flux of KE, so that both PE and KE follow a forward cascade. However, the cross-scale KE flux is small compared with the main source and sink of submesoscales, *i.e.*, baroclinic conversion and vertical mixing. To be more specific, vertical mixing in our simulation dissipates about  $\mathcal{O}(10)$   $\text{mW m}^{-2}$  of KE. This amount is comparable to the dissipation caused by boundary drag (top and bottom), but much higher than the forward KE cascade, near  $0.1 \text{ mW m}^{-2}$  (Contreras et al., 2023b). The importance of cross-scale KE fluxes on the overall submesoscale dynamics thus appears very limited, while on the contrary, the important role of mesoscale straining and frontogenesis is confirmed.

Our results show both similarities and contradictions with Cao et al. (2021). Using a high-resolution forced oceanic simulation of the Kuroshio Current with 500-m grid resolution, they find strong upscale flux of KE ( $SKE$  to  $BKE$ ), and downscale flux of PE ( $SPE$  and  $BPE$ ). Our results are only in agreement with the cascade of potential energy. Cao et al. (2021) analyzed a short period of 2 weeks between April 28 and May 12. During spring, the process of energization of mesoscale eddies by absorption of submesoscale eddies is particularly intense (Contreras et al., 2023b; Schubert et al., 2020; Qiu et al., 2014), and can explain a stronger KE inverse cascade than would appear in the annual mean. In addition, the inclusion in our case of air-sea interaction may also explain some of the discrepancy. The top drag associated with the current feedback effect reduces kinetic energy and thus weakens its cross-scale flux.

Significant seasonal variability exists in the energy budget. Winter was found more energetic than summer. The energy input due to atmospheric forcing (wind stress, heat, and freshwater fluxes) significantly increases in winter. Therefore, the larger energy reservoirs enhance transfer and dissipation. In summer, the energy input is drastically reduced and produce opposite effects.

Previous studies suggested that the intensification of submesoscale activity in winter is caused by an increase of  $APE$  due to wind-induced mixing and heat loss from the ocean (Callies et al., 2015). However, in our simulation,  $APE$  is higher in summer than in winter. This implies an additional pathway promoting mesoscale eddy stirring, frontogenesis and baroclinic conversion (transfer from  $BPE$  to  $SPE$  then to  $SKE$ ). It seems that wind stress ( $FK_B$ ) rather than heat and freshwater fluxes ( $FP_B$ ) play this role in our model, driving large-scale and mesoscale activity.

The inclusion of tides and incoming internal waves in our simulation was accomplished using boundary conditions from a lower resolution (2 km) simulation, as explained in Chapter 5. Due to the relatively low-frequency output of the parent simulation (once every three hours), tides in the high-resolution simulation may be slightly underestimated, although we are confident that the effect is very small based on sensitivity tests. Future studies should improve the representation of tides by considering the methodology proposed in Chapter 5.

An important caveat of our study pertains to the definition of  $APE$ . Currently, there is no consensus on the definition of  $APE$  for the ocean (Huang, 1999) and various propositions exist (Gill, 1982; Kang and Fringer, 2010; Molemaker et al., 2010; Saenz et al., 2015). The most commonly used definition for  $APE$  is the linear definition proposed by Gill (1982), which is used also here because of its low computational cost and simplification of budget equations. Nevertheless, when dealing with nonlinear stratification, this definition can lead to known biases (Kang and Fringer, 2010). The baroclinic conversion terms  $PK_B$  and  $PK_S$  are not affected by the  $APE$  definition, but other terms of the potential energy budget may be sensitive to the choice of definition. Future studies should test alternative definitions (e.g., Molemaker et al. 2010), to assess their impact on the energy budget. However, we expect that our main conclusions will remain valid, at least qualitatively.

Although our simulation takes air-sea interactions into account, we have not assessed their impact on the energy balance. Unlike a forced ocean simulation (not including current feedback to the wind stress), our ocean simulation should have reduced wind work ( $FK_B$  and  $FK_S$ ) and lower values of  $BKE$  and  $SKE$  (Renault et al., 2016a, 2018). In addition, the inclusion of thermal feedback modifies heat fluxes ( $FP_S$  and  $FP_B$ ), leading to a decrease in  $APE$ , which could mitigate (sub)mesoscale eddy activity via baroclinic instability ( $PK_S$  and  $PK_B$ ) (Ma et al., 2016; Bishop et al., 2020; Renault et al., 2023b). The effect of these mechanisms at submesoscale remain incompletely understood, and future studies should examine their role more closely.



# Conclusion and perspectives

## Conclusion

The Gulf Stream (GS) is a crucial component of the global climate and ocean circulation. It is one of the most energetic ocean regions, with warm water transported poleward, leading to an intense exchange of heat flux between the ocean and the atmosphere. Due to this process, the GS aids in regulating the climate of the ocean and continents (Bryden et al., 2005).

The GS has been extensively studied and has shown complex dynamics influenced by multiple mechanisms across varied temporal and spatial scales. At a larger scale, the North Atlantic gyre circulation is determined by the Sverdrup balance between wind stress curl and the differential rotation of the Earth (Sverdrup, 1947; Munk, 1950). However, the western branch of the gyre (the GS) is strongly influenced by topography and the interaction between eddies and mean flow (Kang and Curchitser, 2015; Schoonover et al., 2016; Özgökmen and Chassignet, 2002; Hughes and De Cuevas, 2001; Debreu et al., 2022; Renault et al., 2016a, 2023a).

Numerical ocean models have been a valuable tool for comprehending GS dynamics; however, they exhibit significant solution dispersion and biases when compared to *in-situ* and satellite observations. Although a better resolution of mesoscale activity shows a significant improvement, there is a point in the resolution refinement where the simulations tend to produce an excess of kinetic energy. A realistic representation of kinetic energy sources and sinks is therefore necessary to improve the representation of the GS kinetic energy balance.

Current theory on ocean energy balance is mainly derived from satellite and in-situ observations and numerical models, which describe scales ranging from mesoscale to large-scale circulation (Ferrari and Wunsch, 2009; Wunsch and Ferrari, 2004; Scott and Wang, 2005). However, recent studies have revealed the important role of submesoscale currents, although a complete understanding of this phenomenon is still lacking (Klein et al., 2019). In this study, we describe the pathway of kinetic energy in the GS and identify and quantify the mechanisms that are involved in the dissipation of ocean circulation energy.

In Chapters 4 and 5, the energy cascade in the GS is described using a series of submesoscale-permitting forced oceanic simulations with a grid space of 2 km. The simulations are conducted both without tides (Chapters 4 and 5) and with tides (Chapter 5). The current feedback effect to the wind stress (top drag) was included in both simulations using the stress approach parameterization proposed by Renault et al. (2019a). We estimated the cross-scale kinetic energy flux using the coarse-graining method (Aluie et al., 2018). This method presents multiple advantages compared to spectral analysis. The coarse-graining method not only allows for the description of spatial patterns of energy fluxes, but also avoids windowing procedures while relaxing the assumptions of homogeneity and isotropy in the field. Our results are consistent with the existing theory, indicating that there is a forward cascade at

small scales and an inverse cascade at large scales. We confirm for the GS, through the use of Helmholtz decomposition, that the inverse cascade is driven by balanced motion, while unbalanced and balanced motions interact to produce the forward cascade. Specifically, the forward cascade is driven by ageostrophic advection.

We provide further details on the processes at work in spatial and seasonal patterns. We show that the spatial and temporal variations in the kinetic energy cascades depend on the dominant energy transfer mechanisms. More specifically, Chapter 4 shows that variations in the forward cascade follow those of a strong frontogenesis located on the North Wall of the GS. Meanwhile, submesoscale eddies and fronts also have the potential to energize mesoscale activity through absorption, a process that begins in winter and intensifies the inverse cascade in spring. In Chapter 5, we show that tides affect cross-scale KE fluxes throughout the year, with the greatest impact occurring during the summer months, intensifying the forward cascade. Internal tides (most active in summer) appear to be the main driving force behind this intensification. Our analysis shows that wave-flow interaction dominates wave-wave interaction (wave turbulence). The specific mechanisms involved in wave-flow interaction are unclear, but they seem consistent with the stimulated imbalance process proposed by (Barkan et al., 2017), where externally forced internal waves stimulate a transfer of energy from mesoscale to submesoscale eddies.

Chapters 4 and 5 present an original attempt to quantify and compare GS kinetic energy sinks. In particular, interior dissipation, resulting from the forward cascade, is compared with boundary and numerical dissipation processes. Our results suggest that interior dissipation is about an order of magnitude smaller than top and bottom frictional dissipation. It is therefore essential that models accurately represent dissipation at vertical boundaries.

In addition, numerical dissipation is larger than the flux of KE entrained at small scales — assuming that this dissipation is meant to represent the continuation of a forward cascade at sub-grid scales. As a consequence, it tends to strongly damp submesoscales in the model's dissipation range, *i.e.*, the range defining the effective resolution of the model (5-10  $\delta x$  here). It seems therefore important to maintain that range below the zero crossing of energy flux that separates inverse and forward cascade. It may be so at a model resolution of 2 km, when using a fifth-order (UP5) momentum advection scheme, but not with third-order (UP3). In the latter case, mesoscale energizing by submesoscales is compromised. Testing the model's sensitivity to UP5 and UP3 (Chapter 4), we find, as expected, that the higher-order scheme is less dissipative and that its damping range appears within about 5  $\delta x$ . Dissipation is greater in UP3 and affects a wider spectrum (see examples of dissipation spectra in Soufflet et al. 2016). However, this is not too detrimental to the model solution, given that the energization process (upscale KE flux to the mesoscale) is relatively small compared with mesoscale baroclinic conversion or boundary dissipation (see Chapter 6 and summary below). Interestingly, when using UP5, the decrease in numerical dissipation is partially offset by an increase in frictional dissipation at the vertical boundaries (less numerical dissipation leads to more dissipation at the top and bottom). Consequently, part of mesoscale energization is countered, if not by spurious numerical dissipation, then more realistically by boundary processes (including boundary layer vertical mixing). In Chapter 5, our study reveals that

tides also lead to an amplification of dissipation pathways, which is greater at the bottom. Mesoscale activity in the GS is therefore reduced by the tides. Once again, modifying one energy sink have an impact on the others, which do not necessarily operate in the same way. This underlines the importance of an accurate representation of each sink to maintain an energetically balanced system and realistic circulation.

To provide a comprehensive understanding of the GS energy pathway, Chapter 6 discusses the submesoscale energy cycle with the Lorenz diagram (Lorenz, 1955). Our approach this time involves a fully coupled air-sea model simulation that explicitly takes into account air-sea interaction mechanisms, such as current feedback and thermal feedback that can impact both the kinetic and potential energy reservoirs. The grid resolution of oceanic and atmospheric simulations is 700 m and 2 km, respectively, with a computational domain centered around the GS.

We analyze the budget of both kinetic and potential energy using Reynolds decomposition to separate submesoscales from background scales (planetary and mesoscales) with a cutoff at 16 km. The wind stress is the primary external source of kinetic energy, injecting energy on a large scale. While the heat and freshwater fluxes also inject potential energy on a large scale, their contribution is one order of magnitude smaller than the wind stress. The background potential energy feeds the submesoscale potential energy via a forward potential energy cascade driven by mesoscale stirring. Potential energy then feeds both the background (mesoscale) and submesoscale kinetic energy reservoirs via vertical buoyancy fluxes — associated with interior and surface baroclinic instability and strain-induced frontogenesis. This result is important because it shows that the primary source of energy for submesoscale kinetic energy is provided by potential energy, rather than the transfer from mesoscale kinetic energy through shear production.

With the 16 km cut-off scale, we find that shear production actually results in an upscale transfer of kinetic energy from submesoscale to mesoscale. This study quantitatively confirms that submesoscale processes contribute to energizing the larger scale, but that their contribution is minor compared, for example, to mesoscale baroclinic conversion. At submesoscales below 10 km, the KE cascade changes sign as ageostrophic advection begins to play a more important role (chapters 2 and 6). This is best illustrated by the use of an 8 km cut-off scale to separate background and submesoscale reservoirs. This means that the mesoscale regime can be separated into quasi-balanced and unbalanced dynamical regimes, where flux divergence determines the direction of cross-scale fluxes. However, again, these fluxes, whatever their direction, do not have a very significant impact on the energy budget, as they are minor compared with baroclinic conversion or energy sinks. Consistently with Chapter 4, we also find in Chapter 6 a significant seasonal variability in the energy balance, with winter being the most energetic season.

In summary, the results of this thesis contribute to the knowledge of the energy cycle in the ocean between mesoscale and submesoscale. More specifically, we have identified and quantified the main sources and sinks of energy, as well as, described oceanic scale interaction and the mechanism involved. These results allow us to improve the general outline of the energy pathways of wind-driven circulation (Figure 6.19).

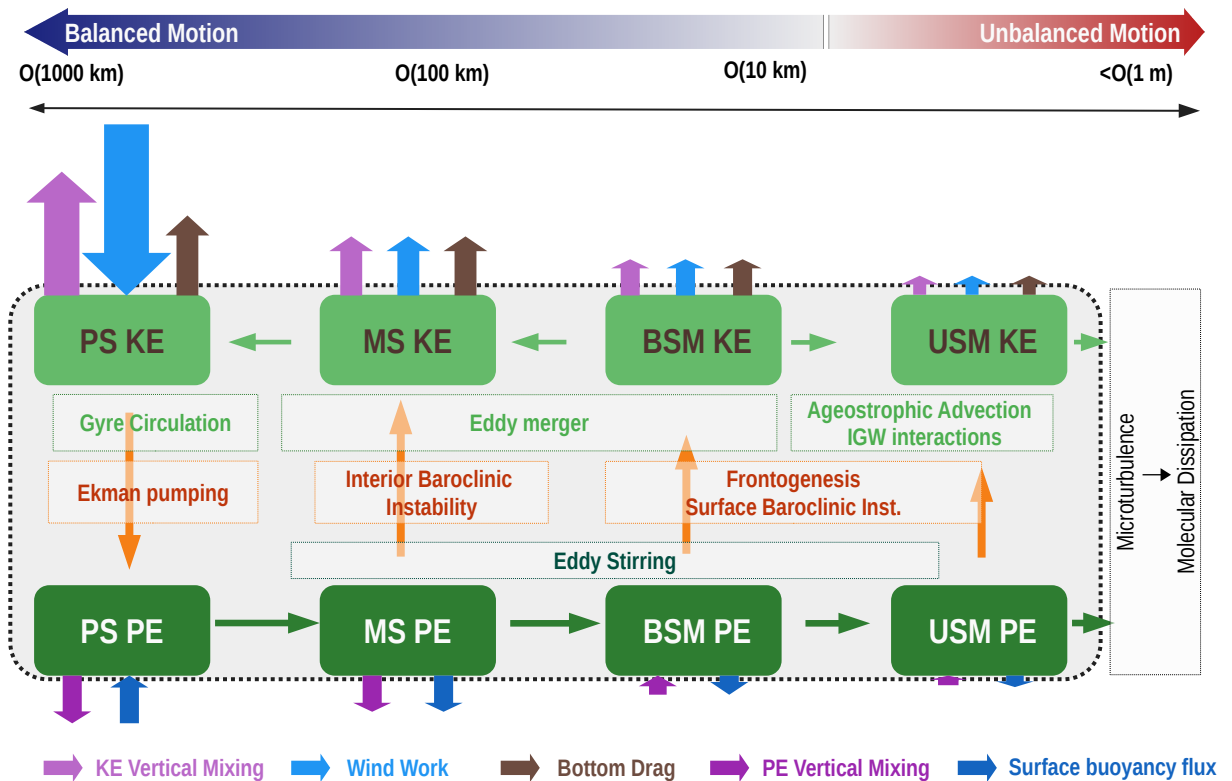


Figure 6.19: Schematic view of the kinetic (KE) and potential (PE) energy cycles of the wind-driven ocean circulation. The motions are decomposed into planetary scale (PS), mesoscale (MS), balanced submesoscale (BSM), and unbalanced submesoscale (USM). Dark and light green arrows represent, respectively, the cross-scale transfer of PE and KE through shear production. The length of the arrows indicates the relative magnitudes of energy exchange. The orange arrows represent the transfer between PE and KE through buoyancy production (baroclinic conversion). The dominant mechanisms involved in energy fluxes are indicated in corresponding colors. The arrows outside the gray area show the contribution of external sources and sinks. Note that the main input of energy is provided by wind work at large scale (at all scales below, wind work is a sink of energy). The scale at which the forward cascade is observed marks the transition to from quasi-balanced to unbalanced submesoscale motions.

## Perspectives

### Disentangle CFB and TFB contributions to submesoscale kinetic and potential energy budgets

Recent studies indicate that the submesoscale is relevant to air-sea interaction (Strobach et al., 2022; Chen et al., 2022; Bai et al., 2023; Su et al., 2018; Renault et al., 2018). For example, submesoscale dynamics develop intense vertical heat transport that can modify heat exchange between the ocean and the atmosphere (Su et al., 2018). Using a high-resolution (2 km) global ocean model, Su et al. (2018) found submesoscale upward heat transport five times greater than that produced by mesoscales. Submesoscales may therefore significantly impact TFB, potentially altering both potential and kinetic energy reservoirs. Previous studies have also shown an increase in CFB at submesoscale (Renault et al., 2018; Chen et al., 2022). Renault et al. (2018) find that CFB dampens submesoscale flows by 17%. They also note an increase in baroclinic energy injection due to the generation of Ekman pumping.

In Chapter 6, we included air-sea interaction in our submesoscale-resolving simulation, but did not specifically investigate the role of TFB or CFB in the submesoscale energy balance. Assessing their contribution would require further coupled air-sea simulations, *e.g.*, removing submesoscale CFB in one simulation and submesoscale TFB in another — this can be done by filtering out the currents or SST fields transferred to the atmospheric model as done by Renault et al. (2019c) for the mesoscale.

Further analysis would be needed to assess how submesoscale ocean dynamics influence the energy balance of the atmosphere on the basis of a Lorenz diagram. This approach would provide valuable information along the lines of that presented by Von Storch et al. (2012).

### Submesoscale influence on inverse energy cascade

At present, there is converging evidence confirming the role of the submesoscale current in energizing the large scale (Qiu et al., 2014; Schubert et al., 2020; Capet et al., 2016; Klein et al., 2008; Contreras et al., 2023b; Balwada et al., 2022; Zhang et al., 2023). It would be interesting to further analyze the relation between this energization and the GS energy sinks. Renault et al. (2019b); Arbic et al. (2013) and Renault et al. (2023a) has shown that an increase in top drag leads to a weaker inverse cascade, *i.e.* a weaker mean and eddy flow, which in turn reduces the initial increase in energy sink (lower top and bottom frictional dissipation). However, these studies did not resolve submesoscale motions. Based on our results, we expect the energizing effect of submesoscales to be partially counterbalanced by an increase in energy sinks, compared to a case with no submesoscales. To test this hypothesis, we could compare two simulations, one with mesoscale resolution and the other with submesoscale resolution. Both simulations should have the same configuration, including the representation of bottom topography.

## Understanding the potential energy pathway

Our results show that potential energy (PE) is a key component of the energy cycle. PE transfers energy to submesoscale and mesoscale KE via baroclinic instability. This transfer from PE is the primary source of submesoscale KE. Yet little attention has been paid to the PE pathway compared to the KE pathway.

A problem faced in the analysis of PE is the definition of APE, since there is no consensus on the definition of APE for the ocean (Huang, 1999). A first step further will be the exploration of alternative definitions (*e.g.*, Molemaker and McWilliams 2010) to assess the PE budget's sensitivity to the choice of APE definition. In addition, future work should explain the energy cascade of potential energy in more detail. This implies the description of the spatial and temporal variability of PE cascade, as well as the mechanisms involved. Furthermore, a more detailed description of the PE sources and sinks should be done, including the analysis of numerical dissipation, possibly by remaining spurious diapycnal mixing in the model (Marchesiello *et al.*, 2009).

## The Energy Cycle in Eastern Boundaries

The aim of this thesis is to understand the path of kinetic energy in the GS, in the hope of contributing to a better prediction of circulation in this region. Nevertheless, some of the results of this study may prove useful in understanding the dynamics of other regions.

A comparable energy pathway can be anticipated in other western boundary currents, especially in the Kuroshio Current, which exhibits dynamics similar to that of the GS. However, our results may not be entirely valid in regions such as eastern boundary currents (EBCs). The dynamics of these regions are different, as they are low-energy, their kinetic energy being almost two orders of magnitude lower than that of the WBCs (the mean current is slow, transporting cool upwelled water to the equator). It is not clear that the EBC energy cycle is driven by the same dominant mechanisms as in WBCs, and that similar, but weaker, energy fluxes and sinks would drive their energy pathway.

The mechanism developed in EBCs may differ from that of WBCs in several ways. Mesoscale eddies are generated throughout the global ocean, but the westward propagation of Rossby waves makes EBC systems more open to the export of eddies (Marchesiello *et al.*, 2003) and therefore different from WBC systems in terms of eddy-mean flow interaction. Although Capet *et al.* (2008d) showed a forward cascade for the California current system (using spectral analysis), we expect it to be weaker than in the GS with its strong eddy activity. On the other hand, intense upwelling develops seasonally along eastern borders, which favors the development of frontogenesis and frontal instabilities. Top drag is of lesser magnitude in EBCs, as is mesoscale EKE, but not in terms of relative importance (Renault *et al.*, 2016a). In fact, the strongly baroclinic nature of currents in these systems necessarily reduces their interaction with the bottom, which should be compensated for by top drag, as recently shown by Renault *et al.* (2023a). Another point of difference is that the heat flux in EBCs is reversed

compared to WBCs, meaning that heat is transferred from the atmosphere to the ocean. This can have an impact on the PE budget, although, as observed in Chapter 6, surface buoyancy flux has a minor contribution to the energy budget.

Future studies should analyze and quantify the energy cycle of EBCs in a way comparable to our GS budget, to broaden our understanding of gyre dynamics. It could also be extended to other regions of the world ocean, in particular the Southern Ocean, which is rich in eddy activity.

### **Expected benefits from the new generation of satellites**

Our analysis requires comparison with observational data, which can be achieved using future generations of satellite altimetry data. The recently launched SWOT (Surface Water and Ocean Topography) altimetry mission is one such source. Data obtained from SWOT altimetry will facilitate the description of motions at scales below 30 km, helping to understand submesoscale effects on ocean dynamics. However, the data can only represent the geostrophic currents, making it impossible to describe the forward cascade of KE. A potential alternative is the Odysea satellite mission (Bourassa et al., 2016; Rodríguez et al., 2018), which aims to consistently measure total surface currents, including geostrophic and ageostrophic components, as well as surface stress. This would make it possible not only to describe the forward cascade, but also to estimate wind work.



# Conclusion et perspectives

## Conclusion

Le Gulf Stream (GS) est un élément crucial du climat mondial et de la circulation océanique. Il s'agit de l'une des régions océaniques les plus énergiques et qui est caractérisée par d'intenses échanges de chaleur, moment et gaz entre l'océan et l'atmosphère. Le GS contribue ainsi à réguler le climat de la Terre.

Le GS a fait l'objet d'études approfondies et a montré une dynamique complexe influencée par de multiples mécanismes à différentes échelles temporelles et spatiales. À grande échelle, la circulation du gyre de l'Atlantique Nord est déterminée par l'équilibre de Sverdrup entre le rotationnel de la tension de vent et la rotation de la Terre (Sverdrup, 1947; Munk, 1950). Cependant, la branche occidentale du gyre (c'est-à-dire le GS) est fortement influencée par la topographie et l'interaction entre les tourbillons et le courant moyen (Kang and Curchitser, 2015; Schoonover et al., 2016; Özgökmen and Chassignet, 2002; Hughes and De Cuevas, 2001; Debreu et al., 2022; Renault et al., 2016a, 2023a).

Les modèles numériques océaniques ont été un outil essentiel pour comprendre la dynamique du GS ; cependant, ils présentent une large dispersion de solutions ainsi que des biais significatifs lorsqu'ils sont comparés aux observations *in situ* et satellite. Ces dernières années, le raffinement de la résolution spatiale dans les modèles numériques a permis une meilleure représentation de l'activité de mésoéchelle et ainsi une nette amélioration de la représentation du GS. Cependant, des biais persistent dans ces simulations, comme par exemple un excès d'énergie cinétique avec comme conséquence un GS trop méandreux et instable. Une compréhension et une représentation réaliste des sources et des puits d'énergie cinétique et potentielle est donc nécessaire pour améliorer les simulations du GS.

La théorie actuelle sur le cycle énergétique des océans est principalement dérivée des observations satellitaires et *in situ* et des modèles numériques, qui ont pu permettre de décrire les échelles spatiales allant de l'échelle planétaire à la mésoéchelle (Ferrari and Wunsch, 2009; Wunsch and Ferrari, 2004; Scott and Wang, 2005). Cependant, des études récentes ont révélé le rôle important des courants à sous-mésoéchelle, bien qu'une compréhension complète de ce phénomène fasse encore défaut (Klein et al., 2019). Le but de cette thèse était ainsi de décrire les routes d'énergie dans le GS ainsi qu'identifier et quantifier les mécanismes qui sont impliqués dans la dissipation de l'énergie de la circulation océanique.

Dans les Chapitres 4 et 5, la cascade d'énergie au niveau du GS est décrite à l'aide d'une série de simulations océaniques forcées à sous-mésoéchelle avec un résolution spatiale de 2 km. Les simulations sont effectuées sans marées (Chapitres 4 et 5) et avec marées (Chapitre 5). L'effet du "Current Feedback", c'est à dire de la rétroaction des courants océaniques sur l'atmosphère (traînée de surface) a été inclue dans les deux simulations en utilisant une paramétrisation proposée par Renault et al. (2019a). Nous avons estimé les flux d'énergie

cinétique entre les échelles spatiales en utilisant la méthode du *coarse-graining* (Aluie et al., 2018). Cette méthode présente de multiples avantages par rapport à l'analyse spectrale. Elle permet non seulement de décrire la variabilité spatiale des flux d'énergie, mais aussi d'éviter les procédures de fenêtrage tout en relâchant les hypothèses d'homogénéité et d'isotropie dans le signal. Nos résultats sont cohérents avec la théorie existante, indiquant qu'il existe une cascade directe aux petites échelles et une cascade inverse aux grandes échelles, mais en apportant des précisions. Nous confirmons pour le GS, par l'utilisation de la décomposition de Helmholtz, que la cascade inverse est induite par les courants géostrophiques ("balanced currents"), tandis que les courants géostrophiques et agéostrophiques interagissent (advection agéostrophique) pour produire une cascade directe vers les petites échelles.

Nous apportons des précisions sur les processus à l'oeuvre dans la variabilité spatiale et saisonnière. Nous montrons que la variation spatiale et temporelle de la cascade d'énergie cinétique dépend des mécanismes dominants des transferts d'énergie. Plus précisément, le Chapitre 4 montre que les variations de la cascade directe suivent celles d'une forte frontogénèse située au niveau de la façade Nord du GS. Par ailleurs, les tourbillons et les fronts de sous-mésoéchelle ont également le potentiel de dynamiser l'activité de mésoéchelle par absorption, un processus qui commence en hiver et intensifie la cascade inverse au printemps. Dans le Chapitre 5, nous montrons que les marées affectent la cascade d'énergie tout au long de l'année, l'impact le plus important se produisant pendant les mois d'été avec une intensification de la cascade directe. Les marées internes (les plus actives en été) semblent être le principal responsable de cette intensification. Notre analyse montre que l'interaction onde-courant domine l'interaction onde-onde (turbulence des ondes). Les mécanismes spécifiques impliqués dans l'interaction onde-courant ne sont pas clairs, mais ils semblent cohérents avec le processus de déséquilibre stimulé proposé par (Barkan et al., 2017), via lequel les ondes internes stimulent un transfert d'énergie des tourbillons de la mésoéchelle à la sous-mésoéchelle.

Les Chapitres 4 et 5 présentent une approche originale visant à quantifier et à comparer les puits d'énergie cinétique du GS. En particulier, la dissipation intérieure, qui résulte de la cascade directe, est comparée aux processus de dissipation numérique et aux processus de dissipation frictionnel aux limites verticales. Nos résultats suggèrent que la dissipation intérieure est d'un ordre de grandeur inférieur à la dissipation frictionnelle en surface et au fond. Il est donc essentiel que les modèles représentent cette dernière avec précision.

De plus, le flux de KE vers les petites échelles est beaucoup plus faible que la dissipation numérique, généralement considérée comme une dissipation sous-maille de l'énergie transférée par la cascade. En conséquence, elle tend à amortir fortement la dynamique de sous-mésoéchelle dans la plage de dissipation du modèle, *i.e.*, la plage définissant sa résolution effective (5-10  $\delta x$  ici). Il semble donc important de maintenir cette plage en dessous du point zéro du flux d'énergie qui sépare la cascade inverse de la cascade directe. Cela peut être le cas lorsque, à une résolution de 2 km, nous utilisons un schéma d'advection de quantité de mouvement du cinquième ordre (UP5), mais pas un schéma du troisième ordre (UP3). Dans ce dernier cas, la dynamisation de la mésoéchelle par la sous-mésoéchelle est compromise. En testant la sensibilité du modèle aux schémas UP5 et UP3 (Chapitre 4), nous constatons, comme prévu, que le schéma d'ordre supérieur est moins dissipatif et que sa plage d'amortissement

apparaît dans un rayon d'environ  $5 \delta x$ . La dissipation est plus importante dans UP3 et affecte un spectre plus large (voir les exemples de spectres de dissipation dans Soufflet et al. (2016)). Cependant, cela n'est pas trop préjudiciable à la solution du modèle, étant donné que le processus d'énergisation (flux de KE vers la mésoéchelle) est relativement faible par rapport à la conversion barocline à mésoéchelle ou à la dissipation en surface et au fond (voir le Chapitre 6 et le résumé ci-dessous). Il est intéressant de noter qu'en utilisant UP5, la diminution de la dissipation numérique est partiellement compensée par une augmentation de la dissipation frictionnelle (moins de dissipation numérique conduit à plus de dissipation en surface et au fond). Par conséquent, l'énergisation de la mésoéchelle est atténuée, si ce n'est par une dissipation numérique artificielle, du moins de manière plus réaliste par des processus physiques (le mélange vertical dans la couche limite et les frictions de fond et de surface). Dans le Chapitre 5, notre étude révèle que les marées conduisent également à une amplification des routes de dissipation, notamment plus importante au fond de l'océan, et une réduction de la cascade inverse. L'activité de mésoéchelle dans le GS est donc réduite par les marées. Une fois de plus, la modification d'un puits d'énergie a un impact sur les autres, qui ne sont pas équivalents du point de vue de leur effet sur la dynamique. Ceci souligne l'importance d'une représentation précise de chaque puits pour maintenir un système énergétiquement équilibré et une circulation réaliste.

Afin d'apporter une compréhension complète des routes d'énergie du GS, le Chapitre 6 examine le cycle énergétique à l'aide d'un diagramme de Lorenz (Lorenz, 1955). Notre approche implique cette fois une simulation couplée océan-atmosphère qui prend ainsi explicitement en compte les mécanismes d'interaction océan-atmosphère, tels que les rétroactions thermique (via la SST) et mécanique (via les courants). Ces dernières peuvent avoir un impact à la fois sur les réservoirs d'énergie cinétique et potentielle. La résolution spatiale de ces simulations océanique et atmosphérique est de 700 m et 2 km, respectivement, avec un domaine de calcul recentré autour du GS.

Nous analysons le budget de l'énergie cinétique et potentielle en utilisant une décomposition de Reynolds pour séparer la sous-mésoéchelle des grandes échelles (planétaires et mésoéchelles) avec une coupure à 16 km. La tension de vent est la principale source externe d'énergie cinétique, injectant de l'énergie à grande échelle. Les flux de chaleur et d'eau douce injectent également de l'énergie potentielle à grande échelle, mais leur contribution est inférieure d'un ordre de grandeur à celle de la tension de vent. L'énergie potentielle à grande échelle alimente l'énergie potentielle à plus fine échelle par une cascade d'énergie potentielle directe entraînée par le brassage des tourbillons de mésoéchelle. L'énergie potentielle alimente ensuite les réservoirs d'énergie cinétique de mésoéchelle et de sous-mésoéchelle par l'intermédiaire de flux verticaux de flottabilité — associés à l'instabilité barocline intérieure et de surface ainsi qu'à la frontogenèse induite par les contraintes de déformation. Ce résultat est important car il montre que la principale source d'énergie cinétique à mésoéchelle est fournie par l'énergie potentielle, plutôt que par le transfert direct de l'énergie cinétique de mésoéchelle (par production de cisaillement).

Avec l'échelle de coupure de 16 km, nous constatons que la production de cisaillement produit en fait un transfert d'énergie cinétique de la sous-mésoéchelle vers la mésoéchelle (cascade

inverse). Cette étude confirme quantitativement que les processus à sous-mésoéchelle contribuent à dynamiser l'échelle supérieure, mais que leur contribution est mineure par rapport, par exemple, à la conversion barocline à mésoéchelle. Ce n'est qu'aux échelles inférieures à 10 km que la cascade de KE change de signe, car l'advection agéostrophique commence à jouer un rôle plus important (Chapitres 2 et 6). L'utilisation d'une échelle de coupure de 8 km pour séparer les réservoirs de sous-mésoéchelle du reste en est la meilleure illustration. Cela signifie que le régime de sous-mésoéchelle peut être séparé en régimes dynamiques quasi-équilibré et déséquilibré, où la divergence des courants détermine la direction des flux inter-échelles. Cependant, une fois encore, ces flux, quelle que soit leur direction, n'ont pas un impact très important sur le budget énergétique, car ils sont mineurs par rapport à la conversion barocline ou aux puits d'énergie. En accord avec le Chapitre 4, nous trouvons également dans le Chapitre 6 une variabilité saisonnière significative dans le budget énergétique, l'hiver étant la saison la plus énergétique.

En résumé, les résultats de cette thèse contribuent à une meilleure connaissance du cycle de l'énergie dans l'océan. Plus spécifiquement, nous avons identifié et quantifié les principales sources et puits d'énergie, ainsi que décrit les interactions d'échelle dans l'océan et les mécanismes impliqués. Ces résultats nous permettent d'améliorer le schéma général du cycle d'énergie dans la circulation océanique (Figure 6.19).

## Perspectives

### Démêler les contributions de CFB et TFB aux bilans d'énergie cinétique et potentielle à sous-mésoéchelle.

Des études récentes indiquent que les interactions océan-atmosphère à sous-mésoéchelle auraient un effet significatif aussi bien pour l'océan que pour l'atmosphère (Strobach et al., 2022; Chen et al., 2022; Bai et al., 2023; Su et al., 2018; Renault et al., 2018). Par exemple, la dynamique de sous-mésoéchelle développe un intense transport vertical de chaleur qui peut modifier les échanges thermiques entre l'océan et l'atmosphère (Su et al., 2018). En utilisant un modèle océanique global (mais forcé) à haute résolution (2 km), Su et al. (2018) a constaté que le transport de chaleur induit par la sous-mésoéchelle était cinq fois plus important que celui produit par la mésoéchelle. Les courants de sous-mésoéchelle pourraient donc avoir un impact significatif sur l'interaction thermique entre l'océan et l'atmosphère, en modifiant les réservoirs d'énergie potentielle et cinétique. Des études antérieures suggèrent également un rôle important de l'interaction mécanique entre les courants et l'atmosphère sur la détermination de l'activité de sous-mésoéchelle (Renault et al., 2018). Renault et al. (2018) ont constaté que cette interaction amortit l'activité de sous-mésoéchelle de 17%. Ils ont également constaté une augmentation de l'injection d'énergie barocline dû au pompage d'Ekman associé au couplage.

Dans le chapitre 6, nous avons développé une simulation couplée qui inclut donc les interactions entre l'océan et l'atmosphère. Cependant, nous n'avons pas étudié spécifiquement

le rôle de ces interactions dans le bilan énergétique à sous-mésoéchelle. L'évaluation de leur contribution nécessiterait d'autres simulations couplées air-mer, *e.g.*, dans lesquelles on pourrait ignorer l'impact de l'interaction thermique ou mécanique en lissant les champs de SST ou de courants de surface envoyés par l'océan à l'atmosphère comme cela a été fait par Renault et al. (2019c) pour la mésoéchelle.

Une analyse plus approfondie serait nécessaire pour évaluer comment la dynamique des océans à sous-mésoéchelle influence le bilan énergétique de l'atmosphère sur la base d'un diagramme de Lorenz. Cette approche fournirait des informations précieuses dans la lignée de celles présentées par Von Storch et al. (2012).

### Influence de la sous-mésoéchelle sur la cascade inverse d'énergie

Actuellement, des preuves convergentes confirment le rôle des courants de sous-mésoéchelle dans l'énergisation des échelles supérieures (Qiu et al., 2014; Schubert et al., 2020; Capet et al., 2016; Klein et al., 2008; Contreras et al., 2023b; Balwada et al., 2022; Zhang et al., 2023).

Il serait intéressant d'analyser plus en détail la relation entre cette énergisation et les puits d'énergie du GS. Renault et al. (2019b); Arbic et al. (2013) et Renault et al. (2023a) ont montré que la prise en compte de la traînée de surface (par l'interaction mécanique entre l'océan et l'atmosphère), entraîne une réduction de la cascade inverse d'énergie. Toutefois, ces études ne prennent pas en compte les processus de sous-mésoéchelle. Sur la base de nos résultats, nous nous attendons à ce que l'effet énergisant de la sous-mésoéchelle soit partiellement contrebalancé par une augmentation des puits d'énergie, par rapport à un cas sans sous-mésoéchelles. Pour tester cette hypothèse, nous pourrions comparer deux simulations, l'une avec une résolution à méso-échelle et l'autre avec une résolution à sous-méso-échelle. Les deux simulations devraient avoir la même configuration, y compris pour la représentation de la topographie.

### Comprendre la voie de l'énergie potentielle

Nos résultats montrent que l'énergie potentielle est un élément clé du cycle énergétique à mésoéchelle et à plus fine échelle. L'énergie potentielle est convertie via l'instabilité barocline, constituant la principale source d'énergie cinétique à mésoéchelle. Cependant, jusqu'à présent, une attention moindre a été accordée à sous-mésoéchelle au chemin d'énergie potentielle par rapport à celui de l'énergie cinétique.

L'un des problèmes rencontrés dans l'analyse de l'énergie potentielle est la définition de l'énergie potentielle disponible (APE), puisqu'il n'y a pas de consensus sur cette définition pour l'océan (Huang, 1999). Une première étape consisterait à explorer d'autres définitions (*e.g.*, Molemaker and McWilliams 2010) afin d'évaluer la sensibilité du budget de l'énergie potentielle au choix de la définition de l'APE. En outre, les travaux futurs devraient expliquer

plus en détail la cascade énergétique de l'énergie potentielle. Cela implique la description de la variabilité spatiale et temporelle de cette cascade, ainsi que des mécanismes impliqués. En outre, une description plus détaillée des sources et des puits d'énergie potentielle devrait être effectuée, y compris l'analyse de la dissipation numérique, en particulier celle du mélange diapycnal artificielle qui subsiste probablement dans le modèle (Marchesiello et al., 2009).

## Le cycle de l'énergie sur les Bord-Est des bassins

L'objectif de cette thèse est de comprendre le cycle de l'énergie cinétique dans le GS, dans l'espoir de contribuer à une meilleure prédiction de la circulation dans cette région. Néanmoins, certains des résultats de cette étude peuvent s'avérer utiles pour comprendre la dynamique d'autres régions.

Un cycle comparable peut être anticipé pour les autres courants de Bord Ouest, en particulier le courant de Kuroshio, qui présente une dynamique similaire à celle du GS. Cependant, nos résultats peuvent ne pas être entièrement valables dans des régions telles que celles des courants de Bord Est (EBCs). La dynamique de ces régions est différente, car elles sont peu énergétiques, leur énergie cinétique étant inférieure de près de deux ordres de grandeur à celle des WBCs (le courant moyen est lent, transportant de l'eau resurgente vers l'équateur). Il n'est pas certain que le cycle énergétique des EBCs soit régi par les mêmes mécanismes dominants que ceux des WBCs, et que les flux et puits d'énergie (nécessairement plus faibles) s'y expriment de manière similaire.

Le mécanisme développé dans les EBCs peut différer de celui des WBCs de plusieurs façons. Les tourbillons de mésoéchelle sont générés comme dans le reste de l'océan, mais la propagation vers l'ouest des ondes de Rossby rend les EBCs plus propices à l'export des tourbillons (Marchesiello et al., 2003) et donc différent des WBCs en termes d'interaction entre tourbillon et courant moyen (avec une cascade inverse éventuellement réduite). Bien que Capet et al. (2008d) ait montré une cascade directe pour le courant de Californie (en utilisant une analyse spectrale), nous nous attendons à ce qu'elle soit plus faible que dans le GS avec sa forte activité tourbillonnaire. Par contre, une intense résurgence d'eau se développe de façon saisonnière le long des Bord Est, ce qui favorise le développement de la frontogenèse et des instabilités frontales. Les puits d'énergie induits par l'interaction des courants avec l'atmosphère sont moins intenses en valeur absolue dans les EBCs (car l'EKE de mésoéchelle est moins forte), mais ce n'est pas le cas en termes relatifs (Renault et al., 2016b,a). Par ailleurs, la nature fortement barocline des courants dans ces systèmes réduit nécessairement leur interaction avec le fond, qui devrait être compensée par la traînée de surface induite par l'interaction courant-vent, comme nous l'avons récemment montré Renault et al. (2023a). Un autre point de différence est que le flux de chaleur dans les EBCs est inversé par rapport aux WBC, ce qui signifie que la chaleur est transférée de l'atmosphère vers l'océan. Cela peut avoir un impact sur le bilan énergétique, même si, comme nous l'avons vu au Chapitre 6, le flux de flottabilité de surface a une contribution mineure au bilan énergétique.

Les études futures devraient analyser et quantifier le cycle énergétique des EBC d'une

manière comparable à notre budget GS, afin d'élargir notre compréhension de la dynamique des gyres. Elles pourraient également être étendues à d'autres régions de l'océan mondial, en particulier à l'océan Austral, qui est riche en activité tourbillonnaire avec un courant moyen particulièrement intense.

### **Bénéfices attendus de la nouvelle génération de satellites**

Notre analyse nécessite une comparaison avec des données observées, ce qui peut être réalisé en utilisant les futures générations de données altimétriques satellitaires. La mission altimétrique SWOT (Surface Water and Ocean Topography) récemment lancée devrait s'avérer utile dans ce sens. Les données obtenues grâce à l'altimétrie SWOT faciliteront la description des mouvements à des échelles inférieures à 30 km, ce qui permettra de comprendre les effets à sous-mésoéchelle sur la dynamique des océans. Cependant, les données ne peuvent représenter que les courants géostrophiques, ce qui rend impossible la description de la cascade directe d'énergie comme nous l'avons démontré dans cette thèse. Une mission complémentaire serait la projet satellite Odysea (Bourassa et al., 2016; Rodríguez et al., 2018), qui vise à mesurer de manière cohérente les courants de surface totaux, y compris les composantes géostrophiques et agéostrophiques, ainsi que la tension de vent. Cela permettrait non seulement de décrire la cascade directe, mais aussi d'estimer les échanges d'énergie entre l'océan et l'atmosphère.



# Bibliography

- Adcroft, A., Marshall, D., 1998. How slippery are piecewise-constant coastlines in numerical ocean models? *Tellus A: Dynamic Meteorology and Oceanography* 50, 95–108.
- Alford, M.H., MacKinnon, J.A., Simmons, H.L., Nash, J.D., 2016. Near-inertial internal gravity waves in the ocean. *Annual review of marine science* 8, 95–123.
- Aluie, H., Eyink, G.L., 2009. Localness of energy cascade in hydrodynamic turbulence. ii. sharp spectral filter. *Physics of Fluids* 21.
- Aluie, H., Hecht, M., Vallis, G.K., 2018. Mapping the energy cascade in the north atlantic ocean: The coarse-graining approach. *Journal of Physical Oceanography* 48, 225–244.
- Arbic, B.K., Flierl, G.R., 2004. Baroclinically unstable geostrophic turbulence in the limits of strong and weak bottom ekman friction: Application to midocean eddies. *Journal of Physical Oceanography* 34, 2257–2273.
- Arbic, B.K., Polzin, K.L., Scott, R.B., Richman, J.G., Shriver, J.F., 2013. On eddy viscosity, energy cascades, and the horizontal resolution of gridded satellite altimeter products. *Journal of Physical Oceanography* 43, 283–300.
- Arbic, B.K., Shriver, J.F., Hogan, P.J., Hurlburt, H.E., McClean, J.L., Metzger, E.J., Scott, R.B., Sen, A., Smedstad, O.M., Wallcraft, A.J., 2009. Estimates of bottom flows and bottom boundary layer dissipation of the oceanic general circulation from global high-resolution models. *Journal of Geophysical Research: Oceans* 114.
- Auer, S.J., 1987. Five-year climatological survey of the gulf stream system and its associated rings. *Journal of Geophysical Research: Oceans* 92, 11709–11726.
- Bai, Y., Thompson, A.F., Villas Bôas, A.B., Klein, P., Torres, H.S., Menemenlis, D., 2023. Sub-mesoscale wind-front interactions: The combined impact of thermal and current feedback. *Geophysical Research Letters* 50, e2023GL104807.
- Balwada, D., Xie, J.H., Marino, R., Feraco, F., 2022. Direct observational evidence of an oceanic dual kinetic energy cascade and its seasonality. *Science Advances* 8, eabq2566.
- Bane Jr, J.M., Dewar, W.K., 1988. Gulf stream bimodality and variability downstream of the charleston bump. *Journal of Geophysical Research: Oceans* 93, 6695–6710.
- Barkan, R., Srinivasan, K., Yang, L., McWilliams, J.C., Gula, J., Vic, C., 2021. Oceanic mesoscale eddy depletion catalyzed by internal waves. *Geophysical Research Letters* 48, e2021GL094376.
- Barkan, R., Winters, K.B., McWilliams, J.C., 2017. Stimulated imbalance and the enhancement of eddy kinetic energy dissipation by internal waves. *Journal of Physical Oceanography* 47, 181–198.

- Barkan, R., Winters, K.B., Smith, S.G.L., 2015. Energy cascades and loss of balance in a reentrant channel forced by wind stress and buoyancy fluxes. *Journal of Physical Oceanography* 45, 272–293.
- Belcher, S., Wood, N., 1996. Form and wave drag due to stably stratified turbulent flow over low ridges. *Quarterly Journal of the Royal Meteorological Society* 122, 863–902.
- Bishop, S., Small, J., Bryan, F., 2020. The global sink of available potential energy by mesoscale air-sea interaction in observations and high-resolution climate models, in: *Ocean Sciences Meeting 2020*, Agu.
- Blumen, W., 1978. Uniform potential vorticity flow: Part i. theory of wave interactions and two-dimensional turbulence. *Journal of the Atmospheric Sciences* 35, 774–783.
- Boccaletti, G., Ferrari, R., Fox-Kemper, B., 2007. Mixed layer instabilities and restratification. *Journal of Physical Oceanography* 37, 2228–2250.
- Bourassa, M.A., Rodriguez, E., Chelton, D., 2016. Winds and currents mission: Ability to observe mesoscale air/sea coupling, in: *Geoscience and Remote Sensing Symposium (IGARSS)*, 2016 IEEE International, IEEE. pp. 7392–7395.
- Brüggemann, N., Eden, C., 2015. Routes to dissipation under different dynamical conditions. *Journal of Physical Oceanography* 45, 2149–2168.
- Bryan, F.O., Böning, C.W., Holland, W.R., 1995. On the midlatitude circulation in a high-resolution model of the north atlantic. *Journal of physical oceanography* 25, 289–305.
- Bryan, F.O., Hecht, M.W., Smith, R.D., 2007. Resolution convergence and sensitivity studies with north atlantic circulation models. part i: The western boundary current system. *Ocean Modelling* 16, 141–159.
- Bryden, H.L., Imawaki, S., 2001. Ocean heat transport. *International Geophysics* 77, 455–474.
- Bryden, H.L., Longworth, H.R., Cunningham, S.A., 2005. Slowing of the atlantic meridional overturning circulation at 25 n. *Nature* 438, 655–657.
- Buckley, M.W., Marshall, J., 2016. Observations, inferences, and mechanisms of the atlantic meridional overturning circulation: A review. *Reviews of Geophysics* 54, 5–63.
- Bühler, O., McIntyre, M.E., 2005. Wave capture and wave–vortex duality. *Journal of Fluid Mechanics* 534, 67–95.
- Callies, J., Ferrari, R., Klymak, J.M., Gula, J., 2015. Seasonality in submesoscale turbulence. *Nature communications* 6, 6862.
- Callies, J., Flierl, G., Ferrari, R., Fox-Kemper, B., 2016. The role of mixed-layer instabilities in submesoscale turbulence. *Journal of Fluid Mechanics* 788, 5–41.
- Cao, H., Fox-Kemper, B., Jing, Z., 2021. Submesoscale eddies in the upper ocean of the kuroshio extension from high-resolution simulation: Energy budget. *Journal of Physical Oceanography* 51, 2181–2201.

- Capet, X., Klein, P., Hua, B.L., Lapeyre, G., McWilliams, J.C., 2008a. Surface kinetic energy transfer in surface quasi-geostrophic flows. *Journal of Fluid Mechanics* 604, 165–174.
- Capet, X., McWilliams, J.C., Molemaker, M.J., Shchepetkin, A.F., 2008b. Mesoscale to submesoscale transition in the california current system. part i: Flow structure, eddy flux, and observational tests. *Journal of physical oceanography* 38, 29–43.
- Capet, X., McWilliams, J.C., Molemaker, M.J., Shchepetkin, A.F., 2008c. Mesoscale to submesoscale transition in the california current system. part ii: frontal processes. *Journal of physical oceanography* 38, 44–64.
- Capet, X., McWilliams, J.C., Molemaker, M.J., Shchepetkin, A.F., 2008d. Mesoscale to submesoscale transition in the california current system. part iii: Energy balance and flux. *Journal of Physical Oceanography* 38, 2256–2269.
- Capet, X., Roulet, G., Klein, P., Maze, G., 2016. Intensification of upper-ocean submesoscale turbulence through charney baroclinic instability. *Journal of Physical Oceanography* 46, 3365 – 3384.
- Charney, J.G., 1971. Geostrophic turbulence. *Journal of the Atmospheric Sciences* 28, 1087–1095.
- Chassignet, E.P., Marshall, D.P., 2008. Gulf stream separation in numerical ocean models. *Geophysical Monograph Series* 177.
- Chassignet, E.P., Xu, X., 2017. Impact of horizontal resolution (1/12 to 1/50) on gulf stream separation, penetration, and variability. *Journal of Physical Oceanography* 47, 1999–2021.
- Chassignet, E.P., Xu, X., Bozec, A., Uchida, T., 2023. Impact of the new england seamount chain on gulf stream pathway and variability. *Journal of Physical Oceanography* .
- Chelton, D.B., Schlax, M.G., Freilich, M.H., Milliff, R.F., 2004. Satellite measurements reveal persistent small-scale features in ocean winds. *science* 303, 978–983.
- Chelton, D.B., Schlax, M.G., Samelson, R.M., 2011. Global observations of nonlinear mesoscale eddies. *Progress in Oceanography* 91, 167–216.
- Chelton, D.B., Wentz, F.J., Gentemann, C.L., de Szoeki, R.A., Schlax, M.G., 2000. Satellite microwave sst observations of transequatorial tropical instability waves. *Geophysical Research Letters* 27, 1239–1242.
- Chen, J., Meneveau, C., Katz, J., 2006. Scale interactions of turbulence subjected to a straining–relaxation–destraining cycle. *Journal of Fluid Mechanics* 562, 123–150.
- Chen, R., Flierl, G.R., Wunsch, C., 2014. A description of local and nonlocal eddy–mean flow interaction in a global eddy-permitting state estimate. *Journal of Physical Oceanography* 44, 2336–2352.
- Chen, X., Dewar, W., Chassignet, E., Bourassa, M., Morey, S., Gopalakrishnan, G., 2022. On the feedback between air-sea turbulent momentum flux and oceanic submesoscale processes. *Journal of Geophysical Research: Oceans* 127, e2022JC018767.

- Colling, A., 2001. Ocean circulation. volume 3. Butterworth-Heinemann.
- Contreras, M., Renault, L., Marchesiello, P., 2023a. Tidal modulation of energy dissipation routes in the gulf stream. *Geophysical Research Letters* 50, e2023GL104946.
- Contreras, M., Renault, L., Marchesiello, P., 2023b. Understanding energy pathways in the gulf stream. *Journal of Physical Oceanography* 53, 719–736.
- Couvelard, X., Marchesiello, P., Gourdeau, L., Lefèvre, J., 2008. Barotropic zonal jets induced by islands in the southwest pacific. *Journal of Physical Oceanography* 38, 2185–2204.
- Craig, A., Valcke, S., Coquart, L., 2017. Development and performance of a new version of the oasis coupler, oasis3-mct\_3.0. *Geoscientific Model Development* 10, 3297–3308.
- Cushman-Roisin, B., Beckers, J.M., 2011. Introduction to geophysical fluid dynamics: physical and numerical aspects. Academic press.
- Debreu, L., Kevlahan, N.R., Marchesiello, P., 2022. Improved gulf stream separation through brinkman penalization. *Ocean Modelling* 179, 102121.
- Debreu, L., Marchesiello, P., Penven, P., Cambon, G., 2012. Two-way nesting in split-explicit ocean models: Algorithms, implementation and validation. *Ocean Modelling* 49, 1–21.
- Dengg, J., 1993. The problem of gulf stream separation: A barotropic approach. *Journal of Physical oceanography* 23, 2182–2200.
- Dewar, W.K., Bane, J.M., 1989. Gulf stream dynamics. part ii: Eddy energetics at 73 w. *Journal of Physical Oceanography* 19, 1574–1587.
- Donlon, C.J., Martin, M., Stark, J., Roberts-Jones, J., Fiedler, E., Wimmer, W., 2012. The operational sea surface temperature and sea ice analysis (ostia) system. *Remote Sensing of Environment* 116, 140–158.
- Ducet, N., Le Traon, P.Y., Reverdin, G., 2000. Global high-resolution mapping of ocean circulation from topex/poseidon and ers-1 and-2. *Journal of Geophysical Research: Oceans* 105, 19477–19498.
- Duda, T.F., Lin, Y.T., Buijsman, M., Newhall, A.E., 2018. Internal tidal modal ray refraction and energy ducting in baroclinic gulf stream currents. *Journal of Physical Oceanography* 48, 1969–1993.
- Dudhia, J., 1989. Numerical study of convection observed during the winter monsoon experiment using a mesoscale two-dimensional model. *Journal of Atmospheric Sciences* 46, 3077–3107.
- Dufau, C., Orszynowicz, M., Dibarboure, G., Morrow, R., Le Traon, P.Y., 2016. Mesoscale resolution capability of altimetry: Present and future. *Journal of Geophysical Research: Oceans* 121, 4910–4927.
- Durrant, D.R., 2010. Numerical methods for fluid dynamics: With applications to geophysics. volume 32. Springer Science & Business Media.

- D'Asaro, E., Lee, C., Rainville, L., Harcourt, R., Thomas, L., 2011. Enhanced turbulence and energy dissipation at ocean fronts. *Science* 332, 318–322.
- Egbert, G.D., Ray, R.D., 2000. Significant dissipation of tidal energy in the deep ocean inferred from satellite altimeter data. *Nature* 405, 775–778.
- Eyink, G.L., 1995a. Exact results on scaling exponents in the 2d enstrophy cascade. *Physical review letters* 74, 3800.
- Eyink, G.L., 1995b. Local energy flux and the refined similarity hypothesis. *Journal of Statistical Physics* 78, 335–351.
- Eyink, G.L., 2005. Locality of turbulent cascades. *Physica D: Nonlinear Phenomena* 207, 91–116.
- Eyink, G.L., Aluie, H., 2009. Localness of energy cascade in hydrodynamic turbulence. i. smooth coarse graining. *Physics of Fluids* 21.
- Ezer, T., 2016. Revisiting the problem of the gulf stream separation: on the representation of topography in ocean models with different types of vertical grids. *Ocean Modelling* 104, 15–27.
- Ezer, T., Atkinson, L.P., Corlett, W.B., Blanco, J.L., 2013. Gulf stream's induced sea level rise and variability along the us mid-atlantic coast. *Journal of Geophysical Research: Oceans* 118, 685–697.
- Fairall, C.W., Bradley, E.F., Hare, J., Grachev, A.A., Edson, J.B., 2003. Bulk parameterization of air–sea fluxes: Updates and verification for the coare algorithm. *Journal of climate* 16, 571–591.
- Ferrari, R., Wunsch, C., 2009. Ocean circulation kinetic energy: Reservoirs, sources, and sinks. *Annual Review of Fluid Mechanics* 41, 253–282.
- Fofonoff, N., 1981. The gulf stream. *Evolution of Physical Oceanography: scientific surveys in honor of Henry Stommel*, 112–139.
- Fox-Kemper, B., Ferrari, R., Hallberg, R., 2008. Parameterization of mixed layer eddies. part i: Theory and diagnosis. *Journal of Physical Oceanography* 38, 1145–1165.
- Frisch, U., 1995. *Turbulence: the legacy of AN Kolmogorov*. Cambridge university press.
- Fu, L.L., 1983. On the wave number spectrum of oceanic mesoscale variability observed by the seasat altimeter. *Journal of Geophysical Research: Oceans* 88, 4331–4341.
- Fu, L.L., Flierl, G.R., 1980. Nonlinear energy and enstrophy transfers in a realistically stratified ocean. *Dynamics of Atmospheres and Oceans* 4, 219–246.
- Garrett, C., Kunze, E., 2007. Internal tide generation in the deep ocean. *Annu. Rev. Fluid Mech.* 39, 57–87.

- Germano, M., 1992. Turbulence: the filtering approach. *Journal of Fluid Mechanics* 238, 325–336.
- Gill, A., Green, J., Simmons, A., 1974. Energy partition in the large-scale ocean circulation and the production of mid-ocean eddies, in: *Deep sea research and oceanographic abstracts*, Elsevier. pp. 499–528.
- Gill, A.E., 1982. *Atmosphere-ocean dynamics*. volume 30. Academic press.
- Glenn, S.M., Ebbesmeyer, C.C., 1994. The structure and propagation of a gulf stream frontal eddy along the north carolina shelf break. *Journal of Geophysical Research: Oceans* 99, 5029–5046.
- Greatbatch, R., Zhai, X., Claus, M., Czeschel, L., Rath, W., 2010a. Transport driven by eddy momentum fluxes in the gulf stream extension region. *Geophysical Research Letters* 37.
- Greatbatch, R.J., Zhai, X., Kohlmann, J.D., Czeschel, L., 2010b. Ocean eddy momentum fluxes at the latitudes of the gulf stream and the kuroshio extensions as revealed by satellite data. *Ocean Dynamics* 60, 617–628.
- Gula, J., Molemaker, M., McWilliams, J., 2015a. Topographic vorticity generation, submesoscale instability and vortex street formation in the gulf stream. *Geophysical Research Letters* 42, 4054–4062.
- Gula, J., Molemaker, M.J., McWilliams, J.C., 2014. Submesoscale cold filaments in the gulf stream. *Journal of Physical Oceanography* 44, 2617–2643.
- Gula, J., Molemaker, M.J., McWilliams, J.C., 2015b. Gulf stream dynamics along the southeastern us seaboard. *Journal of Physical Oceanography* 45, 690–715.
- Gula, J., Molemaker, M.J., McWilliams, J.C., 2016. Submesoscale dynamics of a gulf stream frontal eddy in the south atlantic bight. *Journal of Physical Oceanography* 46, 305–325.
- Haidvogel, D.B., McWilliams, J.C., Gent, P.R., 1992. Boundary current separation in a quasi-geostrophic, eddy-resolving ocean circulation model. *Journal of Physical Oceanography* 22, 882–902.
- Haine, T.W.N., Marshall, J., 1998. Gravitational, symmetric, and baroclinic instability of the ocean mixed layer. *Journal of Physical Oceanography* 28, 634 – 658.
- Hallberg, R., 2013. Using a resolution function to regulate parameterizations of oceanic mesoscale eddy effects. *Ocean Modelling* 72, 92–103.
- Han, J., Pan, H.L., 2011. Revision of convection and vertical diffusion schemes in the ncep global forecast system. *Weather and Forecasting* 26, 520–533.
- Heiderich, J., Todd, R.E., 2020. Along-stream evolution of gulf stream volume transport. *Journal of Physical Oceanography* 50, 2251–2270.

- Hewitt, H.T., Bell, M.J., Chassignet, E.P., Czaja, A., Ferreira, D., Griffies, S.M., Hyder, P., McClean, J.L., New, A.L., Roberts, M.J., 2017. Will high-resolution global ocean models benefit coupled predictions on short-range to climate timescales? *Ocean Modelling* 120, 120–136.
- Hogg, N.G., Johns, W.E., 1995. Western boundary currents. *Reviews of Geophysics* 33, 1311–1334.
- Hogg, N.G., Pickart, R.S., Hendry, R.M., Smethie Jr, W.J., 1986. The northern recirculation gyre of the gulf stream. *Deep Sea Research Part A. Oceanographic Research Papers* 33, 1139–1165.
- Holland, W.R., 1967. On the wind-driven circulation in an ocean with bottom topography. *Tellus* 19, 582–600.
- Holland, W.R., 1973. Baroclinic and topographic influences on the transport in western boundary currents. *Geophysical Fluid Dynamics* 4, 187–210.
- Hong, S.Y., Lim, J.O.J., 2006. The wrf single-moment 6-class microphysics scheme (wsm6). *Asia-Pacific Journal of Atmospheric Sciences* 42, 129–151.
- Hong, S.Y., Noh, Y., Dudhia, J., 2006. A new vertical diffusion package with an explicit treatment of entrainment processes. *Monthly weather review* 134, 2318–2341.
- Hoskins, B., 1974. The role of potential vorticity in symmetric stability and instability. *Quarterly Journal of the Royal Meteorological Society* 100, 480–482.
- Hoskins, B.J., 1982. The mathematical theory of frontogenesis. *Annual review of fluid mechanics* 14, 131–151.
- Hoskins, B.J., Bretherton, F.P., 1972. Atmospheric frontogenesis models: Mathematical formulation and solution. *Journal of the atmospheric sciences* 29, 11–37.
- Hua, B.L., Haidvogel, D.B., 1986. Numerical simulations of the vertical structure of quasi-geostrophic turbulence. *Journal of Atmospheric Sciences* 43, 2923–2936.
- Huang, R.X., 1999. Mixing and energetics of the oceanic thermohaline circulation. *Journal of Physical Oceanography* 29, 727–746.
- Hughes, C.W., de Cuevas, B.A., 2001. Why western boundary currents in realistic oceans are inviscid: A link between form stress and bottom pressure torques. *Journal of Physical Oceanography* 31, 2871 – 2885.
- Hughes, C.W., De Cuevas, B.A., 2001. Why western boundary currents in realistic oceans are inviscid: A link between form stress and bottom pressure torques. *Journal of Physical Oceanography* 31, 2871–2885.
- Hurlburt, H.E., Hogan, P.J., 2000. Impact of 1/8 to 1/64 resolution on gulf stream model–data comparisons in basin-scale subtropical atlantic ocean models. *Dynamics of Atmospheres and Oceans* 32, 283–329.

- Jamet, Q., Deremble, B., Wienders, N., Uchida, T., Dewar, W., 2021. On wind-driven energetics of subtropical gyres. *Journal of Advances in Modeling Earth Systems* 13, e2020MS002329.
- Jamet, Q., Leroux, S., Dewar, W.K., Penduff, T., Le Sommer, J., Molines, J.m., Gula, J., 2022. Non-local eddy-mean kinetic energy transfers in submesoscale-permitting ensemble simulations. *Journal of Advances in Modeling Earth Systems* 14.
- Jousse, A., Hall, A., Sun, F., Teixeira, J., 2016. Causes of wrf surface energy fluxes biases in a stratocumulus region. *Climate Dynamics* 46, 571–584.
- Kang, D., Curchitser, E.N., 2015. Energetics of eddy-mean flow interactions in the gulf stream region. *Journal of Physical Oceanography* 45, 1103–1120.
- Kang, D., Fringer, O., 2010. On the calculation of available potential energy in internal wave fields. *Journal of Physical Oceanography* 40, 2539–2545.
- Keeley, S., Sutton, R., Shaffrey, L., 2012. The impact of north atlantic sea surface temperature errors on the simulation of north atlantic european region climate. *Quarterly Journal of the Royal Meteorological Society* 138, 1774–1783.
- Kelley, D.H., Ouellette, N.T., 2011. Spatiotemporal persistence of spectral fluxes in two-dimensional weak turbulence. *Physics of Fluids* 23.
- Kelly, K.A., Gille, S.T., 1990. Gulf stream surface transport and statistics at 69 w from the geosat altimeter. *Journal of Geophysical Research: Oceans* 95, 3149–3161.
- Kelly, S.M., Lermusiaux, P.F., Duda, T.F., Haley Jr, P.J., 2016. A coupled-mode shallow-water model for tidal analysis: Internal tide reflection and refraction by the gulf stream. *Journal of Physical Oceanography* 46, 3661–3679.
- Kessouri, F., Bianchi, D., Renault, L., McWilliams, J.C., Frenzel, H., Deutsch, C.A., 2020. Submesoscale currents modulate the seasonal cycle of nutrients and productivity in the california current system. *Global Biogeochemical Cycles* 34, e2020GB006578.
- Khatri, H., Griffies, S.M., Uchida, T., Wang, H., Menemenlis, D., 2021. Role of mixed-layer instabilities in the seasonal evolution of eddy kinetic energy spectra in a global submesoscale permitting simulation. *Geophysical Research Letters* 48, e2021GL094777.
- Klein, P., Hua, B.L., Lapeyre, G., Capet, X., Le Gentil, S., Sasaki, H., 2008. Upper ocean turbulence from high-resolution 3d simulations. *Journal of Physical Oceanography* 38, 1748–1763.
- Klein, P., Lapeyre, G., Siegelman, L., Qiu, B., Fu, L.L., Torres, H., Su, Z., Menemenlis, D., Le Gentil, S., 2019. Ocean scale interactions from space. *Earth And Space Science* 6, 795–817.
- Klymak, J.M., 2018. Nonpropagating form drag and turbulence due to stratified flow over large-scale abyssal hill topography. *Journal of Physical Oceanography* 48, 2383–2395.

- Kundu, P.K., Cohen, I.M., Dowling, D.R., 2015. Fluid mechanics. Academic press.
- Kuo, Y.H., Gyakum, J.R., Guo, Z., 1995. A case of rapid continental mesoscale cyclogenesis. part i: Model sensitivity experiments. *Monthly weather review* 123, 970–997.
- Kwon, Y.C., Hong, S.Y., 2017. A mass-flux cumulus parameterization scheme across gray-zone resolutions. *Monthly Weather Review* 145, 583–598.
- Lapeyre, Klein, 2006. Dynamics of the upper oceanic layers in terms of surface quasigeostrophy theory. *Journal of physical oceanography* 36, 165–176.
- Large, W.G., McWilliams, J.C., Doney, S.C., 1994. Oceanic vertical mixing: A review and a model with a nonlocal boundary layer parameterization. *Reviews of geophysics* 32, 363–403.
- Larrañaga, M., Renault, L., Jouanno, J., 2022. Partial control of the gulf of mexico dynamics by the current feedback to the atmosphere. *Journal of Physical Oceanography* 52, 2515–2530.
- Laurindo, L.C., Mariano, A.J., Lumpkin, R., 2017. An improved near-surface velocity climatology for the global ocean from drifter observations. *Deep Sea Research Part I: Oceanographic Research Papers* 124, 73–92.
- Le Provost, C., Lyard, F., 1997. Energetics of the m2 barotropic ocean tides: an estimate of bottom friction dissipation from a hydrodynamic model. *Progress in Oceanography* 40, 37–52.
- Lee, R.W., Woollings, T.J., Hoskins, B.J., Williams, K.D., O'Reilly, C.H., Masato, G., 2018. Impact of gulf stream sst biases on the global atmospheric circulation. *Climate Dynamics* 51, 3369–3387.
- Lemarié, F., 2015. Numerical modification of atmospheric models to include the feedback of oceanic currents on air-sea fluxes in ocean-atmosphere coupled models. Technical Report RT-464. INRIA Grenoble - Rhône-Alpes ; Laboratoire Jean Kuntzmann ; Université de Grenoble I - Joseph Fourier ; INRIA. URL: <https://hal.inria.fr/hal-01184711>.
- Lemarié, F., Debreu, L., Shchepetkin, A., McWilliams, J.C., 2012. On the stability and accuracy of the harmonic and biharmonic isoneutral mixing operators in ocean models. *Ocean Modelling* 52, 9–35.
- Leonard, A., 1975. Energy cascade in large-eddy simulations of turbulent fluid flows, in: *Advances in geophysics*. Elsevier. volume 18, pp. 237–248.
- Lévy, M., Franks, P.J., Smith, K.S., 2018. The role of submesoscale currents in structuring marine ecosystems. *Nature communications* 9, 1–16.
- Lorenz, E.N., 1955. Available potential energy and the maintenance of the general circulation. *Tellus* 7, 157–167.
- Ma, X., Jing, Z., Chang, P., Liu, X., Montuoro, R., Small, R.J., Bryan, F.O., Greatbatch, R.J., Brandt, P., Wu, D., et al., 2016. Western boundary currents regulated by interaction between ocean eddies and the atmosphere. *Nature* 535, 533–537.

- MacKinnon, J.A., Winters, K., 2005. Subtropical catastrophe: Significant loss of low-mode tidal energy at 28.9°. *Geophysical Research Letters* 32.
- Maltrud, M.E., McClean, J.L., 2005. An eddy resolving global 1/10 ocean simulation. *Ocean Modelling* 8, 31–54.
- Marchesiello, P., Capet, X., Menkes, C., Kennan, S.C., 2011. Submesoscale dynamics in tropical instability waves. *Ocean Modelling* 39, 31–46.
- Marchesiello, P., Debreu, L., Couvelard, X., 2009. Spurious diapycnal mixing in terrain-following coordinate models: The problem and a solution. *Ocean Modelling* 26, 156–169.
- Marchesiello, P., McWilliams, J.C., Shchepetkin, A., 2001. Open boundary conditions for long-term integration of regional oceanic models. *Ocean modelling* 3, 1–20.
- Marchesiello, P., McWilliams, J.C., Shchepetkin, A., 2003. Equilibrium structure and dynamics of the california current system. *Journal of Physical Oceanography* 33, 753 – 783.
- de Marez, C., ahaye, N.J., Gula, J., 2020. Interaction of the gulf stream with small scale topography: a focus on lee waves. *Scientific report* 10, 2332.
- Marshall, D.P., Tansley, C.E., 2001. An implicit formula for boundary current separation. *Journal of physical oceanography* 31, 1633–1638.
- Maximenko, N.A., Bang, B., Sasaki, H., 2005. Observational evidence of alternating zonal jets in the world ocean. *Geophysical research letters* 32.
- McWilliams, J.C., 1989. Statistical properties of decaying geostrophic turbulence. *Journal of Fluid Mechanics* 198, 199–230.
- McWilliams, J.C., 2008. The nature and consequences of oceanic eddies. *Ocean modeling in an eddying regime* 177, 5–15.
- McWilliams, J.C., 2016. Submesoscale currents in the ocean. *Proceedings of the Royal Society A: Mathematical, Physical and Engineering Sciences* 472, 20160117.
- McWilliams, J.C., 2021. Oceanic frontogenesis. *Annual Review of Marine Science* 13, 227–253.
- McWilliams, J.C., Gula, J., Molemaker, M.J., 2019. The gulf stream north wall: Ageostrophic circulation and frontogenesis. *Journal of Physical Oceanography* 49.
- Meinen, C.S., Baringer, M.O., Garcia, R.F., 2010. Florida current transport variability: An analysis of annual and longer-period signals. *Deep Sea Research Part I: Oceanographic Research Papers* 57, 835–846.
- Menesguen, C., Le Gentil, S., Marchesiello, P., Ducouso, N., 2018. Destabilization of an oceanic meddy-like vortex : energy transfers and significance of numerical settings. *Journal of Physical Oceanography* 48, 1151–1168.
- Minobe, S., Miyashita, M., Kuwano-Yoshida, A., Tokinaga, H., Xie, S.P., 2010. Atmospheric response to the gulf stream: Seasonal variations. *Journal of Climate* 23, 3699–3719.

- Mlawer, E.J., Taubman, S.J., Brown, P.D., Iacono, M.J., Clough, S.A., 1997. Radiative transfer for inhomogeneous atmospheres: Rrtm, a validated correlated-k model for the longwave. *Journal of Geophysical Research: Atmospheres* 102, 16663–16682.
- Molemaker, M.J., McWilliams, J.C., 2010. Local balance and cross-scale flux of available potential energy. *Journal of Fluid Mechanics* 645, 295–314.
- Molemaker, M.J., McWilliams, J.C., Capet, X., 2010. Balanced and unbalanced routes to dissipation in an equilibrated eady flow. *Journal of Fluid Mechanics* 654, 35–63.
- Morrow, R., Le Traon, P.Y., 2012. Recent advances in observing mesoscale ocean dynamics with satellite altimetry. *Advances in Space Research* 50, 1062–1076.
- Mukul Tewari, N., Tewari, M., Chen, F., Wang, W., Dudhia, J., LeMone, M., Mitchell, K., Ek, M., Gayno, G., Wegiel, J., et al., 2004. Implementation and verification of the unified noah land surface model in the wrf model (formerly paper number 17.5), in: *Proceedings of the 20th conference on weather analysis and forecasting/16th conference on numerical weather prediction*, Seattle, WA, USA.
- Munk, W., Wunsch, C., 1998. Abyssal recipes ii: Energetics of tidal and wind mixing. *Deep Sea Research Part I: Oceanographic Research Papers* 45, 1977–2010.
- Munk, W.H., 1950. On the wind-driven ocean circulation. *Journal of Atmospheric Sciences* 7, 80–93.
- Nakamura, H., Sampe, T., Tanimoto, Y., Shimpo, A., 2004. Observed associations among storm tracks, jet streams and midlatitude oceanic fronts. *Earth's Climate: The Ocean–Atmosphere Interaction*, *Geophys. Monogr* 147, 329–345.
- Nasser, A.A., Madec, G., de Lavergne, C., Debreu, L., Lemarié, F., Blayo, E., 2023. Sliding or stumbling on the staircase: Numerics of ocean circulation along piecewise-constant coastlines. *Journal of Advances in Modeling Earth Systems* 15, e2022MS003594. E2022MS003594 2022MS003594.
- Nikurashin, M., Ferrari, R., 2010. Radiation and dissipation of internal waves generated by geostrophic motions impinging on small-scale topography: Application to the southern ocean. *Journal of Physical Oceanography* 40, 2025–2042.
- Nikurashin, M., Vallis, G.K., Adcroft, A., 2013. Routes to energy dissipation for geostrophic flows in the southern ocean. *Nature Geoscience* 6, 48–51.
- Olson, D.B., Brown, O.B., Emmerson, S.R., 1983. Gulf stream frontal statistics from florida straits to cape hatteras derived from satellite and historical data. *Journal of Geophysical Research: Oceans* 88, 4569–4577.
- Özgökmen, T.M., Chassignet, E.P., 2002. Dynamics of two-dimensional turbulent bottom gravity currents. *Journal of Physical Oceanography* 32, 1460–1478.

- Özgökmen, T.M., Chassignet, E.P., Paiva, A.M., 1997. Impact of wind forcing, bottom topography, and inertia on midlatitude jet separation in a quasigeostrophic model. *Journal of physical oceanography* 27, 2460–2476.
- O’Neill, L.W., Chelton, D.B., Esbensen, S.K., 2010. The effects of sst-induced surface wind speed and direction gradients on midlatitude surface vorticity and divergence. *Journal of Climate* 23, 255–281.
- Paiva, A., Hargrove, J., Chassignet, E., Bleck, R., 1999. Turbulent behavior of a fine mesh (1/12) numerical simulation of the north atlantic. *Journal of marine systems* 21, 307–320.
- Pedlosky, J., 2013. *Geophysical fluid dynamics*. Springer Science & Business Media.
- Penven, P., Echevin, V., Pasapera, J., Colas, F., Tam, J., 2005. Average circulation, seasonal cycle, and mesoscale dynamics of the peru current system: A modeling approach. *Journal of Geophysical Research: Oceans* 110.
- Piomelli, U., Cabot, W.H., Moin, P., Lee, S., 1991. Subgrid-scale backscatter in turbulent and transitional flows. *Physics of Fluids A: Fluid Dynamics* 3, 1766–1771.
- Qiu, B., Chen, S., Klein, P., Sasaki, H., Sasai, Y., 2014. Seasonal mesoscale and submesoscale eddy variability along the north pacific subtropical countercurrent. *Journal of Physical Oceanography* 44, 3079–3098.
- Qiu, B., Nakano, T., Chen, S., Klein, P., 2017. Submesoscale transition from geostrophic flows to internal waves in the northwestern pacific upper ocean. *Nature Communications* 8, 14055.
- Rai, S., Hecht, M., Maltrud, M., Aluie, H., 2021. Scale of oceanic eddy killing by wind from global satellite observations. *Science Advances* 7, eabf4920.
- Rainville, L., Pinkel, R., 2006. Propagation of low-mode internal waves through the ocean. *Journal of Physical Oceanography* 36, 1220–1236.
- Renault, L., Arsouze, T., Ballabrera-Poy, J., 2021. On the influence of the current feedback to the atmosphere on the western mediterranean sea dynamics. *Journal of Geophysical Research: Oceans* 126, e2020JC016664.
- Renault, L., Lemarié, F., Arsouze, T., 2019a. On the implementation and consequences of the oceanic currents feedback in ocean-atmosphere coupled models. *Ocean Modelling* , 101423.
- Renault, L., Marchesiello, P., Contreras, M., 2023a. Coaction of top and bottom drags in gulf stream dynamics. *Journal of Geophysical Research: Oceans* 128, e2022JC018939.
- Renault, L., Marchesiello, P., Masson, S., McWilliams, J.C., 2019b. Remarkable control of western boundary currents by eddy killing, a mechanical air-sea coupling process. *Geophysical Research Letters* 46, 2743–2751.
- Renault, L., Masson, S., Arsouze, T., Madec, G., McWilliams, J.C., 2020. Recipes for how to force oceanic model dynamics. *Journal of Advances in Modeling Earth Systems* 12, e2019MS001715.

- Renault, L., Masson, S., Oerder, V., Colas, F., McWilliams, J., 2023b. Modulation of the oceanic mesoscale activity by the mesoscale thermal feedback to the atmosphere. *Journal of Physical Oceanography* .
- Renault, L., Masson, S., Oerder, V., Jullien, S., Colas, F., 2019c. Disentangling the mesoscale ocean-atmosphere interactions. *Journal of Geophysical Research: Oceans* 124, 2164–2178.
- Renault, L., McWilliams, J.C., Gula, J., 2018. Dampening of submesoscale currents by air-sea stress coupling in the californian upwelling system. *Scientific reports* 8, 1–8.
- Renault, L., McWilliams, J.C., Masson, S., 2017. Satellite observations of imprint of oceanic current on wind stress by air-sea coupling. *Scientific reports* 7, 17747.
- Renault, L., Molemaker, M.J., Gula, J., Masson, S., McWilliams, J.C., 2016a. Control and stabilization of the gulf stream by oceanic current interaction with the atmosphere. *Journal of Physical Oceanography* 46, 3439–3453.
- Renault, L., Molemaker, M.J., McWilliams, J.C., Shchepetkin, A.F., Lemarié, F., Chelton, D., Illig, S., Hall, A., 2016b. Modulation of wind work by oceanic current interaction with the atmosphere. *Journal of Physical Oceanography* 46, 1685–1704.
- Rhines, P.B., 1975. Waves and turbulence on a beta-plane. *Journal of Fluid Mechanics* 69, 417–443.
- Rhines, P.B., 1977. The dynamics of unsteady currents. *The sea* 6, 189–318.
- Risien, C.M., Chelton, D.B., 2008. A global climatology of surface wind and wind stress fields from eight years of quikscat scatterometer data. *Journal of Physical Oceanography* 38, 2379–2413.
- Robinson, A.R., 2012. *Eddies in marine science*. Springer Science & Business Media.
- Rocha, C.B., Gille, S.T., Chereskin, T.K., Menemenlis, D., 2016. Seasonality of submesoscale dynamics in the kuroshio extension. *Geophysical Research Letters* 43, 11–304.
- Rodríguez, E., Wineteer, A., Perkovic-Martin, D., Gál, T., Stiles, B.W., Niamsuwan, N., Monje, R.R., 2018. Estimating ocean vector winds and currents using a ka-band pencil-beam doppler scatterometer. *Remote Sensing* 10, 576.
- Roulet, G., Mcwilliams, J.C., Capet, X., Molemaker, M.J., 2012. Properties of steady geostrophic turbulence with isopycnal outcropping. *Journal of Physical Oceanography* 42, 18–38.
- Roulet Guillaume, K.P., 2009. Available potential energy diagnosis in a direct numerical simulation of rotating stratified turbulence.
- Saba, V.S., Griffies, S.M., Anderson, W.G., Winton, M., Alexander, M.A., Delworth, T.L., Hare, J.A., Harrison, M.J., Rosati, A., Vecchi, G.A., et al., 2016. Enhanced warming of the northwestern atlantic ocean under climate change. *Journal of Geophysical Research: Oceans* 121, 118–132.

- Saenz, J.A., Tailleux, R., Butler, E.D., Hughes, G.O., Oliver, K.I., 2015. Estimating Lorenz's reference state in an ocean with a nonlinear equation of state for seawater. *Journal of Physical Oceanography* 45, 1242–1257.
- Salmon, R., 1980. Baroclinic instability and geostrophic turbulence. *Geophysical & Astrophysical Fluid Dynamics* 15, 167–211.
- Sanchez-Franks, A., Flagg, C., Rossby, T., 2014. A comparison of transport and position between the Gulf Stream east of Cape Hatteras and the Florida Current. *Journal of Marine Research* 72, 291–306.
- Sasaki, H., Klein, P., Qiu, B., Sasai, Y., 2014. Impact of oceanic-scale interactions on the seasonal modulation of ocean dynamics by the atmosphere. *Nature Communications* 5, 5636.
- Schoonover, J., Dewar, W., Wienders, N., Gula, J., McWilliams, J.C., Molemaker, M.J., Bates, S.C., Danabasoglu, G., Yeager, S., 2016. North Atlantic barotropic vorticity balances in numerical models. *Journal of Physical Oceanography* 46, 289–303.
- Schoonover, J., Dewar, W.K., Wienders, N., Deremble, B., 2017. Local sensitivities of the Gulf Stream separation. *Journal of Physical Oceanography* 47, 353–373.
- Schubert, R., Gula, J., Greatbatch, R.J., Baschek, B., Biastoch, A., 2020. The submesoscale kinetic energy cascade: Mesoscale absorption of submesoscale mixed layer eddies and frontal downscale fluxes. *Journal of Physical Oceanography* 50, 2573–2589.
- Scott, R.B., Arbic, B.K., 2007. Spectral energy fluxes in geostrophic turbulence: Implications for ocean energetics. *Journal of Physical Oceanography* 37, 673–688.
- Scott, R.B., Wang, F., 2005. Direct evidence of an oceanic inverse kinetic energy cascade from satellite altimetry. *Journal of Physical Oceanography* 35, 1650–1666.
- Scott, R.B., Xu, Y., 2009. An update on the wind power input to the surface geostrophic flow of the world ocean. *Deep Sea Research Part I: Oceanographic Research Papers* 56, 295–304.
- Seidov, D., Mishonov, A., Reagan, J., Parsons, R., 2019. Resilience of the Gulf Stream path on decadal and longer timescales. *Scientific Reports* 9, 11549.
- Sen, A., Scott, R.B., Arbic, B.K., 2008. Global energy dissipation rate of deep-ocean low-frequency flows by quadratic bottom boundary layer drag: Computations from current-meter data. *Geophysical Research Letters* 35.
- Seo, H., O'Neill, L.W., Bourassa, M.A., Czaja, A., Drushka, K., Edson, J.B., Fox-Kemper, B., Frenger, I., Gille, S.T., Kirtman, B.P., et al., 2023. Ocean mesoscale and frontal-scale ocean–atmosphere interactions and influence on large-scale climate: A review. *Journal of Climate* 36, 1981–2013.

- Shakespeare, C.J., Taylor, J., 2014. The spontaneous generation of inertia–gravity waves during frontogenesis forced by large strain: Theory. *Journal of fluid mechanics* 757, 817–853.
- Shchepetkin, A., McWilliams, J., 2003. A method for computing horizontal pressure-gradient force in an oceanic model with a nonaligned vertical coordinate. *Journal of Geophysical Research C: Oceans* 108, 35–1.
- Shchepetkin, A.F., McWilliams, J.C., 2005. The regional oceanic modeling system (roms): a split-explicit, free-surface, topography-following-coordinate oceanic model. *Ocean modelling* 9, 347–404.
- Shchepetkin, A.F., McWilliams, J.C., 2009. Correction and commentary for “ocean forecasting in terrain-following coordinates: Formulation and skill assessment of the regional ocean modeling system” by haidvogel et al., *j. comp. phys.* 227, pp. 3595–3624. *Journal of Computational Physics* 228, 8985–9000.
- Siegelman, L., 2020. Energetic submesoscale dynamics in the ocean interior. *Journal of Physical Oceanography* 50, 727–749.
- da Silva, A.M., Young, C.C., Levitus, S., 1994. Atlas of surface marine data 1994, volume 1: algorithms and procedures .
- Skamarock, W.C., Klemp, J.B., Dudhia, J., Gill, D.O., Barker, D.M., Duda, M.G., Huang, X.Y., Wang, W., Powers, J.G., et al., 2008. A description of the advanced research wrf version 3. NCAR technical note 475, 113.
- Small, R.d., deSzoeke, S.P., Xie, S., O’neill, L., Seo, H., Song, Q., Cornillon, P., Spall, M., Minobe, S., 2008. Air–sea interaction over ocean fronts and eddies. *Dynamics of Atmospheres and Oceans* 45, 274–319.
- Smith, K.S., Vallis, G.K., 2001. The scales and equilibration of midocean eddies: Freely evolving flow. *Journal of Physical Oceanography* 31, 554–571.
- Smith, R.D., Maltrud, M.E., Bryan, F.O., Hecht, M.W., 2000. Numerical simulation of the north atlantic ocean at 1/10. *Journal of Physical oceanography* 30, 1532–1561.
- Soufflet, Y., Marchesiello, P., Lemarié, F., Jouanno, J., Capet, X., Debreu, L., Benshila, R., 2016. On effective resolution in ocean models. *Ocean Modelling* 98, 36–50.
- Spall, M.A., 1996. Dynamics of the gulf stream/deep western boundary current crossover. part i: Entrainment and recirculation. *Journal of physical oceanography* 26, 2152–2168.
- Srinivasan, K., Barkan, R., McWilliams, J.C., 2022. A forward energy flux at submesoscales driven by frontogenesis. *Earth and Space Science Open Archive* , 41.
- Srinivasan, K., McWilliams, J.C., Molemaker, M.J., Barkan, R., 2019. Submesoscale vortical wakes in the lee of topography. *Journal of Physical Oceanography* 49, 1949–1971.
- Stewart, R.H., 2008. Introduction to physical oceanography. Robert H. Stewart.

- Stommel, H., 1948. The westward intensification of wind-driven ocean currents. *Eos, Transactions American Geophysical Union* 29, 202–206.
- Strobach, E., Klein, P., Molod, A., Fahad, A.A., Trayanov, A., Menemenlis, D., Torres, H., 2022. Local air-sea interactions at ocean mesoscale and submesoscale in a western boundary current. *Geophysical Research Letters* 49, e2021GL097003.
- Su, Z., Torres, H., Klein, P., Thompson, A.F., Siegelman, L., Wang, J., Menemenlis, D., Hill, C., 2020. High-frequency submesoscale motions enhance the upward vertical heat transport in the global ocean. *Journal of Geophysical Research: Oceans* 125, e2020JC016544.
- Su, Z., Wang, J., Klein, P., Thompson, A.F., Menemenlis, D., 2018. Ocean submesoscales as a key component of the global heat budget. *Nature communications* 9, 1–8.
- Sverdrup, H.U., 1947. Wind-driven currents in a baroclinic ocean; with application to the equatorial currents of the eastern pacific. *Proceedings of the National Academy of Sciences* 33, 318–326.
- Talandier, C., Deshayes, J., Treguier, A.M., Capet, X., Benshila, R., Debreu, L., Dussin, R., Molines, J.M., Madec, G., 2014. Improvements of simulated western north atlantic current system and impacts on the amoc. *Ocean Modelling* 76, 1–19.
- Tansley, C.E., Marshall, D.P., 2000. On the influence of bottom topography and the deep western boundary current on gulf stream separation. *Journal of marine research* 58, 297–325.
- Thomas, L.N., 2012. On the effects of frontogenetic strain on symmetric instability and inertia-gravity waves. *Journal of Fluid Mechanics* 711, 620–640.
- Thomas, L.N., Lee, C.M., 2005. Intensification of ocean fronts by down-front winds. *Journal of Physical Oceanography* 35, 1086–1102.
- Thomas, L.N., Taylor, J.R., Ferrari, R., Joyce, T.M., 2013. Symmetric instability in the gulf stream. *Deep Sea Research Part II: Topical Studies in Oceanography* 91, 96–110.
- Thorpe, S.A., 2005. *The turbulent ocean*. Cambridge University Press.
- Tiedtke, M., 1989. A comprehensive mass flux scheme for cumulus parameterization in large-scale models. *Monthly weather review* 117, 1779–1800.
- Tomczak, M., Godfrey, J.S., 2003. *Regional oceanography: an introduction*. Daya books.
- Tomita, H., Kutsuwada, K., Kubota, M., Hihara, T., 2021. Advances in the estimation of global surface net heat flux based on satellite observation: J-ofuro3 v1. 1. *Frontiers in Marine Science* 8, 612361.
- Torres, H.S., Klein, P., Menemenlis, D., Qiu, B., Su, Z., Wang, J., Chen, S., Fu, L.L., 2018. Partitioning ocean motions into balanced motions and internal gravity waves: A modeling study in anticipation of future space missions. *Journal of Geophysical Research: Oceans* 123, 8084–8105.

- Tréguier, A.M., Deshayes, J., Lique, C., Dussin, R., Molines, J.M., 2012. Eddy contributions to the meridional transport of salt in the north atlantic. *Journal of Geophysical Research: Oceans* 117.
- Trossman, D.S., Arbic, B.K., Straub, D.N., Richman, J.G., Chassignet, E.P., Wallcraft, A.J., Xu, X., 2017. The role of rough topography in mediating impacts of bottom drag in eddying ocean circulation models. *Journal of physical oceanography* 47, 1941–1959.
- Tulloch, R., Marshall, J., Hill, C., Smith, K.S., 2011. Scales, growth rates, and spectral fluxes of baroclinic instability in the ocean. *Journal of Physical Oceanography* 41, 1057–1076.
- Uchida, T., Balwada, D., Abernathey, R., McKinley, G., Smith, S., Levy, M., 2019. The contribution of submesoscale over mesoscale eddy iron transport in the open southern ocean. *Journal of Advances in Modeling Earth Systems* 11, 3934–3958.
- Uchida, T., Le Sommer, J., Stern, C., Abernathey, R.P., Holdgraf, C., Albert, A., Brodeau, L., Chassignet, E.P., Xu, X., Gula, J., et al., 2022. Cloud-based framework for inter-comparing submesoscale-permitting realistic ocean models. *Geoscientific Model Development* 15, 5829–5856.
- Vallis, G.K., 2017. *Atmospheric and oceanic fluid dynamics*. Cambridge University Press.
- Von Arx, W., Bumpus, D., Richardson, W., 1955. On the fine-structure of the gulf stream front. *Deep Sea Research (1953)* 3, 46–65.
- Von Storch, J.S., Eden, C., Fast, I., Haak, H., Hernández-Deckers, D., Maier-Reimer, E., Marotzke, J., Stammer, D., 2012. An estimate of the lorenz energy cycle for the world ocean based on the storm/ncep simulation. *Journal of physical oceanography* 42, 2185–2205.
- Vreman, B., Geurts, B., Kuerten, H., 1994. Realizability conditions for the turbulent stress tensor in large-eddy simulation. *Journal of Fluid Mechanics* 278, 351–362.
- Warren, B.A., 1963. Topographic influences on the path of the gulf stream. *Tellus* 15, 167–183.
- Weatherly, G.L., 1984. An estimate of bottom frictional dissipation by gulf stream fluctuations. *Journal of marine research* 42, 289–301.
- Webster, F., 1961. The effect of meanders on the kinetic energy balance of the gulf stream. *Tellus* 13, 392–401.
- Wenegrat, J.O., Thomas, L.N., Sundermeyer, M.A., Taylor, J.R., D’Asaro, E.A., Klymak, J.M., Shearman, R.K., Lee, C.M., 2020. Enhanced mixing across the gyre boundary at the gulf stream front. *Proceedings of the National Academy of Sciences* 117, 17607–17614.
- Winters, K.B., Lombard, P.N., Riley, J.J., D’Asaro, E.A., 1995. Available potential energy and mixing in density-stratified fluids. *Journal of Fluid Mechanics* 289, 115–128.
- Wunsch, C., Ferrari, R., 2004. Vertical mixing, energy, and the general circulation of the oceans. *Annu. Rev. Fluid Mech.* 36, 281–314.

- 
- Xu, Y., Fu, L.L., 2012. The effects of altimeter instrument noise on the estimation of the wavenumber spectrum of sea surface height. *Journal of Physical Oceanography* 42, 2229–2233.
- Zhang, C., Wang, Y., Hamilton, K., 2011. Improved representation of boundary layer clouds over the southeast pacific in arw-wrf using a modified tiedtke cumulus parameterization scheme. *Monthly Weather Review* 139, 3489–3513.
- Zhang, R., Vallis, G.K., 2007. The role of bottom vortex stretching on the path of the north atlantic western boundary current and on the northern recirculation gyre. *Journal of Physical Oceanography* 37, 2053–2080.
- Zhang, Z., Liu, Y., Qiu, B., Luo, Y., Cai, W., Yuan, Q., Liu, Y., Zhang, H., Liu, H., Miao, M., et al., 2023. Submesoscale inverse energy cascade enhances southern ocean eddy heat transport. *Nature Communications* 14, 1335.

